MODELLING INTERACTIONS OF ATMOSPHERIC PRESSURE PLASMAS WITH LIQUIDS

by

Wei Tian

A dissertation submitted in partial fulfillment
of the requirements for the degree of
Doctor of Philosophy
(Nuclear Engineering and Radiological Sciences)
in the University of Michigan
2015

Doctoral Committee:

Professor Mark J. Kushner, Chair
Professor Iain D. Boyd
Professor John E. Foster
Professor Yue Ying Lau
Professor Alexander Thomas

To those who always stand by me.
Thank for your continued support and encouragement.
To share this great moment with my loved ones.

ACKNOWLEDGEMENTS

I would never have been able to finish my dissertation without the guidance of my committee members, help from my friends, and support from my family and girlfriend. I would like to express my deepest gratitude to my advisor, Dr. Mark J. Kushner, for his hands-on and visionary guidance, caring and patience. His guidance was as micro as typing two spaces after a period and as macro as pointing the future of my research. I kept his words in my mind, "By finishing this, you won't be rich but you'll be famous!" and I still wish the day comes. I am grateful to him. He provided me with great opportunities to get exposure to the plasma community. During the Ph.D. study, I attended 18 conferences, symposia, and international workshops. I fortunately got inspiring comments and feedbacks from the world's top researchers, and even involved in discussion on the future of our field. He is the most diligent and enthusiastic researcher I've ever known. He is always passionate, hardworking and eager about contributing to this society and guiding his students. During the weekdays and weekends, he was helping me debugging codes, revising papers, and giving board talks. It was his working so hard that made it possible for me to complete my degree.

A great deal of credit is due to my dissertation committee: Dr. Iain D. Boyd, Dr. John E. Foster, Dr. Yue Ying Lau, and Dr. Alexander Thomas for serving on my committee and all the insightful comments they provided me throughout the process; this work would not be possible without their help.

To my current and former labmates: Mingmei Wang, Sang-Heon Song, Michael Logue, Jun-Chieh Wang, Seth Norberg, Pen Tian, Yiting Zhang; Shuo Huang, Amanda Lietz, Chenhui Qu, their companionship was invaluable. Special thanks go to Dr. Zhongmin Xiong and Dr. Natalia Babaeva for all the guidance and conversations we had; thanks to Julia for helping me through all the processes and paper work.

I would like to thank my parents for supporting me from the other side of ocean and aiding for me these days so that I can concentrate on my dissertation. Thanks to my girlfriend, Yijin Wu, as well for encouraging me at hard times, caring me and sharing the life moments.

I also give my thanks to the snowy long winter in Ann Arbor, I therefore spent longer time on research and communicating with colleagues.

I wish to thank all my wonderful friends for being always right behind me. Because of them, the road to the doctor degree was filled with joy and surprise. I cherish all the great moments we shared: stupid drinking game at parties, BBQs at Gallup Park, studying at library, catching the deadlines-I will carry that along with me.

TABLE OF CONTENTS

LIST OF TABLES

LIST OF FIGURES

ABSTRACT

Plasmas in contact with water are being widely investigated for their ability to produce chemically reactive species, energetic photons and localized high electric field for environmental and biomedical applications, like water purification and medical treatment. Understanding the interaction of plasma with liquid still remains a challenge due to the complexity induced by multiphases (gas phase and liquid phase) and temporal scales (from nanoseconds to minutes), and the difficulty of quantitative diagnostics on the plasma dynamics and aqueous species. In this thesis, results from a computational investigation of plasmas in contact with liquids are discussed with the goal of improving our fundamental understanding of the interaction of plasma with liquid, and to suggest ways to control outcomes in applications of interest. In this thesis, the following problems are discussed:

Plasmas in bubbles in water are used for water purification with the advantage of low electric field compared to direct breakdown inside liquid, where extremely high electric field is required, on the order of MV/cm. Bubbles are created artificially by inletting gases through nozzles. The characteristics of the discharges in bubbles in water are discussed for bubbles of 2 mm in diameter with filled gases of He, Ar and N_2. After breakdown in bubbles, the discharge develops along the bubble-liquid interface and intersects the water vapor evaporated from the liquid surface. This surface hugging behavior is important for production of chemically reactive species. Images and optical spectra from computational results are compared to experiments. Plasma emission are found to depend in large part on electron impact dissociative excitation of water vapor, electron impact excitation of dissociation products and excitation transfer from the plasma excited injected bubble gases to water vapor. Variations in the contributions of these processes are responsible for differences in the observed optical spectra and differences in radical production.

Atmospheric dielectric barrier discharges (DBDs) in treatment of liquid covered tissue are used for medical treatment, like skin disinfection and chronic wound healing. Tissue is often covered by a thin layer of liquid, which is typically hundreds of microns thick and serum-like water containing dissolved gases, salts and organic substances. The characteristics of the atmospheric DBDs interacting with liquid layer covered tissue are discussed. The breakdown and avalanche of the discharge act like traditional DBDs. When the plasma reaches the liquid, the plasma produced species are solvated and initiate aqueous reactions. Incident electron and ions lose their kinetic energy and instantaneously solvate in the liquid. The dissolution rates of neutral species are determined by Henry's law equilibrium. UV/VUV photons also reach the liquid resulting in ionization and dissociation of water molecules. Both short-lived radicals, like hydroxyl and superoxide, and long-lived reactive species, like hydrogen peroxide and ozone, are observed and their production pathways are discussed. The pH value of the liquid is reduced by the DBDs treatment. The fluences of reactive species to the underlying tissue are recorded and found to be sensitive to dissolved oxygen, alkane-like hydrocarbons, UV/VUV photons and the thickness of liquid layer.

The plasma dose, which is determined by the fluences of reactive radicals, is crucial for tissue treatment. Overdose could result in normal cell death while insufficient dose cannot kill bacteria. The characteristics of liquid covered tissue treatment by a 100-pulse atmospheric DBDs followed by a 10 second afterglow are discussed. The multipulse DBDs are operated in two schemes, a stationary scheme where the plasma streamer strikes at the same location of the liquid layer and a random scheme where the plasma streamer randomly strikes at the liquid layer. The two schemes result in different fluences into the underlying tissue in terms of uniformity. The alternation of characteristics of the liquid layer is observed after multipulses. The liquid layer is acidified and the power of peroxynitrite is enhanced. The conductivity of the liquid layer is increased and will possibly affect the discharge. The liquid layer becomes ozone-rich and nitrous acid will be slowly converted to nitric acid by ozone. The frequency of multipulse DBDs is found to influence the interaction between pulses. Higher frequency enhances the interactions between pulses; and vice versa.

CHAPTER 1 INTRODUCTION

The use of atmospheric pressure plasmas has expanded from traditional applications such as plasma display panels (PDP), UV/VUV photon sources, and plasma-assisted combustion, to more recently in liquid-related applications in environmental cleaning such as water purification and removal of hazardous materials and plasma medicine such as wound healing and cancer treatment. The atmospheric pressure plasmas in and in contact with liquids have their unique advantages such as the ability to produce a mixed cocktail of reactive species, UV/VUV photons and strong electric fields, and to access small spaces. Specifically, bactericidal deactivation found in atmospheric pressure plasmas is extremely beneficial in biomedical treatment.

Although plasmas are relatively easy to generate at atmospheric pressure, it is extremely complex to generate them when liquids are involved. The characteristics of plasmas in chemistry and dynamics are affected by liquids. In this thesis, a numerical simulation is used to increase our fundamental understanding of the interaction of plasmas with liquids and to provide directions for applications of interest. In this chapter, liquid-related applications, fundamentals of atmospheric pressure plasmas, and the interaction of plasmas with liquids will be introduced.

1.1 Overview of plasmas

Plasmas, also called the fourth state of matter, consist of charged and neutral particles, which exhibit quasi-neutrality and collective behavior.[1-4] Almost 99% of the matter in the

visible universe is in the plasma state, which covers a wide range of pressures, temperatures, and electron densities. The classification of plasmas is shown in Fig. 1.1. Plasma is usually produced through ionization with the atoms or molecules dissociated into electrons, positive ions, and negative ions. Although there are free charges and ambipolar pairs in plasmas, negative and positive charges compensate each other and hence plasmas maintain quasi-neutrality.[2] A gas can be either completely ionized or weakly ionized. A certain degree of ionization is necessary for a gas to exhibit electromagnetic properties like electrical conductivity and to behave as a plasma. In thermal equilibrium, the degree of ionization is determined by the Saha equation [3] and a temperature. Thermal equilibrium refers to the state in which all particles are at the same temperature by having sufficient collisions. Examples include the natural fusion reactor (the Sun) and arcs as used in street lamps.[1] A plasma can also be in non-thermal equilibrium, in which the temperature of heavy particles is much lower than the electron temperature.[1,3]

In non-equilibrium plasmas, also known as low temperature plasma, the temperature of heavy particles normally ranges from 300 K to 1,000 K while the electron temperature can reach as high as above 10,000 K to 50,000 or 1 eV to 5 eV.[4] The momentum transfer between electrons and heavy particles is not sufficient to equilibrate temperatures. The power applied to plasmas favors electrons. Hence, electron temperature is considerably higher than the temperature of neutrals and ions. Additionally, the electron-induced de-excitation rate of the heavy particles is generally lower than the corresponding electron-induced excitation rate, because of a significant radiative de-excitation rate.[5] Therefore, the electron energy distribution departs from a Maxwellian distribution. Examples include corona discharges and glow discharges. In spite of the high electron temperature, the kinetic energy carried by electrons is still low due to their small mass and therefore the plasma is only partially ionized.

This benefits applications of low temperature plasmas that come in contact with heat-sensitive materials such as textile and biomedical tissue, which cannot resist high temperatures. The degree of ionization of low temperature plasmas varies usually from 10^{-4} to 10^{-2}.[3,4] Therefore, neutral particles dominate the gas and so do the collisions with neutral particles.

Low temperature plasmas can be classified by the operating pressure as low pressure plasmas and high pressure plasmas. Low pressure plasmas have been widely used for surface treatment of solid materials.[6] In most low pressure plasmas, the pressure ranges from 1 mTorr to 1 Torr, with the corresponding electron density ranging from 10^{8} to 10^{13} cm^{-3}. At low pressure, a uniform plasma can be produced in large volumes favoring industrial applications like wafer etching and film deposition.[6] High pressure plasmas usually operate at pressures from above 100 Torr. One of the widely used high pressure plasmas is atmospheric pressure plasma. This has technical significance, because in contrast with low pressure plasmas, no reaction vessel is required to maintain a pressure level.

Atmospheric pressure plasmas have widespread applications such as ozone production[7,8], nanoparticle synthesis[9,10], surface functionalization of materials[11,12], and disinfection.[13,14] In the gas phase, a conductive channel will be formed rapidly when a sufficient voltage is applied. The minimum required voltage is called breakdown voltage. The breakdown voltage is governed by Paschen's curve, which is shown in Fig. 1.2 for air, helium, argon, neon, hydrogen, and nitrogen.[15] At atmospheric pressure, the breakdown voltage is extremely high at small or large electrode distance and the lowest voltage requires a specific distance. For air, the minimum breakdown voltage is about 327 V at 7.5 μm, which is about 0.45 MV/cm. At atmospheric pressure, the mean free paths between electrons and heavy particles are so short that plasmas are collision-dominated and often confined to a small volume.

1.2 Atmospheric Pressure Dielectric Barrier Discharge

The dielectric barrier discharge (DBD) at atmospheric pressure is a widely used type of atmospheric pressure plasma. A dielectric barrier is used to limit electric current and prevent spark formation [4,6], which is accompanied by local overheating and generation of local shock waves and noise. Hence DBD is also known as a "silent" discharge. Typical DBD configurations are shown in Fig. 1.3. A DBD device usually has one or more dielectric barriers, which are located in the current path between metal electrodes. The dielectric barrier can be made from glass, quartz, ceramics, water, or other materials of low dielectric loss and high breakdown strength. The breakdown voltage of a DBD is determined by Paschen's law, which also depends on the gas mixture. The gap of a DBD is typically from 0.1 mm to 10's cm, and the driving frequencies typically ranges from 1 Hz to 10's MHz. For a DBD gap of a few mm, the required AC driving voltage with frequency 500 Hz to 500 kHz is typically about 10 kV in air.[3]

An atmospheric pressure DBD usually consists of a large number of current filaments which are also known as streamers.[16,17] A snapshot of DBD in a 1 mm air gap photographed through a transparent dielectric is shown in Fig. 1.4(a). The dots represent the end-view of the streamers, which spread over the whole DBD zone uniformly. Another example can be seen in Fig. 1.4(b) on side-view, in which the streamers can be seen clearly. The streamers are usually produced under conditions such as in a large gap, higher pressure, or applied with overvoltage (applied voltage above the breakdown voltage). After applied voltage, a streamer starts with an electron avalanche between electrodes. The initial electrons, which could result from space free charges, emission from dielectrics, or laser induced ionizations, drift along the electric field, gain energy, and ionize the gas to produce more electrons. This multiplication of electrons in cascade

ionization is called an avalanche. At this stage, the applied electric field is not disturbed by space charges produced by the avalanche. As the avalanche develops and the electron density increases, the space-charge effect becomes important. The applied electric field is affected in a large part by the electric field induced by the space charges. A strong electric field, which can be higher than the external electric field, is formed in front of the avalanche head, where the significant space charges lie. Ionizations induced by this electric field then produce more electrons, which sustain the process. At this point, the avalanche starts to transform into a streamer, a self-sustained, thin and local plasma channel. The streamer finally reaches one or both electrodes and then forms a conductive channel. There are two typical streamers, negative streamer and positive streamer, shown in Fig. 1.5. Positive streamer starts from the anode and propagates towards the cathode. Although the electric field is strong at the head of the streamer, the propagation of the streamer also relies on the electrons produced ahead of the streamer. These electrons can be produced by photoionization or the electron detachment process near the anode, or photoemission from the cathode. A negative streamer starts from the cathode and propagates towards the anode. Since the electrons drift along with the streamer, fast electrons moving in front of the streamer start the cascade making the photon source unnecessary. Positive and negative streamers can occur at the same time in opposite directions if the streamer starts at the middle of the gap. The positive streamer propagates towards the cathode, while the negative streamer propagates towards the anode.[4,18]

The evolution of a DBD is based on the birth and death of streamers, and is shown in Fig. 1.6. After the voltage is applied, streamers are produced in a DBD. During the voltage cycle, streamers develop and propagate towards the opposite surface depending on the polarity of the voltage. When streamers strike the dielectric, the dielectric surface is electrically charged and

the local potential drop across the gap is reduced. Once the gap voltage drops below the self-sustaining value, the streamer extinguishes. Depending on the AC frequency, the surface charges on the dielectrics and the residual metastable species in the gap can last up to the next cycle and assist with the production of the following streamers. When the polarity changes on the next cycle, streamers are formed and propagate backwards to the other dielectric surface. They then follow the same process, thereby forming a DBD. [19-21]

Due to a different structure, power supply, plasma temperature, and gas composition, DBDs can be used in various applications such as gas cleaning (removal of volatile organic and inorganic compounds)[22,23], gas synthesis (production of hydrocarbons and ozone)[24,25], material processing (surface cleaning, activation and coating)[26-28], and UV/VUV photon sources.[29,30] Currently, DBDs are being used in environmental and biomedical applications, which will be discussed in Sec. 1.4 and 1.5.

1.3 Plasmas interacting with liquids

The recent increase of interest in plasmas applied to environmental and biomedical applications introduces liquids to plasmas. Plasmas interacting with liquids such as water are able to produce a variety of reactive products. Plasma produced energetic electrons, ions, free radicals, and UV/VUV photons, [31,32], which in contact with water produce active species in liquids. These reactive products can either directly act on the targets or produce radicals by further reacting with water molecules. Therefore, plasmas in contact with liquids have a strong capacity to oxidize, which is often referred to as an advance oxidation technology to remove organic and inorganic substances in water.[33,34] In the last two decades, applications have shifted towards biological, chemical, material, and environmental areas.[32,35-37] Applications

of plasmas in contact with liquids rely on the plasma produced reactive products, which are shown in Fig. 1.7.[38] They are summarized below.

Electrons: Electrons produced in the gas phase plasmas are accelerated in electric fields and can deliver kinetic energy to targets. The energy carried by electrons can vary from 0.1 eV to more than 20 eV, enabling the breakage of chemical bonds of most target molecules. Energetic electrons ionize and dissociate water molecules to produce water ions, H_2O^+, and hydroxyl radicals, OH. One incident electron could yield more ionization and dissociation depending on the electron energy. In water, the electric fields are typically not large enough to directly produce reactive species. Low-energy electrons, which are not able to ionize and dissociate water molecules, get solvated in water and later produce OH^- through chemical reactions. With dissolved oxygen in water, low-energy electrons can also attach to oxygen to form superoxide, O_2^-. These reactions associated with the electrons occur very fast, in less than a nanosecond.[32, 39-41]

Ions: Plasma produced ions are not as energetic as electrons, but can still react with target molecules with significant reaction rates. The ionization potential of water is 12.6 eV, which is smaller than most of the major ions produced in plasmas (N_2^+, N_4^+, O_2^+, etc.). When striking the water surface, the major ions charge exchange with water molecules to form water ions, H_2O^+. This reaction likely occurs in tens of ps to perhaps 1 ns at most.[40] Water ions (H_2O^+) then charge exchange with water molecules to form hydronium (H_3O^+) and hydroxyl (·OH). This charge exchange occurs in a few μs. Negative ions entering the liquid from the gas phase, usually solvate, as their equivalent aqueous forms since their energies are low. These ions either react with targets or alter the characteristics of liquids, such as conductivity and pH value.[41-42]

Photons: The excitation of liquid molecules and gaseous species by atmospheric-pressure plasmas lead to the production of UV/VUV photons through the relaxation processes. The photons in the near UV region (230 nm – 300 nm) are well known to be hazardous to bacteria.[31,32] The UV light at around 260 nm (UVC) is able to initiate the formation of pyrimidine dimers by two pyrimidine molecules (thymine and cytosine) adjacent to each other on the same strand of DNA. The pyrimidine dimers interrupt DNA pairing and can cause mutations during DNA replication.[31] Overdose exposure to UV radiation can directly cause normal cell death.[32] Instead of directly reacting with bacteria, UV/VUV photons can also ionize and dissociate water molecules, the threshold energy of which is 7.6 eV for dissociation and 12.6 eV for ionization. The products of ionization and dissociation can later react with targets. In some cases, although they do not remove volatile organic compounds (VOCs) directly, UV/VUV photons are able to weaken the bonds in VOCs and assist with the oxidization processes by reactive species.[43-44]

Chemically reactive species: Chemically reactive species, such as hydrogen peroxide (H_2O_2), hydroxyl (OH) and ozone (O_3) are produced in plasmas in contact with liquids. These reactive species have high oxidization potentials, shown in Table 1.1, leading to a high degree of reactivity with inorganic and organic compounds, hazardous materials, and cells.[31,32] For example, the radical, ozone (O_3), with oxidization potential of 2.07 eV is able to remove organic and inorganic matter as well as micro-pollutants, such as pesticides, and is therefore widely used for the purpose of water purification, including our daily drinking water.[45-47] Another highly reactive product, hydroxyl (OH), is a free radical with oxidization potential of 2.8 eV, only second to fluorine atoms. It is believed to be the most significant contributor to reactivity in atmospheric pressure plasmas, with the reaction rate much higher than other species in most

cases.[47,48] Chemically reactive species also play a fundamental role in the antibacterial and antiviral defense as well in the cellular signal. Cellular responses to different reactive species depend on their concentration. For instance, hydrogen peroxide (H_2O_2) either stimulates cell proliferation at low concentration or induces cell apoptosis at high concentration.[49,50] Nitric oxide ($NO^{\cdot}$) at low concentration inhibits lipid peroxidation and protein oxidation by reactive oxygen species. At high concentration, nitric oxide ($NO^{\cdot}$) interrupts the intercellular and extracellular signals, causing cell apoptosis, especially in neurons.[51-53] Reactive species can also affect the cellular signal through alterations in intracellular redox state and oxidative modification of proteins involved in signal pathways. [54]

Electric currents: Charge species, electrons and ions, are accelerated by the electric field and then strike the tissue during plasma treatment, which causes electric currents. The natural resistance of dry skin is 10 kΩ.[31] The resistivity of blood varies from 1 Ω·m to 15 Ω·m.[55] In the traditional DBD devices, the tissue works as an electrode by design. The conductive current passing this tissue is small—typically a few tens of μA, which is far lower than the suggested current limits to human, 0.5 mA at 1 kHz, rising to 20 mA at 100 kHz.[56] When using plasma jets as sources, currents through the tissue can be neglected.

Electric field: Electric field can affect cell membranes by causing electroporation, which increases the permeability of the cell membrane. It was observed in experiments that an electric field above 1 kV/cm can induce electroporation and extremely high electric filed , tens of kV/cm, can result in significant cell death.[57] High electric fields can be directly generated from applied voltage or charging of lipid membranes. Membrane proration usually results in the loss of genetic material from cells or in cell uptake of chemicals and drugs. In plasma treatment, electroporation can assist with the delivery of reactive species into cells.[57,58]

1.4 Plasmas in water treatment

The current demand for water treatment is high, because of increased pollution from industrial sources and agricultural emissions and shrinking sources of freshwater. In industrial and agricultural emissions, organic compounds is a major group of pollutants that are of worldwide concern, due to their ability to cause severe problems in the environment and human health.[59,60] However, conventional water treatment technology with essential functions of sedimentation, filtration and disinfection, does not directly address the removal of organic compounds. Alternative advanced methods must not only address organic pollutants, but also be efficient enough to manage contaminants resulting from a chemical accident or an uncontrolled release.[61]

One of the innovative methods is advanced oxidation processes (AOPs), which involves an introduction of energy (e.g., chemical, electrical, and radiative) into the reaction zone to produce highly chemically reactive species, like hydroxyl radicals and ozone.[45-47,62] Atmospheric pressure plasmas in contact with liquids, as one of the AOPs, has been recently developed for removal of organic compounds due to its environmental compatibility and high removal efficiency. The plasma produced reactive products have already been discussed in Sec. 1.3. A combined process of AOPs including ozonation, UV photolysis and acidification makes the plasma degradation process very competitive.

The group of B.R. Locke *et al* has done pioneering and landmark work on the investigation of plasma produced reactive species by using point-plate discharges in contact with water.[63-65] In their experiments, the high voltage electrode is submerged in liquid while the ground electrode is suspended above the liquid. Substantial amounts of short lived radicals and hydrogen peroxide are produced in the liquid phase for organic abatement. The electrical

discharge can also occur above the liquid surface, which enhances the production of active species and provides ozone in an oxygen-containing gas atmosphere thereby improving contaminant removal by diffusing into liquid phase. As a result, hybrid gas–liquid reactors generally perform better for water treatment compared to the liquid discharge reactors and gas discharge reactors.

The gliding arc discharge (GAD) was introduced as an innovative technology consisting of ‘‘knife-edge’’ divergent electrodes, dielectric covers, high voltage power supply, and the nozzle.[66-69] In gliding arc discharge processes, high voltage is introduced and electrical breakdown occurs at the narrowest point. As a high velocity gas flows through the nozzle, the discharge moves towards the open end of the divergent electrodes to form a plasma plume. A larger yield of short-lived active species are produced by the discharge, which is widely utilized for different wastewater remediation.[66] One example is treating concentrated phenol solution in which 44.6% abatement was achieved by the gas gliding arc discharge reactor.[69]

Since breakdown directly in liquids requires extremely high electric field, bubbles are usually created in liquids to reduce the difficulty of initiating discharges. Foster *et al* investigated the breakdown process in an isolated bubble unattached to electrodes in water.[70,71] The propagation of liquid streamers from the electrode to the surface of the bubble was observed along with the formation of plasma within the bubble. Plasma produced radicals, like OH and H_2O_2, were detected. Energy yields for hydrogen peroxide in a variety of bubble systems were summarized by B. R. Locke *et al*.[64] In general, higher efficiency near 1 g kWh^{-1} was shown in these bubble systems than in the cases with direct discharge in the liquid or discharge over the liquid. The bubble discharge was applied to de-color an indigo solution

whose original color was blue.[72] Generation of both H_2O_2 and OH radicals were detected and the maximum rate of de-colorization of indigo solution was found to be 67%.

1.5 Plasmas in biomedical treatment

The idea of employing plasmas in biomedical applications can be traced back to Siemens in the late 1850s when he used a dielectric barrier discharge to generate ozone to sterilize biologically contaminated water.[36] During the mid-1900s, the applications of plasmas in biomedical treatment relied mainly on the thermal effects, which was utilized for tissue removal, sterilization, and cauterization.[32,36] Meanwhile, plasmas have been used for a long time in the food industry and in dental procedures such as implants, due to their antibacterial properties.[31,73,74] Only in the last two decades, atmospheric-pressure low-temperature plasmas has drawn increased attention, specifically in healthcare applications such as wound healing[75-77] and stem cell replication[78,79]. Scientific and systematic investigations began on the interaction among plasmas, liquids, and biological cells.[75-79] A typical configuration of plasmas interacting with liquid covered tissue is shown in Fig. 1.8.

The interest in plasmas used in biomedical treatment was developed and spread over the world by the success of clinical trials. Impressive results were presented in *in vitro* experiments and cell culture studies. Clinical experiments indicate that atmospheric plasmas can offer solutions to treat lesions that cannot be treated otherwise, such as diabetic ulcers and burn wounds.[75,80-82] The capability of atmospheric argon plasmas in the healing of chronic and acute wounds has been studied in clinical trials with over 3,500 patients. Some plasma devices have been used in hospitals for many years in Germany.[81,82] The treatment of several forms of cancer has also been explored. An *in vivo* experiment was reported by Vandamme *et al* [83-

86] using human U87 glioblastoma cells as heterotopic subcutaneous xenotransplants in nude mice. A marked anti-tumor effect was observed after a plasma treatment period of five consecutive days.[84] Beneficial effects of plasma treatment on pancreas carcinoma cells was reported by Pertecke *et al*.[85] Necrotic death and apoptotic death of leukemia cancer cells were shown in Thiyagarajan's experiments[86] after higher doses and lower doses of plasma treatment, respectively.

Meanwhile, research is being conducted on the dynamics of the plasma itself and the interaction mechanisms between the plasma and the cells, tissues, and organisms. A series of investigations on dynamics of atmospheric plasma jets were reported by Laroussi *et al*.[36,87-89] The plasma jet was made of hollow dielectric tube with two disk electrodes and operated with pulse at 1 – 10 kHz. By using high speed camera, they found that the plasma jet is not continuous, but rather a fast moving donut-shape "bullet", which can be controlled by the initiation time and external electric field. Kanazawa *et al* [90] observed the hydroxyl radical, OH, both in gas phase and liquid phase in surface discharges on liquids. Bruggeman *et al* [79,91,92] measured the concentration of hydrogen peroxide, nitrite and nitrate ions in liquids as a function of plasma treatment time by using a remote atmospheric pressure plasma jet. These reactive species are considered to play a key role in biomedical treatment. However, direct detection of interaction of these species with biomedical molecules is challenging. Computational works are used to address these issues. Bogaerts et al investigated the interaction of O and OH radicals with lipids in the skin barrier [93], ion transport through electropores of cell membrane [94], and reactive species interacting with DNA [95] by using molecular dynamics model. Babaeva et al investigated the reactive fluxes delivered by dielectric barrier

discharge filaments to slightly wounded skin [96] and the intracellular electric fields [97] by using a fluid model.

1.6 Recent computational modeling of plasmas in contact with liquids

In order to interpret experimental data, to assess the performance of various reactors, and to provide guidance for reactor designs, it is important to develop accurate computational models of plasmas in contact with liquids. In view of the physics, one of the challenges is understanding of physical and chemical processes at the gas-liquid interface, where the abilities of diagnostics are limited. Computational models fill this knowledge gap and provide valuable insight into the interactions.

Due to the intrinsic characteristics of plasma-liquid interactions, computational modeling is generally challenged in addressing widely varying time and length scales, from nanoseconds to minutes and from nanometers to centimeters.[98-100] A number of gas phase models were developed early to investigate discharges with the addition of water vapor. Ozone generation was one of the topics concerned with the role of water on affecting the yield of ozone, O_3, as well as hydrogen peroxide, H_2O_2.[101-103] Peyrous [101,102] studied the temporal evolution of O_3 and H_2O_2 through a kinetic simulation of corona discharges. The results from dry and humid air were compared and discussed. The density of H_2O_2 is significantly increased when water vapor is present. Humidity and temperature have cumulative effects on O_3 production, which shows a saturation during multiple pulses. The effects of water vapor on the formation of H_2O_2 were also extensively analyzed for helium discharges by Kong et al [103] using a global model incorporating 50 species and 577 reactions. In their model, the growing water ion clusters dominate the formation and transport of charged species when the water concentration is above

~100 ppm. Other models also consider the effects of water vapor on the nitrogen oxide chemistry.[104,105] Although further work is still needed to address water vapor under different discharge conditions, these modeling approaches are relatively well established.

Since plasma jets are widely used in plasmas in contact with liquids, an increasing number of computational works have been reported on modeling plasma jets. Sakiyama and Graves [106] developed a 2-D model using a finite element analysis of a plasma jet occurring in helium with trace nitrogen gas. They investigated the transition between corona-mode and glow-mode of the discharge. Later, they created a 1-D plug-flow model of a surface microdischarge into humid air with over 50 species and 600 reactions.[107] Another global plug-flow model with over 2,000 reactions was developed by Gaens and Bogaerts [108] to represent an argon plasma jet. Norberg and Kushner [109,110] used a 2-D fluid model to investigate the dynamics of plasma jets as well as the plasma produced species. The effects of the gas flow on plasma produced species were discussed and the results showed a clear decrease in the density of ozone with high flow rates. In these models, the characteristics of plasmas were investigated with several sets of chemical reaction mechanisms. The reaction mechanisms can be used in various discharge conditions.

The new challenge involves modeling the interactions of plasmas with liquids, especially at gas-liquid interfaces. So far only a few computational studies deal directly with these interactions. Babaeva and Kushner [111] computationally investigated the energy and angular distribution of ions onto polymer surfaces delivered by dielectric barrier discharges in air by using a 2-D fluid model. They also used the model to investigate gas phase discharges inside bubbles in liquids.[112] Norberg and Kushner modelled the interactions of plasma jets with liquid surfaces, in remote mode and contact mode.[113] Liu and Kong et al [114] created a

semi-1-D model to address plasma-biofilm and plasma-tissue interactions. To model the biofilm and tissue, a reactive penetration model was developed for mass transfer of highly transient plasma species across the gas–liquid boundary. This model can be further linked to simulation of molecular dynamics. A few models focused on the electric discharges directly in liquids.[115] These discharges are often operated with high power (typically 10's to 100's kV) with/without arc-like sparks, creating phase changes, shock waves and UV light. The coupling of physical phenomena to chemical reactions in such systems is very complicated and has not yet been extensively developed.

1.7 Issues to Be Discussed

The goal of this thesis is to improve the fundamental understandings of plasma-liquid interactions in scenarios of interest, like plasmas in bubbles in water and plasma treating liquid covered tissue, and also to suggest ways to obtain the desired outcomes by controlling the operating parameters for various applications. The works in this thesis are done by using a 2-D multi-fluid simulation platform, *nonPDPSIM*, which will be discussed in Chapter 2.

In Chapter 3, plasmas in bubbles in water used for water purification and medical treatment will be discussed. The gas forming the bubble is potentially a design parameter for water purification as the type and rate of production of active species may be controllable by the type of gas in the bubble. The dynamics of plasmas in bubbles in water sustained in different gases, N_2, Ar and He was computationally investigated. Images and optical spectra will be compared to experiments. The differences in plasma dynamics and spatial distribution of the plasma (e.g., volume discharge or surface hugging) when using different gases depend in large part on the electron energy relaxation length, and the rate of diffusion of water vapor into the

interior of the bubble. Electron impact dissociative excitation of water vapor, electron impact excitation of dissociation products and excitation transfer from the plasma excited injected bubble gases to water vapor all contribute to plasma emission. Variations in the contributions of these processes are responsible for differences in the observed optical spectra and differences in radical production.

In Chapter 4, the interaction of plasmas with liquids for biomedical applications, like skin sterilization and wound healing, will be discussed. Tissues treated by atmospheric pressure dielectric barrier discharges (DBDs) in plasma medicine are often covered by a thin layer of liquid, typically a blood serum like water with dissolved gases and proteins up to hundreds of micrometers thick. The water layer, 50–400 μm thick, contains dissolved oxygen and alkane-like hydrocarbons. The liquid processes the plasma-produced radicals and ions prior to their reaching the tissue. The DBDs are operated with multiple pulses at 100 Hz followed by a 1 s afterglow. Gas phase reactive oxygen and nitrogen species (RONS) intersect the water-vapor saturated air above the liquid and then solvate when reaching the water. The photolysis of water by plasma-produced UV/VUV plays a significant role in the production of radicals. Without hydrocarbons, nitrate, peroxynitrite and hydronium dominate the water ions with hydronium determining the pH of the liquid. The dominant RONS in the liquid are ozone, hydrogen peroxide and nitrogen acids. Dissolved oxygen assists the production of nitric acid and peroxynitrous acid during the afterglow. With hydrocarbons, reactive oxygen species are largely consumed, leaving an alkyl radical to reach the tissue. An alkyl radical is an alkane missing on hydrogen. These results are sensitive to the thickness of the water layer.

In Chapter 5, the long-term effects of multipulse DBDs on treatment of wet tissue will be discussed. The desired outcomes of wet tissue treatment by DBDs depend on the plasma dose

which determines the integral fluence of radicals, ions, electric fields and UV/VUV photons incident onto the tissue. These fluences are controlled by power, frequency and treatment time. The DBDs were simulated for 100 pulses at different repetition rates and liquid thicknesses followed by 10 seconds of afterglow. Two discharge schemes were investigated – stationary and random. In the stationary scheme, the DBD plasma streamer continues to strike at the same location on the liquid layer whereas in the random scheme the plasma streamer randomly strikes on liquid layer. These differences in streamer locations strongly affect the spatial distribution of solvated species such as OH_{aq} and H_2O_{2aq} ("$_{aq}$" represents an aqueous species) which have high rates of solvation. The spatial distributions of species such as NO_{aq} which have low rates of solvation are less affected by the location of the streamer due to remediating diffusion in the air. The end result is that fluences to the tissue are sensitive to the spatial location of the streamer due to the ensuing reactions in the liquid between species that have low and high rates of solvation. These reactions can be controlled not only through location of the streamer but also repetition rate.

1.8 Tables

Table 1.1 Oxidization potentials of reactive species.[43-46]

Oxidants	Oxidization potentials (V)
OH	2.80
H_2O_2	1.78
O	2.42
O_3	2.07
O_2	1.23

1.9 Figures

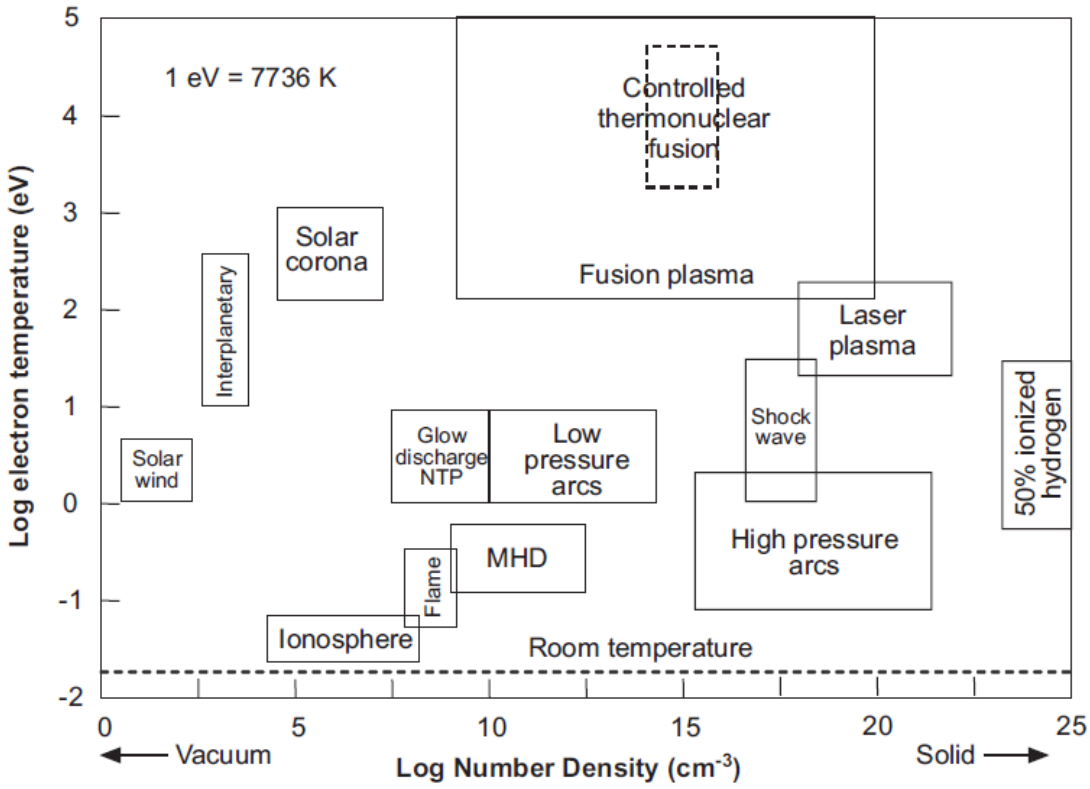

Figure 1.1 Classification of plasmas.[2]

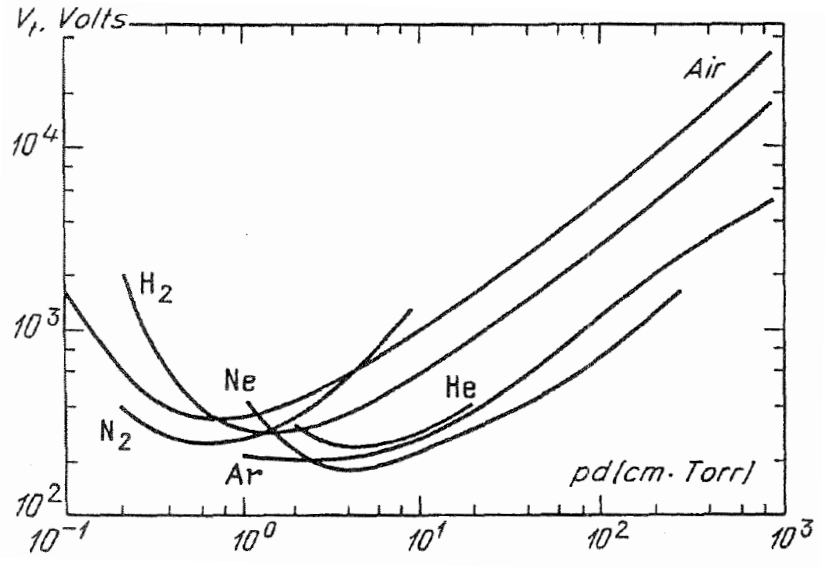

Figure 1.2 The breakdown voltage versus pd value for air, helium, argon, neon, hydrogen and nitrogen.[6]

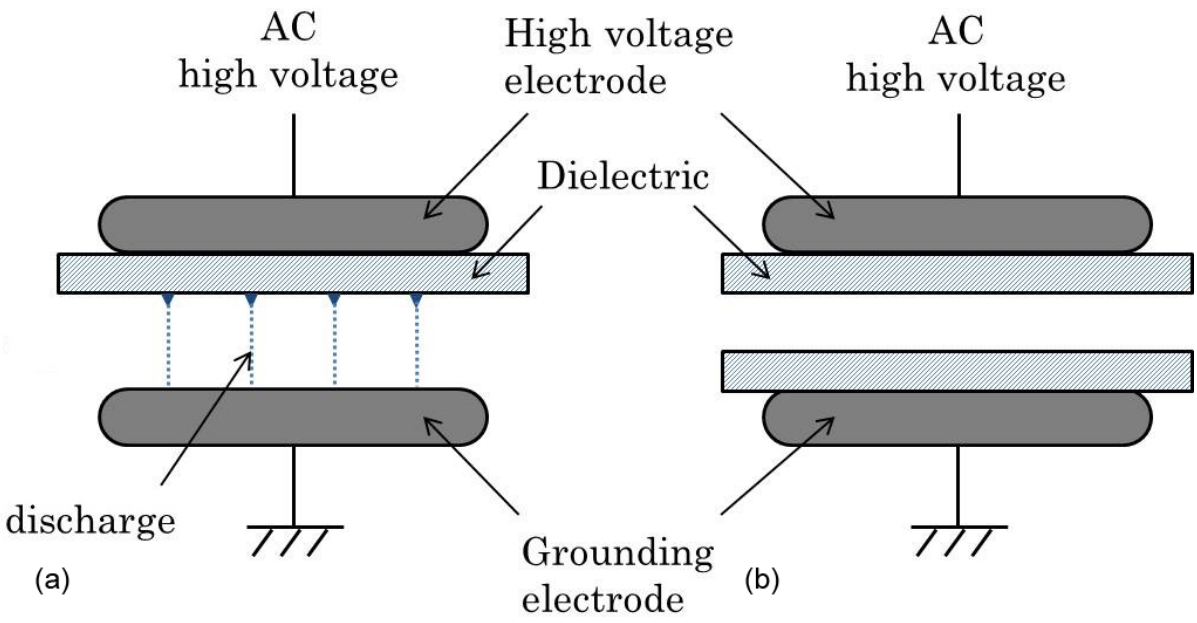

Figure 1.3 Typical DBD configuration. (a) DBD with one dielectric barrier covered upper electrode and (b) with two dielectric barriers covered electrodes.

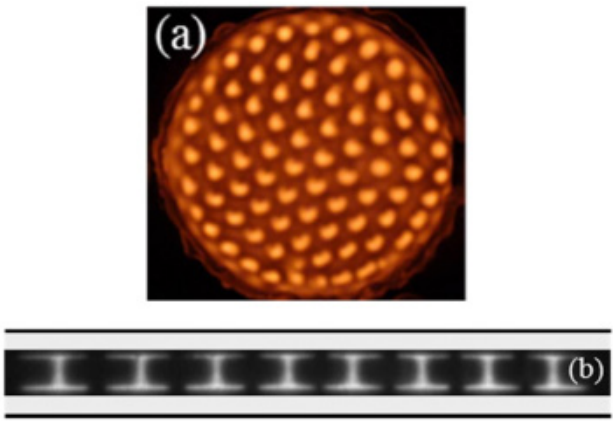

Figure 1.4 (a) End view and (b) side view of a nitrogen DBD at 100 Torr with AC of 500 V at 45 kHz. Gap length and dielectric layer thickness are both 1 mm. [26]

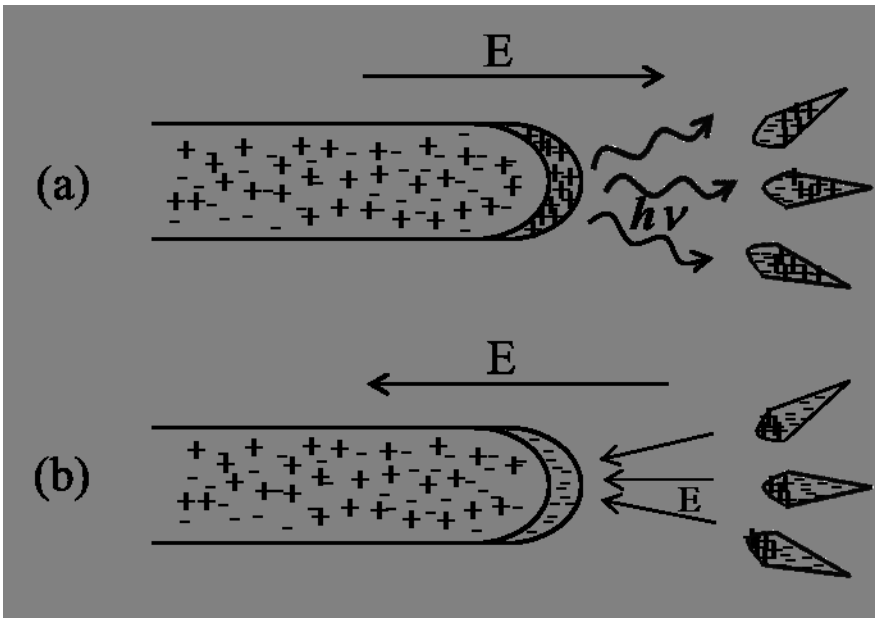

Figure 1.5 (a) Positive streamer propagating along the electric field with photoionization ahead of the streamer. (b) Negative Streamer propagating against the electric field with fast electron ionization ahead of the streamer.[4]

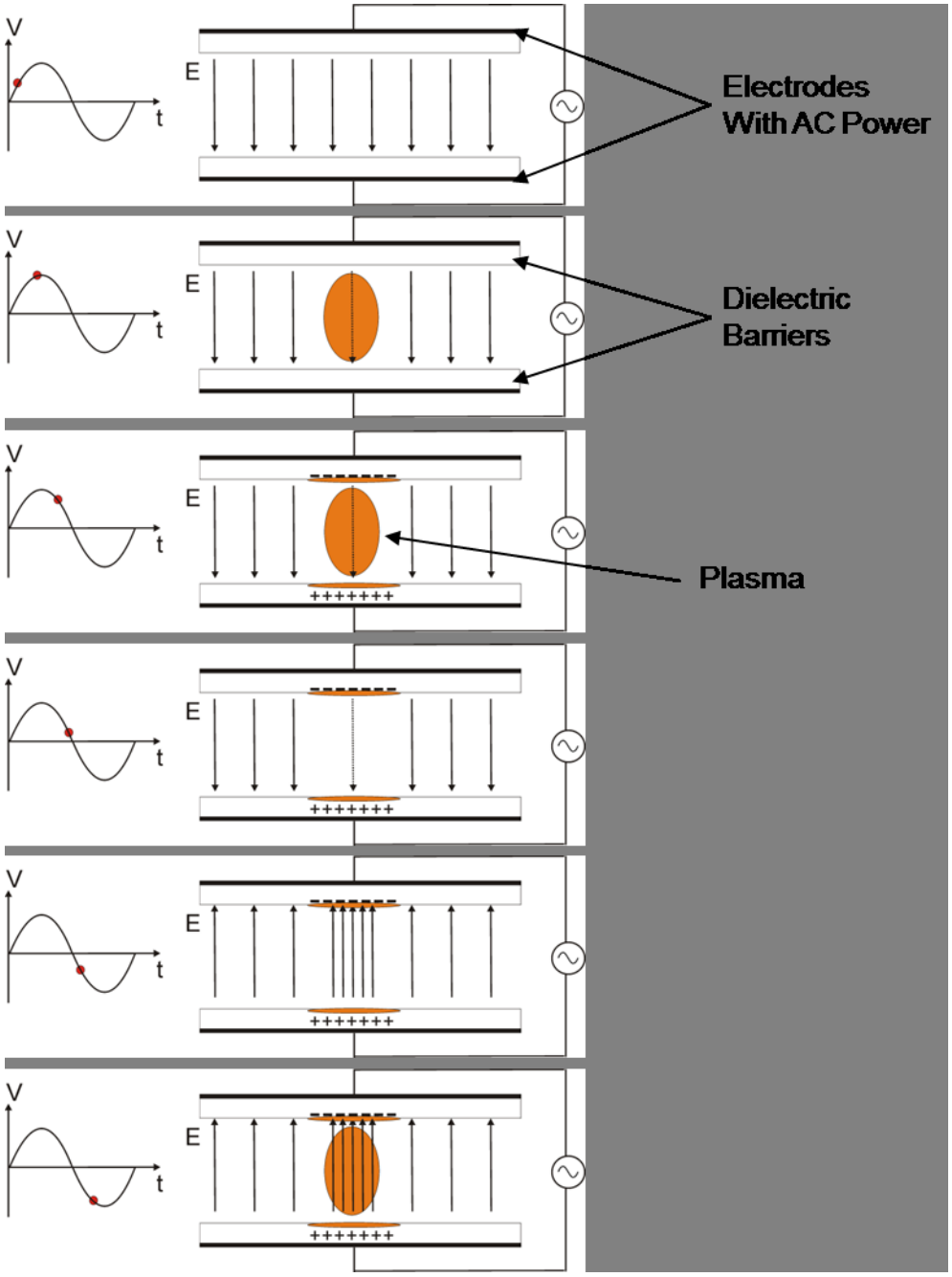

Figure 1.6 Typical evolution of a DBD in a full cycle.

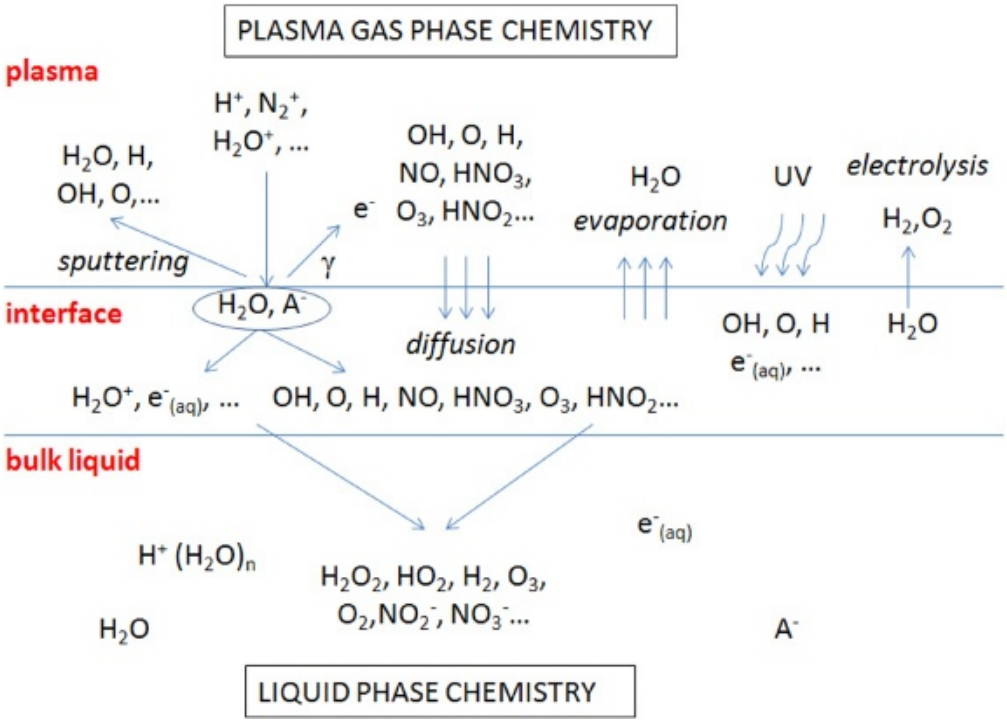

Figure 1.7 Schematic overview of some important transfer processes at the plasma–liquid interface. Note that some processes are polarity dependent. More details can also be found in Ref. [xx].

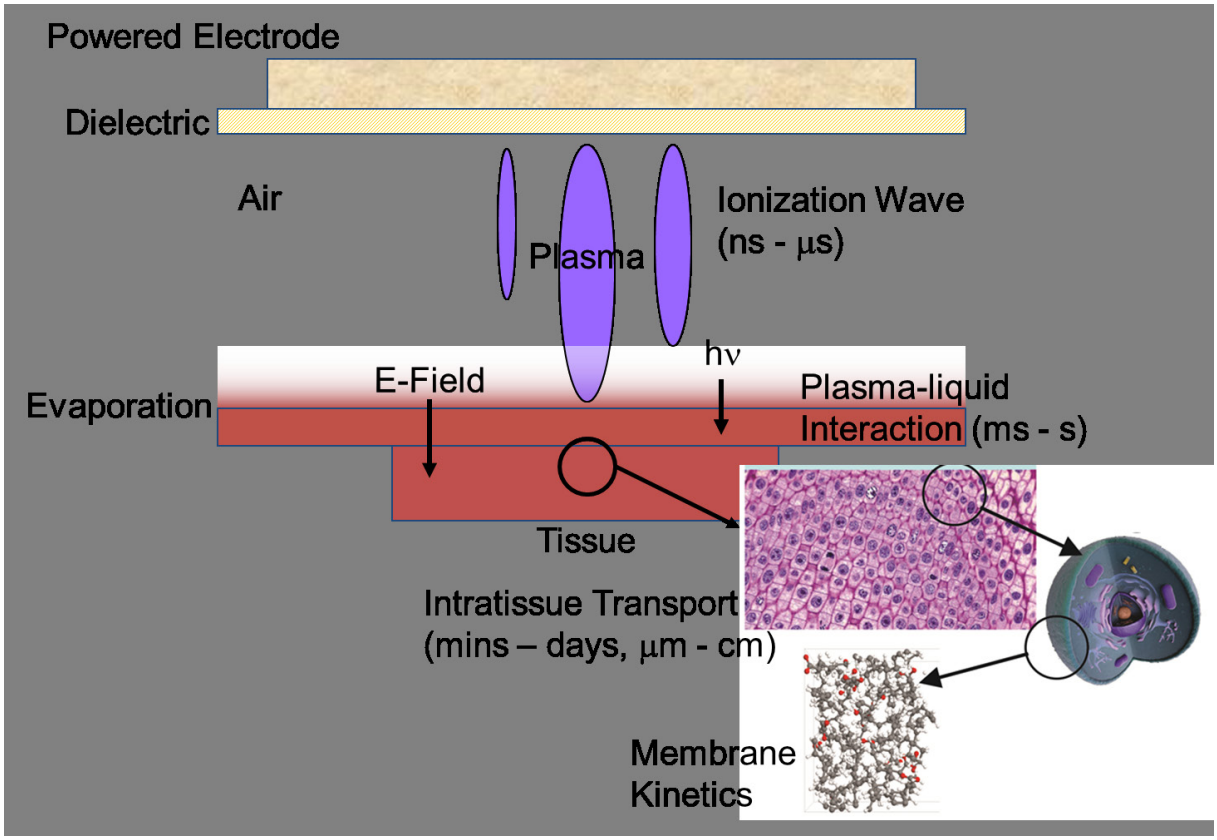

Figure 1.8 Configuration of a DBD interacting with wet tissue. The tissue is covered by a thin liquid layer. Power electrode is at the top and covered by a dielectric barrier. Plasma is produced in the gap.

1.10 References

[1] F. F. Chen, "Introduction to plasma physics and controlled fusion", 2nd Edition (Springer, 2006), page 2 – 10. Book

[2] Z. Rahman, H. Rahman, Md. A. Rahman, Int. J. Math. Phys. Sci. Res. **2**, 127(2015)

[3] J. A. Bittencourt, "Fundamentals of plasma physics" (Springer, 2004), page 180 – 192. Book

[4] A. Fridman and L. A. Kennedy, "Plasma physics and engineering" (CRC Press, 2004), page 123 – 144. Book

[5] M. Moisan, M. D. Calzada A. Gamero and A. Sola, J. Appl. Phys. **80**, 46 (1996).

[6] P. K. Chu and X. Lu, "Low temperature plasma technology: methods and applications" (CRC Press, 2013), page 41 – 60. Book

[7] H. L. Chen, H. M Lee, Sh. H. Chen and M. B. Chang, Ind. Eng. Chem. Res. **47**, 2122(2008)

[8] M. A. Malik, Ind. Eng. Chem. Res. **53**, 12305(2014)

[9] T. A. Kareem and A. A. Kaliani, Ionics **18**, 315(2012)

[10] N. J. Kramer, E. S. Aydil and U. R. Kortshagen, J. Phys. D: Appl. Phys. **48**, 035205(2015)

[11] T. Jacobs, R. Morent, N. D. Geyter, P. Dubruel and C. Leys, Plasma Chem. Plasma Process. **32**, 1039(2012)

[12] R. J. Zaldivar, J. P. Nokes, P. M. Adams, K. Hammoud and H. I. Kim, Carbon **50**, 2966(2012)

[13] M. J. Pavlovich, Z. Chen, Y. Sakiyama, D. S. Clark and D. B. Graves, Plasma Process. Polym. **10**, 69(2013)

[14] N. De Geyter and R. Morent, Ann. Rev. Biomed. Eng. **14**, 255(2012)

[15] K. H. Becker, U. Kogelschatz, K. H. Schoenbach and R. J. Barker, "Non-equilibrium air plasmas at atmospheric pressure" (CRC Press, 2004), page 5 – 14. Book

[16] Y. P. Raizer, "Gas discharge physics" (Springer, 2011), page 2 – 21. Book

[17] M. A. Lieberman and A. J. Lichtenberg, "Principles of plasma discharges and materials processing" 2nd Edition (Wiley-Interscience, 2005), page 5 – 35. Book

[18] A. Fridman, A. Chirokov and A. Gutsol, J. Phys. D: Appl. Phys. **38**, R1 (2005).

[19] U. Kogelschatz, B. Eliasson and W. Egli, J. Phys. IV **7**, 47 (1997)

[20] U. Kogelschatz, Plasma Chem. Plasma Process. **23**, 1 (2003)

[21] A. Chirokov, A. Gutsol and A. Fridman, Pure Appl. Chem. **77**, 487 (2005).

[22] Baeva, H. Gier, A. Pott, J. Uhlenbusch, J. Hoschele and J. Steinwandel, Plasma Chem. Plasma Process. **21,** 225 (2001)

[23] Baeva, H. Gier, A. Pott, J. Uhlenbusch, J. Hoschele and J. Steinwandel, Plasma Sources Sci. Technol. **11,** 1 (2002)

[24] M. Okumoto and A. Mizuno, Catal. Tdoay **71,** 211(2001)

[25] B. Eliasson, M. Hirth and U. Kogelschatz, J. Phys. D: Appl. Phys. **20**, 1421 (1987).

[26] J. M. Thiebaut, T. Belmonte, D. Chaleix, P. Choquet, G. Baravian, V. Puech and H. Michel, Surf. Coat. Technol. **169** 181 (2003)

[27] F. Massines and G. Gouda, J. Phys. D: Appl. Phys. **31**, 3411 (1998).

[28] R. Foest, F. Adler, F. Sigeneger and M. Schmidt, Surf. Coat. Technol. **163,** 323 (2003)

[29] H. H. Kim, Plasma Proces. Polym. **1**, 91 (2004)

[30] G. Borcia, C. A. Anderson and N. M. D. Brown, Plasma Sources Sci. Technol. **12**, 335 (2003)

[31] M. G. Kong, G. Kroesen, G. Morfill, T. Nosenko, T. Shimizu, J. van Dijk and J. L.

Zimmermann, New J. Phys. **11**, 115012 (2009)

[32] A. Fridman and G. Friedman, "Plasma Medicine" (Wiley, 2013), page 2 – 18. Book

[33] J. E. Foster, B. Sommers and S. Gucker, Jpn. J. Appl. Phys. **54**, 01AF05 (2015)

[34] B. Jiang, J. Zheng, S. Qiu, M. Wu, Q. Zhang, Z. Yan and Q. Xue, Chem. Eng. J. **236**, 348 (2014)

[35] Th. von Woedtke, S. Reuter, K. Masur, K. D. Weltmann, Phys. Rep. **530**, 291(2013)

[36] M. Laroussi, IEEE Trans. Plasma Sci. **36**, 1612 (2008)

[37] G. Fridman, G. Friedman, A. Gutsol, A. B. Shekhter, V. N. Vasilets and A. Fridman, Plasma Process. Polym. **5**, 503 (2008)

[38] P. Bruggeman and C. Leys, J. Phys. D: Appl. Phys. **42**, 053001(2009)

[39] P. Ceccato, "Filamentary plasma discharge inside water: initiation and propagation of a plasma in dense medium", Eng. Sci. Ecole Polytechnique X, 2009

[40] W. J. Chase and J. W. Hunt, j. Phys. Chem. 79, 2835(1975)

[41] K. P. Maddena and S. P. Mezyka, J. Phys. Chem. Ref. Data **40**, 023103 (2011)

[42] C. P. Kelly, C. J. Cramer and D. G. Truhlar, J. Phys. Chem. B **32**, 16066 (2006)

[43] M. Mohseni and J. L. Zhao, J. Chem. Technol. Biotechnol. **81**, 146 (2006)

[44] H. Huang, D. Y. C. Leung, G. Li, M. K. H. Leung and X. Fu, Catal. Today **175**, 310 (2011)

[45] K. L. Rakness, "Ozone in drinking water treatment: process design, operation and optimization", (American Waterworks Association, 2005) page 4 – 36. Book

[46] B. Langlais, D. A. Reckhow and D. R. Brink, "Ozone in water treatment: applications and engineering", (CRC Press, 1991) page 5 – 26. Book

[47] W. H. Glaze, J.-W. Kang and D. H. Chapin, Ozone Sci. Eng. 9, 335 (1987)

[48] J. L. Acero, K. Stemmler and U. von Gunten, Environ. Sci. Technol. **34**, 591 (2000)

[49] R. H. Burdon, Free Radical Bio. Med. **18**, 775 (1995)

[50] P.-F. Li, R. Dietz and R. von Harsdorf, Circulation **96**, 3602 (1997)

[51] A. Martínez-Ruiz, S. Cadenas and S. Lamas, Free Radic. Biol. Med. **51**, 17 (2011).

[52] N. Hogg and B. Kalyanaraman, Biochimica et Biophysica Acta **1411**, 378 (1999).

[53] B. Brune, Cell Death Differ. **10**, 864 (2003).

[54] K. Apel and H. Hirt, Annu. Rev. Plant Bio. **55**, 373 (2004)

[55] L. A. Geddes and H. Kidder, Med. Bio. Eng. **14**, 180 (1976)

[56] W. H. Olson, "Medical Instrumentation", (Webster, 1992) page 751 – 880 Book

[57] G. Saulis, Food Eng. Rev. **2**, 52(2010)

[58] S. Y. Ho and G. S. Mittal, Crit. Rev. Biotechnol. **16**, 349 (1996)

[59] P. H. Gleick, Ecol. Appl. **8**, 571 (1998)

[60] J. S. Zogorski, J. M. Carter, T. Ivahnenko, W. W. Lapham, M. J. Moran, B. L. Rowe, P. J. Squillace and P. L. Toccalino, "The quality of our Nation's waters – volatile organic compounds in the Nation's ground water and drinking-water supply wells", U. S. Geological Survey Circular **1292**, 101 (2006)

[61] B. Tansel, Reccent Pat. Chem. Eng. **1**, 17 (2008)

[62] R. Andreozzi, V. Caprio, A. Insola and R. Marotta, Catal. Today **53**, 51 (1999)

[63] A. A. Joshi, B. R. Locke, P. Arce and W. C. Finney, J. Hazard. Mater. **41**, 3 (1995)

[64] B. R. Locke and K.-Y. Shih, Plasma Sources Sci. Technol. **20**, 034006 (2011)

[65] B. R. Locke, M. Sato, P. Sunka, M. R. Hoffmann and J.-S. Chang, Ind. Eng. Chem. Res. **45**, 882 (2006)

[66] R. Burlica, M. J. Kirkpatrick and B. R. Locke, J. Electrostat. **64**, 35 (2006)

[67] Zh. Bo, J.-H. Yan, X.-D. Li, Y. Chi, K.-F. Cen and B. G. Cheron, Plasma Chem. Plasma

Process. **27**, 546 (2007)

[68] A. Fridman, S. Nester, L. A. Kennedy, A. Saveliev and O. Mutaf-Yardimci, Prog. Energ. Combust. Sci. **25**, 211 (1999)

[69] J.-H. Yan, C.-M. Du, X.-D. Li, X.-D. Sun, M. J. Ni, K. F. Cen and B. G. Cheron, Plasma Sources Sci. Technol. **14**, 637 (2005)

[70] S. N. Gucker, B. S. Sommers and J. E. Foster, IEEE Trans. Plasma Sci. **42**, 2636 (2014)

[71] J. E. Foster, B. S. Sommers, S. N. Gucker and I. M. Blankson, IEEE Trans. Plasma Sci. **40**, 1311 (2012)

[72] M. Sato, D. Kon-no, T. Ohshima and A. T. Sugiarto, J. Adv. Oxid. Technol. **8**, 198 (2005)

[73] S. Deng, R. Ruan, C. K. Mok, G. Huang, X. Lin and P. Chen J. Food Sci. **72**, 62 (2007)

[74] M. Deilmann, H. Halfmann, N. Bibinov, J. Wunderlich and P. Awakowicz, J. Food Prot. **71**, 2119 (2008)

[75] A. V. Nastuta, I. Topala, C. Grigoras, V. Pohoata and G. Popa, J. Phys. D: Appl. Phys. **44**, 105204 (2011)

[76] G. Lloyd, G. Griedman, S. Jafri, G. Schultz, A. Fridman and K. Harding, Plasma Process. Polym. **7**, 194 (2010)

[77] G. Isbary, J. Heinlin, T. Shimiz, J. L. Zimmermann, G. Morfill, H.-U. Schmidt, R. Monetti, B. Steffes, W. Bunk, Y. Li, T. Klaempfl, S. Karrer, M. Landthaler and W. Stolz, Brit. J. Dermatol. **167**, 404 (2012)

[78] Y. Yang, Y. I Cho and A. Fridman, "Plasma discharge in liquid: water treatment and applications", (CRC Press, 2012) page 13 – 43. Book

[79] C. A. J. van Gils, S. Hofmann, B. K. H. L. Boekema, R. Brandenburg and P. J. Bruggeman,

J. Phys. D: Appl. Phys. **46**, 175203 (2013)

[80] J. Heinlin, G. Isbary, W. Stolz, G. Morfill, M. Landthaler, T. Shimizu, B. Steffes, T. Nosenko, J. L. Zimmermann and S. Karrer, J. Eur. Acad. Dermatol. Venereol. **25**, 1 (2011)

[81] G. Isbary, G. Morfil, H. U. Schmidt, M. Georgi, K. Ramrath, J. Heinlin, S. Karrer, M. Landthaler, T. Shimizu, B. Steffes, W. Bunk, R. Monetti, J. L. Zimmermann, R. Pompl and W. Stolz, Brit. J. Dermatol. **163**, 78 (2010)

[82] G. Isbary, T. Shimizu, J. L. Zimmermann, H. M. Thomas, G. Morfil and W. Stolz, New Microbes New Infect. **1**, 41 (2013)

[83] J. Schlegel, J. Koritzer and V. Boxhammer, Clin. Plasma Med. **1**, 2 (2013)

[84] M. Vandamme, E. Robert, S. Dozias, J. Sobilo, S. Lerondel, A. L. Pape and J.-M. Poivesle, Plasma Process. Polym. **7**, 264 (2010)

[85] L. I. Partecke *et al*, BMC Cancer **12**, 473 (2012)

[86] M. Thiyagarajan, L. Waldbeser and A. Whitmill, Stud. Health Technol. Inform. **173**, 515 (2012)

[87] E. Karakas, M. Koklu and M. Laroussi, J. Phys. D: Appl. Phys. **43**, 155202 (2010)

[88] M. Laroussi, W. Hynes, T. Akan, X. Lu and C. Tendero, IEEE Trans. Plasma Sci. **36**, 1298 (2008)

[89] M. Laroussi and X. Lu, Appl. Phys. Lett. **87**, 113902 (2005)

[90] S. Kanazawa, H. Kawano, S. Watanabe, T. Furuki, S. Akamine, R. Ichiki, T. Ohkubo, M. Kocik and J. Mizeraczyk, Plasma Sources Sci. Technol. **20**, 034010 (2011)

[91] P. Bruggeman and D. C. Schram Plasma Sources Sci. Technol. **19**, 045025 (2010)

[92] P. Bruggeman and C. Leys, J. Phys. D: Appl. Phys. **42**, 053001 (2009)

[93] J. van der Paal, S. Aernouts, A. C. T. van Duin, E. C. Neyts and A. Bogaerts, J. Phys. D:

Appl. Phys. **46**, 395201 (2013)

[94] E. C. Neyts, M. Yusupov, C. C. Verlackt and A. Bogaerts, J. Phys. D: Appl. Phys. **47**, 293001 (2014)

[95] M. Yusupov, E. C. Neyts, P. Simon, G. Berdiyorov, R. Snoeckx, A. C. T. van Duin and A. Bogaerts, J. Phys. D: Appl. Phys. **47**, 025205 (2014)

[96] N. Yu. Babaeva and M. J. Kushner, J. Phys. D: Appl. Phys. **46**, 125201 (2013).

[97] N. Yu. Babaeva, W. Tian and M. J. Kushner, J. Phys. D: Appl. Phys. **47**, 235201 (2014).

[98] D. Bessiers, J. Paillol, A. Bourdon, P. Segur and E. Marode, J. Phys. D: Appl. Phys. **40**, 6559(2007)

[99] J. van Dijk, K. Peerenboom, M. Jimenez, D. Mihailova and J. van der Mullen, J. Phys. D: Appl. Phys. **42**, 194012(2009)

[100] J. van Dijk, G. M. w. Kroesen and A. Bogaerts, J. Phys. D: Appl. Phys. **42**, 190301(2009)

[101] R. Peyrous, Ozone Sci. Eng. **12**, 19(1990)

[102] R. Peyrous, Ozone Sci. Eng. **12**, 40(1990)

[103] D. X. Liu, P. Bruggeman, F. Iza, M. Z. Rong and M. G. Kong, Plasma Sources Sci. Technol. **19**, 2(2010)

[104] B. R. Locke, P. Lukes and J. L. Brisset, "Elementary chemical and physical phenomena in electrical discharge plasma in gas-liquid environments and in liquids", Wiley-VCH, Weinheim, 2012

[105] J. S. Chang, Plasma Sources Sci. Technol. **17**, 045004(2008)

[106] Y. Sakiyama and D. B. Graves, J. Phys. D: Appl. Phys.**39**, 3644(2006)

[107] Y. Sakiyama, D.B. Graves, H-W. Chang, T. Shimizu, and G. Morfill, J. Phys. D: Appl. Phys. **45**, 425201 (2012)

[108] W. Van Gaens and A. Bogaerts, J. Phys. D: Appl. Phys. **46**, 275201 (2013)

[109] S. A. Norberg, E. Johnsen and M. J. Kushner, J. Appl. Phys.**118**, 013301 (2015)

[110] S. A. Norberg, E. Johnsen and M. J. Kushner, Plasma Sources Sci. Technol. **24**, 035026 (2015)

[111] N. Y. Babaeva and M. J. Kushner, J. Phys. D: Appl. Phys. **41**, 062004 (2008).

[112] N. Y. Babaeva and M. J. Kushner, J. Phys. D **42**, 132003 (2009).

[113] S. A. Norberg, W. Tian,E. Johnsen and M. J. Kushner, J. Phys. D: Appl. Phys.**47**, 475203 (2014).

[114] C. Chen, D. X. Liu, Z. C. Liu, A. J. Yang, H. L. Chen, G. Shama and M. G. Kong, Plasma Chem. Plasma Process. **34**, 403(2014)

[115] B. R. Locke and S. M. Thagard, Chem. Plasma Process. **32**, 875(2012)

CHAPTER 2 DESCRIPTION OF THE MODEL

2.1 Introduction

This chapter describes the model platform, *nonPDPSIM*, used in this thesis. This model is a two-dimensional, multi-fluid hydrodynamic model targeting plasmas at high pressure. It was originally written by Dr. Shahid and Prof. Mark J. Kushner for simulating plasma display panel (PDP) cells and later extended by Dr. Xiong, Dr. Babaeva, Dr. Wang, and Dr. Norberg to address microdischarges and plasma jets.[1-6] A block diagram of the model platform is shown in Fig. 2.1.[5] In this code, Poisson's equation and continuity equation are simultaneously solved using the Newton implicit method for electric potential and densities of charged species (electrons and ions). The surface charges on the materials are also included. The densities of neutral species are updated later through the neutral continuity equation. The electron temperature is obtained by solving the electron energy equation and the rate coefficients and transport coefficients of electrons are obtained from local solutions of Boltzmann's equation for electron energy distribution (EED). After densities are updated, radiation transport is addressed by using Green's function propagator. The photon radiation comes from the high-lying excited states and carries energy to induce ionization and dissociation. Secondary electrons are optional, produced by ion and photon fluxes onto surfaces. Finite volume techniques are used to discretize the differential equations in an unstructured mesh with multiple refinement zones. The detailed algorithms used in this model are described in the following sections.

2.2 Geometry and Mesh Generation

Finite volume techniques are used to discretize the differential equations in *nonPDPSIM*. The numerical grid is unstructured and meshed using the software SKYMESH2. SKYMESH2 is an automatic mesh generator for two-dimensional meshes and was developed by SkyBlue systems. This software is no longer commercially available. There are three essential files in SKYMESH2 for geometry generation. They include the geometry file, the points file, and the edge file. The fundamental parameters of the model geometry are defined in the geometry file. The geometry can be Cartesian or cylindrically symmetric. The coordinates of the vertices are defined in the points file. The connectivity of the geometry regions are defined in the edge file. After the geometry is created, the unstructured mesh with triangular elements can be generated. The refinement file can be used to define the mesh resolution in different regions. Finer resolution of features is necessary for regions of interest, while coarser resolution in other regions saves computational time. The boundary conditions, such as geometry boundaries and plasma region boundaries, are defined in the boundary condition file. Once the unstructured mesh is generated, it is kept static throughout the simulation process.

In *nonPDPSIM,* the partial differential equations are discretized using the Vertex-Centered Finite Volume Method (VC-FVM), which defines the finite volume around a vertex. The unstructured mesh generated by SKYMESH2 is usually a triangular grid. The finite volume is defined by joining the circum-center of the triangles. An example of mesh cell is shown in Fig. 2.2. The vertices in the mesh are called “nodes”. Around Node 1, Node 2 – 7 form 6 triangular grids. The circum-centers of each triangle, noted as A - F, are connected to construct a “cell”. The cell volume for node 1 is the summation of the volumes shared between the node and each of its neighbors. For example, the cell volume between node 1 and node 3 is

$V_{1,3} = \frac{ab\sin(\alpha)}{2} \times D$, where D is depth in the case of Cartesian meshes or the radial portions in the case of cylindrically symmetric meshes. The total cell volume for node 1 is $V_1 = \sum_{j=2}^{7} V_{1,j}$. The cell areas, like A_{EF}, is the distance between center E and F multiplied by geometric depth D, $A_{EF} = \sqrt{(x_E - x_F)^2 + (y_E - y_F)^2} \times D$. All the geometrical factors, like cell volumes and areas, are computed at the beginning of the execution of the program and cannot be changed later. A typical example of model geometry and its unstructured mesh is shown in Fig. 2.3. This model geometry is used for simulation of dielectric barrier discharges, which is discussed in Chapter 5.

Each node is assigned to a material with properties such as conductivity, permittivity, resistivity, work function, metallic or non-metallic, its ability to emit secondary electrons or have surface charges, and initial temperature. When different materials share the same node, rules dictate which materials have priority over others. Metallic materials take priority when the node lies on the edge between a metal and a non-metal. Similarly, non-plasma material has higher priority, when the node is designated to belong to non-plasma material and when it lies on the edge between plasma material and non-plasma materials. Among dielectric materials, the ones with larger dielectric constants always have higher priority on the shared nodes.

2.3 Fundamental equations

The main simulation consists of integrating the following set of coupled equations simultaneously for charged species and electric potential. They are,

$$-\nabla \cdot (\varepsilon \nabla \Phi) = \sum_j N_j q_j + \rho_s, \tag{2.1}$$

$$\frac{\partial N_i}{\partial t} = -\nabla \cdot \vec{\phi}_i + S_i, \tag{2.2}$$

$$\frac{\partial \rho_s}{\partial t} = \left[\sum_i q_i (-\nabla \cdot \vec{\phi}_i + \mathrm{S_i}) - \nabla \cdot (\sigma(-\nabla \Phi)) \right]_{material}, \tag{2.3}$$

where i, ε, Φ, ρ_s, N, ϕ, σ, S, and q refer to charged species, permittivity, electric potential, surface charge density, charged species number density, species flux, material conductivity, source terms, and elementary charge respectively. In Poisson's equation, both volume charges and surface charges are included. The electric potential is solved in the whole computational domain except for electrodes where the electric potentials are given as boundary conditions. In transport equation for charged species, the source function, S_i, includes collisional terms which locally change the species density, such as electron impact ionization, heavy particle reactions, photoionization, secondary electron emission, field emission, and surface reaction. The flux is computed by using drift-diffusion approximation since the momentum transfer collisional frequency is larger than the electric driving frequency at high pressure (> 100's Torr). In drift-diffusion regime, the drift velocity of charged species instantaneously responds to the applied electric field.

$$\vec{\phi}_{DD} = \frac{q}{|q|} \mu N \vec{E} - D \nabla N \tag{2.4}$$

where D, μ, and E are diffusion coefficients, mobility, and electric field. In *nonPDPSIM*, the drift-diffusion flux is computed either directly or using Scharfetter-Gummel scheme.[7,8] In surface charge equation, the surface charge density is determined by the fluxes of charged species onto the surface and the dielectric relaxation by conductivity of the material. The system of equations (Eq. (2.1) – Eq. (2.3)) are solved simultaneously for the electric potential (Φ), species densities (N), and surface charges (ρ_s).

These equations are numerically discretized by using finite volume techniques as mentioned in Sec. 2.2. The geometrical factors, like cell volumes and areas, are taken into account in the operators. For example, Poisson's equation in inner material with constant dielectric constant is discretized to

$$\frac{1}{V_i}\sum_{j=1}^{N}[\frac{\phi_j-\phi_i}{l_{i,j}}\times A_{i,j}]=\frac{1}{\varepsilon_i}(\sum_k N_k q_k+\rho_s), \tag{2.5}$$

where V_i, ϕ_i and ε_i are the total cell volume, potential and dielectric constant for node i, $l_{i,j}$ and $A_{i,j}$ are the distance and area between node i and node j, N_k and q_k are the number density and charges of species k at node i, and ρ_s is the total surface charge density, respectively. In transport equations, drift-diffusion fluxes are formulated using the Scharfetter-Gummel method, which provides an optimized and stable approach. The flux ($\phi_{i,j}$) between node i and j is given by

$$\vec{\phi}_{i,j}=v_{i,j}\left(\frac{N_i-N_j\exp(-v_{i,j}\Delta_{i,j}/D_{i,j})}{1-\exp(-v_{i,j}\Delta_{i,j}/D_{i,j})}\right), \tag{2.6}$$

$$v_{i,j}=\frac{q}{|q|}\mu_{i,j}\vec{E}_{i,j},\quad D_{i,j}=\frac{D_i+D_j}{2},\quad \mu_{i,j}=\frac{\mu_i+\mu_j}{2},$$

where $v_{i,j}$ and $\Delta_{i,j}$ are drift velocity and distance between nodes i and j, respectively.

These equations are solved for electric potential at every node in the whole domain, for densities of charged species at every node in plasma domain, and for surface charges at every dielectric node bordering the plasma. The solution is obtained by using a fully implicit Newton iterative method. Eq.(2.1) – Eq.(2.3) are rewritten in terms of new functions F_1, F_2 and F_3

$$F_1=\nabla\cdot(\varepsilon\nabla\Phi)+\sum_j N_j q_j-\rho_s=0, \tag{2.7}$$

$$F_2 = \frac{\partial N_i}{\partial t} + \nabla \cdot \vec{\phi}_i - S_i = 0, \tag{2.8}$$

$$F_3 = \frac{\partial \rho_s}{\partial t} - \left[\sum_i q_i (-\nabla \cdot \vec{\phi}_i + \mathrm{S_i}) - \nabla \cdot (\sigma(-\nabla \Phi)) \right]_{material} = 0, \tag{2.9}$$

which can be linearized using first order Taylor series expansion

$$F_i(X_j(t+\Delta t)) = F_i(X_j(t)) + \frac{\partial F_i(X_j(t))}{\partial X_j} \Delta X_j, \tag{2.10}$$

$$\Delta X_j = X_j(t+\Delta t) - X_j(t),$$

where $F_i(X_j(t+\Delta t))$ is function F_i and variable X_j at time *(t + Δt)*. A matrix form $\vec{J} \cdot \Delta X = B$ then can be constructed and shown below, where matrix $\vec{J}$ is the Jacobian matrix, ΔX is a vector which contains the unknown variables, and *B* is a vector that contains evaluation of functions F_1 to F_3 at time *t* on node *i* to *k*.

$$\begin{bmatrix}
\frac{\partial F_{1,i}}{\partial \Phi_i} & \frac{\partial F_{1,i}}{\partial N_i} & \frac{\partial F_{1,i}}{\partial \rho_{s,i}} & .. & \frac{\partial F_{1,i}}{\partial \Phi_{i+k}} & \frac{\partial F_{1,i}}{\partial N_{i+k}} & \frac{\partial F_{1,i}}{\partial \rho_{s,i+k}} \\
\frac{\partial F_{2,i}}{\partial \Phi_i} & \frac{\partial F_{2,i}}{\partial N_i} & \frac{\partial F_{2,i}}{\partial \rho_{s,i}} & .. & \frac{\partial F_{2,i}}{\partial \Phi_{i+k}} & \frac{\partial F_{2,i}}{\partial N_{i+k}} & \frac{\partial F_{2,i}}{\partial \rho_{s,i+k}} \\
\frac{\partial F_{3,i}}{\partial \Phi_i} & \frac{\partial F_{3,i}}{\partial N_i} & \frac{\partial F_{3,i}}{\partial \rho_{s,i}} & .. & \frac{\partial F_{3,i}}{\partial \Phi_{i+k}} & \frac{\partial F_{3,i}}{\partial N_{i+k}} & \frac{\partial F_{3,i}}{\partial \rho_{s,i+k}} \\
... & ... & ... & .. & ... & ... & ... \\
\frac{\partial F_{1,i+k}}{\partial \Phi_i} & \frac{\partial F_{1,i+k}}{\partial N_i} & \frac{\partial F_{1,i+k}}{\partial \rho_{s,i}} & .. & \frac{\partial F_{1,i+k}}{\partial \Phi_{i+k}} & \frac{\partial F_{1,i+k}}{\partial N_{i+k}} & \frac{\partial F_{1,i+k}}{\partial \rho_{s,i+k}} \\
\frac{\partial F_{2,i+k}}{\partial \Phi_i} & \frac{\partial F_{2,i+k}}{\partial N_i} & \frac{\partial F_{2,i+k}}{\partial \rho_{s,i}} & .. & \frac{\partial F_{2,i+k}}{\partial \Phi_{i+k}} & \frac{\partial F_{2,i+k}}{\partial N_{i+k}} & \frac{\partial F_{2,i+k}}{\partial \rho_{s,i+k}} \\
\frac{\partial F_{3,i+k}}{\partial \Phi_i} & \frac{\partial F_{3,i+k}}{\partial N_i} & \frac{\partial F_{3,i+k}}{\partial \rho_{s,i}} & .. & \frac{\partial F_{3,i+k}}{\partial \Phi_{i+k}} & \frac{\partial F_{3,i+k}}{\partial N_{i+k}} & \frac{\partial F_{3,i+k}}{\partial \rho_{s,i+k}}
\end{bmatrix}
\begin{bmatrix}
\Delta \Phi_i \\ \Delta N_i \\ \Delta \rho_i \\ .... \\ \Delta \Phi_{i+k} \\ \Delta N_{i+k} \\ \Delta \rho_{i+k}
\end{bmatrix}
=
\begin{bmatrix}
-F_{1,i} \\ -F_{2,i} \\ -F_{3,i} \\ ... \\ -F_{1,i+k} \\ -F_{2,i+k} \\ -F_{3,i+k}
\end{bmatrix}, \tag{2.11}$$

The Jacobian matrix describes the effect of perturbation of variables on the functions F_1 to F_3. Matrix solvers such as dslucs, dslugm obtained from the SLAP Sparse Matrix Library [9] or

sparskit [10] obtained from the University of Minnesota are used. These solvers use bi-conjugate gradient matrix solution methods with incomplete LU factorization for preconditioning. Therefore, the solving process needs an initial estimated solution for each variable,

$$X_{j,guess} = X_j(t) + (X_j(t_1) - X_j(t_2)) \times \frac{\Delta t_1}{\Delta t_2}, \tag{2.12}$$

where $X_{j,guess}$ is the guessed solution, Δt_1 and Δt_2 are the preceding time steps. After the Jacobian matrix $\vec{J}$ is solved, the increment ΔX is obtained by inverting the Jacobian matrix and solving $\Delta X = (\vec{J})^{-1} \cdot B$. The solutions at time *(t + Δt)* is updated, $X(t + \Delta t) = X(t) + \Delta X$. This process will be iterated until the variables converge to $\Delta X_j / X_j \le \varepsilon_{\max}$, where $\varepsilon_{\max}$ is the error criterion which is the specified tolerance.

If the system of Eq.(2.1) – Eq.(2.3) are solved using explicit method, the time step is limited by the ratio of the permittivity of free space to the plasma conductivity ($\Delta t < \varepsilon_0 / \sigma$, where ε_0 is the dielectric constant of free space and σ is the plasma conductivity), typically on time scale of picosecond. Implicit Newton iterative method used here allows for a larger time step. Although a larger time step could reduce the computing time, more Newton iterations resulting from a larger time step also significantly increases the computing load. Therefore, an optimization needs to be considered between a larger time step and less Newton iterations in order to minimize the computing load. In the model, time step can be dynamic and is determined according to the difficulty that the matrix solver encountered. With increasing number of Newton iterations for matrix solver to find a converged solution, the time step for the next calculation will be reduced accordingly and vice versa. The typical number of Newton iterations is 10 – 20 and the corresponding time step for atmospheric pressure plasma simulations is 10^{-12} – 10^{-11} seconds.

2.4 Electron Energy Distribution and Electron Temperature

In low temperature plasma, the electron energy distribution function (EEDF) plays an important role in determining the coefficients for electron transport and reactions. If elastic collisions dominate the electron energy losses ($P_{eV} << \frac{2m}{M}\varepsilon_e \nu_e$, where P_{eV} is the energy loss other than elastic collisions, m and M are mass of electrons and neutral species respectively, ε_e is the electron kinetic energy, ν_e is the elastic collision frequency)[11]. The EEDF is Maxwellian and gives electron temperature as

$$T_e = \frac{e^2 E^2 M}{3m^2 \nu_{en}^2}, \tag{2.13}$$

where T_e is electron temperature, e is unit charge, E is average value of electric field, m and M are mass of electrons and neutral species, respectively, ν_{en} is the collision frequency between electrons and neutral species. However, this is true when the ionization degree is high. Electron-electron collisions drive the distribution towards a Maxwellian shape. Inelastic collisions of electrons with heavy particles lead to a drop of the EEDF at higher electron energies. Electrons lose their energy through inelastic collisions, like excitation and ionization. Hence the EED is highly deviated from Maxwellian distribution and must be obtained from solving Boltzmann equation. The Boltzmann equation describes the evolution of the distribution function, f, in a six-dimensional phase space:

$$\frac{df}{dt} = \frac{\partial f}{\partial t} + \vec{v} \cdot \nabla_r f + \frac{\vec{F}}{m} \cdot \nabla_v f = I_{coll}(f), \tag{2.14}$$

where ∇_r and ∇_v denote the electron distribution function gradients related to space and velocity coordinates, and $I_{coll}(f)$ is the collisional term. There is no generalized solution for Boltzmann equation.

In high pressure plasmas, the electron collision frequency (including elastic and inelastic collisions) is usually larger than electron energy relaxation frequency, $\nu_{eq} > \frac{1}{E}\frac{\partial E}{\partial t}$,where ν_{eq} is the collision frequency and E is energy. The electron energy gained from the electric field is locally balanced by the energy loss in collisional process, so local field approximation (LFA) applies. The transport and reaction coefficients then depend only on the local electric field. The EED is independent in space ($\nabla_x \cdot (\vec{v} f(\vec{v})) = 0$) and stationary ($\partial f(\vec{v})/\partial t = 0$). Boltzmann equation then becomes,

$$\frac{\vec{F}}{m} \times \nabla_v f - I_{coll}(f) = 0 . \qquad (2.15)$$

With high collision frequency at high pressure, EED approaches isotropic. In the model a two-term spherical harmonic expansion is used to solve this equation for a wide range of values for *E/N*. Since no analytic solution is available, a lookup table is created from solving the Boltzmann equation. The look up table consists of transport coefficients, electron impact reaction rates, electron temperature (T_e), and momentum transfer collision frequency (ν_m) as a function of *E/N*. This lookup table is interpolated to obtain the coefficients at any T_e. Because the solution of Boltzmann equation strongly depends on the gas composition, the lookup table is periodically updated during execution of the model as the composition of the electron collision partners varies. Moreover, different Boltzmann lookup tables can be computed for different regions, which have different gas compositions.

Electron temperature can be easily derived from Maxwellian EED. However, it is difficult to define an electron temperature from arbitrary EED resulting from Boltzmann equation. In the model, electron temperature is obtained from solving electron energy equation.[12]

$$\frac{\partial}{\partial t}\left(\frac{3}{2}n_e T_e\right) = \vec{j}\cdot\vec{E} - \nabla\cdot\vec{q}_e - n_e\sum_i \Delta\varepsilon_i k_i N_i, \tag{2.16}$$

$$\vec{q}_e = \frac{5}{2}\vec{\phi}_e T_e - \lambda\nabla T_e, \text{ and } \vec{j} = q_e\vec{\phi}_e,$$

where n_e is electron density, k_i is the rate coefficient for power loss for collision of electrons with species *i* having density N_i and electron energy loss $\Delta\varepsilon_i$, $\vec{\phi}_e$ is the electron flux, λ is electron thermal conductivity, and T_e is the electron temperature expressed in terms of average energy defined as $\varepsilon = 3T_e/2 = \int_0^\infty f(\varepsilon')\varepsilon' d\varepsilon'$. The flux density of electron energy $\vec{q}_e$ is composed of the hydrodynamic flux of enthalpy and the heat conduction flux. The electron energy equation is integrated in a time step using the method of successive over-relaxation (SOR) with an SOR parameter α_{SOR} of 1.7 – 1.8 specified in the input file. The electron transport coefficients, rate coefficients, and collision frequency for use in solving electron energy equation are obtained from Boltzmann lookup tables.

Unlike electrons, the transport and reaction coefficients for ions and neutral species are not sensitive to *E/N* of our interest, and hence they are not governed by Boltzmann equation. The mobilities of ions at a given pressure are constant, and the diffusion coefficients of ions are given by the Einstein relation. The diffusion coefficients of neutral species are determined by the Lennard-Jones approximation. The reaction coefficients for ions and neutral species are normally of the Arrhenius form,

$$k = A\left(\frac{T_g}{300}\right)^n \exp(-\frac{E_a}{T_g}), \tag{2.17}$$

where *k*, *A*, T_g and E_a are rate coefficient, Arrhenius coefficient, gas temperature, and activation energy respectively.

2.5 Radiation Transport

Photo-induced reactions, like photoionization and photo-dissociation, are also considered in the model. In positive streamer avalanche, seed electrons ahead of the avalanche can be produced by photons from high-lying excited states. In humid air, water molecules are able to become dissociated by energetic photons. The photoelectron emission from selected surfaces plays an important role in sustaining the plasma as well. This radiation transport is addressed using a Green's function approach. In our model, the photo-ionization source ($cm^{-3}s^{-1}$) for species *i* at location $\vec{r}_l$ resulting from photon emission by species *j* at location $\vec{r}'_m$ is

$$S_i(\vec{r}_l) = N_i(\vec{r}_l)\sum_j A_j \int \sigma_{ji} N_j(\vec{r}'_m) G_j(\vec{r}'_m, \vec{r}_l) d^3\vec{r}'_m \,, \tag{2.18}$$

$$G_j(\vec{r}'_m, \vec{r}_l) = \frac{\exp\left(-\left|\vec{r}'_m - \vec{r}_l\right| / \lambda_j\right)}{4\pi\left|\vec{r}'_m - \vec{r}_l\right|^2} = \frac{\exp\left(-\sum_k \int_{\vec{r}_m'}^{\vec{r}_n''} \sigma_{jk} N_k(\vec{r}''_n) d\vec{r}''_n\right)}{4\pi\left|\vec{r}'_m - \vec{r}_l\right|^2},$$

where N_j is the radiating species density with Einstein coefficient A_j, and σ_{ji} is the photo-ionization cross section for species *i* by photons emitted from species *j*. In traversing the plasma, the photons are absorbed by species *k* with cross section σ_{jk}. The probability of survival of the photons emitted at $\vec{r}_m$' to reach location $\vec{r}_l$ with absorption length λ_j is taken into account. The Green function propagator $G_j(\vec{r}_m', \vec{r}_l)$ also accounts for physical obstructions and view angles that might block the radiation. In practice, $G_j(\vec{r}_m', \vec{r}_l)$ is computed only for a specified volume around $\vec{r}_m$'. The radiation transport module is periodically called during the execution of the model.

2.6 Neutral Transport Equation

The transport for each neutral species is calculated using a time-slicing technique after updates of densities of charged species. The transport equation for neutral species includes sources due to volumetric and surface reactions and the contributions of advective flow fields if any,

$$\frac{\partial N_i}{\partial t} = -\nabla \cdot (\vec{v} N_i) - D_i \nabla N_i + S_v + S_s , \tag{2.19}$$

where N_i is the neutral density, $\vec{v}$ is the flow velocity, D_i is the diffusion coefficient, S_v is the source term due to volumetric reactions, and S_s is the source term due to surface reactions. In the time-slicing approach, the neutral densities are kept constant while the integration of equations for charged species; and vice versa. The neutral transport equations are solved in both the gas phase and liquid phase.

In the model, the diffusion coefficients were estimated by using their Lennard-Jones parameters and modified hard-sphere collisions [13],

$$D_{12} = 0.001858 \sqrt{\frac{M_1 + M_2}{M_1 M_2}} \frac{T^{3/2}}{p \sigma_{12}^2 \Omega_D} \tag{2.20}$$

where T is the gas temperature (K), M_1 and M_2 are molecular weights of water and the gas within the bubble, p (atm) is the total pressure of the binary mixture, σ_{12} is the Lennard-Jones parameter defined by $\sigma_{12} = 1/2(\sigma_1 + \sigma_2)$, Ω_D is the temperature-dependent collision integral.[13] The diffusion coefficients depend dominantly on the density of background species. For example, the air density is less than liquid density by a factor of 1000. It results in 1,000 times smaller diffusion coefficient for a species in liquid than in air.

In the update of neutral densities, are explicit or implicit method can be used. In the explicit calculation, higher order Runge-Kutta methods are used. A successive-over-relaxation (SOR) technique with an SOR parameter α_{SOR} of 1.7 – 1.8 is used for the implicit calculation.

For DBDs in contact with liquid, a series of short pulses are followed by a longer period where the plasma is essentially absent but plasma activated neutral processes proceed. In the af-

terglow, continuing integration of the Poisson's equations along with transport equations for charged species is computational time-consuming and not necessary. It would be beneficial if only neutral transport equation is solved. The timestep then can increase to as large as microseconds, which is sufficient to address the transport in liquid. To address plasma dynamics, full equations described in Sec. 2.3 are solved. In the afterglow, only transport equation for neutral species is solved. The transport across the gas-liquid interface will be discussed in the following section.

2.7 Liquid Phase and Solvation

When plasmas are in and in contact with liquids, a gas phase and a liquid phase are involved. The modeling of plasmas in the gas phase is discussed in the preceding sections. The modeling of liquids is different. The liquid density is higher than atmospheric gas density by a factor of 10^3. This density results in an extremely high collision frequency (up to 10^{14} Hz) and small transport length (several nanometers) and is very difficult for the model to resolve. In this model, the liquid plasma is treated identically to a gas plasma as a partially ionized substance with higher density and specified susceptibility per atom or molecule to provide the known permittivity. For example, water is assigned with a density of 3×10^{22} cm^{-3}, relative dielectric constant value of 2.375×10^{-21} per molecule, which makes the dielectric constant of water about 81. Surface tension is addressed by specifying species those are able to pass through the gas-liquid interface. Electrons and gaseous ions are able to cross the interface and get solvated in the liquid, while solvated electrons and ions stay in the liquid and do not cross back to the gas phase. Although gaseous species and their aqueous counterparts share the same properties, like mass and charges, they are treated as different species in the model so that a different reaction mechanism can be used. For example, OH and NO_2 react in gas phase with rate coefficient of 4×10^{-11} cm^3s^{-1} [14] while OH_{aq} ($_{aq}$ means an aqueous species) and NO_{2aq} react in liquid phase with rate coefficient of 7.1×10^{-12} cm^3s^{-1} [15]. Liquid is allowed to evaporate into the gas as the natural liquid does. The evaporation occurs at the liquid surface where the source is given by its vapor pressure and depends strongly on the temperature and vapor density above the liquid surface. In plasmas in contact with water, water evaporation significantly humidifies the gas and influences the discharges.

The solvation process is one of the most important gas-liquid interactions. The water molecule is polarized. When positive ions are solvated, they are surrounded by water molecules with the O-atom oriented towards the positive ions. When negative ions are solvated, they go through a similar process but with the H-atom angled towards the negative ions. These processes are fast, on a time scale of less than nanoseconds. So in our model, the solvation rates of ions are assumed to be instantaneous. Diffusion of neutral species into water is limited by Henry's law equilibrium at the surface layer. Henry's law states that the amount of a given gas that dissolves in water is directly proportional to the partial pressure of that gas in equilibrium with that liquid. The proportional factors are called Henry's law constants. The Henry's law constant is a measure of the solvation rates of species into a liquid. Henry's law only describes the dynamic equilibrium of solvation. However, the actual rate of solvation is not necessarily known. In our model, the rate of solvation is given in analogy to the Noyes–Whitney formula[16],

$$\frac{dn_j}{dt} = Kn_i \max\{D_i\left(h - \frac{n_j}{n_i}\right),0\} \tag{2.21}$$

where n_i and n_j are the densities of the species in gas and water, respectively, K is geometric factor which accounts for the divergence operator at the surface, D_i is the diffusion coefficient in the gas phase and h is Henry's law constant. The diffusion is shut off when the equilibrium density at the surface is reached. Otherwise, the rate of solvation is linearly scaled down with the solvated density by the factor of $\left(h - \frac{n_j}{n_i}\right)$. The more solvated species, the slower the speed of solvation.

At the beginning, species naturally diffuse into the liquid and get solvated. Since the diffusion of solvated species in the liquid is at least 1,000 times slower than the diffusion of gaseous species, they accumulate at the liquid surface. This accumulation decreases further solvation from the gas to liquid phase unless they react and are removed. When the densities of solvated species rise to equilibrium level, according to Henry's law the solvation process stops. Until the solvated species diffuse deeper into the liquid and densities at the liquid surface below the equilibrium level, solvation stops. For example, assume the initial density of O_3 in the gas phase is 10^{16} cm^{-3} and there is no O_{3aq} in liquid phase. At the beginning, its effective diffusion coefficient is 0.22 cm^2/s. As O_3 begins to solvate in liquid and the equivalent diffusion coefficient decreas-

es. The Henry's law constant for O_3 is 0.3. When the density of O_{3aq} at the liquid surface increases 1.5×10^{15} cm^{-3}, the equivalent diffusion coefficient reduces to half of its original value, 0.11 cm^2/s. The corresponding solvation is slowed down to half speed. When the density of O_{3aq} at the liquid surface reaches 3.0×10^{15} cm^{-3}, which is the equilibrium value, the equivalent diffusion coefficient is reduced to zero, which means that no further solvation proceeds. The density of O_{3aq} cannot exceed 3.0×10^{15} cm^{-3}. Since the equilibrium is only established locally at the liquid surface, the equivalent diffusion coefficient can increase above zero as long as the density of O_{3aq} decreases below 3.0×10^{15} cm^{-3} due to diffusion deeper into liquid. Then the solvation proceeds.

The speed of solvation depends strongly on the Henry's law constant. Diffusion coefficients are obtained from fundamental atomic properties. Usually, it is larger for small molecules or atoms and smaller for large molecules or atoms. The difference of diffusion coefficients for different species, such as OH and NO, varies from a factor of 1 to 2, depending largely on their mass. But their Henry's constants can vary from 25 to 10^{-3}. The speed of solvation of NO is much slower than that of OH, based largely on Henry's law constants and not diffusion rates.

2.8 Aqueous Reaction Mechanism

The reaction mechanism in water was developed from the environmental science community [17], and is listed in Appendix I. The reaction mechanism contains solvation, charge exchange, hydrolyzation, dissociation and ionization of water molecules, and analogy reactions to gas phase counterparts. A general mechanism of reaction pathways is shown in Fig. 2.4.

Electrons: When plasmas contact water, electrons solvate into the water. In the model, the kinetic energy of electrons is not considered when electrons interact with water. That is, electrons entering the liquid are assumed to be at liquid temperature. This current assumption results in loss of energy input into water and could be resolved in the future work. Since the water is exposed to open air, the aqueous oxygen in water is likely in equilibrium with gaseous oxygen. Therefore, there is already 10 ppm dissolved oxygen in most water samples. Most solvated electrons in water immediately attach to O_{2aq} and form $O_2^-{}_{aq}$, which is a very important negative ion in water. Without nitrogen oxides in water, $O_2^-{}_{aq}$ could be the terminal ion. Otherwise,

$O_2^-{}_{aq}$ will react with nitrogen oxides to form nitrous and nitric ions. Electrons can also attach to water molecules and then dissociate water molecules to H_{aq} and $OH^-{}_{aq}$.

Negative ions: When negative ions solvate in water, they charge exchange with oxygen to form $O_2^-{}_{aq}$, and with water molecules to dissociate water molecules to H_{aq} and $OH^-{}_{aq}$. In water containing OH_{aq}, negative ions also charge exchange with OH_{aq} to form $OH^-{}_{aq}$. To some extent, negative ions can be seen as carrier of electrons, so their reaction pathways are very similar to electrons.

Positive ions: When positive ions having an ionization potential larger than water solvate in water, they charge exchange with water molecules and form water ions. Water ions quickly further react with water molecules to form hydronium, $H_3O^+{}_{aq}$, and a hydroxyl radical, OH_{aq}. Hydronium, $H_3O^+{}_{aq}$, is the terminal positive ion in most cases.

Photons and excited states: Both photons and excited states deliver their energy to water. Photons and excited states with sufficient energies result in dissociation and ionization of water molecules when they hit the water. The photons and excited states with lower energies lose their energy when entering the water, since no excited states of water molecules are considered in the model.

H_{2aq} and H_2O_{2aq}: One of paths to H_{2aq} and H_2O_{2aq} originates with their gaseous counterparts in humid air. Water vapor diffusing into the active plasma from the liquid undergoes dissociative excitation and attachment to produce H and HO, which then solvate in water. H_{aq} and OH_{aq} can also be produced directly in water by dissociation and charge exchange of water molecules. H_{aq} and OH_{aq} are transient species which do not last long in water. They form H_{2aq} and H_2O_{2aq} by mutual reactions, respectively. H_{aq} also reacts with dissolved oxygen to produce HO_{2aq}, which either reacts with NO_{aq} to form acids or hydrolyzes to $H_3O^+{}_{aq}$ and $O_2^-{}_{aq}$. OH_{aq} is very reactive and reacts with most nitrogen oxides such as NO_{aq} and NO_{2aq}.

Ozone: The formation of aqueous ozone, O_{3aq}, in water is straightforward. The majority of O_{3aq} result from solvation of gaseous O_3. In air discharges, gaseous ozone, O_3, starts with the production of O atoms from electron dissociative excitation and dissociative attachment of O_2 with small contributions from dissociative ionization. Three body collisions of O and O_2 then produce O_3. O is very reactive and little O can reach the water to solvate. In the absence of or-

ganic molecules, O_{3aq} is a fairly stable agent. O_{3aq} is primarily consumed by oxidation reactions with NO_{aq}, NO_{2aq} and $NO_2^-{}_{aq}$.

Nitrogen-containing species: All the aqueous nitrogen-containing species result from the solvation of gaseous nitrogen-containing species. The majority of them will be eventually converted to acids which quickly hydrolyze, forming terminal species of $H_3O^+{}_{aq}$, $NO_2^-{}_{aq}$, $NO_3^-{}_{aq}$ and $ONOO^-{}_{aq}$ ions. The detailed reaction pathways are shown in Fig. 2.5. In plasmas, N and O atoms are produced through direct dissociation of N_2 and O_2, or recombinative dissociation of N_2^+ and O_2^+. N and O atoms then reacts to produce N_xO_y (NO, NO_2, NO_3, N_2O_3, N_2O_4 and N_2O_5) which reacts with water vapor to form HNO_x (HNO_2, HNO_3 and HOONO) in humid air. N_xO_y solvates in water slowly, while HNO_x solvates quickly. N_xO_y solvates to N_xO_{yaq} and is slowly converted to HNO_{xaq} by reacting with OH_{aq}, HO_{2aq} and H_{aq}. HNO_{xaq} quickly hydrolyze to $H_3O^+{}_{aq}$, $NO_2^-{}_{aq}$, $NO_3^-{}_{aq}$ and $ONOO^-{}_{aq}$, which are terminal ions in water.

Hydrocarbons: In treatment of wet tissue, the water most likely contains a generic hydrocarbon alkane, RH_{aq}. Under these circumstances, reactive oxygen species (ROS) such as O_{3aq}, OH_{aq} and H_2O_{2aq} are largely consumed by RH_{aq}, leaving $R\cdot_{aq}$ (alkyl radical) in water. The reactivity of ROS is converted to the reactivity of $R\cdot_{aq}$.

2.9 Figures

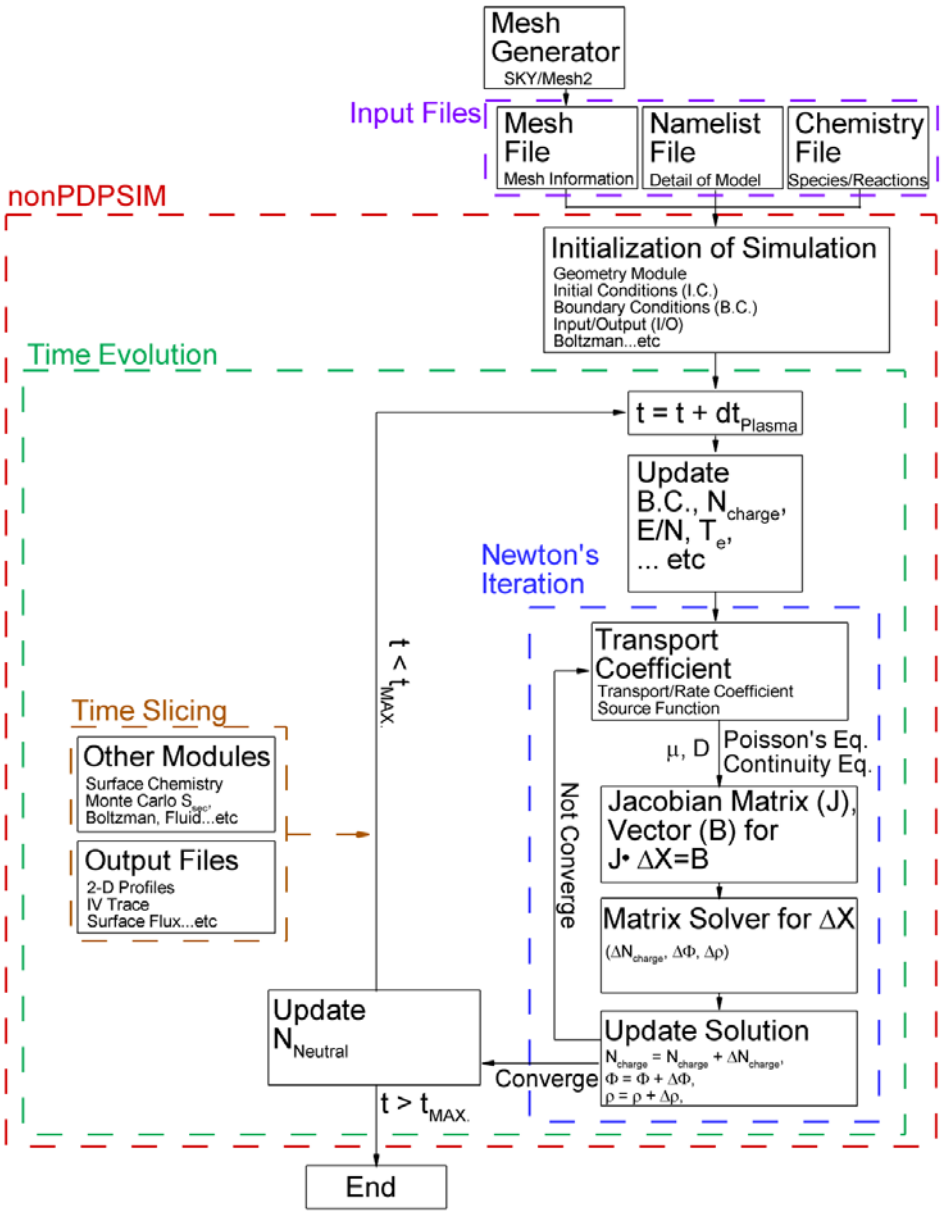

Figure 2.1 Block diagram of nonPDPSIM.[5]

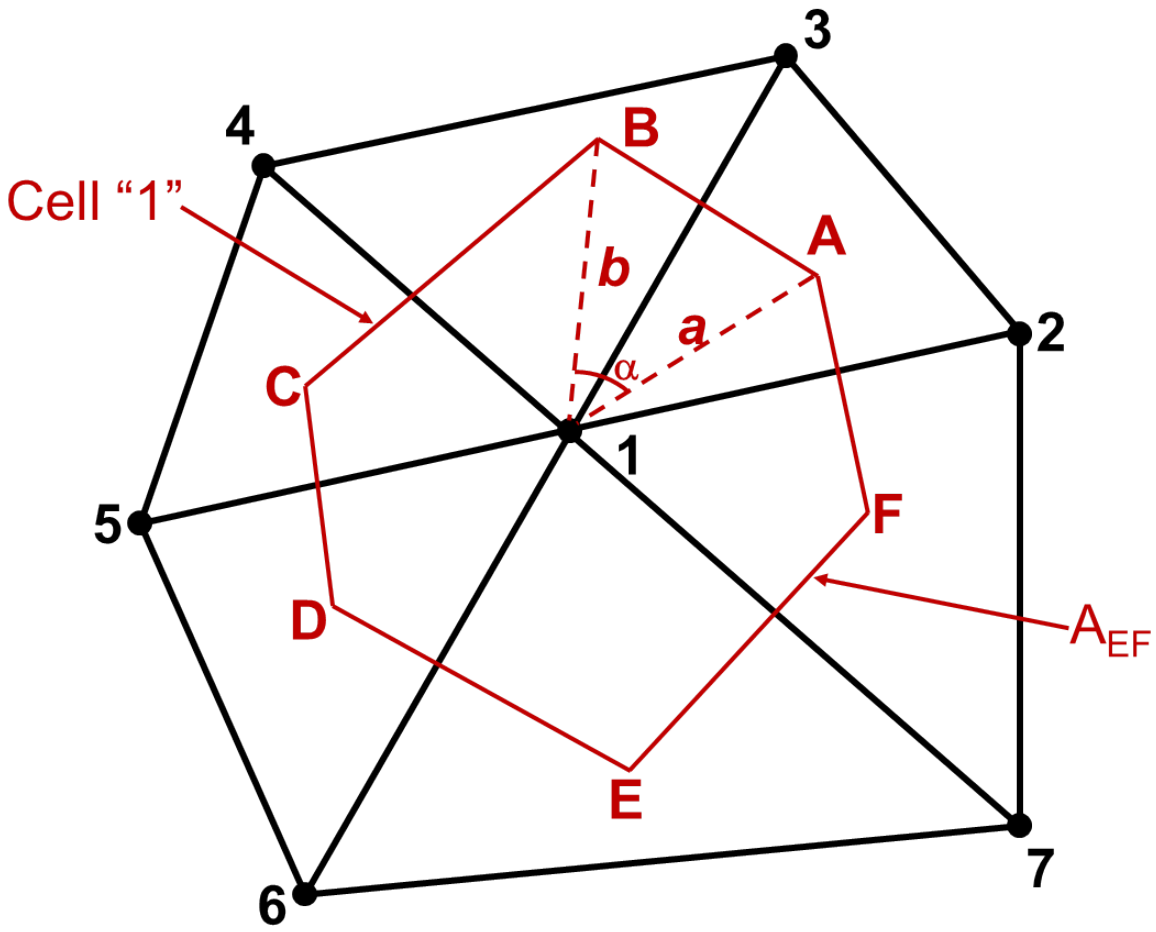

Figure 2.2 Control volume (CV) mesh and actual mesh. The vertex-centered control volume is constructed by identifying the intersections of the perpendicular bisectors between a node and it nearest neighbors; the “cell corners” (A, B, C, D, E, or F) are defined as the intersections of the perpendicular bisectors. Areas are defined as red line connecting the perpendicular bisectors. Actual mesh consists of vertices, faces, and cells. Nodes (no. 1–7) and black lines which connect the nodes are output from the mesh generator.

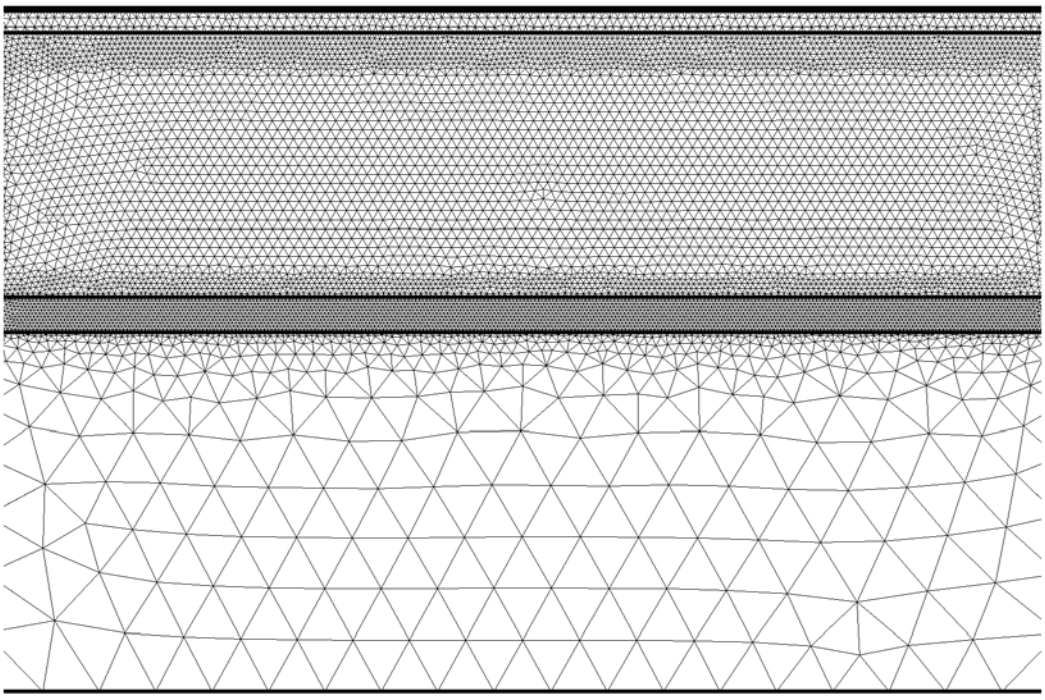

Figure 2.3 Model geometry and unstructured mesh used for the simulation of dielectric barrier discharges. Mesh size varies from 100 μm at the bottom to 10 μm at the middle.

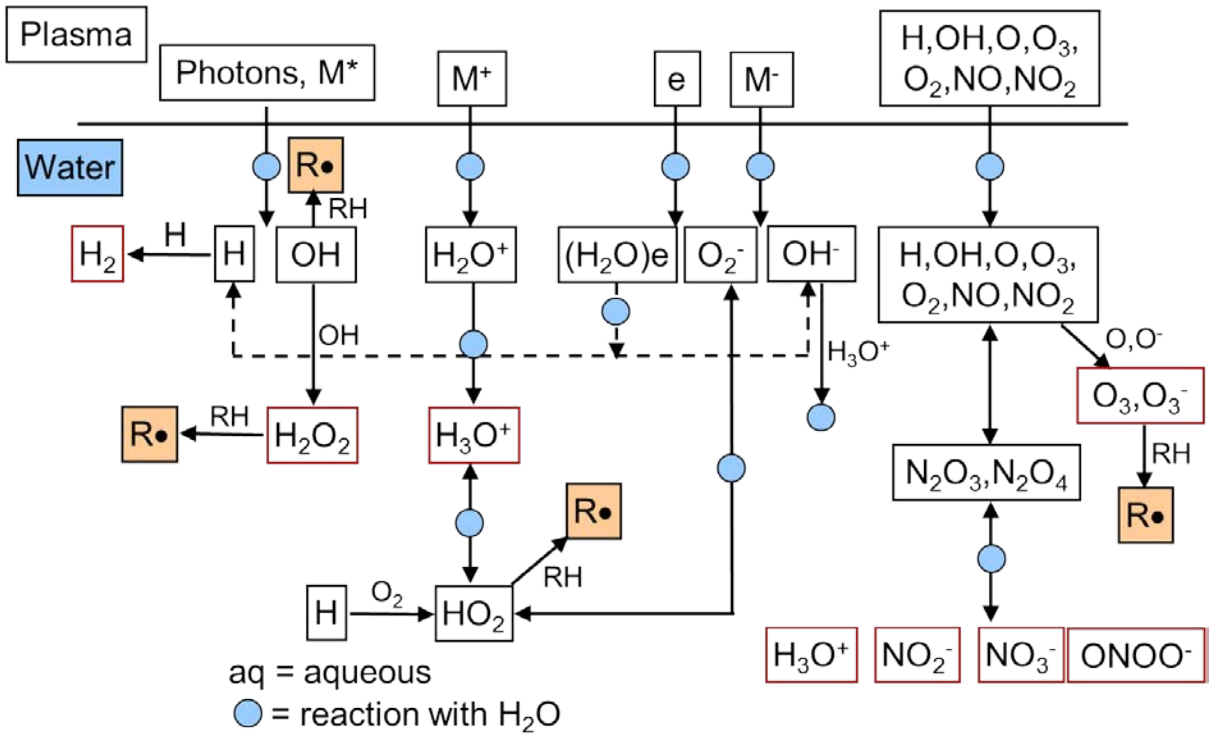

Figure 2.4 The diagram of aqueous reaction mechanism. Red boxes indicate terminal species.

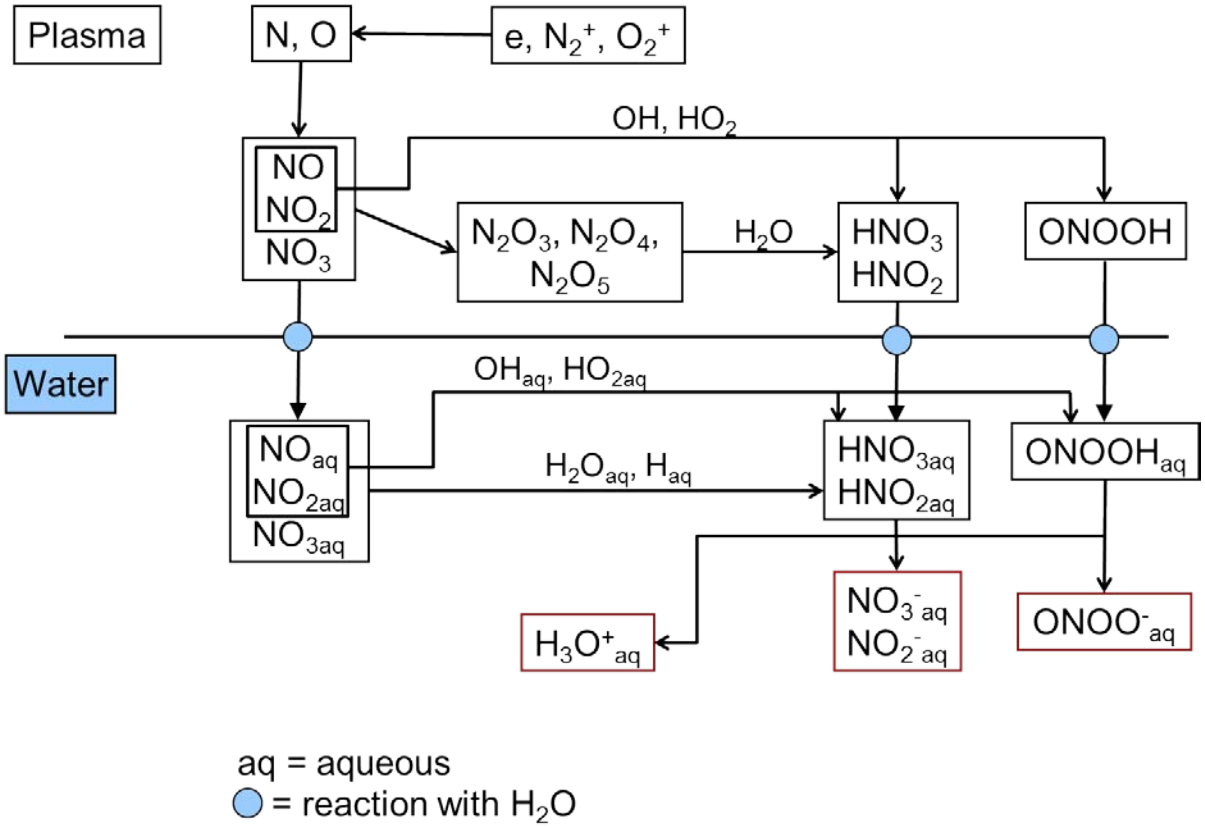

Figure 2.5 The diagram of reaction mechanism of nitrogen-containing species. Red boxes indicate terminal species.

2.10 References

[1] Rauf and M. Kushner, J. Appl. Phys., 85, 3460 (1999).

[2] Z. Xiong and M. J. Kushner, J. Phys. D: Appl. Phys. **43**, 505204 (2010).

[3] A. N. Bhoj, PHD Thesis, University of Illinois, 2006. (**http://uigelz.eecs.umich.edu/theses.html**)

[4] R. A. Arakoni, PHD Thesis, University of Illinois, 2007. (**http://uigelz.eecs.umich.edu/theses.html**)

[5] J-C. Wang, PHD Thesis, University of Michigan, 2014. (**http://uigelz.eecs.umich.edu/theses.html**)

[6] S. Norburg, PHD Thesis, University of Michigan, 2014. (**http://uigelz.eecs.umich.edu/theses.html**)

[7] D. L. Scharfetter, and H. K. Gummel, IEEE Trans. Electron Devices. ED-16, 64 (1969).

[8] Scharfetter-Gummel discretization scheme for drift-diffusion equations

[9] SLAP Sparse Matrix Library, http://www.netlib.org

[10] Y.Saad, Department of Computer Science and Engg., University of Minnesota http://www-users.cs.umn.edu/~saad/software/SPARSKIT/sparskit.html

[11] A. Fridman and G. Friedman, “Plasma Medicine” (Wiley, Oxford, 2013), page 183 – 192.

[12] Y. P. Raizer, “Gas Discharges Physics”, Springer 1991

[13] J. Hirschfelder, C. F. Curtiss and R. B. Bird, “Molecular Theory of Gases and Liquids”, New York: Wiley, 1954.

[14] *NIST Chemical Kinetics Database*, [Online]. Available: http://kinetics.nist.gov/kinetics/index.jsp

[15] *NDRL/NIST Solution Kinetics Database*, [Online]. Available:

http://kinetics.nist.gov/solution/

[16] R. E. Skyner, J. L. McDonagh, C. R. Groom, T. van Mourik and J. B. O. Mitchell, Phys. Chem. Chem. Phys. **17**, 6174 (2015).

[17] K. P. Maddena and S. P. Mezyka, J. Phys. Chem. Ref. Data **40**, 023103 (2011).

CHAPTER 3 SIMULATIONS OF IMAGES AND OPTICAL SPECTRA OF PLASMAS SUSTAINED IN BUBBLES IN WATER*

3.1 Introduction

Plasmas in water are being investigated for their ability to produce chemically reactive species such as hydrogen peroxide [1], hydroxyl radicals [2] and oxygen radicals [3] for applications ranging from environmental cleanup [3] and chemical processing [4] to healthcare.[5] Electric discharges in liquid have been reported in the absence of a vapor phase when using the fast-rising high-voltage pulse.[6] However, from the perspective of high average power industrial applications, it is likely that radical formation in discharges in liquids dominantly occurs in a pre-existing vapor phase or a vapor phase produced by the discharge itself. Formation of the vapor phase by the discharge is energetically costly as the heat of formation of the gas must be invested before significant radical production occurs. Large voltages are also required to produce the requisite E/N (electric field/gas number density) to produce the discharge in a liquid, whose densities are typically 1000 times that of atmospheric pressure gas.

An alternative approach is to inject atmospheric pressure bubbles into the liquid and sustain the discharge in the bubbles. Due to the low molecular density in the bubble compared to the liquid, a significantly lower voltage will initiate the plasma in the bubble compared to the liquid. For sufficiently small bubbles and residence times of the bubble in the liquid, the majority of radicals produced in the bubble will likely diffuse into the liquid. The composition

*The results discussed and portion of the text appearing in this chapter were previously published in Wei Tian *et al*, "Plasmas sustained in bubbles in water: optical emission and excitation mechanisms", J. Phys. D: Appl. Phys. **47**, 055202(2014)

of the radicals produced in the bubble is determined by the gas used to make the bubble and the vapor of the liquid that diffuses into the bubble. It has been proposed that initiating and propagating discharges in liquid are likely enabled (or at least enhanced) by pre-existing bubbles. Even in degassed water, there probably are pre-existing bubbles of 100's nm in diameter.[7]

Discharges in bubbles in water are more complex than their counterparts in the gas phase due to the close proximity of the gas-water interface. In actual practice, discharges in bubbles can significantly deform and in some cases burst the bubble.[8] Even in the absence of these morphological changes, the gas-vapor interface is critical to the characteristics of the plasma in a bubble, and especially a plasma-in-a-bubble-in-water (PBW).

In one arrangement of PBW, the bubble is attached to an electrode immersed in water. The discharge voltage is low enough that the discharge occurs only in the bubble (and not in the water). For initially deionized or low conductivity water, the water essentially operates as a dielectric on the timescales of the discharge pulse, and so the discharge is terminated when charge accumulates at the surface of the water, much like a dielectric barrier discharge (DBD). Prior modeling results [9] and experimental observations [10] have shown that under select conditions, the discharge in a PBW propagates along the vapor-water boundary. This surface-hugging-discharge mode is a consequence of the electric field enhancement that occurs across a curved boundary between two materials having different dielectric constants ($\varepsilon/\varepsilon_0$= 1 for the bubble and 80 for water). These plasma dynamics fortunately concentrate the discharge power at the location where the water vapor density is likely highest and so the production of oxidizing radicals is large. PBWs can appear as both a volumetric DBD [11] and as a surface discharge, the latter of which is a variant of a DBD [9,10]. For large bubbles, PBWs tend to hug the water surface whereas in smaller bubbles and with larger voltages, the discharge tends to more uniformly fill the bubble.[9]

With the goal of quantifying the basic physical and chemical processes of PBW, in this chapter, we discuss results from a computational investigation of the plasma dynamics of electrical discharges in idealized bubbles in water. A single discharge pulse is investigated in PBWs through He, Ar and N_2 filled bubbles. The bubbles are modeled as being static since the discharge occurs and evolves in nanoseconds, and so no deformation of the bubble occurs in the model.[9] The water is represented as a dielectric material so no reactions occur inside the

water. Synthesized images and optical spectra from the bubbles are compared to recent experiments by Tachibana *et al*.[10] In these experiments, the bubbles were distorted by the discharges after the current pulse terminated. However, during the short current pulse, the bubbles were largely undisturbed. A new bubble was created for the next discharge pulse so the distortion of the previous bubble was not important. In this chapter, we discuss excitation mechanisms in the bubble during the discharge pulse prior to distortions being important.

We found that the electron temperature, T_e, within the PBW is higher for atomic gases and lower for molecular gases, which result in strong and weak optical emissions, respectively. In addition to differences in T_e, excitation transfer processes from the electronically excited bubble gases to water vapor also contribute to differences in the optical emission. These results are also influenced by the different rates of diffusion of water vapor from the surface of the water into the interior of the bubble. The electron energy relaxation length, λ_e, defined by the characteristic distance electrons travel before dissipating their energy through collisions, is affected by this diffusion of water vapor into the bubble.

The model used in this investigation is described in Sec. 3.2 followed by a discussion of simulated PBW in Sec. 3.3. Our concluding remarks are in Sec. 3.4.

3.2 Description of the Model and Reaction Mechanism

The model used in this chapter, *nonPDPSIM*, has been described in detail in Chapter 2. The model uses an unstructured triangular mesh for the sub-picosecond time steps necessary to resolve the discharge dynamics. The electric field at the gas-liquid interface is carefully calculated by considering the difference of dielectric constants. The model addresses UV/VUV radiation generated by high lying excited states. The radiation is attenuated by absorption in propagating through the plasma [12]. Radiation transport also provides photon fluxes to surfaces. The model also includes photoionization and photodissociation of H_2O.

In experiments by Tachibana [10], He, Ar and N_2 were used to create bubbles in the water at the tip of an electrode. The bubble evolves in size from a seed bubble to a sphere in 23 ms. A pulse is then applied at 15 ms when the bubbles grow to 3 mm in diameter. Due to the

short time between creating the bubble and pulsing the discharge, apparently water vapor is not likely to be uniformly saturating the gas. To address these conditions, water vapor is allowed to diffuse for 1 ms prior to applying voltage into the bubble, which is formed at time t = 0 consisting only of the pure injected gas. The water vapor density at the water surface is given by the saturated water vapor pressure at room temperature (27 Torr).[13] Binary diffusion coefficients, D_{12}, for H_2O through the fill gas of the bubbles were estimated using their Lennard-Jones parameters and modified hard-sphere collisions[14],

$$D_{12} = 0.001858\sqrt{\frac{M_1 + M_2}{M_1 M_2}}\frac{T^{3/2}}{p\sigma_{12}^2\Omega_D}$$

where T is the gas temperature (K), M_1 and M_2 are molecular weights of water and the gas within the bubble, p (atm) is the total pressure of the binary mixture, σ_{12} is the Lennard-Jones parameter defined by $\sigma_{12} = 1/2(\sigma_1 + \sigma_2)$, Ω_D is the temperature-dependent collision integral.[14] The Lennard-Jones parameters used here and the derived diffusion coefficients are listed in Table 3.1.

Given the computational scale of the 2-dimensional calculation, a reduced reaction mechanism was used for He, Ar and N_2 with added H_2O, and is shown in Table 3.2. The reaction mechanism was chosen to be a self-consistent system that captures the pertinent plasma processes on the < 1 μs timescale and neutral processes on longer time scales, while also being compatible with the increased computational load of this 2D simulation. Ions which are unique for each gas fill of the bubble are He^+, He_2^+; Ar^+, Ar_2^+; and N_2^+, N_4^+. Ions which occur in all three gas fills are H_2O^+, H^+, OH^+, O^- and OH^-. Excited states of the rare gases are intended to be lumped states. He^*, He^{**}, and He^{***} are nominally He(2^3S), He(2^1P) and He(3^3P). Ar^* represents the two metastable states of the Ar(1s) manifold, Ar($1s_1$) and Ar($1s_3$). Ar** represents the two radiative states of the manifold, Ar($1s_2$) and Ar($1s_4$). Ar^{***} nominally represents Ar(4p) and higher states. The states N_2^*, N_2^{**} and N_2^{***} are nominally N_2(A) and N_2(B); N_2(a'); N_2(C) and higher states, respectively. The vibrationally excited states of N_2 were lumped into N_2(v). The excited states of H and OH are also taken into account. H^*, H^{**}, H^{***} and OH^* are nominally H(n=2), H(n=3), H(n=4) and OH(A), respectively.

At atmospheric pressure, the collision frequency is sufficiently high that excitation transfer from excited states of He, Ar and N_2 to H_2O can be an important (and perhaps a

dominant) method to produce excited states of H and OH. The experiments [10] measured total optical emission and selectively, using filters, optical emission from the OH(A-X) transition at 306 nm and the H(n=3-2) transition, H_α, at 656 nm. Electron impact dissociative excitation of H_2O producing of OH(A) requires at least 9.0 eV. The dissociative excitation of H_2O producing H(n=2), H(n=3), H(n=4) requires 15.4 eV, 18.5 eV and 19.3 eV, respectively. Given the lower threshold for producing OH(A), excitation transfer to H_2O from any excited state of He and Ar can produce OH(A). The rate coefficients for these excitation transfer reactions are nearly gas kinetic. Excitation transfer from excited states of N_2 occurs only for N_2(C) and higher states, which are likely not to be heavily populated since energy is consumed in a large part by lower level excitations. Excitation transfer to H_2O resulting in H_α radiation requires as a product H(n=3), or 18.5 eV of energy. Only He excited states have sufficient energy to do so, and so H_α radiation observed from bubbles in Ar and N_2 must proceed through electron impact dissociative excitation of H_2O or direct electron impact excitation of H atoms.

We assumed that all ions neutralize on solid surfaces and return to the gas phase as their neutral counterparts, and that excited species return as their ground states. As a result, charges accumulate on non-conducting surfaces. At water surfaces, ions and neutral radicals naturally solvate with some probability and remain in the water. As an extreme case, we assumed that the water surface is absorbing for neutral radicals and ions with charge accumulating at the surface.

Tachibana [10] reported on spatially dependent total optical emission and H_α emission at 656.3 nm. The former was obtained with a digital camera without a filter with exposure over the entire discharge period. For the latter, emission was observed through a band-pass filter centered at 658 nm with a 10 nm bandwidth. Time and spatially integrated emission was also reported for H_α and OH(A-X). In our model, the total emission for each gas mixture was synthesized by integrating over time the density of excited species emitting in the visible weighted by their corresponding Einstein A coefficients. For H_α emission, we computed the intensity by integrating over time the density of H(n=3) weighted by its corresponding Einstein A coefficient. The images taken in the experiment were the projection of the emission from the spherical bubble, which included contributions from individual streamers at different azimuthal locations. Our simulation is cylindrically symmetric and so a 1-to-1 correspondence with experimental

images is not directly possible. However, the comparison of computed trends with experiment provides insights to the location of formation of excited states.

3.3 Plasma Dynamics in He, Ar and N_2 in Bubbles in Water

The model geometry is shown in Fig. 3.1. The entire computational domain is 50 mm × 50 mm. The bubble region is enlarged with elsewhere filled by water, which in our model is treated as a non-conductive material with a dielectric constant of $\varepsilon/\varepsilon_0 = 80$. The bubble with a diameter of 2 mm is attached to a metal tube having a 0.3 mm inner diameter which also serves as the powered electrode. The metal tube is covered with a 3.6 mm thick dielectric ($\varepsilon/\varepsilon_0 = 4$). The top and right boundaries sufficiently far away from the bubble are grounded and do not significantly affect the predicted plasma properties inside the bubble. The system is cylindrically symmetric across the center line on the left boundary. The discharge starts and develops inside the bubble. Surface charge is allowed to accumulate at the bubble-surface consistent with the incident plasma fluxes, since the dielectric relaxation time of the water (> 100 ns) is long enough compared to the time of propagation of the surface discharge within the bubble (about 10 ns). We assumed that all ions neutralize on the water surface and return to the gas phase as their neutral counterparts, and that excited species return as their ground states. Secondary electron emission from the water surface is also included when ions and photons strike the bubble-water interface. The plasma dynamics we investigated are on the nanosecond time scale, so deformation of the bubble taking place on microsecond time scales is not considered.

A 2-dimensional unstructured mesh is used for the numerical grid. The mesh consists of approximately 10,000 nodes, of which about 7000 nodes are in the plasma region inside the bubble with refinement along the bubble-water interface. The smallest distances between the nodes in the gas phase in the center of the bubble are about 50 μm, decreasing to less than 5 μm near the boundary. This mesh scale is enough to resolve the surface charge propagation with sheath estimated to be about 10-20 μm.

A cloud of plasma of 10^9 cm^{-3} with a radius of 50 μm at the powered electrode is used to initiate the discharge, which avalanches after voltage is applied. The discharge propagation is assisted by the secondary emission from bubble-water interface, where secondary emission

coefficient is 0.15 for ions and 0.001 for photons. In the experiments by Tachibana *et al*[10], the voltage rises in about 100 ns and remains 15 kV for 5 μs, which requires too much computation load. In our model, the 15 kV pulse is applied much faster and shorter, with a rise time of 0.1 ns, 15 ns width and falling time of 1 ns. The plasma computation then proceeds for 50 ns, which is a long enough time to capture the characteristics of the discharge while having a reasonable computation time.

Water vapor densities in the He, Ar and N_2 bubbles at the time the voltage is applied, approximately 1 ms after bubble formation, are shown in Fig 3.2. $[H_2O]$ is 5.8×10^{17} cm^{-3} at the boundary of the bubble in each case, given by the room temperature vapor pressure of water, 27 Torr. The diffusion coefficient of H_2O in He is larger due to smaller collision cross section. $[H_2O]$ is 4×10^{15} cm^{-3} in the center of the H3 bubble, about a factor of two larger than the density of H_2O in the center of the Ar and N_2 bubbles. These differences in the distribution of water vapor impact the production of H and OH.

3.3.1 Discharge Dynamics

The time evolutions of electron density, n_e, electron temperature, T_e, and *E/N* (electric field/gas number density) during the discharge are shown in Fig. 3.3 for PBW in He, Ar and N_2 for a step function in voltage to positive 15 kV. The discharge forms and propagates in the bubble within 10 ns. The discharge starts at the tip of the powered electrode where the initial electrons are seeded, likely by emission from either the electrode or the water. The electric field is refracted towards the gas-water interface due to the curvature of bubble boundary and different dielectric constants between the gas and water, which also produces electric field enhancement.[11] Therefore, once the discharge begins, it is directed along the interface of the gas and water, as observed in the experiments of Tachibana and others.[8,12] Charge accumulating on the surface of the interface then provides the functionality of a dielectric barrier discharge. The propagation of the surface streamer is sustained by electric field enhancement at the head of the streamer, producing maximum E/N of 4,000 – 7,000 Td (1 Td = 10^{-17} V-cm^2). This space charge produced electric field enhancement is in addition to the natural enhancement due to the curvature and gradient in dielectric constant, and produces T_e of 8-10 eV in Ar and N_2,

and up to 35 eV in He at the leading edge of the surface hugging ionization wave. He has largest threshold energies for electron impact excitation and ionization but with smaller cross sections, so electrons can maintain a large T_e in these large E/N. Once the discharge propagates across the inner surface of the bubble, the deposited surface charge screens out the electric field into the water at which time the T_e and ionization rates decrease. Surface hugging discharges also occur in pure, dry gases and are not necessarily correlated to the higher H_2O vapor density near the interface.

The peak electron density occurs in the vicinity of the electrode where electric field enhancement is the largest. The maximum electron densities in He and Ar are comparable, 1-2 $\times$ 10^{16} cm^{-3}, due in large part to step-wise ionization, though this is a less important factor in He since the excitation threshold is fractionally closer to the ionization threshold in He. The electron density in the N_2 bubble is about an order of magnitude smaller, a consequence of the shorter energy relaxation distance which deposits proportionately more power in non-ionizing modes (i.e., vibrational excitation). Note that the surface discharge circumnavigates the inner surface of the bubble in He and Ar within 1 ns, more quickly in He. The surface hugging ionization wave stalls before reaching the opposite pole in N_2.

3.3.2 Optical Emission Compared to Experiments

The synthesized, time integrated total optical emission and H_α (656.3 nm) emission from the He, Ar and N_2 bubbles are compared to experiments [10] in Fig. 3.4. The total intensity is dominated by emission from excited states of the injected gases rather than emission from the water vapor. In the experiments, the He discharge appears to have stronger emission at the interface and to be weaker at the center of the bubble. (Recall that the experiments are plane views of emission through the bubble and so the emission from the center of the bubble actually contains contributions from the surface facing the observer.) The total emission in the Ar discharge appears more uniform than from He but closer analysis suggests that the emission results from the contributions of many surface filaments, and not necessarily from the volume. Very clear filamentary discharge structures are observed at the surface in the N_2 bubble with little optical emission from the center of the bubble. It appears that most of the surface

discharges in the N_2 bubble do not circumnavigate the bubble whereas the surface discharges do circumnavigate the bubbles in He and Ar.

These experimental trends for total emission are captured by the synthesized emission from the model. The predicted total emission is most uniform in the He bubble and most filamentary in the N_2 bubble. The emission along the surface of the gas-water interface is significantly more intense in the Ar bubble whereas the emission is weaker but deeper into the bubble for the He discharge, observations which correlate with the experiments. The total emission clearly circumnavigates the bubbles in He and Ar, and does not circumnavigate the bubble in N_2. The total optical emission weakly correlates with the distribution of H_2O vapor.

The experimental H_α emission intensities are significantly more confined to the surface of the bubble with contributions from individual surface streamers clearly seen in Fig. 3.4(b). The emission intensities are strongest from the PBW in He, weaker for Ar, and near the detection limit in the N_2 bubble. These trends are well reproduced by the synthesized H_α emission produced by the model. In the computed results, the H_α emission is more volumetric from the He bubble, while the emission is confined along the interface for the Ar or N_2 bubbles. Since H_α emission comes from dissociative excitation of water vapor and excitation of its dissociation fragments, the distribution of water vapor directly contributes to the spatial distribution of the H_α emission. The more intense emission and somewhat more uniform emission from the He bubble has at least two sources – the H_2O vapor has diffused deeper into the bubble and T_e is larger, which more efficiently produces dissociative excitation of the H_2O. The more confined and weaker emission from PBW in N_2 results from the more concentrated water vapor near the boundary and the lower T_e.

The synthesized OH(A-X) emission is also shown in Fig. 3.4(c). The OH(A-X) emission follows the same trends as H_α emission – deeper into the bubble in the case of He and more confined along the interface for Ar and N_2. This is an expected result as the OH(A-X) emission, as does the H_α emission, ultimately originates from dissociative excitation from water vapor. However the OH(A-X) emission in Ar and N_2 bubble are stronger than H_α. The reason will be discussed below.

The distribution of plasma and optical emission are in part explained by the electron energy relaxation lengths, λ_e, shown in Fig. 3.5 for 1 atm. The energy relaxation length can be seen as a distance that electrons can travel without significantly losing their energy. These values were computed from stationary solutions of Boltzmann's equation using a 2-term spherical harmonic expansion for gases with different concentrations of water vapor.[15] The λ_e for pure water vapor is shown in each plot as a reference. The λ_e for pure gases decreases with increasing electron energy as inelastic collisions begin to dominate. λ_e for He is about 2 mm below 5-6 eV and decreases to 0.1 mm as electron energy increases to 10 eV. The bubble is 2 mm in diameter. In Ar, λ_e is larger than 10 mm below 4 eV and quickly decreases to 0.01 mm at 8 eV. N_2 and H_2O have small λ_e , about 0.01 mm, except in the purely elastic regime at $T_e < 0.1$ eV.

λ_e for gases with 3% water vapor, as shown in Fig. 3.5(b), represents the conditions for our PBW discharges near the water surface. λ_e in He and Ar has a significant drop at $T_e < 4$-5 eV whereas λ_e is not significantly affected in N_2 above 0.5 eV. For the computed range of T_e, λ_e for N_2 is always much smaller than the size of the bubble, so that energetic electrons are confined to the boundary of the bubble where they are accelerated by the large E/N near the interface. In Ar, λ_e drops to the thickness of the water layer as T_e increases above 4 eV. However electrons which scatter out of the dense water layer will have proportionally longer λ_e in the portion of the bubble that has less water vapor. This length approaches the size of the bubble size in the purer gas. A similar trend occurs in He though λ_e is longer at higher T_e than in Ar, thereby enabling somewhat more uniform rates of excitation, as observed in the plasma density and optical emission. The differences in λ_e diminish for gas mixtures with higher fractions of H_2O as electron energy losses are dominated by the water, as shown in Fig. 3.5(c).

The relative volume-averaged, time integrated intensities of optical emission from excited hydrogen atoms, H_α (656.3 nm), and from OH(A-X) (306.4 nm) are shown in Fig. 3.6(a). These values were obtained from the model by performing a volume and time integral of the excited densities weighted by their spontaneous emission coefficients. The model was normalized to the experiment for H_α emission from the PBW in He. Both the model and the

experiments show the trend that the emission from both species is most intense from PBW in He bubbles and least intense from N_2 bubbles. The H_α emission from the He bubble is significantly more intense than emission from the Ar bubble (a factor of 5), which in turn is more intense than from the N_2 bubble (another factor of 5). The OH(A-X) emission is overall less intense, and scales on a relative basis similarly to the H_α emission, with a factor of 2 decrease from He to Ar, and from Ar to N_2.

The production of H(n=3) and OH(A) comes through at least three channels – direct electron impact excitation of ground state H(n=1) and OH(X), electron impact dissociative excitation of H_2O, and excitation transfer from excited electronic states of He, Ar or N_2 to H_2O. These processes are shown in Table III with their respective threshold potentials. The relative contributions of these three channels that produce H(n=3) and OH(A) are shown in Fig. 3.6(b). Excitation transfer to H_2O strongly dominates the production of OH(A) in Ar and N_2 discharges, and is nominally the highest contributor in He plasmas. The trend is nearly the reverse for excitation of H(n=3) – direct electron impact excitation of ground state H dominates in Ar and N_2 discharges whereas excitation transfer dominates in He discharges. The H_α line is more intense in He discharges than in Ar or N_2 discharges in part due to excitation transfer from excited states of He to H_2O, which dissociates the water and produces H(n=3). Excited states of Ar or N_2 are not energetic enough to produce such emission. Excited states of He, Ar and N_2 can all excitation transfer to H_2O to produce OH(A), and so the emission intensities are more nearly equal.

The average densities of the ground states H(n=1) and OH(X) are in the range of 10^{13} to 10^{14} cm^{-3}, while the peak depletion of H_2O is only about 10% near the powered electrode. This significant density of ground state H and OH enables significant opportunity for direct electron impact excitation. The electron impact dissociative excitation of H_2O to produce H(n=3) has a higher threshold energy than direct excitation of the ground state. In turn, the rate coefficient for direct excitation is larger than that for dissociative excitation of H_2O for the entire range of T_e in the plasma. As a result, the direct electron impact excitation of H(n=1) contributes more to the optical emission than dissociative excitation in the Ar and N_2 discharges. In He discharges, excitation transfer dominates.

The time and spatially integrated relative emission intensities for H_α and OH(A-X) as a function of applied voltage, are shown in shown in Fig. 3.7. (The discharge cannot be sustained in N_2 bubbles for voltages less than 15 kV.) The relative increase of optical emission with increasing voltage is smallest for discharges in He bubbles and greatest for discharges in N_2 bubbles. T_e increases with applied voltage during the surface hugging ionization wave but is relatively constant in the plasma column behind the ionization wave while current flows to charge the capacitance of the surface of the bubble. The increase in emission is largely due to the longer current pulse at nearly constant T_e required to charge the bubble capacitance as the voltage increases.

Production of H(n=3) is dominated by excitation transfer in He discharges. In Ar and N_2 discharges, production of H(n=3) is dominated by direct electron impact of H atoms following dissociative excitation transfer to H_2O. The accumulation of H(n=1) during the longer current pulse in Ar and N_2 discharges enables proportionately larger H_α emission due to the accumulation of the ground state species. Similar trends apply for OH emission where the accumulation of OH(X) enables direct electron impact excitation of OH(A). At the time of the discharge in Ar and N_2 bubbles, the water vapor is most dense near the boundary and is more confined than in the He bubbles. The discharges in Ar and N_2 bubbles also occur closer to the boundary. The disproportionate increase in OH(A-X) emission that occurs in in Ar and N_2 discharges may partly result from the discharge preferentially occurring through the more dense H_2O vapor layer at the surface of the bubble.

3.3.3 Fluences of Reactive Oxygen Species

One of the applications of plasmas in bubbles is to purify water. This purification results, in part, from the diffusion of reactive oxygen species (ROS) created in the bubble into the water. To estimate the possible effectiveness of these processes, the fluxes of OH and H_2O_2 onto the water surface were integrated as a function of time for 1 s after the discharge pulse to provide fluences (cm^{-2}). These fluences are shown in Fig. 3.8 for a discharge voltage of 15 kV as a function of position along the gas-water interface from the electrode to the top of the bubble. Since energy deposition is largest near the electrode, the fluences are highest at the bottom of the

bubble, decreasing along the surface to the top of the bubble. OH is produced by dissociation of H_2O (by electron impact or excitation transfer) and its density exceeds that of H_2O_2 during the short discharge pulse. However, after the discharge pulse, OH is consumed by its mutual reaction in the gas phase in formation of H_2O_2 resulting in the H_2O_2 fluences generally being one-order of magnitude larger than the OH fluences. The largest H_2O_2 fluences are produced by discharges in He bubbles, in large part because the electron temperature is the highest which then produces the highest rates of H_2O dissociation. Discharges in N_2 bubbles generally produce the smallest fluences of H_2O_2 due to the disproportionate amount of power spent in nondissociative modes.

Virtually all of the positive ions striking the surface of the water undergo charge exchange with liquid H_2O to produce H_2O^+ which then quickly charge exchanges to make H_3O^+ and OH. The H_3O^+ acidifies the water and the OH dominantly forms H_2O_2. Although these sources are important in many circumstances, for our conditions the fluences of charged species onto the surface of the water are lower than those for neutral species by about a factor of 10^3.

3.4 Concluding Remarks

The properties of pulsed discharges in He, Ar and N_2 bubbles in water were computationally investigated and the results are compared to experiments.[10] The discharges typically propagate along the surface of the where the gradient in dielectric constant is largest, producing electric field enhancement. The diffusion of water vapor into the bubble requires a finite time and so the gas adjacent to the gas-water interface has a higher density of H_2O than in the interior, which is coincidentally where the discharge also propagates. The optical emission from the bubbles reflects these discharge patterns, being more uniform in the He filled bubble where electron energy relaxation lengths are longer, and more confined along the interface for N_2 bubbles where the energy relaxation length is smallest. Total optical emission is more volumetrically distributed (though heavily weighted towards the boundary), while H_α and OH(A-X) emissions are generally confined to the surface where both the H_2O vapor density and electron temperature are largest. The formation of OH(A) is dominated by dissociative excitation transfer to H_2O from excited states of He, Ar and N_2. The formation of H(n=3) is

dominated by electron impact excitation of ground state H in Ar and N_2 discharges, and dissociative excitation transfer to H_2O in He discharges. For otherwise the same conditions the emission of intensities and ROS fluences to the bubble-water surface are largest in He bubbles. These results suggest that some degree of optimization or customization of radical production from PBW is possible by choice of the gas forming the bubble.

In summary, this chapter aims at understanding plasma dynamic processes and kinetic reactions with water vapor sustained in bubbles in water. The computational results are compared to the experiments in optical emission, which provides us insight into the pathways of excitation and radiation, like excitation transfer. The modeling also provides valuable suggestions for optimization of radical production. For example, the efficiency of OH production in N_2 discharges is high at high voltage while the efficiency in He discharge is high at low voltage. The computational investigation not only provides us with understandings of the processes of plasmas inside bubbles in water but also with practical optimization.

3.5 Tables

Table 3.1: Lennard-Jones Radius and Binary Diffusion Coefficient of H_2O in each Gas at 1 atm.

	Lennard-Jones Radius ($\overset{o}{A}$)[14]	H_2O Diffusion coefficient (cm^2/s)
H_2O	2.52	0.51
He	2.58	0.66
Ar	3.42	0.20
N_2	3.68	0.23

Table 3.2. He/H_2O, Ar/H_2O and N_2/H_2O Reaction Mechanism.

Reaction	Rate Coefficient[a]	Ref.
He Reactions		
$e + He \rightarrow He + e$	b	[16]
$e + He \leftrightarrow He^{*} + e$	b,c	[17]
$e + He \leftrightarrow He^{**} + e$	b,c	[17]
$e + He \leftrightarrow He^{***} + e$	b,c	[17]
$e + He^{*} \leftrightarrow He^{**} + e$	b,c	[17]
$e + He^{*} \leftrightarrow He^{***} + e$	b,c	[17]
$e + He^{**} \leftrightarrow He^{***} + e$	b,c	[17]
$e + He \rightarrow He^{+} + e + e$	b	[18]
$e + He^{*} \rightarrow He^{+} + e + e$	b	[19]
$e + He^{**} \rightarrow He^{+} + e + e$	b	[19]
$e + He^{***} \rightarrow He^{+} + e + e$	b	[19]
$e + He^{+} \rightarrow He^{*}$	$6.76 \times 10^{-13}\ T_e^{-0.5}$	[20]
$e + e + He^{+} \rightarrow He^{*} + e$	$6.2 \times 10^{-27}\ T_e^{-4.4}\ cm^6s^{-1}$	[20]
$e + He + He^{+} \rightarrow He^{*} + He$	$6.6 \times 10^{-30}\ T_e^{-2}\ cm^6s^{-1}$	[21]
$e + He_2^{+} \rightarrow He^{*} + He$	$7.12 \times 10^{-15}\ (T_e/T_g)^{-1.5}$	[16]
$e + He + He_2^{+} \rightarrow He_2^{*} + He$	$1.5 \times 10^{-27}\ cm^6s^{-1}$	[16]
$e + He + He_2^{+} \rightarrow He^{*} + He + He$	$3.5 \times 10^{-27}\ cm^6s^{-1}$	[16]
$e + e + He_2^{+} \rightarrow He_2^{*} + e$	$1.2 \times 10^{-21}\ cm^6s^{-1}$	[16]
$e + e + He_2^{+} \rightarrow He^{*} + He + e$	$2.8 \times 10^{-20}\ cm^6s^{-1}$	[16]
$e + He_2^{*} \rightarrow He + He + e$	3.8×10^{-9}	[16]
$(He^{*}, He^{**}, He^{***}) + (He^{*}, He^{**}, He^{***}) \rightarrow He + He^{+} + e$	$5 \times 10^{-10}\ T_n^{0.5}$	[16],[e]
$He^{+} + He \rightarrow He + He^{+}$	$6 \times 10^{-10}\ T_n^{0.5}$	[22]
$He^{+} + He + He \rightarrow He + He_2^{+}$	$1.41 \times 10^{-31}\ T_n^{-0.5}\ cm^6s^{-1}$	[23]
$(He^{*}, He^{**}, He^{***}) + He + He \rightarrow He + He_2^{*}$	$1.6 \times 10^{-32}\ cm^6s^{-1}$	[16],e
Ar Reactions		
$e + Ar \rightarrow Ar + e$	b	[24]

$e + Ar \leftrightarrow Ar^{*} + e$	b,c	[24]
$e + Ar \leftrightarrow Ar^{**} + e$	b,c	[24]
$e + Ar \leftrightarrow Ar^{***} + e$	b,c	[24]
$e + Ar^{*} \leftrightarrow Ar^{**} + e$	b,c	[24]
$e + Ar^{*} \leftrightarrow Ar^{***} + e$	b,c	[25]
$e + Ar^{**} \leftrightarrow Ar^{***} + e$	b,c	[25]
$e + Ar \rightarrow Ar^{+} + e + e$	b	[18]
$e + Ar^{*} \rightarrow Ar^{+} + e + e$	b	[26]
$e + Ar^{**} \rightarrow Ar^{+} + e + e$	b	[26]
$e + Ar^{***} \rightarrow Ar^{+} + e + e$	b	[19]
$e + Ar^{+} \rightarrow Ar^{***}$	$4 \times 10^{-13} T_e^{-0.5}$	[27]
$e + e + Ar^{+} \rightarrow Ar^{***} + e$	$5 \times 10^{-27} T_e^{-4.5}$ cm^6s^{-1}	[27]
$e + Ar_2^{*} \rightarrow Ar_2^{+} + e + e$	$9 \times 10^{-8} T_e^{0.7}$	[28]
$e + Ar_2^{*} \rightarrow Ar + Ar + e$	1×10^{-7}	[28]
$e + Ar_2^{+} \rightarrow Ar^{***} + Ar$	$5.38 \times 10^{-8} T_e^{-0.66}$	[28]
$(Ar^{*}, Ar^{**}, Ar^{***}) + (Ar^{*}, Ar^{**}, Ar^{***}) \rightarrow Ar + Ar^{+} + e$	$5 \times 10^{-10} T_n^{0.5}$	[28],e
$Ar^{+} + Ar \rightarrow Ar + Ar^{+}$	$5.66 \times 10^{-10} T_n^{0.5}$	[22]
$Ar^{+} + Ar + Ar \rightarrow Ar + Ar_2^{+}$	$1.41 \times 10^{-31} T_n^{-0.5}$ cm^6s^{-1}	[28]
$(Ar^{*}, Ar^{**}, Ar^{***}) + Ar + Ar \rightarrow Ar + Ar_2^{*}$	1.14×10^{-32} cm^6s^{-1}	[28],e
N_2 Reactions		
$e + N_2 \rightarrow N_2 + e$	b	[29]
$e + N_2 \leftrightarrow N_2^{*} + e$	b,c	[29]
$e + N_2 \leftrightarrow N_2^{**} + e$	b,c	[29]
$e + N_2 \leftrightarrow N_2^{***} + e$	b,c	[29]
$e + N_2^{*} \leftrightarrow N_2^{**} + e$	b,c	[29]
$e + N_2^{*} \leftrightarrow N_2^{***} + e$	b,c	[29]
$e + N_2^{**} \leftrightarrow N_2^{***} + e$	b,c	[29]
$e + N_2 \rightarrow N_2^{+} + e + e$	b	[29]
$e + N_2^{*} \rightarrow N_2^{+} + e + e$	b	[29]
$e + N_2^{**} \rightarrow N_2^{+} + e + e$	b	[29]

$e + N_2^{***} \rightarrow N_2^+ + e + e$	b	[29]
$e + N_2 \rightarrow N + N + e$	b	[30]
$e + N_2 \leftrightarrow N_2(v) + e$	b,c	[29]
$e + N_2(v) \rightarrow N_2(v) + e$	b	[29]
$e + N_2(v) \leftrightarrow N_2^* + e$	b,c	[29]
$e + N_2(v) \rightarrow N_2^+ + e + e$	b	[29]
$e + N \rightarrow N + e$	b	[31]
$e + N \leftrightarrow N^* + e$	b,c	[32]
$e + N \rightarrow N^+ + e + e$	b	[33]
$e + N^* \rightarrow N^+ + e + e$	b	[32]
$e + N_2^+ \rightarrow N^* + N$	$2 \times 10^{-7}\ T_e^{-0.5}$	[34]
$e + N_4^+ \rightarrow N_2 + N_2$	$2 \times 10^{-7}\ T_e^{-0.5}$	[34],d
$N^* + N_2 \rightarrow N + N_2$	2.4×10^{-14}	[35]
$N_2^* + N_2 \rightarrow N_2 + N_2$	1×10^{-11}	[36]
$N_2^{**} + N_2 \rightarrow N_2 + N_2$	1×10^{-11}	[36],d
$N_2^{**} + N_2 \rightarrow N_2^{***} + N_2$	1×10^{-11}	[36],d
$N_2^{***} + N_2 \rightarrow N_2^* + N_2$	1×10^{-11}	[36],d
$N_2^* + N_2^* \rightarrow N_2 + N_2^{**}$	1×10^{-10}	[37]
$N_2(v) + N_2 \rightarrow N_2 + N_2$	1×10^{-11}	[36],d
$N_2(v) + N \rightarrow N_2 + N$	1×10^{-11}	[36],d
$N_2^{***} + N_2^* \rightarrow N_4^+ + e$	5×10^{-11}	[38]
$N_2^{***} + N_2^{**} \rightarrow N_4^+ + e$	5×10^{-11}	[38],d
$N_2^{***} + N_2^{***} \rightarrow N_4^+ + e$	2×10^{-10}	[38]
$N^+ + N \rightarrow N + N^+$	5×10^{-12}	[39],d
$N_2^+ + N \rightarrow N_2 + N^+$	5×10^{-12}	[39]
$N_2^+ + N^* \rightarrow N_2 + N^+$	1×10^{-10}	[39]
$N_2^+ + N_2 + N_2 \rightarrow N_2 + N_4^+$	$6.8 \times 10^{-29}\ T_n^{-1.64}$	[39]
$N_4^+ + N_2 \rightarrow N_2 + N_2 + N_2^+$	$9.35 \times 10^{-13}\ T_n^{1.5}$	[39]
<u>H_2O, OH, H Reactions</u>		
$e + H_2O \rightarrow H_2O + e$	b	[40]
$e + H_2O \rightarrow H_2O(v1,2; v3,4) + e$	b	[40],g

$e + H_2O \rightarrow H_2O^+ + e + e$	b	[40]
$e + H_2O \rightarrow O^- + H_2$	b	[40]
$e + H_2O \rightarrow OH^- + H$	b	[40]
$e + H_2O \rightarrow OH + H + e$	b	[40]
$e + H_2O \rightarrow OH + H^* + e$	b	[40]
$e + H_2O \rightarrow OH + H^{**} + e$	b	[40]
$e + H_2O \rightarrow OH + H^{***} + e$	b	[40]
$e + H_2O \rightarrow OH^* + H + e$	b	[40]
$e + H_2O^+ \rightarrow OH + H$	$5.1 \times 10^{-8}\ T_e^{-0.5}$	[41]
$e + H \rightarrow H + e$	b	[42]
$e + H \leftrightarrow H^* + e$	b,c	[43]
$e + H \leftrightarrow H^{**} + e$	b,c	[43]
$e + H \leftrightarrow H^{***} + e$	b,c	[43]
$e + H^* \leftrightarrow H^{**} + e$	b,c	[43]
$e + H^* \leftrightarrow H^{***} + e$	b,c	[43]
$e + H^{**} \leftrightarrow H^{***} + e$	b,c	[43]
$e + OH \rightarrow OH^* + e$	$2.7 \times 10^{-10}\ T_e^{0.5}$	[44]
$e + OH^* \rightarrow O + H + e$	$1.5 \times 10^{-7}\ T_e^{-0.75} \exp(-3.9/T_e)$	[45]
$H_2O^+ + H_2O \rightarrow H_2O + H_2O^+$	5.1×10^{-11}	[39],d
$(H^*, H^{**}, H^{***}) + H_2O \rightarrow H + H_2O$	9.1×10^{-9}	[46],d,e
$(H^{**}, H^{***}) + H_2O \rightarrow H^* + H_2O$	9.1×10^{-9}	[46],e
$H^{***} + H_2O \rightarrow H^{**} + H_2O$	9.1×10^{-9}	[46],d
$OH^* + H_2O \rightarrow OH + H_2O$	9.1×10^{-9}	[46],d
$OH^- + H \rightarrow H_2O + e$	1.8×10^{-9}	[47],d
$(OH, OH^*) + H \rightarrow H_2O$	$6.87 \times 10^{-31} T_n^{-2}$	[48],d,e
$(OH, OH^*) + (OH, OH^*) + M \rightarrow H_2O_2 + M$	$6.9 \times 10^{-31} T_n^{-0.8}\ cm^6 s^{-1}$	[48],e,j
$H_2 + HO_2 \rightarrow H_2O_2 + H$	$5 \times 10^{-11} \exp(-T_g/11310)$	[48]
$HO_2 + HO_2 \rightarrow H_2O_2 + O_2$	$8.05 \times 10^{-11} T_n^{-1}$	[48]
$HO_2 + HO_2 + M \rightarrow H_2O_2 + O_2 + M$	$1.9 \times 10^{-33} \exp(980/T_g)\ cm^6 s^{-1}$	[48],d,j
$HO_2 + H_2O \rightarrow H_2O_2 + OH$	$4.65 \times 10^{-11} \exp(-11647/T_g)$	[48]
$H + H_2O_2 \rightarrow HO_2 + H_2$	$8 \times 10^{-11} \exp(-4000/T_g)$	[48]

$H + H_2O_2 \rightarrow OH + H_2O$	$4 \times 10^{-11}\exp(-2000/T_g)$	[48]
$O_2 + H_2O_2 \rightarrow HO_2 + HO_2$	$9 \times 10^{-11}\exp(-19965/T_g)$	[48]
$O + H_2O_2 \rightarrow HO_2 + OH$	$1.4 \times 10^{-12}\exp(-2000/T_g)$	[48]
$O^* + H_2O_2 \rightarrow O_2 + H_2O$	5.2×10^{-10}	[48]
$OH + H_2O_2 \rightarrow HO_2 + H_2O$	$2.9 \times 10^{-12}\exp(-160/T_g)$	[48]
$H_2O_2 \rightarrow OH + OH$	$1.96 \times 10^{-09} T_n^{-4.86}\exp(-26800/T_g)\ s^{-1}$	[48]
$(H, H^*, H^{**}, H^{***}) + H_2O_2 \rightarrow OH + H_2O$	$4 \times 10^{-11}\exp(-2000/T_g)$	[49],e
$OH^- + OH^+ + M \rightarrow H_2O_2 + M$	$2 \times 10^{-25} T_n^{-2.5}\ cm^6 s^{-1}$	h,j
$OH^- + H^+ + M \rightarrow H_2O + M$	$2 \times 10^{-25} T_n^{-2.5}\ cm^6 s^{-1}$	h,j
$OH^- + H_2O^+ + M \rightarrow OH + H_2O + M$	$2 \times 10^{-25} T_n^{-2.5}\ cm^6 s^{-1}$	h,j
$O^- + OH^+ + M \rightarrow HO_2 + M$	$2 \times 10^{-25} T_n^{-2.5}\ cm^6 s^{-1}$	h,j
$O^- + H^+ + M \rightarrow OH + M$	$2 \times 10^{-25} T_n^{-2.5}\ cm^6 s^{-1}$	h,j
$O^- + H_2O^+ + M \rightarrow O + H_2O + M$	$2 \times 10^{-25} T_n^{-2.5}\ cm^6 s^{-1}$	h,j
$O^- + O \rightarrow O_2 + e$	5×10^{-10}	[38]
<u>Excitation and Charge Transfer</u>		
$He^+ + H_2O \rightarrow He + H_2O^+$	6.05×10^{-11}	[50]
$He^+ + H_2O \rightarrow He + H + OH^+$	2.86×10^{-10}	[50]
$He_2^+ + H_2O \rightarrow He + He + H_2O^+$	6.05×10^{-11}	[50],d
$He_2^+ + H_2O \rightarrow He + He + H + OH^+$	2.86×10^{-10}	[50],d
$(He^*, He^{**}, He^{***}) + H_2O \rightarrow He + H_2O^+ + e$	6.6×10^{-10}	[50],e
$(He^*, He^{**}, He^{***}) + H_2O \rightarrow He + OH + H^+ + e$	2.6×10^{-11}	[50],d,e
$(He^*, He^{**}, He^{***}) + H_2O \rightarrow He + OH^* + H^+ + e$	2.6×10^{-11}	[50],d,e
$(He^*, He^{**}, He^{***}) + H_2O \rightarrow He + H + OH^+ + e$	1.5×10^{-10}	[50],e
$(He^*, He^{**}, He^{***}) + H_2O \rightarrow He + OH + H$	1.5×10^{-10}	[51],e
$(He^*, He^{**}, He^{***}) + H_2O \rightarrow He + OH^* + H$	1.5×10^{-10}	[51],d,e
$(He^*, He^{**}, He^{***}) + H_2O \rightarrow He + OH + H^*$	1.5×10^{-10}	[51],d,e
$(He^*, He^{**}, He^{***}) + H_2O \rightarrow He + OH + H^{**}$	1.5×10^{-10}	[51],d,e

$(He^*, He^{**}, He^{***}) + H_2O \rightarrow He + OH + H^{***}$	1.5×10^{-10}	[51],d,e
$He_2^* + H_2O \rightarrow He + He + H_2O^+ + e$	6.6×10^{-10}	[50]
$He_2^* + H_2O \rightarrow He + He + (OH, OH^*) + H^+ + e$	2.6×10^{-11}	[50],e
$He_2^* + H_2O \rightarrow He + He + H + OH^+ + e$	1.5×10^{-10}	[50]
$He_2^* + H_2O \rightarrow He + He + H_2O^+ + e$	6.6×10^{-10}	[51]
$He_2^* + H_2O \rightarrow He + He + OH + (H, H^*, H^{**}, H^{***})$	1.5×10^{-10}	[51],e
$He_2^* + H_2O \rightarrow He + He + OH^* + H$	1.5×10^{-10}	[51],d
$He^+ + O^- + M \rightarrow He + O + M$	$2 \times 10^{-25} T_n^{-2.5}\ cm^6 s^{-1}$	h,j
$He_2^+ + O^- + M \rightarrow He + He + O + M$	$2 \times 10^{-25} T_n^{-2.5}\ cm^6 s^{-1}$	h,j
$He^+ + OH^- + M \rightarrow He + OH + M$	$2 \times 10^{-25} T_n^{-2.5}\ cm^6 s^{-1}$	h,j
$He_2^+ + OH^- + M \rightarrow He + He + OH + M$	$2 \times 10^{-25} T_n^{-2.5}\ cm^6 s^{-1}$	h,j
$Ar^+ + H_2O \rightarrow Ar + H_2O^+$	1.5×10^{-10}	[39]
$Ar_2^+ + H_2O \rightarrow Ar + Ar + H_2O^+$	1.5×10^{-10}	[39],d
$(Ar^*, Ar^{**}, Ar^{***}) + H_2O \rightarrow Ar + OH + H$	4.8×10^{-10}	[52],d,e
$(Ar^*, Ar^{**}, Ar^{***}) + H_2O \rightarrow Ar + OH^* + H$	4.8×10^{-10}	[52],d,e
$Ar_2^* + H_2O \rightarrow Ar + Ar + (OH, OH^*) + H$	4.8×10^{-10}	[52],d,e
$Ar^+ + O^- + (Ar, H_2O) \rightarrow Ar + (Ar, H_2O) + O$	$2 \times 10^{-25} T_n^{-2.5}\ cm^6 s^{-1}$	h,e
$Ar_2^+ + O^- + (Ar, H_2O) \rightarrow Ar + Ar + (Ar, H_2O) + O$	$2 \times 10^{-25} T_n^{-2.5}\ cm^6 s^{-1}$	h,e
$Ar^+ + OH^- + (Ar, H_2O) \rightarrow Ar + (Ar, H_2O) + OH$	$2 \times 10^{-25} T_n^{-2.5}\ cm^6 s^{-1}$	h,e
$Ar_2^+ + OH^- + (Ar, H_2O) \rightarrow Ar + Ar + (Ar, H_2O) + OH$	$2 \times 10^{-25} T_n^{-2.5}\ cm^6 s^{-1}$	h,e
$N_2^+ + H_2O \rightarrow N_2 + H_2O^+$	2.4×10^{-9}	[39]
$N^+ + H_2O \rightarrow N + H_2O^+$	2.4×10^{-9}	[39],d
$N_4^+ + H_2O \rightarrow N_2 + N_2 + H_2O^+$	2×10^{-10}	[39]
$N_2^+ + O^- + M \rightarrow N_2 + O + M$	$2 \times 10^{-25} T_n^{-2.5}\ cm^6 s^{-1}$	h,j
$N_4^+ + O^- + M \rightarrow N_2 + N_2 + O + M$	$2 \times 10^{-25} T_n^{-2.5}\ cm^6 s^{-1}$	h,j
$N_2^+ + OH^- + M \rightarrow N_2 + OH + M$	$2 \times 10^{-25} T_n^{-2.5}\ cm^6 s^{-1}$	h,j
$N_4^+ + OH^- + M \rightarrow N_2 + N_2 + OH + M$	$2 \times 10^{-25} T_n^{-2.5}\ cm^6 s^{-1}$	h,j

$(N_2^{**}, N_2^{***}) + H_2O \rightarrow N_2 + OH + H$	4.5×10^{-10}	[53],d,e
$N_2^{**} + H_2O \rightarrow N_2 + OH^* + H$	4.5×10^{-10}	[53],d
Radiative Transitions		
$He^{**} \rightarrow He$	$5.7 \times 10^4\ s^{-1}$	[48],i
$He^{***} \rightarrow He^*$	$9.5 \times 10^6\ s^{-1}$	[48]
$He^{**} \rightarrow He^*$	$1.0 \times 10^7\ s^{-1}$	[48]
$He_2^* \rightarrow He + He$	$1 \times 10^7\ s^{-1}$	[54]
$Ar^{***} \rightarrow Ar^*$	$3.3 \times 10^7\ s^{-1}$	[48]
$Ar^{***} \rightarrow Ar$	$3.1 \times 10^5\ s^{-1}$	[48],i
$Ar^{**} \rightarrow Ar$	$5.3 \times 10^5\ s^{-1}$	[48],i
$Ar_2^* \rightarrow Ar + Ar$	$6 \times 10^7\ s^{-1}$	[28]
$N_2^{***} \rightarrow N_2$	$2 \times 10^5\ s^{-1}$	[48],i
$N_2^{**} \rightarrow N_2^*$	$3 \times 10^7\ s^{-1}$	[39],d
$N_2^{***} \rightarrow N_2^*$	$2 \times 10^6\ s^{-1}$	[48],d
$N^* \rightarrow N$	$6 \times 10^7\ s^{-1}$	[48]
$H^* \rightarrow H$	$4.7 \times 10^8\ s^{-1}$	[48]
$H^{**} \rightarrow H$	$5.6 \times 10^7\ s^{-1}$	[48]
$H^{**} \rightarrow H^*$	$4.4 \times 10^7\ s^{-1}$	[48]
$H^{***} \rightarrow H^*$	$8.4 \times 10^6\ s^{-1}$	[48]
$OH^* \rightarrow OH$	$1.3 \times 10^6\ s^{-1}$	[55]
Photoionization		
$h\nu + H_2O \rightarrow H_2O^+ + e$	$1 \times 10^{-17}\ cm^2$	[12],d

a) Rate coefficients have unit of cm^3s^{-1} unless noted otherwise. Electron temperature T_e is in eV. Gas temperature T_g is in K. T_n is the normalized gas temperature, (T_g/300)

b) Rate coefficient was obtained by solving Boltzmann's equation for the electron energy distribution. Cross sections for the process are from the indicated reference.

c) Cross section and rate coefficient obtained by detailed balance.

d) Approximated by analogy.

e) Reactants and products in parenthesis denote the same rate coefficient was used for all species.

f) Electron impact excitation into vibrational states 1-8 was lumped into a single vibrational state $N_2(v)$.

g) Electron energy loss in exciting H_2O to vibrational states was included in calculation of the electron energy distribution, however $H_2O(v)$ was not explicitly followed as an excited state in the model.

h) Charge neutralization reactions. Rate coefficients are estimated by the recombination reactions in the afterglow.

i) The radiation trapping factor is estimated to be 10^3 to 10^4 for UV and VUV emission.

j) M = He, Ar, N_2, H_2O

Table 3.3. Dissociative excitation reactions by electron impact and excitation transfer.

Electron Impact Direct Excitation	
$e + H(n=1) \rightarrow H(n=3) + e$ (12.04 eV)	$e + OH(X) \rightarrow OH(A) + e$ (4.04 eV)
Electron Impact Dissociative Excitation	
$e + H_2O \rightarrow H(n=3) + OH + e$ (18.3 eV)	$e + H_2O \rightarrow H + OH(A) + e$ (9 eV)
Excitation Transfer	
He^* (19.8 eV)+ $H_2O \rightarrow H(n=3) + OH + He$	He^* (19.8 eV)+ $H_2O \rightarrow H + OH(A) + He$
	Ar^* (11.6 eV)+ $H_2O \rightarrow H + OH(A) + Ar$
	N_2^* (11.0 eV) + $H_2O \rightarrow H + OH(A) + N_2$

* The lowest excited state that is able to excitation transfer.

3.6 Figures

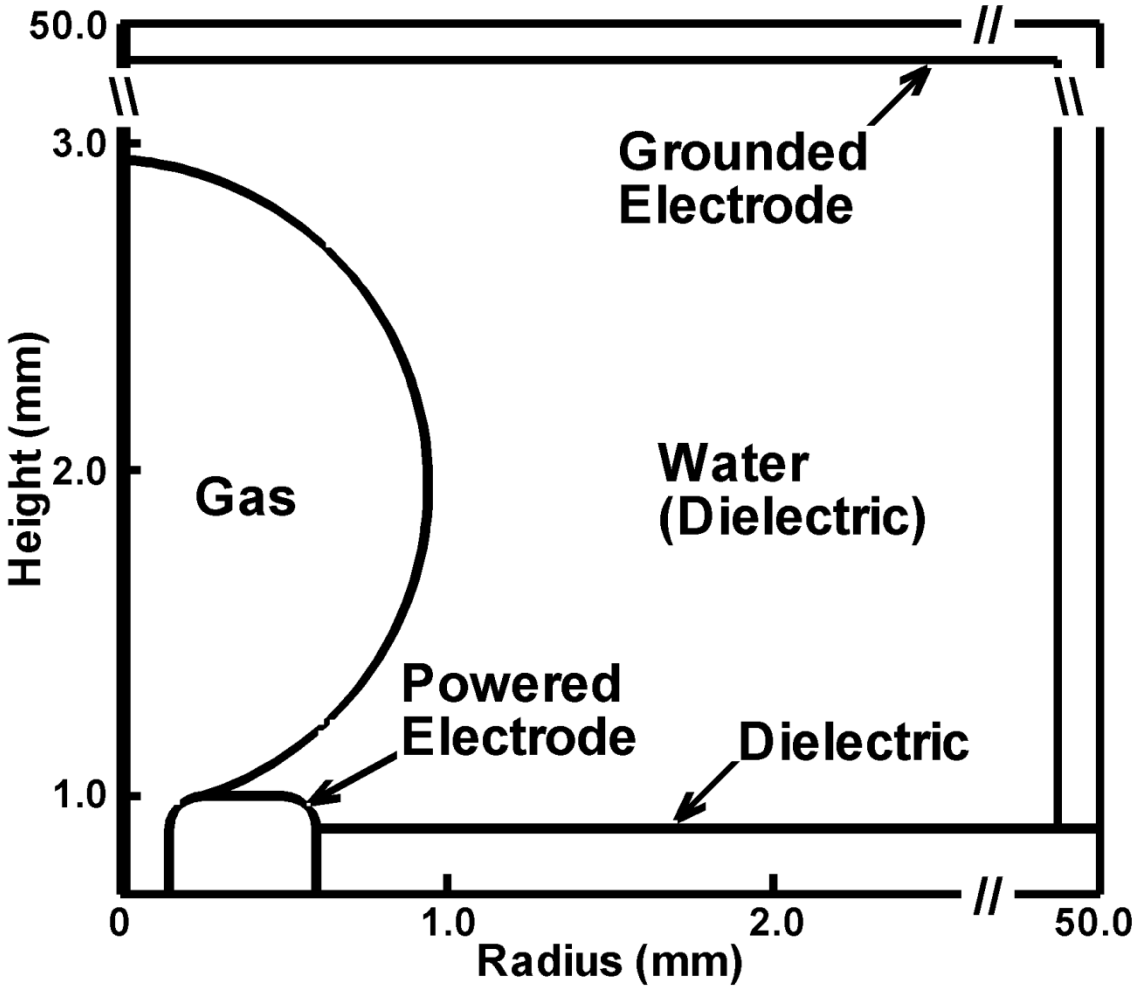

Figure 3.1 Schematic of the geometry highlighting the computational domain in the vicinity of the bubble. The domain is cylindrically symmetric across the left boundary.

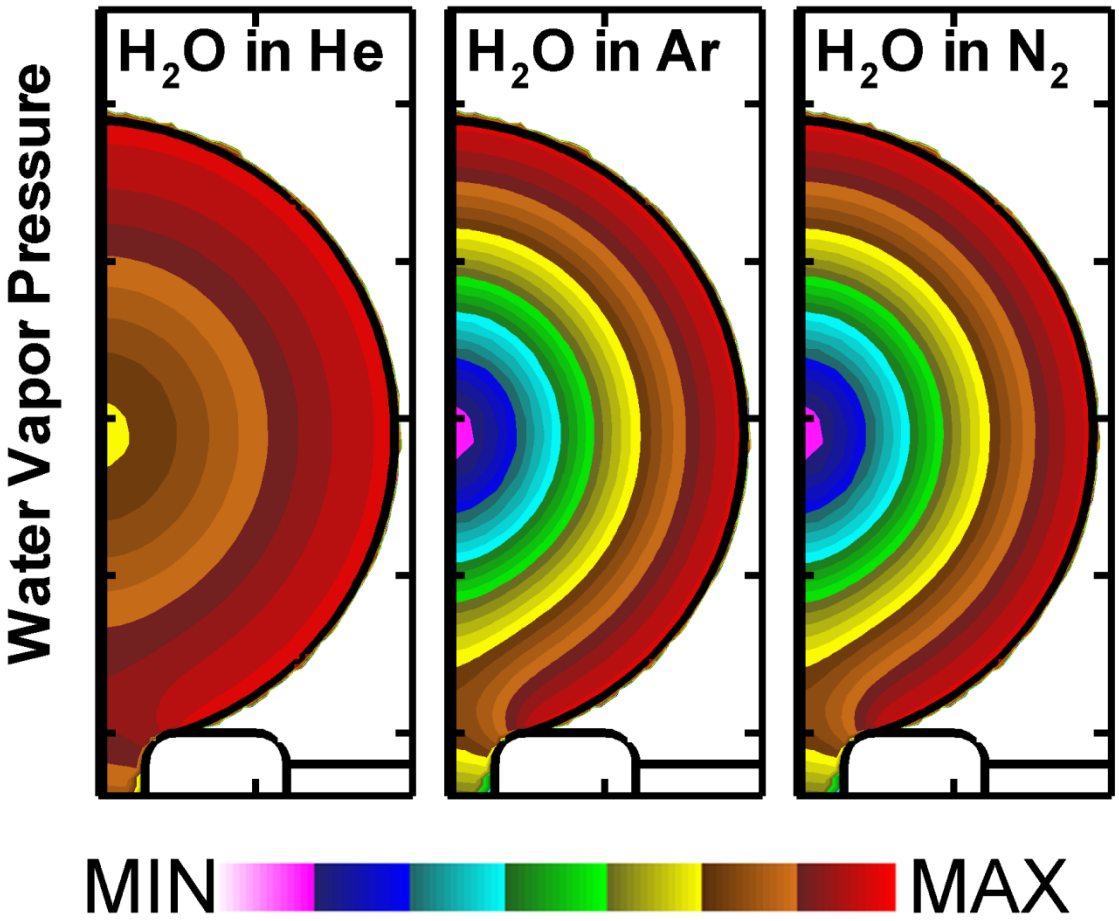

Figure 3.2 The density of water vapor inside the bubble after 1 ms. The density of the saturated water vapor at the water boundary is 3% of the injected gases at 300 K. The contours are plotted on a log scale over three decades.

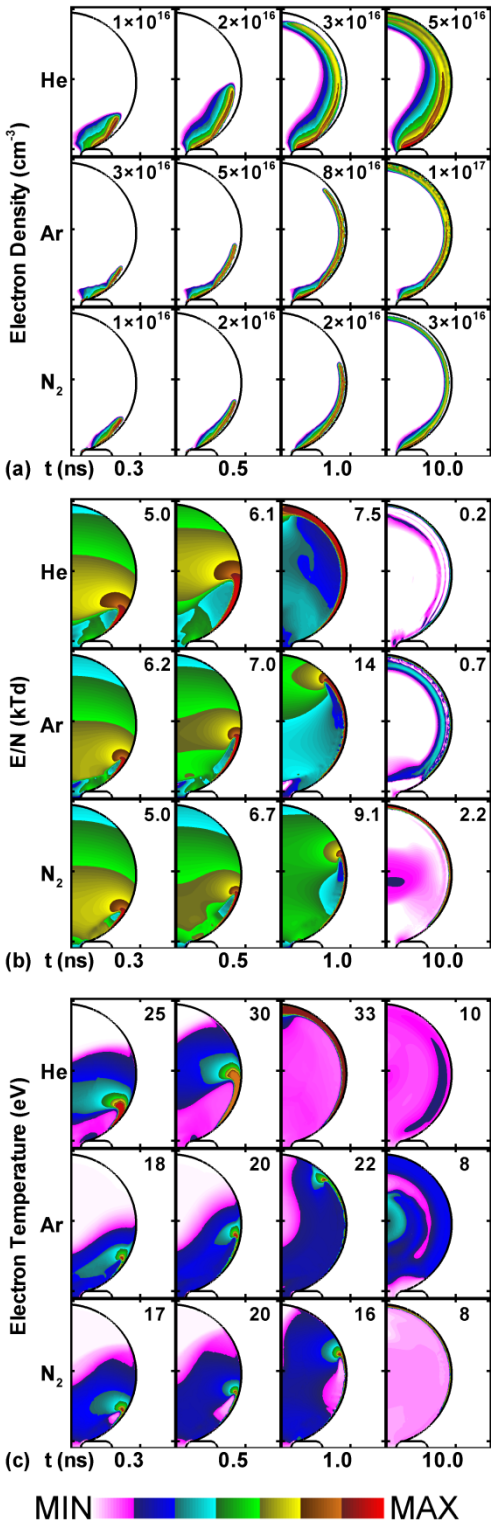

Figure 3.3 Time evolution of plasma properties for discharges in He, Ar and N_2 bubbles. (a) Electron density, (b) E/N and (c) electron temperature. The discharges are surface hugging where the electric field enhancement is the largest. The contours are plotted on a log scale over three decades with maximum values shown in each frame.

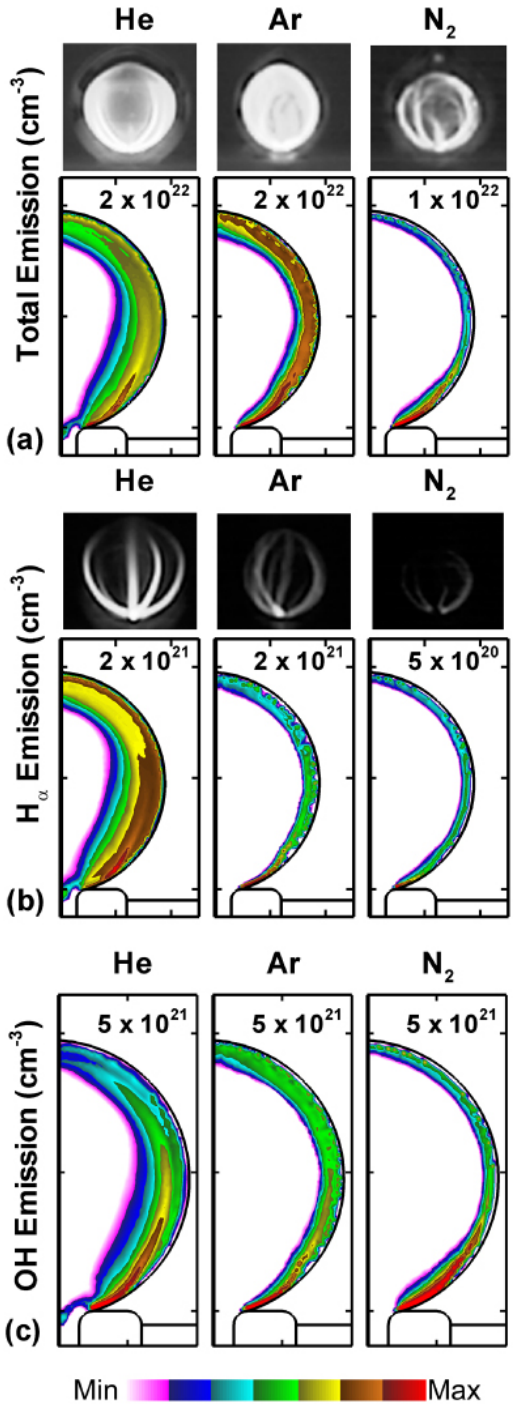

Figure 3.4 Time integrated emission intensity from discharges sustained in He, Ar and N_2 bubbles: (a) total visible emission, (b) H_α (656.3 nm) and (c) OH(A–X) (306.4 nm) The top row for total and H_α emission are images from the experiments [11]. The contours are plotted on a 3-decade log scale with the maximum values noted in each frame.

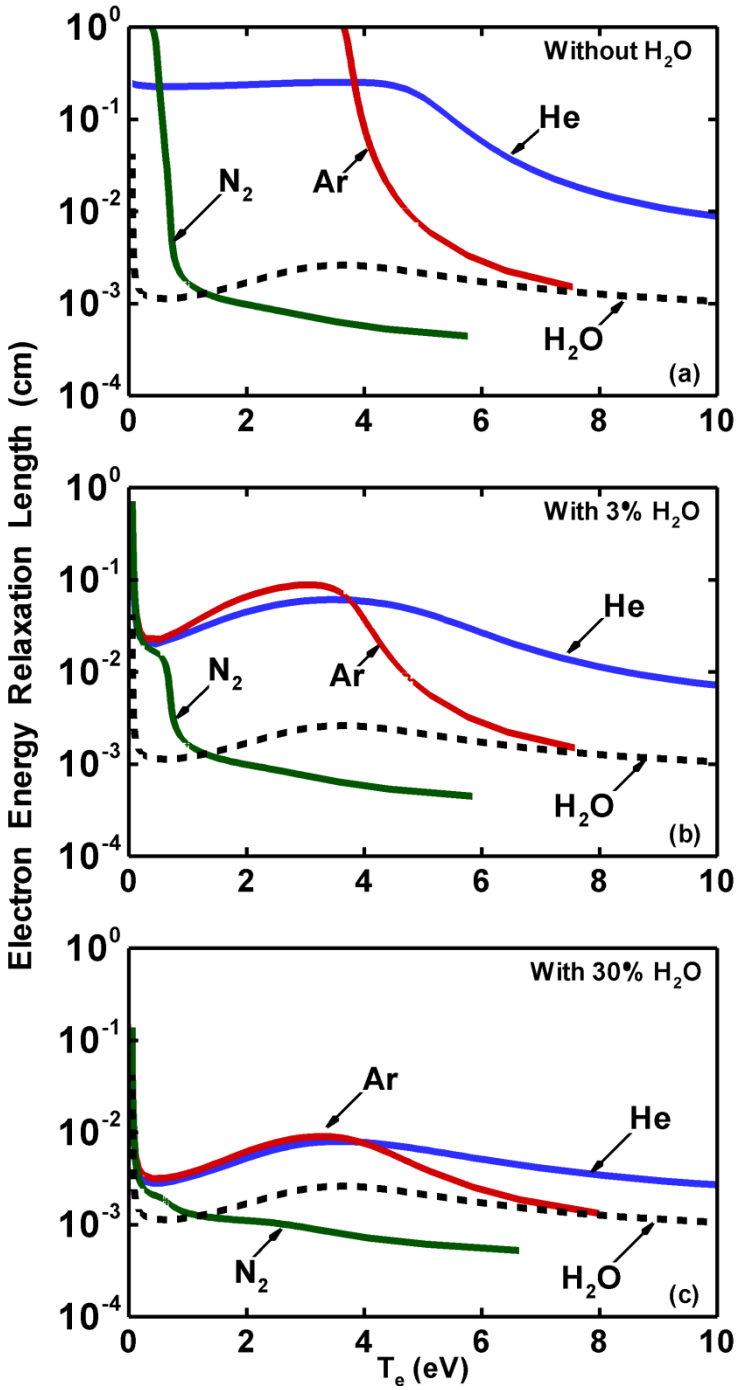

Figure 3.5 Electron energy relaxation length, λ_e, in He, Ar and N_2 at 1 atm with different water vapor concentrations. (a) 0%, (b) 3%, (c) 30%. Small amounts of water vapor significantly lower λ_e in He and Ar.

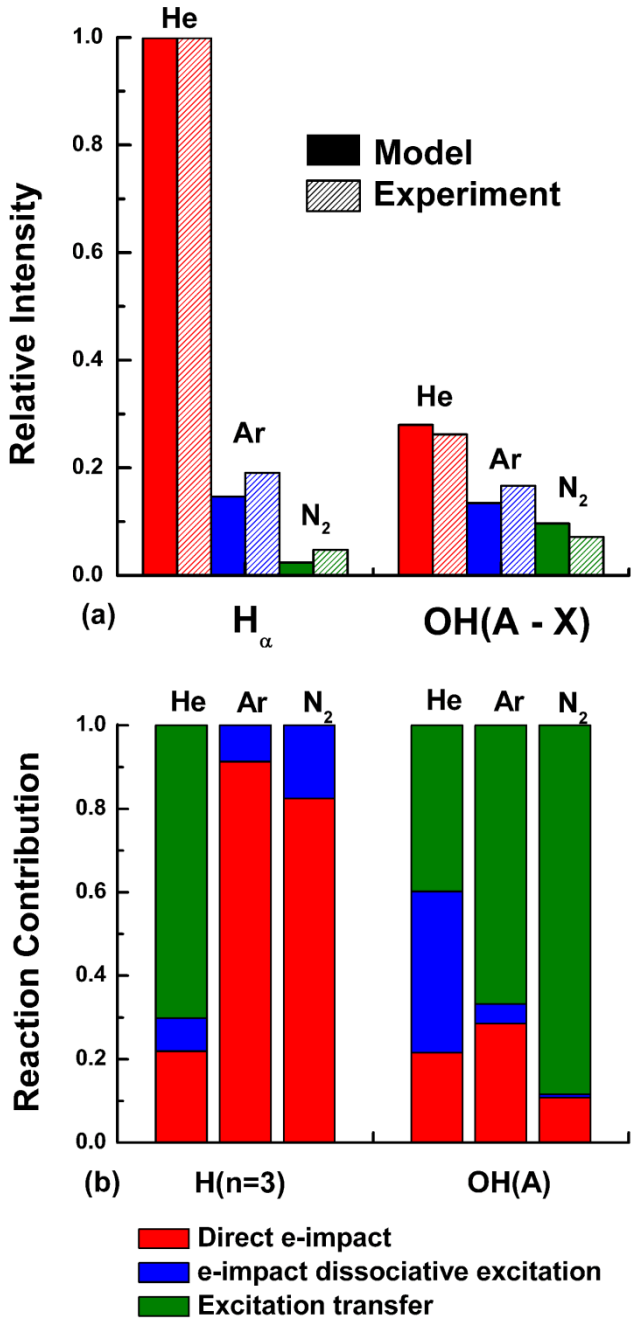

Figure 3.6 Optical emission properties from discharges in bubbles. (a) Relative intensities of H_α (656.3 nm) and OH(A-X) (306.4 nm) emission from discharges sustained in bubbles of He, Ar and N_2 in water. Predictions from the model (solid) are compared to experiments (hashed). The intensities are normalized to the H_α emission intensity in He. (b) Fractional contributions of direct electron impact, dissociative electron impact and excitation transfer to formation of emitting states.

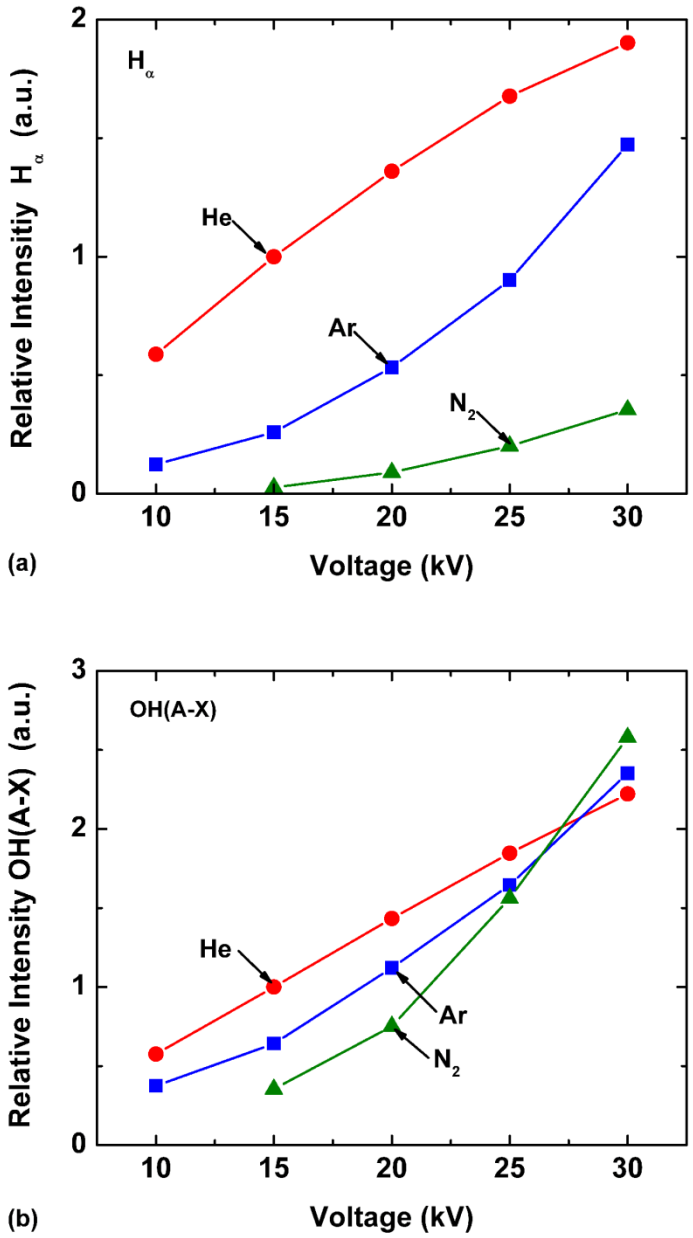

Figure 3.7 Time and spatially integrated intensities of (a) H_α (656.3 nm) and (b) OH(A-X) (306.4 nm) with different applied voltages. The intensities are normalized to the H_α emission intensity and OH(A-X) emission intensity in He discharge at 15 kV.

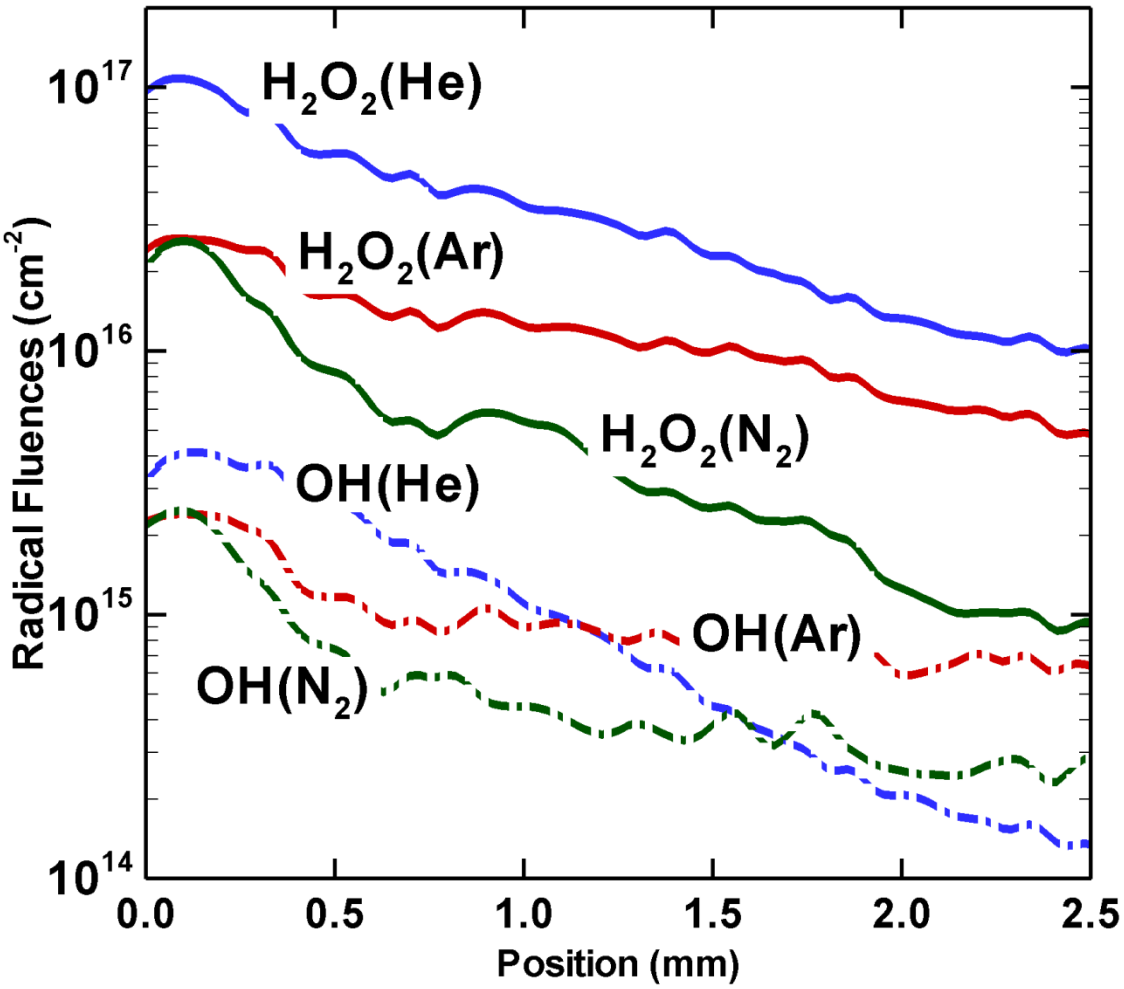

Figure 3.8 OH and H_2O_2 fluences to the bubble-water interface over a period of 1.0 s for a discharge voltage of 15 kV.

3.7 References

[1] B. R. Locke and K.-Y. Shih, Plasma Sources Sci. Technol. 20, 034006 (2011).

[2] D. Dobrynin, A. Fridman and A. Y. Starikovskiy, IEEE Trans. Plasma Sci. 40, 2163 (2012).

[3] M. A. Malik, A. Ghaffar and S. A. Malik, Plasma Sources Sci. Technol. 10, 82 (2001).

[4] R. Burlica, M. J. Kirkpatrick and B. R. Locke, Journal of Electrostatics 64, 35 (2006).

[5] M. G. Kong, G. Kroesen, G. Morfill, T. Nosenko, T. Shimizu, J. V. Dijk and J. L. Zimmermann, New J. Phys. 11, 115012 (2009).

[6] A. Starikovskiy, Y. Yang, Y. I. Cho and A. Fridman, Plasma Sources Sci. Technol. 20, 024003 (2011).

[7] W. An, K. Baumung and H. Bluhm, J. Appl. Phys. 101, 053302 (2007).

[8] J. Foster, B. S. Sommers, S. N. Gucker, I. M. Blankson and G. Adamovsky, IEEE Trans. Plasma Sci. 40, 1311 (2012).

[9] N. Y. Babaeva and M. J. Kushner, J. Phys. D: Appl. Phys. 42, 132003 (2009).

[10] K. Tachibana, Y. Takekata, Y. Mizumoto, H. Motomura and M. Jinno, Plasma Sources Sci. Technol. 20, 034005 (2011).

[11] H. Aoki, K. Kitano and S. Hamaguchi, Plasma Sources Sci. Technol. 17, 025006 (2008).

[12] R. D. Hudson, Rev. Geophys. Space Phys. 9, 305 (1971).

[13] "NIST Thermophysical Properties of Fluid Systems," [Online]. Available: http://webbook.nist.gov/chemistry/fluid/.

[14] J. Hirschfelder, C. F. Curtiss and R. B. Bird, “Molecular Theory of Gases and Liquids”, New York: Wiley, 1954.

[15] W. L. Morgan and B. M. Penetrante, Comput. Phys. Comm. 58, 127 (1990).

[16] R. Deloche, P. Monchicourt, M. Cheret and F. Lambert, Phys. Rev. A 13, 1140 (1976).

[17] L. L. Alves, G. Gousset and C. M. Ferreira, J. Phys. D 25, 1713 (1992).

[18] D. Rapp and P. Englander-Golden, J. Chem. Phys. 43, 1464 (1965).

[19] L. Vriens, Phys. Lett. 8, 260 (1964).

[20] G. Bekefi, Radiation Processes in Plasmas, New York: Wiley, 1966.

[21] F. Emmert, H. H. Angermann, R. Dux and H. Langhoff, J. Phys. D 21, 667 (1988).

[22] H. W. Ellis, R. Y. Pai and E. W. McDaniel, At. Data Nucl. Data Tables 17, 177 (1976).

[23] Q. Wang, D. J. Economou and V. M. Donnelly, J. Appl. Phys. 100, 023301 (2006).

[24] K. Tachibana, Phys. Rev. A 34, 1007 (1986).
[25] P. Zapesochyni and L. L. Shimon, Opt. Spectrosc. 11, 155 (1966).
[26] R. H. McFarland and J. D. Kinney, Phys. Rev. A 137, 1058 (1965).
[27] M. A. Biondi in Principles of Laser Plasmas, G. Bekefi, ed. (New York: Wiley, 1976).
[28] F. Kannari, A. Suda, M. Obara and T. Fujioka, IEEE J. Quant. Electron. 19, 1587 (1983).
[29] Y. Itikawa, M. Hayashi, A. Ichimura, K. Onda, K. Sakimoto, K. Takayanagi, M. Nakamura, H. Nishimura and T. Takayanagi, J. Phys. Chem. Ref. Data 15, 985 (1986).
[30] A. V. Phelps and L. C. Pitchford, Phys. Rev. 31, 2932 (1985).
[31] S. Geltman, Quant J. Spectrosc. Radiat. Transfer 13, 601 (1973).
[32] R. Henry, P. G. Burke and A.-L. Sinfailam, Phys. Rev. 178, 218 (1969).
[33] A. Smith, Phys. Rev. 127, 1647 (1962).
[34] Mitchell, Physical Reports 186, 215 (1990).
[35] C. Person and D. O. Ham, Radiat. Phys. Chem. 31, 1 (1988).
[36] G. Piper, J. Chem. Phys. 87, 1625 (1987).
[37] G. Piper, J. Chem. Phys. 88, 231 (1988).
[38] Kossyi, A. Y. Kostinsky, A. A. Matveyev and V. P. Si, Plasma Sources Sci. Technol. 1, 207 (1992).
[39] Y. Ikezoe, S. Matsuoka, M. Takebe and A. Viggiano, Gas Phase Ion-Molecule Reaction Rate Constants Through 1986,, Ion Reaction Research Group of the Mass Spectroscopy Society of Japan, Tokyo, 1987.
[40] Y. Itikawa and N. Mason, J. Phys. Chem. Ref. Data 34, 1 (2005).
[41] R. Rowe, F. Vallee, J. L. Queffelec, J. C. Gomet and M. Morlais, J. Chem. Phys. 88, 845 (1988).
[42] P. Banks, Planet. Space Sci. 14, 1085 (1966).
[43] R. K. Janev, W. D. Langer, D. J. Evans and D. E. Post, Elementary Processes in Hydrogen and Helium Containing Plasmas, Berlin: Springer, 1987.
[44] K. N. Joshipuru, M. Vinodkumar and U. M. Patel, J. Phys. B:At. Mol. Opt. Phys. 34, 509 (2001).
[45] R. Riahi, P. Teulet, Z. B. Lakhdar and A. Gleizes, Eur. Phys. J. D 40, 223 (2006).
[46] T. I. Quickenden, S. M. Trotman, J. A. Irvin and D. F. Sangster, Chem. Phys. 71, 497 (1979).

[47] K. P. Madden and S. P. Mezyk, J. Phys. Chem. Ref. Data 40, 023103(2011).

[48] "NIST Chemical Kinetics Database.," [Online]. Available: http://kinetics.nist.gov/kinetics/index.jsp.

[49] F. J. Gordillo-Vazquez, J. Phys. D: Appl. Phys. 41, 234016 (2008).

[50] T. J. Miller, P. Farquhar and K. Willacy, Astron. Astrophys. Suppl. Ser. 121, 139 (1997).

[51] R. A. Sanders and E. E. Muschlitz, Int. J. Mass Spectrosc. Ion Phys. 23, 99 (1977).

[52] H. D. Jong, Chem. Phys. Lett. 25, 129 (1974).

[53] S. V. Pancheshnyi, S. M. Starikovskaia and A. Y. Starikovskii, Chem. Phys. 262, 349 (2000).

[54] G. V. Naidis, J. Phys. D: Appl. Phys. 44, 215203 (2011).

[55] W. R. Binns and J. L. Ahl, J. Chem. Phys. 68, 538 (1978).

CHAPTER 4 ATMOSPHERIC PRESSURE DIELECTRIC BARRIER DISCHARGES INTERACTING WITH LIQUID COVERED TISSUE

4.1 Introduction

Atmospheric dielectric barrier discharges (DBDs) are being investigated for use in healthcare [1-3] such as wound healing[2,3], killing bacteria[4], and sterilization of surfaces[5,6] due to their intrinsic stability against arcing.[7] The use of atmospheric DBDs for wound healing and skin treatment is still at an early stage, and is an active area of research in which clinical studies are in progress.[8,9] Many such applications involve DBDs (or other plasmas) in contact with liquids such as in the treatment of wounds. Most wounds in their early stages are covered with a water-like liquid resembling blood serum (93% water and 7% proteins).[10] The thickness of the liquid layer is typically a few hundred microns. The plasma produced reactive fluxes first react with the hundreds of microns thick liquid layer. The liquid then acts as a filter which modifies the plasma produced fluxes prior to those fluxes or their reaction products reaching the underlying tissue. The mechanisms for DBDs delivering reactivity through the liquid layer to the tissue below are not clear.

The recent interest in plasma medicine has motivated works investigating *plasmas-onto-water* (POW). For example, *plasma-activated-water* (PAW) results from exposure of water to plasmas.[11-13] This process results in the water having long-lived biocidal properties [11] which have been attributed to formation of, for example, peroxynitrites.[13] More general studies of POW have investigated the formation of acids, reactive oxygen species (ROS) and reactive nitrogen species (RNS).

The typical DBD used to treat tissue or wounds consists of a powered electrode covered

[*]The results discussed and portion of the text appearing in this chapter were previously published in Wei Tian *et al*, "Atmospheric pressure dielectric barrier discharges interacting with liquid covered tissue", J. Phys. D: Appl. Phys. **47**, 165201(2014)

by an insulator. The treated tissue is separated from the dielectric by a few mm, and serves as a floating electrode.[7] The tissue is often covered by a liquid layer, which is typically hundreds of microns thick. The liquid is mostly water which may contain dissolved gases, such as O_{2aq} or CO_{2aq}, and organic compounds such as proteins as contained in blood serum.[10] ($_{aq}$ denotes an aqueous species.) In this configuration, the liquid layer is directly exposed to the chemically reactive neutral radicals, electrons, ions and UV/VUV radiation produced by the plasma.

The discharge becomes more complex when considering the coupled plasma-liquid system. From simply a circuit perspective, the liquid is a lossy dielectric which contributes to the series capacitance of the DBD and so contributes to power loss. The liquid surface, water in our case, evaporates water vapor to humidify the air close to the surface. The locally more humid air changes the plasma characteristics, particularly with respect to the production of hydroxyl radicals. Once radicals and ions either diffuse into or are formed in the water (that is, solvated species) a second hierarchy of reactions begins. The duration of an individual plasma filament in the DBD is relatively short, a few to tens of ns. Many water related reactions, such as solvation of electrons and charge exchange, have similarly short (or shorter) timescales. However, the reaction chain initiated in the water by the plasma can evolve over seconds to minutes. For example, hydrogen peroxide, H_2O_{2aq}, is formed by the reaction of two hydroxyl radicals, OH_{aq}, which result from OH solvating into the water. Aqueous ozone, O_{3aq} is formed through solvation of gaseous O_3. Both H_2O_{2aq} and O_{3aq} can persist in the water for up to days. These long-lived species in part explain why PAW maintains its chemical reactivity for long times after exposure to plasma.[11,14]

In this chapter, we report on results from a 2-dimensional computational investigation of DBDs in contact with water covered tissue. A 3-pulse negative discharge and its 1-20 second afterglow is investigated in both the gas phase and liquid phase. The underlying tissue is modeled as a dielectric material with no conductivity. The effect of liquid conductivity will be discussed in Chapter 6. The liquid layer is treated identically to gas as a partially ionized substance but with a higher density and specified permittivity. So from a computational perspective, the same equations (e.g., continuity, energy, radiation transport, Poisson's equation) are solved both in the gas phase and the liquid phase, albeit with different species and reaction mechanisms

In the DBDs, the gas phase plasma is produced with multiple -18 kV pulses at 100 Hz followed by a 1 s afterglow in most cases. RONS produced in the gas phase intersect the water vapor saturated air above the liquid and then solvate when reaching the liquid. Photoionization and photodissociation of water by the plasma produced UV/VUV radiation plays a significant role in the radical production. Pure water, water with dissolved O_{2aq} and water having a generic hydrocarbon alkane, RH_{aq}, were investigated. Alkanes, RH_{aq}, are the simplest organic molecules consisting of only carbon and hydrogen and with only single bonds between carton atoms. Without RH_{aq}, $O_2^-{}_{aq}$, $ONOO^-{}_{aq}$ and hydronium ($H_3O^+{}_{aq}$) dominate the water ions with $H_3O^+{}_{aq}$ determining the pH. The dominant RONS in the liquid are O_{3aq}, H_2O_{2aq}, and HNO_{xaq}. The formation of $HOONO_{aq}$ is also included since $HOONO_{aq}$ has a high oxidizing potential. For liquids containing RH_{aq}, ROS are largely consumed, leaving $R\bullet_{aq}$ (alkyl radical) to reach the tissue. $R\bullet_{aq}$ is RH_{aq} missing a hydrogen atom.

The model used in this investigation is described in Sec. 4.2 followed by a discussion of simulated DBDs in contact with a thin water layer in Sec. 4.3. Our concluding remarks are in Sec. 4.4.

4.2 Description of the Model

The model used in this investigation is *nonPDPSIM* and the gas phase portions of the model are described in detail in Chapter 2. In extending *nonPDPSIM* to the liquid phase, we attempted to make a minimum of limiting assumptions. The numerical mesh is divided into zones which are specified as being gas or liquid. Computationally and algorithmically, the liquid zone is treated identically to the gas phase. The same equations (e.g., Poisson's, transport and energy conservation, radiation transport) are solved in the liquid as in the gas. In order to properly include the larger dielectric constant of the liquid, an atomic permittivity is specified for each species so that the number density weighted permittivity yields the proper dielectric constant. Transport coefficients for neutral and charged species, and absorption cross sections, are determined by the local densities on a mesh-point-by-mesh-point basis.

The rate of transport of gas phase species into the liquid is determined by Henry's law considerations.[15,16] Henry's law states that at a constant temperature and at equilibrium, the

density of a gas dissolved in a liquid, water in this case, is proportional to the partial pressure of the gas in the vapor phase. Proportionality constants for use in Henry's law for water are shown in Table 4.1. Henry's law constant is a measure of the solubility of a gas phase species into a liquid. Henry's law only describes the dynamical equilibrium of solvation – the relative concentrations of the gas and liquid phase species at the interface. The actual rate of solvation is not necessarily known. In our model, the rate of solvation is given in analogy to the Noyes–Whitney formula[17,18],

$$\frac{dn_{aq}}{dt} = \frac{KD_g}{h}\left(hn_g - \min\left(n_{aq}, hn_g\right)\right) \qquad (1)$$

where n_{aq} is the density of the species at the surface of the water and n_g is the density of the species directly above the liquid in the gas phase. K is geometric factor which accounts for the spatial distribution of numerical mesh points, D_g is the diffusion coefficient in the gas phase, and h is the Henry's law constant. If the only source of the solvated species in the water is from the gas phase, then diffusion from the gas phase into the liquid stops when the equilibrium density of n_{aq} at the surface is reached. If the value of n_{aq} is reduced by either diffusion into the liquid or by reactions so that at the surface $n_{aq} < h \cdot n_g$, then solvation of gas phase species restarts. If diffusion of n_{aq} into the liquid from the surface is slow, solvation may slow to a negligible rate in spite of an abundance of gas phase species, since the density of n_{aq} at the surface is at equilibrium with the gas phase. This occurs even though n_{aq} may have a much smaller density deeper into the liquid and the average value of n_{aq} in the liquid layer is much smaller than the equilibrium value. All of the gas phase ions of interest have ionization potentials that are much larger than the surface energy or surface tension of the liquid. As a result, we assumed that ions are solvated without constraints.

In the absence of other data, Lennard-Jones parameters were used to compute diffusion coefficients in the liquid. This practice produces diffusion coefficients that are about 1000 times smaller in the liquid than in the gas phase. The differences in diffusion coefficients for different species, such as OH and NO, vary by factors of 2-3, depending on their mass and Lennard Jones parameters. However, the Henry's law constants for these species can vary by a factor of 10^4. The solvation rate of NO into the liquid is much slower than that of OH due to its relative Henry's law values and subsequent reactivity, and not because of large differences in their

intrinsic rates of diffusion.

Due to their higher potential energies, we assumed that all ions, as well as electrons, and pass directly into the liquid. That is, the liquid mesh point having a gas phase mesh point as a neighbor receives charged species with a rate of diffusion (or drift in the electric field) given by their gas phase transport coefficients. For these species the diffusion coefficient for transport into the liquid is given by the gas phase values. For transport of the charged species out of the liquid into the gas, the liquid transport coefficients are used, which effectively traps the charged species in the liquid. From a practical perspective, the diffusion out of the water of dissolved gas phase ions or electrons is highly unlikely since their rates of solvation or charge exchange are large.

The exception to these practices is the evaporation of the water. We do not explicitly address the surface tension of the water-gas interface. Instead, we assume that the gas phase density of water at the liquid surface is given by its saturated vapor pressure, which is 27 Torr at 300 K. The corresponding water vapor density is then used as a boundary value for diffusion of water vapor from the interface into the gas.

Radiation transport is addressed in the same manner as described in Chapter 2 while accounting for local values of absorption cross sections and densities of either gas or liquid phase species. For example, the photon flux originating from emission by species *k* at mesh point *i* arriving at mesh point *j* is given by

$$\phi_k(\vec{r}_j) = A_k N_k(\vec{r}_i) \exp\left(-\int_{r_i}^{r_j} \sum_m N_m(\vec{r}\,') \sigma_{km} d\vec{r}\,' \right) f(\vec{r}_i, \vec{r}_j) \qquad (2)$$

where N_k is the density of the emitting species having Einstein coefficient A_k, the sum is over absorbing species having density N_m and absorption cross section σ_{km}, and f is a function to account for the reduction in flux due to obscurations and expansion of the photon front, which has a different form for a specific coordinate system. The integral accounts for absorption along the trajectory of the photon, which naturally accounts for the transition from the gas phase into the water. We do not account for the refraction of light at the boundary of the gas-liquid interface. Although refraction is important for photons that have a long mean free path in the water, for the results discussed here, we only considered transport of UV and VUV capable of photolyzing or photoionizing the water. From a practical perspective, the mean free path for

these photons in the water is only a few to 10 microns, and so the change in their direction due to refraction is not important.

The Cartesian geometry used in this investigation is shown in Fig. 4.1. The left and right boundaries (not shown in Fig. 1) use reflective boundary conditions and are placed sufficiently far away that they do not influence the calculation. (The full width of the computational domain is 4 mm.) The powered electrode is at the top and is covered by a dielectric 0.12 mm thick having a dielectric constant of $\varepsilon/\varepsilon_0$=3. The gap between the dielectric and the surface of the water is 1.5 mm and initially filled with humid air. The tissue at the bottom of the domain is 2 mm thick and is represented as a dielectric with relative permittivity of $\varepsilon/\varepsilon_0$=5 and no conductivity. An electrical ground plan is below the tissue. The tissue is covered by a water layer having $\varepsilon/\varepsilon_0$=80 and is 200 μm thick in the base case. The numerical grid consists of 10,526 nodes and 20,747 volume elements, of which 8,681 nodes and 17,225 volume elements are in the plasma region in the gas and liquid layer. The volume near the liquid-gas interface is refined with smaller dimensions, about 20 μm compared to 50 μm in the remote gas gap. These mesh spacing will not resolve the dynamics of double layers or other charge layers that may form at the surface of the liquid, as these structures may be as thin as a few nm.[19]

The liquid is basically water with dissolved oxygen O_{2aq} of 8 ppm [20] at room temperature and under atmospheric pressure. We have not considered any initial conductivity of the liquid as may occur in many biological liquids due to the presence of the electrolytes. The change in conductivity of the liquid that results from plasma treatment is self-consistently accounted for through the evolution of the ion content of the liquid and the resulting charge density that is included in the solution of Poisson's equation. The reaction mechanism in the water has been described in Chapter 2 and is shown in Table 4.2.

The VUV/UV radiation generated by high lying excited states of N_2 is attenuated by absorption in propagating through the plasma and into the water or onto solid surfaces.[25] In this model, photons are emitted from the highly excited states of N_2, involving $N_2(b')$ with energy of 12.8 eV and $N_2(c')$ with energy of 12.9 eV O_2 in the gas phase undergoes ionization and H_2O_{aq} undergoes both ionization and dissociation. The mean free path of VUV/UV photons (> 12 eV) is extremely short, about tens of nanometers.

Three discharge pulses in the air gap at 100 Hz are simulated followed by a 1 s afterglow for the base case. Each discharge pulse lasts approximately for 5 ns. The gas is initially slightly

humid air, $N_2/O_2/H_2O$ = 79.9/20/0.1 at 300 K and 1 atm. Before the first pulse, water is evaporated into the gap for 10 ms. The discharge is initiated by seeding a neutral plasma of 10^9 cm^{-3} near the insulator with a diameter of 100 um. (The final values are insensitive to the density and size of this initial spot of plasma.) The discharge is then sustained by the secondary electron emission from the insulator surface, for which the emission coefficient is 0.15 for ions and 0.001 for photons. The voltage applied to the powered electrode rises to -18 kV in 0.1 ns and falls at the end of 4 ns to 0 kV in 1 ns. The interpulse period is 10 ms during which recombination, ion-ion neutralization and diffusion extinguish the plasma. The discharge is reinitialized in the same manner for the 2nd and 3rd pulses. During the interpulse periods and 1 s afterglow, Poisson's equation is not solved and quasi-neutrality is assumed, producing essentially ambipolar transport. Since electrons which do not recombine either attach (first to O_2 in the gas phase) in less than 1 μs, or solvate in the liquid in less than 1 ns, there is little electron enhanced ambipolar transport. Diffusion is more akin to diffusion with the free diffusion coefficients of the ions. At the start of the next pulse, the charged species are forced to be absolutely neutral prior to restart Poisson's equation. This is done by adjusting the densities of N_2^+ or O_2^- in gas phase and $H_3O^+_{aq}$ and $O_2^-{}_{aq}$ in liquid phase. We have not included advective gas transport in the work discussed here – all transport is diffusive. In work to be reported elsewhere, a wind of only tens of cm-s^{-1} is sufficient to affect the plasma-water interaction.

We have assumed that the underlying tissue consumes radical species produced in the liquid, and so acts as a sink for these species. We have not addressed the change in the biochemistry of the tissue resulting from those reactions as being beyond the scope of this study. It is this consumption of radicals by the tissue that in part is responsible for the dependence of radical fluences to the tissue on thickness of the liquid layer.

4.3 DBD Plasma Filaments Incident onto Water

The time evolution of a typical DBD filament incident onto the water surface is shown in Fig. 4.2 where the gas phase electron density, n_e, electron temperature, T_e, E/N (electric field/gas number density) and electron impaction ionization source, S_e, are shown. The discharge starts at the top electrode where the cloud of initial plasma is seeded. The density of the seed electrons was optimized to be 10^9 cm^{-3} with 0.1 mm diameter and placed near the upper dielectric, which

does not affect the discharge property. The lower limit of seed electrons to initiate the discharge is 10^8 cm^{-3}. Upon application of the -18 kV pulse, the electrons avalanche downward, at first in a Townsend-like mode, and then in a streamer-like mode and reach the liquid layer in 1.7 ns with density of 10^{13} cm^{-3}. At this time *E/N* is fairly uniform in the gap, around 100 Td (1 Td = 10^{-17} V-cm^2). T_e is about 4 eV and the ionization source is 10^{22} $cm^{-3}s^{-1}$. Once the discharge reaches and begins to charge the liquid layer, a backward streamer develops and finally reaches the top insulator at 2.7 ns. At that point, a conductive channel forms and the electron density increases to 2×10^{14} cm^{-3}. A sheath begins to form at the dielectric surface, the *E/N* near the insulator reaches 1000 Td and T_e increases to 8 eV. The ionization source, 10^{23} $cm^{-3}s^{-1}$, is then confined to a thin surface layer which spreads along the dielectric. Once bridging the gap, the discharge spreads over the surface of the insulator and the water layer, as wide as 1 mm. The spread is wider on the insulator since its capacitance is smaller.

Considering the negative polarity of the pulse, positive ions striking the insulator surface produce secondary electrons to maintain the streamer while the surface of the dielectric charges. As a result the electron density near the top insulator is as high as 5×10^{14} cm^{-3}. On the other hand, the water layer is to some degree a sink where electrons strike and quickly become solvated. As a result, the electron density is lower, 10^{13} cm^{-3}, at the surface of the water.

4.3.1 Water Evaporation

The air is initially slightly humid, having 0.1% H_2O (2.5×10^{16} cm^{-3}), and is humidified as water evaporates into the gap. The water vapor density across gap at the time the voltage is applied is shown in Fig. 4.3(a). The density of H_2O is 5×10^{17} cm^{-3} at the water surface, as given by the room temperature vapor pressure of water, 27 Torr.[20] At the top of the gap, the density of H_2O is 7×10^{16} cm^{-3}. The densities of plasma produced H_2O^+ and OH are shown in Fig. 4.3(b), with and without evaporation. In the absence of evaporation, the maximum density of gas phase H_2O^+ and OH above the water are 3.1×10^{11} cm^{-3} and 1.1×10^{12} cm^{-3}. With evaporation, the densities are 1.5×10^{12} cm^{-3} and 1.2×10^{13} cm^{-3}. The saturated water vapor above the liquid significantly increases the densities of ROS in close vicinity of the water surface. We provide this comparison to emphasize the sensitivity of the results discussed below to the environmental conditions. For example, how long the DBD source is positioned above the

water layer, a few degree change in water temperature (thereby affecting the vapor pressure), and cross currents of air blowing across the liquid are all capable of changing the humidity within the gas, and so affecting the final outcome of ROS production.

4.3.2 General Sequence of Aqueous Reactions

The general sequence of reactions we will discuss below are summarized here. The notation typically used for liquid phase reactions expresses second order rate coefficients with units of $(\text{mole/liter})^{-1}s^{-1}$ or M^{-1}-s^{-1}. A gas kinetic rate coefficient refers to a reaction that has no activation barrier nor steric hindrance, and so reactions occur with every collision. For atoms and molecules with moderate molecular weights at room temperature, a gas kinetic rate coefficient is about 10^{-10} cm^3s^{-1}. So the equivalent gas kinetic rate coefficient in the liquid phase is about 6×10^{10} $M^{-1}s^{-1}$. We call these reactions *equivalent gas kinetic* (EGK). Reactions with liquid water having a EGK rate coefficient occur in a few ps.

Positive Ions: The ionization potential of water is 12.6 eV, which is smaller than all of the major ions produced in the streamer ($N_2^{+,}$ $N_4^{+,}$, $O_2^{+,}$, $O_3^{+,}$, O_4^{+}). When striking the water surface, the major ions charge exchange with H_2O_{aq} to form $H_2O^+_{aq}$. The rate coefficient is likely near EGK and so given the water density of 3×10^{22} cm^{-3}, this reaction likely occurs at most tens of ps to perhaps 1 ns. $H_2O^+_{aq}$ then charge exchanges with H_2O_{aq} to form $H_3O^+_{aq}$, hydronium, and OH_{aq}. With a rate coefficient of 6×10^3 $M^{-1}s^{-1}$, this charge exchange occurs in a few μs.

Electrons: Electrons striking the water solvate to form e_{aq} within a few ps. e_{aq} is an electron surrounded by water molecules, and can be thought of as a low mobility and somewhat low reactivity electron. It is here where the purity of the water is important. e_{aq} slowly reacts with H_2O_{aq} to form $H\bullet_{aq}$ and OH^-_{aq}, with reaction times of a few ms. e_{aq} will attach to O_{2aq} to form $O_2^-_{aq}$ with a rate coefficient 2×10^{10} $M^{-1}s^{-1}$, nearly EGK It is common for water to have dissolved O_{2aq}, in our case O_{2aq} = 8 ppm or 4×10^{-4} M, which produces attachment times of about 100 ns. Similar attachment or dissociative attachment reactions having EGK rate coefficients occur with (reactions products are in parenthesis) H_2O_{2aq} (OH_{aq} + OH^-_{aq}), OH_{aq} (OH^-_{aq}), and O_{aq} (O^-_{aq}).

Negative Ions: We have assumed that negative ions entering the liquid from the gas

phase will solvate as equivalent aqueous forms. The major negative ions in the gas phase are O_2^- and O^-. When reaching the water, O_2^- is solvated to $O_2^-{}_{aq}$ in a few ps, which is one of the dominant negative ions in the liquid. As mentioned above, electron attachment to produce $O_2^-{}_{aq}$ is fast, in a microsecond, and produces more $O_2^-{}_{aq}$ than the solvation of the gas phase negative ion. Another source of $O_2^-{}_{aq}$ comes from the hydrolysis of HO_{2aq}, which is produced by H_{aq} combining with O_{2aq}. This process is slow, occurring in a few ms, and depends strongly on the production of H_{aq} in the water. Once formed, $O_2^-{}_{aq}$ reacts with dissolved NO_{aq} with a rate coefficient of 3.6×10^9 $M^{-1}s^{-1}$, or charge exchanges with OH_{aq} to form $OH^-{}_{aq}$ with a rate coefficient of 6×10^9 $M^{-1}s^{-1}$. These relative branching for these reactions depend on the densities of NO_{aq} and OH_{aq}. OH_{aq} is produced in the water during the current pulse by photodissociation of water while NO_{aq} is produced by solvation of gas phase NO during the afterglow. As a result, the $O_2^-{}_{aq}$ charge exchange with OH_{aq} occurs earlier than the reaction with NO_{aq}. O^-, as well as its solvated counterpart, $O^-{}_{aq}$, is highly reactive. $O^-{}_{aq}$ reacts with e_{aq} to dissociate H_2O_{aq} to form $OH^-{}_{aq}$ with a rate coefficient 2.2×10^{10} $M^{-2}s^{-1}$; or neutralizes $H_3O^+{}_{aq}$ to form OH_{aq} with a rate coefficient 2.3×10^{10} $M^{-1}s^{-1}$. Both reactions are nearly EGK. The density of $O^-{}_{aq}$ diminishes in a microsecond or less after the discharge pulse. Since the maximum density of $O^-{}_{aq}$ is only 10^{12} cm^{-3} in water and the $H_3O^+{}_{aq}$ density does not rise before the density of $O^-{}_{aq}$ diminishes, these reactions do not significantly affect the liquid chemistry.

ROS: The most important ROS in water for these conditions are OH_{aq}, H_2O_{2aq} and O_{3aq}. OH_{aq} can be produced directly in water or through solvation of gas phase OH. OH_{aq} is produced in the water by photolysis, electron impact dissociation at the surface (though this is not important for these conditions), charge exchange of $H_2O^+{}_{aq}$ with water and ion-ion recombination. These reactions occur in short times – from sub-microsecond for photolysis, to tens of microseconds for ion-ion recombination. In the afterglow, the gas phase OH solvates into the water in milliseconds as the OH diffuses into the water with a large Henry's law constant, 6.92×10^2. H_2O_{2aq} is produced in a few ms by the mutual reaction of OH_{aq} with a rate coefficient of 5.5×10^9 $M\text{-}s^{-1}$, about 0.1 EGK In the afterglow, gas phase H_2O_2 also solvates into the water with a large Henry's law constant, 1.92×10^6, which also contributes to the density of H_2O_{2aq}. O_{3aq} is not directly produced in the water since the density of O_{aq} is small. In the gas phase, O is produced through electron impact dissociation of O_2 and dissociative excitation transfer from $N_2(A)$ but quickly combines with O_2 to form O_3. So little O survives to diffuse into

the water while dissociation of O_{2aq} is difficult. Solvation of gas phase O_3 dominates the production of O_{3aq}. Although O_3 has a small Henry's law constant, 0.3 (much smaller than for OH and H_2O_2) its large density, as high as 10^{15} cm^{-3} after a few pluses still produces a high aqueous density of O_{3aq}, averaging 5×10^{14} cm^{-3}.

RNS: The dominant reactive nitrogen species in water for our conditions are HNO_{2aq}, HNO_{3aq} and $HOONO_{aq}$, and their conjugate ions, $NO_2^-{}_{aq}$, $NO_3^-{}_{aq}$ and $ONOO^-{}_{aq}$. The RNS can be formed in both the gas and liquid phase, and the formation channels are similar. The aqueous RNS originate as N_xO_y (NO, NO_2, NO_3, N_2O_3, N_2O_4, N_2O_5), which is mainly formed in the gas phase during the afterglow a few milliseconds after the discharge pulse. Of the N_xO_y, NO dominates with a maximum density of 10^{14} cm^{-3} followed by NO_2 with a density of 10^{12} cm^{-3} for the few discharge pulses we simulated. Other nitrogen species have densities below 10^{11} cm^{-3}. HNO_2, either in gas phase or in the liquid, is produced by three body reactions, for example, NO + OH + M, with a rate coefficient of 6×10^{-31} cm^6s^{-1} in gas phase or 2×10^{10} $M^{-2}s^{-1}$ in the liquid. NO and NO_2 have small Henry's law coefficients, 0.044 and 0.28, respectively. The solvation processes of NO and NO_2 are therefore slow enough that HNO_2 has sufficient time to be formed in gas phase. On the other hand, HNO_2 has a large Henry's law constant, 1.15×10^3 which allows gas phase HNO_2 to rapidly solvate. Therefore, the solvation process plays a significant role, 40%, in aqueous HNO_{2aq} production.

HNO_3 forms through similar channels as HNO_2. HNO_3 is formed, either in the gas phase or in the liquid, by NO + HO_2 + M with a rate coefficient of 2×10^{-30} cm^6s^{-1} in the gas phase or 8×10^9 $M^{-1}s^{-1}$ in the liquid; and by OH + NO_2 + M with a rate coefficient of 1.7×10^{-30} cm^6s^{-1} in the gas phase or 3×10^{10} $M^{-1}s^{-1}$ in the liquid. In the gas phase, the density of NO_2 is lower than NO by a factor of nearly 100 after 3 pulses and the density of HO_2 is even lower , $\approx 10^9$ cm^{-3}. As a result, the latter reaction is more important in forming HNO_3, and the density of HNO_3 (10^{11} cm^{-3}) is much smaller than HNO_2 (10^{12} cm^{-3}) for the number of discharge pulses we simulated. However, HNO_3 has a larger Henry's law constant (4.8×10^6) than HNO_2 (1.15×10^6). The end results is that solvation of HNO_3 from the gas phase contributes 11% of the HNO_{3aq}.

HOONO, an isomer of HNO_3, forms through different channels. HOONO has a linear molecular structure and higher oxidizing energy.[28] HOONO is produced, either in the gas phase or in the liquid, by reactions of NO + HO_2, with a rate coefficient of 2.31×10^{-13} cm^3s^{-1} in gas phase or 3.2×10^9 $M^{-1}s^{-1}$ in the liquid; and by reactions of NO_2 + OH, with a rate coefficient

of 1.57×10^{-11} cm^3s^{-1} in gas phase or 1.2×10^{10} $M^{-1}s^{-1}$ in the liquid. Similar to HNO_3 production, the latter reaction is more prominent. The ratio of HOONO to HNO_3 in the gas phase is about 40% in our model. The Henry's law constant of HOONO is basically the same as for HNO_3, and so its solvation is rapid. The conjugate ions of these acids come from their hydrolysis. HNO_{2aq} is a weak acid and about 1% of HNO_{2aq} hydrolyzes in water and so the density of $NO_2^-{}_{aq}$ is only about 10^{11} cm^{-3}. HNO_{3aq} and $HOONO_{aq}$ are stronger acids and essentially completely hydrolyze in water resulting in the density of $NO_3^-{}_{aq}$ and $ONOO^-{}_{aq}$ being 10^{13} cm^{-3}.

Photons: The threshold energy for photo-dissociation of H_2O_{aq} is 7.6 eV and that for photo-ionization is 12.6 eV, both of which are lower in energy than VUV photons expected to be produced by the electron avalanche onto the surface of the water. The cross section for both of these processes is 1×10^{-20} cm^2, which yields a mean free path for absorption of VUV photons in the water of about 30 μm.

4.3.3 Gas-Liquid Interactions

The sum of the electron and negative ion densities, and positive ion densities are shown in Fig. 4.4 in the gas phase and in the liquid. The gas phase densities are shown at the end of the current pulse. The enlargements of densities in the liquid are at times during the pulse, interpulse afterglow and during the terminal afterglow following the third pulse. (Recall that the discharge pulses begin at t = 0 s, 10 ms and 20 ms, and the last afterglow extends to 1 s.) For the negative species, the densities of e_{aq}, and the sum of $NO_3^-{}_{aq}$ and $O_2^-{}_{aq}$ are shown. For the positive species, $H_2O^+{}_{aq}$ and $H_3O^+{}_{aq}$ are shown. As a negative discharge, electrons in the gas phase are accelerated by the applied electric field into the surface of the water where then essentially immediately solvate to form e_{aq}. In the model, the electrons lose all their kinetic energy when enter the liquid. Since the mobility of e_{aq} is smaller by a factor of at least 10^4 than in the gas phase due to the higher density of collision partners and larger effective mass, there is net negative charging of the surface of the water similar to the surface of the dielectric in a DBD. On the first discharge pulse, there are few other species in the water other than dissolved oxygen, O_{2aq}. As a result, during the first early afterglow e_{aq} primarily attaches to O_{2aq} to form $O_2^-{}_{aq}$. This attachment occurs within a few μs. During the discharge pulse photo-dissociation of H_2O_{aq}

generates OH_{aq}, which provides another prompt partner for attachment. The dissociative attachment to H_2O_{aq} to form H_{aq} and OH^-_{aq} occurs in significant numbers only in the terminal afterglow.

During the interpulse and terminal afterglows, NO_x from the gas phase diffuses into the water, which then opens channels for other attachment processes. The reaction flow chart can be seen in Fig. 2.5. Diffusion of NO into the liquid enables charge exchange between NO_{aq} and $O_2^-_{aq}$ to form $NO_3^-_{aq}$. The sequence of events that occurs during and after each discharge pulse is drift of gas phase electrons into the liquid, rapid solvation to form e_{aq}, followed by two charge exchanges to form $O_2^-_{aq}$ and $NO_3^-_{aq}$. The rate of the second charge exchange reaction increases as the fluence of NO_x from the gas phase into the water increases with each successive discharge pulse. The rate of the first charge exchange depends on the density of dissolved O_{2aq}. Since the dissolved O_{2aq} is a function of water temperature, we expect that the rate at which these initiating attachment processes occur will also be temperature dependent. During later discharge pulses and during the terminal afterglow, nitric acid, HNO_3 is formed in the gas phase and diffuses into the water. $NO_3^-_{aq}$ is then also generated by the hydrolysis of HNO_{3aq}, which then also produces hydronium, $H_3O^+_{aq}$. During the terminal afterglow, the end products of the hydrolysis and charge exchange result in $O_2^-_{aq}$ and $NO_3^-_{aq}$ being the dominant negative ions. These ions diffuse through the 200 μm water later to reach the underlying tissue. At the end of the 1 s afterglow, the combined densities of $O_2^-_{aq}$ and $NO_3^-_{aq}$ above the tissue is 2.5×10^{13} cm^{-3}, or a molar density of 4.2×10^{-8} M. Recall that this density results from 3 discharge pulses.

The sum of the positive ions is shown in Fig. 4.4(b). In the gas phase just above the water at the end of the current pulse, the dominant positive ions are N_2^+ (6.6×10^9 cm^{-3}), N_4^+ (4.1×10^{11} cm^{-3}), O_2^+ (1.1×10^{13} cm^{-3}) and H_2O^+ (6.1×10^{11} cm^{-3}). O_2^+ dominates the positive ions since it has lower ionization potential. The density of H_2O^+ is second to O_2^+ and exceeds that of N_4^+ due to the high water vapor concentration at the surface of the water. Due to this being a negative discharge, the net drift of positive ions is towards the top insulator, and so during the discharge pulse, the fluence of positive ions into the water is smaller than for electrons. N_2^+ and O_2^+ solvate and quickly charge exchange to form $H_2O^+_{aq}$, whereas H_2O^+ directly solvates to form $H_2O^+_{aq}$. The production of $H_2O^+_{aq}$ water is significantly enhanced by photoionization. Photoionization contributes 62% to the initial production of $H_2O^+_{aq}$, a process which is enabled by the plasma touching the water and so allowing the plasma generated VUV to reach the surface

of the water. An equal rate of photodissociation occurs, which is an important source of OH_{aq} and H_{aq}. In the absence of H diffusing from the gas phase into the water, there are few ways to produce of H_{aq} outside of photodissociation. These photolysis reactions producing $H_2O^+_{aq}$, OH_{aq} and H_{aq} may be a distinguishing feature between remote and direct plasma exposure of water.

$H_2O^+_{aq}$ penetrates only a few microns into the water before forming hydronium $H_3O^+_{aq}$, a reaction which also produces OH_{aq}. Direct charge exchange and photoionization are the dominant sources of $H_3O^+_{aq}$ prior to the terminal afterglow. During the terminal afterglow, $H_3O^+_{aq}$ is also formed from the hydrolysis of neutral hydroperoxyl radicals (HO_{2aq}), nitrous acid (HNO_{2aq}) and nitric acid (HNO_{3aq}). The majority of $H_3O^+_{aq}$ is ultimately produced by these hydrolysis reactions during the afterglow. $H_3O^+_{aq}$ is produced dominantly by HNO_{3aq} hydrolysis, while in the absence of nitrogen species HO_{2aq} could be the dominant source providing $H_3O^+_{aq}$. $H_3O^+_{aq}$ is the terminal positive ion, which drifts through the water layer to the underlying tissue. At the end of the terminal 1 s afterglow, the density of $H_3O^+_{aq}$ above the tissue is 2.3×10^{14} cm^{-3}, or a molar density of 3.8×10^{-7} M. The persistence of $H_3O^+_{aq}$ has been observed experimentally to last for as long as days.[11]

$H_3O^+_{aq}$ is responsible for the acidification of the water and lowering of its pH value. Experimentally, the pH of distilled water has been reduced to as low as 4 after 3 minutes of plasma treatment.[13] For the results discussed here, in which we have simulated only 3 pulses, the local maximum density of $H_3O^+_{aq}$ is 3×10^{15} cm^{-3} (or 5×10^{-6} M) producing a local pH value of 5.3, and an average pH value of about 6 and so the water is only weakly acidified. More pulses will produce a lower pH value and a more acidic solution. For example, after simulating 6 pulses the maximum density of $H_3O^+_{aq}$ is 5×10^{15} cm^{-3} (or 8×10^{-6} M), producing a local pH value of 5.1, and an average pH value of about 5.8. Since $H_3O^+_{aq}$ to some degree accumulates on a pulse-to-pulse basis, it is not unexpected to produce small pH values after many pulses.

Experimental investigations have suggested that bacteria killing species in water include hydroxyl radicals,[29] hydrogen-peroxide and ozone[30], collectively known as reactive oxygen species (ROS); and reactive nitrogen species (RNS) in the form of nitric acid[13,29] and peroxynitrite[31]. Unlike gas phase charged species, which largely recombine or neutralize prior to diffusing to the surface of the liquid, the lifetimes of neutral radicals are long enough that these plasma produced species are able to diffuse into the water without significant losses. Species such as O_3 and N_xO_y which accumulate in the gas phase pulse-to-pulse represent a large

reservoir of reactivity which eventually diffuses into the liquid. This reactivity is enhanced by Henry's law constants larger than 1.0 for most neutral radicals except NO, NO_2 and O_3. This means that the water is able to quickly solvate the neutral radicals resulting in the water layer absorbing more neutral radicals than charged species.

One of the possible interactions of ROS with cell membranes is peroxidation of the membrane lipids. OH_{aq} and H_2O_{2aq} are highly reactive radicals, with oxidizing potential of 2.8 eV and 1.78 eV, respectively. A synergistic effect in bacteria killing involving OH_{aq} and H_2O_{2aq} can become even stronger in low pH environments.[13,30] The densities of OH and H_2O_2 in the gas phase from the end of the current pulse to 3 ms are shown in Fig. 4.5. The densities of OH_{aq} and H_2O_{2aq} at times from the end of the current pulse to the end of the terminal afterglow are also shown. OH in the gas phase is dominantly produced by electron impact dissociation of water vapor and so its density is largest near the surface of the liquid where the water vapor density is the highest. The density of OH is also high near the top insulator because the electron density and temperature are high there. OH is depleted by diffusion into the water or formation of H_2O_2. The maximum density of OH at the end of the current pulse (5 ns) is 1.3×10^{13} cm^{-3}. By 3 ms, the density of OH has decreased to 9.1×10^{11} cm^{-3}. During the interpulse afterglow, the majority of OH has been depleted and the H_2O_2 density is 3.3×10^{11} cm^{-3}. H_2O_2 continues to accumulate pulse-to-pulse, from 3.3×10^{11} cm^{-3} at 3 ms to 1.6×10^{12} cm^{-3} at 23 ms. H_2O_2 has a larger Henry's law constant than OH and therefore more rapidly solvates into the water.

In addition to diffusion and solvation processes, OH_{aq} is also produced by photodissociation at the surface of the water by VUV produced by the plasma, and by formation of $H_3O^+_{aq}$ by charge exchange with $H_2O^+_{aq}$. Through this charge exchange process, every positive ion incident onto the water produces at least one OH_{aq}. In spite of its short duration, a large photon flux onto the surface of the water still results in a significant production of OH_{aq}. For example, integrated over the three pulses simulated here, the proportion of OH_{aq} initially produced by photodissociation is 39%, by charge exchange is 27%, and by solvation of OH is only 3%. The timings of these contributions are quite different. Photodissociation and charge exchange occur nearly coincident with the discharge pulse whereas diffusion occurs throughout the afterglow.

The mean free path for charge exchange and photo-dissociation is at best 20-30 μm, so the majority of the OH_{aq} is produced at the top of the liquid, which is also the entry point for OH

diffusing from the gas phase. The maximum density of OH_{aq} at the top of the water layer is 1.6 × 10^{15} cm^{-3} (or 2.6 × 10^{-6} M) at 10 μs after the discharge pulse. Since diffusion through the water layer is slow, the majority of OH_{aq} mutually reacts to form H_2O_{2aq} before OH_{aq} can reach the underlying tissue for a 200 μm thick water layer. H_2O_{2aq} has a lower oxidizing potential than OH_{aq}, but it is nevertheless an efficient agent to transport the oxidizing power originally generated by electron impact processes in the gas phase through the water. In the absence of hydrocarbon species, H_2O_{2aq} is the terminal species in this reaction chain, which then diffuses through the water layer to reach the underlying tissue. The maximum density of H_2O_{2aq} near the surface is 1.5 × 10^{15} cm^{-3} (or 2.5 × 10^{-6} M). At the end of the terminal afterglow, the density of H_2O_{2aq} at the tissue is 5.5 × 10^{13} cm^{-3} (or 9.2 × 10^{-8} M). In our mechanism, H_2O_2 reacts with the tissue and so the fluence to the tissue (integrated flux) is perhaps the better measure of reactivity. Fluences are discussed below.

Although H_2O_{2aq} is fairly stable in water in the absence of hydrocarbon in our model, H_2O_{2aq} can be photolyzed to OH by UV fluxes (250−300 nm) [32] or dissociate in the presence of ferrous ions, Fe^{2+}_{aq}.[33] Although not included in our mechanism, we do not expect the photolysis of H_2O_{2aq} to be significant. The photons are produced by the short discharge and active afterglow which terminates before large amounts of H_2O_{2aq} are formed. However, it may be that in a pulse-periodic steady state, photolysis of H_2O_{2aq} is important. In the H_2O_{2aq} decomposition by Fe^{2+}_{aq}, (the Fenton reaction), OH_{aq} and OH^-_{aq} are produced, and the ferrous ion becomes a ferric ions, Fe^{3+}_{aq}. In our mechanism we have not included ferrous or ferric ions, however, blood and blood serum do contain ferrous ions which are responsible for transport of oxygen.[10] In the case of treating blood or blood serum in a wound, it is possible that H_2O_{2aq} diffuses deeply into the liquid layer where it subsequently dissociates into OH_{aq} by reacting with ferrous ions. The relative proportion of Fe^{2+}_{aq} in blood serum is small compared to blood, and so in water-like liquid layers in the absence of hydrocarbons, the rate of decomposition of H_2O_{2aq} is likely small.

O_3 is another powerful oxidizing agent, which is known for bacterial killing and has been correlated with the biocidal properties of PAW generated by a remote plasma.[34] O_3 has a oxidizing potential of 2.07 eV. When dissolved, O_{3aq} can react with and oxidize organic compounds either directly or via radical intermediates such as OH. The densities of O and O_3 in the gas phase are shown in Fig. 4.6 from the end of the discharge pulse to the end of the first

afterglow period. The densities of HO_{2aq} and O_{3aq} are also shown at times during the afterglow periods. O is dominantly produced in the gas phase during the current pulse by dissociation of O_2 by direct electron impact and by excitation transfer from $N_2(A)$. The O density peaks to 1.5×10^{15} cm^{-3} at 3 μs and quickly decays to 7.3×10^{13} cm^{-3} at 30 μs. The majority of O is consumed in the formation of O_3 in the afterglow and is regenerated by the next discharge pulse.

In the absence of hydrocarbons in the gas phase, O_3 is long lived and accumulates on a pulse-to-pulse basis, up to 6×10^{14} cm^{-3} at 23 ms. This accumulation enables O_3 to diffuse into water and be solvated. Although water is less likely to absorb as much O_3 as H_2O_2 due to the smaller Henry's law constant (0.3) for O_3, its larger density and continuous flux incident onto the surface of the water results in a large density of O_{3aq}. As shown in Fig. 4.6, the O_{3aq} reaches a maximum density of 10^{17} cm^{-3} (1.6×10^{-4} M) larger than the density of H_2O_{2aq}. This large density of O_{3aq} is consistent with rapid rates of ozonation of water by remote plasmas and their subsequent role in bacteria killing.[34] The rate of solvation of O atoms is negligible compared to O_{3aq} due to the consumption of O atoms in the gas phase to make O_3, and there is a negligible production of O_{aq} due to dissociation of H_2O_{aq}. To produce O_{aq} from H_2O_{aq} through either photo-dissociation or electron impact dissociation requires an energy larger than 13.5 eV.[35] As a result, O_{3aq} in liquid water results dominantly from the diffusion of O_3 from the gas phase. In the absence of hydrocarbons, O_{3aq} is a terminal species and will reach the underlying tissue. Due to its nearly exclusive gas phase source and low reactivity in the water, the solvation and transport of O_{3aq} is much the same for both direct and indirect plasma sources.

HO_{2aq}, shown in Fig. 4.6, is dominantly formed at the top of the water layer by H_{aq} combining with dissolved O_{2aq}. The production of H_{aq} is nearly the same as the OH_{aq}, as the production of both are dominated by the dissociation of H_2O_{aq}, with secondary sources by diffusion of H and OH from the gas phase. The dissociation of H_2O_{aq} is largely due to photo-dissociation at the top of the water layer. Unlike terminal species such as O_{3aq}, HO_{2aq} is a transient species. It is consumed by hydrolyzing into $H_3O^+_{aq}$ and $O_2^-{}_{aq}$, or assisting NO_{aq} to form HNO_{3aq}. The maximum density of HO_{2aq} is 2×10^{15} cm^{-3} (3.3×10^{-6} M). In water layers in contact with air discharges, there can be a large enough density of NO_{aq} that HO_{2aq} is more consumed by the formation of HNO_{3aq} than by hydrolysis. In remote plasma jets where the fluxes of NO into the water may be low, HO_{2aq} will instead hydrolyze and be an important source of $H_3O^+_{aq}$.

The nitrogen oxide chemistry in the water is, for all practical purposes, initiated by gas phase species diffusion into the water as there is few native nitrogen containing species in the water, at least for our conditions. The density of dissolved nitrogen oxide species initially in the water is typically small. There are a variety of nitrogen oxide species (e.g., NO, NO_2, N_2O, N_2O_3, N_2O_4, N_2O_5) produced in the gas discharge, which is initiated by the formation of NO. The densities of a selection of these species are shown in Fig. 4.7. NO dominates the nitrogen oxide species and is mainly produced in the afterglow. The inventory accumulates during each pulse. Its maximum density increases from 5×10^{13} cm^{-3} at 3 ms to 8×10^{13} cm^{-3} at 23 ms. Like O_3, multiple pulses significantly increase the NO density in gas phase. N_xO_y, nitrogen species other than NO (e.g., NO_2, N_2O, N_2O_3, N_2O_4, N_2O_5), also follows a similar trend of accumulating pulse to pulse but in general have densities smaller than NO by a factor of 100. The density of N_xO_y increases from 2×10^{11} cm^{-3} at 3 ms to 5×10^{11} cm^{-3} at 23 ms. Since N_xO_y originates from the reaction of NO and O_2, the accumulation of NO during each pulse produces a significant increment of N_xO_y.

As the OH density increases with successive pulse due to dissociation of water, reactions with of NO and NO_2 produce HNO_2, HNO_3 and HOONO, producing maximum densities above the water of 8×10^{12} cm^{-3}, 9×10^{11} cm^{-3} and 4×10^{11} cm^{-3} at 23 ms. The peroxynitrous acid, HOONO, is produced through reactions of NO_2 + OH and NO + HO_2. Both OH and HO_2 originate with H_2O, so the maximum density of HOONO is close to the water surface where the water vapor density is higher. The same formation process applies to HNO_2 and HNO_3, shown as HNO_x in Fig. 4.7. The densities of other nitrogen oxide species are low. All of these species diffuse into the water, and hydrolyze. The absorption and solvation processes of acid species (e.g., HNO_2 and HNO_3) from gas phase into the water are more rapid than for N_xO_y, (e.g., NO and NO_2). As a result, the formation of aqueous acid species can be correlated to gas phase acid formation.

The peroxynitrite $ONOO^-_{aq}$ is toxic to cells due to its higher oxidizing potential and its ability to diffuse through several cell diameters and cell walls before reacting.[36-38] It is also able to initiate lipid peroxidation, causing cell wall damage.[36-38] Its conjugate acid, peroxynitrous acid, HOONO can also react with biological molecules through various mechanisms.[39] Although the production of peroxynitrous acid in liquid is well known, its production in the gas phase is not clear. Atkinson *et al* [40] suggested that the production of

HOONO in the gas phase cannot be ignored and Wennberg *et al* [41] has made spectroscopic observations of gas-phase HOONO. Both HNO_3 and HOONO are likely produced in the gas phase by reactions of NO_2 with OH, and NO with HO_2 as discussed above.[42-44] When OH reacts with the O atom in ONO (the same as NO_2 but representing the molecular structure), the linear molecule HOONO is produced. When OH reacts with the N atom in ONO, the nonlinear HNO_3 is produced. HOO (the same as HO_2 but representing its molecular structure) also has a linear molecular structure and is more likely to bond with the O atom in NO to form HOONO. In order to form HNO_3, HO_2 needs to restructure itself.

In experiments [41,42], HOONO was determined by a ratio of HOONO/HNO_3, which ranges from 5% to 30%. Rate coefficients for reaction of OH and NO_2, 1.57×10^{-11} $cm^{-3}s^{-1}$; and for reaction of HO_2 and NO, 2.31×10^{-13} $cm^{-3}s^{-1}$, [43,44] produce a ratio of HOONO/HNO_3 of ≈40% in the gas phase. The production of HOONO and HNO_3 consumes a small portion of the NO and NO_2. Given the narrow gap between the DBD applicator and the surface of the water, the majority of NO, NO_2 will eventually become solvated in the water and form $HOONO_{aq}$. This solvation dominates the production of $HOONO_{aq}$. The solvation of gas phase HOONO accounts for 11% of total $HOONO_{aq}$ production given HOONO has much larger Henry's law constant, 4.8×10^6. In remote plasma treatment of water, the proportion of reactivity in the water produced by solvation of gas phase neutral species is larger than for direct plasma treatment where photons and ions make important contributions. As a result the contribution of gas phase HOONO to production of $HOONO_{aq}$ is likely more important in remote plasma treatment.

All of these nitrogen oxide species from the gas phase diffuse into the water layer and slowly convert to HNO_{xaq} (e.g., HNO_{2aq}, HNO_{3aq} and $HOONO_{aq}$). HNO_{3aq} is primarily formed through reactions of NO_{aq} with HO_{2aq} or NO_{2aq} with OH_{aq}. Note that both of these channels are sensitive to dissolved O_{2aq}, and to photodissociation that produces H_{aq} and OH_{aq},. In aqueous solution, $HOONO_{aq}$ is formed through reaction of NO_{aq} and HO_{2aq} at 3.2×10^9 $M^{-1}s^{-1}$[23] and reaction of NO_{2aq} and OH_{aq} 1.2×10^{10} $M^{-1}s^{-1}$.[23] The former reaction dominates since NO_{aq} is much larger than NO_{2aq}. We assumed that the branching ratios for the formation of HNO_{3aq} is analogous to the gas phase reactions. So the ratio of $HOONO_{aq}$ to HNO_{3aq} is also about 40%. HNO_{3aq} is also produced by the reaction NO_{2aq} + NO_{2aq} + H_2O_{aq}, however the reaction probability is small and so is not an important process.

HNO_{3aq} and $HOONO_{aq}$ quickly hydrolyze in water to form $H_3O^+_{aq}$, $NO_3^-{}_{aq}$ and $ONOO^-$

$_{aq}$. $ONOO^-_{aq}$ has a linear molecular structure and a high oxidizing potential.[36] In addition to the hydrolysis, the reaction between $O_2^-_{aq}$ and NO_{aq} nearly doubles the production of $NO_3^-_{aq}$ and $ONOO^-_{aq}$. HNO_{2aq} is mainly produced by reactions between NO_{aq} and OH_{aq}. Since both NO_{aq} and OH_{aq} have large densities in the liquid, HNO_{2aq} dominates over HNO_{3aq} and $HOONO_{aq}$. However, HNO_{2aq} is a weaker acid and only about 1% of HNO_{2aq} hydrolyzes in the water. As a result, the density of $NO_2^-_{aq}$ is large and HNO_{2aq} persists longer in water prior to hydrolyzing.

As a result of these hydrolyzing reactions, $H_3O^+_{aq}$, $NO_3^-_{aq}$ and $ONOO^-_{aq}$ are the major terminal species of RNS diffusion into the water from the gas phase. These species accumulate pulse to pulse in the liquid and eventually diffuse to the tissue. The densities $NO_3^-_{aq}$ and $ONOO^-_{aq}$ during the pulses and at the end of the terminal afterglow are shown in Fig. 4.7. At the end of the 1s afterglow, the density of $NO_3^-_{aq}$ above the tissue is 4×10^{13} cm^{-3} (6.7×10^{-8} M) and for $ONOO^-_{aq}$ is 2×10^{13} cm^{-3} (3.3×10^{-8} M).

4.3.4 pH Value of Liquid Layer

The acidification of water by plasma exposure has been observed experimentally. In experiments by Hamaguchi *et al* [20], the pH value of water decreased from 5.7 to 4.3 in 300 s by plasma jet treatment. Hamaguchi *et al* also found a critical pH of the solution, ≈4.7, below which the bactericidal effect becomes particularly strong. In experiments by Weltman *et al*[45], an indirect surface DBD was used for water treatment, resulting in a decrease of pH from 7 to less than 4 in the first 5 min of plasma treatment, followed by a slight further decrease reaching more or less stable pH values between 2 and 3 within 30 min depending on the sample volume. This acidification of water is important in bacteria killing. The experimental results by Graves *et al* [34] showed a strong antibacterial effect in non-buffered PAW and a small antibacterial effect in buffered PAW. Lukes *et al* [31] also reported that the reactivity of peroxynitrites can depend strongly on the pH value and are highly reactive under acidic conditions.

In our model, we assume that all hydronium ions are active ions, so the pH value is determined by the concentration of $H_3O^+_{aq}$. After 3 pulses, the average pH is 6 whereas after 6 pulses the average pH is 5.8. However, the hydronium ions do not increase in direct proportion to plasma treatment time. This could be due to neutralizing reactions between electrons and hydronium ions as the density of hydronium ions rise, or could be due to our treating a thin water

layer where species react with the underlying tissue. The increment of hydronium ions by successive pulse decreases and the density of hydronium appears to saturate in the long term. We can still make a rough prediction of the long term acidification. Extrapolating our results for 100 pulses, 500 ns of plasma treatment and 1 s total treatment time, the pH value could drop to as low as 4.0. For 30,000 pulses, 150 μs of plasma treatment and 5 min total treatment, the pH value can drop to 3.0, in which the water is significantly acidified. In such an acidic environment, rate coefficients in our mechanism could be altered.

4.3.5 Results Under Various Conditions

These just discussed results are sensitive to a number of factors, both environmental and geometrical. For example, the densities of H_2O_{2aq}, O_{3aq}, HO_{2aq} and $ONOO^-_{aq}$ are shown in Fig. 4.8 for the base case, when excluding photolysis reactions, when excluding dissolved O_{2aq} and when including a generic dissolved alkane hydrocarbon RH_{aq}. For plasmas which are in close proximity (physically in contact with) water, even short mean free path UV/VUV photons are incident onto the water. These photons photolyze the water with nearly unity probability, producing H_{aq} and OH_{aq}. For our conditions, production of any species that trace their origin to H_{aq} and OH_{aq} are dominated by these photolysis on short times. H_2O_{2aq} comes from the recombination of OH_{aq} and formation HO_{2aq} depends on H_{aq}. There are few other sources of H_{aq} and OH_{aq} in the water other than diffusion of their gas phase analogues into the water. So H_2O_{2aq} and HO_{2aq} are particularly sensitive to photolysis on shorter time scales and their densities decrease by 20 in the absence of photolysis. For many seconds to minutes exposure, we expect that the buildup of gas phase densities of, H, OH, and H_2O_2 and their diffusion into the water will bolster the densities of H_2O_{2aq} and HO_{2aq} in the absence of photolysis.

$ONOO^-_{aq}$ is produced through OH_{aq} reacting with NO_{2aq}, and HO_{2aq} reacting with NO_{aq}; therefore, $ONOO^-_{aq}$ is also sensitive to photolysis. However there are other sources of $ONOO^-_{aq}$. As mentioned above HOONO is produced in gas phase and then solvated in water and eventually hydrolyzed to $ONOO^-_{aq}$. The production of the precursors to HOONO in the gas phase is very sensitive to the gas humidity (not shown here) and so small changes in humidity will correlate with changes in $ONOO^-_{aq}$. The solvation of HOONO in the afterglow contributes 11% to the production of $HOONO_{aq}$. O_{3aq} is less sensitive to the absence of UV/VUV fluxes as O atoms are

not directly produced in large numbers by photolysis. O_{3aq} is generated dominantly by diffusion of O_3 from the gas phase.

When excluding O_{2aq}, the production of HO_{2aq} is severely diminished as its major source is reaction of photolysis produced H_{aq} with O_{2aq}. One unintended consequence is that large densities of H_{aq} persist in the absence of O_{2aq}. Although not overly important, these H_{aq} reduce the density of OH_{aq} by recombination. The density of $ONOO^-_{aq}$ is also reduced in the absence of O_{2aq} due to the lack of reactions between OH_{aq} and HO_{2aq}. The production of H_2O_{2aq} is not directly associated with O_{2aq}, however the large amount of otherwise slowly reacting H_{aq} recombines with OH_{aq} to reduce the feedstock reactants which form H_2O_{2aq}. Again, O_{3aq} is not affected by lack of dissolved O_{2aq} since little O_{3aq} is produced by reactions between O_{aq} and O_{2aq} – little O from the gas phase avoids forming O_3 to diffuse into the water.

The presence of dissolved hydrocarbons in the liquid, in our case a generic alkane RH_{aq} can have a major impact on ROS. These hydrocarbons are basic organic compounds that contain only carbon and hydrogen. ROS most commonly reacts with RH_{aq} by H-atom abstraction from the C-H bond to form an alkyl radical, $R\bullet_{aq}$. The reaction of ROS with RH_{aq} occurs at rates approaching EGK. For example, the reaction of OH_{aq} with simple hydrocarbons proceeds at rates of $10^7 - 10^9$ $M^{-1}s^{-1}$ ($10^{-14} - 10^{-12}$ cm^3/s).[26,27] The rate coefficients of reactions of H_2O_{2aq} and O_{3aq} with RH_{aq}, though smaller than for OH_{aq}, are significant, $10^5 - 10^8$ $M^{-1}s^{-1}$ ($10^{-16} - 10^{-13}$ cm^3/s). To provide perspective, if an ROS species has a rate coefficient of 10^7 $M^{-1}s^{-1}$ for reaction with an RH_{aq} having a density of 1 ppm (parts-per-million) in water, the reaction time is about 2 ms. So it is expected that ROS will be sensitive to even small amounts of RH_{aq}.

The densities of H_2O_{2aq}, O_{3aq} and HO_{2aq} are shown in Fig. 4.8 for 30 ppm of RH_{aq}. For all practical purposes, these species do not penetrate beyond the surface layers of the water. The reactivity that the ROS bring to the water is converted to $R\bullet_{aq}$. Of course, the precise identity of $R\bullet_{aq}$ depends on the type of RH_{aq}, and there will likely be subsequent reactions of $R\bullet_{aq}$ with other RH_{aq} and solvated species. For long chain alkanes, it is also possible that there will be multiple hydrogen abstractions from the alkane to produce multiple free radical sites. The important point is that for biological liquids where there is a significant mole fraction of hydrocarbons, the vast majority of ROS likely reacts with the dissolved hydrocarbons before reaching the underlying tissue, with the majority of that reactivity being initially converted to $R\bullet_{aq}$. In another scenario, RH_{aq} may protect against cell damage by ROS. Once generated, $R\bullet_{aq}$

has many potential outcomes. $R\bullet_{aq}$ may abstract hydrogen from a protective agent and be restored to its original state[46] or may acquire an electron from other molecules, which prominently involves diffusible thiol compounds, such as glutathione.[47] $R\bullet_{aq}$ may also combine with O_{2aq}, resulting in formation of peroxyl radical, $ROO\bullet_{aq}$. The $ROO\bullet_{aq}$ is able to react with another hydrocarbon RH_{aq} molecule to form $ROOH_{aq}$ and propagate the chain to produce another $R\bullet_{aq}$.[48] For our conditions, this reaction chain proceeds slowly on time scales beyond what was considered here. In order for ROS activity from the gas phase to directly reach the tissue, a long term plasma treatment is necessary to produce more ROS to completely consume the RH_{aq}. In our model having thin water layers, at least 30,000 pulses, a 5 minute treatment, would be needed to consume the RH_{aq}.

4.3.6 Evolution of Aqueous Species

Time-dependent densities of solvated neutral species at the surface of the water directly under the impact point of the streamer are shown in Fig. 4.9. The time axis was rescaled to be relative to the start of each discharge pulse. Charged particle densities are shown in Fig. 4.9(a). The initial fluxes of charged species into the water are electrons and water ions. All electrons striking the liquid are rapidly solvated to form e_{aq}, whose density rises in 5 ns corresponding with the avalanche time of the discharge. The density of e_{aq} rapidly drops due in large part to the attachment to dissolved O_{2aq}, which produces the increase in the density of $O_2^-{}_{aq}$. The water ions, $H_2O^+{}_{aq}$, decay slower than electrons. They react with H_2O_{aq} to form $H_3O^+{}_{aq}$ and meanwhile OH_{aq} is produced. The density of $H_3O^+{}_{aq}$ rises later than $O_2^-{}_{aq}$ but eventually reaches the same level as $O_2^-{}_{aq}$ and so the macroscopic neutrality of water layer is maintained. The densities of $NO_3^-{}_{aq}$ and $OONO^-{}_{aq}$ increase late in the afterglow of the first pulse due to the slower formation of nitrogen oxide species in gas phase during the afterglow. Following the 2nd and 3rd pulses, the long lived species $O_2^-{}_{aq}$, $H_3O^+{}_{aq}$, $NO_3^-{}_{aq}$ and $OONO^-{}_{aq}$ accumulate. During the terminal afterglow following the 3rd pulse, the densities of all species decrease due to diffusion through the water to the underlying tissue.

The densities of neutral species are shown in Fig. 4.9(b). The density of OH_{aq} has a sharp rise in 5 ns due to the photolysis of liquid water and a slow increase over many μs due to the diffusion and solvation of OH from the gas phase. The reaction of $H_2O^+{}_{aq}$ with H_2O_{aq} also

contributes about 27% to the initial rise of OH_{aq}. The mutual reaction of OH_{aq} to form H_2O_{2aq} results in the decrease of OH_{aq} and rise of H_2O_{2aq}. The density of O_{3aq} continues to rise during each pulse as the fluence of O_3 from the gas phase increases. In the absence of organic matter, O_{3aq} is relatively stable and so its density accumulates until depleted by diffusion. HO_{2aq}, is a transient agent which assists in the production of nitric and peroxynitrous acids. Although HO_{2aq} reaches a high density, it is consumed eventually through these acid forming reactions. H_{2aq} follows the same trend of H_2O_{2aq}. Because H_{aq} is consumed in the formation of HO_{2aq}, the H_{2aq} density is quite low. During the terminal afterglow, the densities of these neutral species fall due to diffusion into the water layer.

Reuter *et al* [49] reported on quantitative measurements of OH_{aq} and $O_2^-{}_{aq}$ in aqueous solution after plasma treatment. In their experiment, the OH_{aq} density is as large as 1.8 μM after a 3-min plasma treatment, then decrease to 0.25 μM in 20 hr and remains constant for 74 hr. Shown in Fig. 4.9 in our model, the OH_{aq} density at the top of the water in our model peaks at 3.2 μM and then falls to 0.01 μM after 0.1 ms. The conversion of OH_{aq} to H_2O_{2aq} in our model using conventional rate coefficients is much faster than reported in their experiment. This may be due to the DMPO/OH adduct in the experiment which traps the OH_{aq} and slows down the conversion to H_2O_{2aq}. The peak value of OH_{aq} density in our model is close to that in the experiment however, taking into account the short plasma treatment in our model, the OH_{aq} production rate is larger than that in the experiment. This is also consistent given that we are modeling direct plasma exposure of the water and the experiment is for remote exposure. Reuter *et al* [49] also measured the $O_2^-{}_{aq}$ and concluded that $O_2^-{}_{aq}$ is more stable than OH_{aq}, which is consistent with our predicted results.

The aqueous radical production channels and their relative contributions are shown in Table 4.3. These results were produced by integrating the rate of production over the entire water volume for 1 s and then normalizing to total production rate. Photodissociation is the major source to producing OH_{aq}, accounting for 39% of total production, although photodissociation lasts for only tens of ns. Charge exchange ($H_2O^+_{aq}$ reacting with H_2O_{aq}) and ion recombination ($H_3O^+_{aq}$ reacting with OH^-_{aq}) have contributions of 28% and 25%, respectively. Since $H_2O^+_{aq}$ is largely produced by photoionization, the charge exchange source of OH_{aq} traces its origin to photoionization. Therefore, the photon induced production of OH_{aq} contributes almost 70% of the total. Electron recombination (e_{aq} and $H_2O^+_{aq}$) lasts for only

several ns, and contributes 4% to production of OH_{aq}. The solvation of OH through diffusion from the gas phase contributes 3%, but lasts for milliseconds and is the dominant source during the interpulse period. Since the majority of OH in a narrow gap system will eventually be solvated in the liquid layer, the contribution to solvation depends largely on the OH density produced in gas phase. In global modeling of repetitively pulsed DBDs in humid air for similar conditions, the density of OH reaches a quasi-steady state value of 10^{12} for low power deposition [12] and 10^{13} cm^{-3} for high power deposition after tens of pulses[50], which is commensurate with the few pulse values calculated here. So for direct plasma exposure with narrow gaps, the proportion of OH_{aq} produced by direct solvation by OH is likely small. For remote plasma exposure, the solvation of OH is likely to be the dominant source of OH_{aq}.

H_2O_{2aq} is dominantly produced through the mutual reaction of OH_{aq}, 88% of the total, which is also the major sink of OH_{aq}. OH_{aq} is also consumed though reacting with NO_{aq} and NO_{2aq}. Since NO and NO_2 require milliseconds to diffuse to and solvate in the water, the majority of OH_{aq} has already converted to H_2O_{2aq}. Under quasi-steady state operation, the proportion of OH_{aq} consumed by reactions with NO_{aq} and NO_{2a} is likely higher. The reaction of H_{aq} with HO_{2aq} and solvation of H_2O_2 contribute the remaining 8% and 4%, respectively. HO_{2aq} is dominantly produced through H_{aq} reacting O_{2aq} in liquid layer, essentially 100%. Different from HO_{2aq}, O_{3aq} is produced only through gas phase solvation processes.

Aqueous RNS basically comes from the reaction of OH_{aq} and HO_{2aq} with NO_{aq} and NO_{2aq}. Solvation of HNO_2 is the major source for producing HNO_{2aq}, 40% of total production. In the gas phase, the three body reaction, NO + OH + M, produces a 10^{12} cm^{-3} of HNO_2, one order of magnitude higher than HNO_3 and HOONO. So the solvation process is significant. OH_{aq} reacting with NO_{aq}, and N_2O_{3aq} reacting with H_2O_{aq} produce 27% and 26% of HNO_{2aq}. The three body reaction, NO_{aq} + NO_{2aq} + H_2O_{aq} contributes only 10%. HNO_{3aq} and $HOONO_{aq}$ have similar production channels in which NO_{aq} reacting with HO_{2aq} dominates due to the higher density of NO_{aq} compared to NO_{2aq}. The contribution of this reaction to production of HNO_{3aq} and $HOONO_{aq}$ is 89%. Solvation of HNO_3 and HOONO both contribute 11% to the total production. A third reaction, NO_{2aq} + NO_{2aq} + H_2O_{aq}, also contributes to HNO_{3aq} production. However, this reaction is less than 1% but may become more significant in a long term when more NO_2 is produced in the gas phase and especially after HO_{2aq} is exhausted. Similar to OH_{aq} production, HNO_{3aq} and $HOONO_{aq}$ are more likely to be produced in the liquid phase rather than

by solvation.

Since HNO_{3aq} and $HOONO_{aq}$ are strong acids, they almost completely hydrolyze to ions, $NO_3^-{}_{aq}$ and $ONOO^-_{aq}$, respectively. The production channels of these ions are therefore also represented by the production channels of their conjugate acids. $NO_3^-{}_{aq}$ can also result from reaction of NO_{aq} and $O_2^-{}_{aq}$, which almost doubles its production, resulting in $NO_3^-{}_{aq}$ being the major negative ion in the liquid.

4.3.7 Fluences of Aqueous Species

In treating liquid covered tissue, it is the fluences (time integrated fluxes) of the species that transport through the liquid layer to the tissue that determine the outcome. As we have discussed, even thin layers of water over tissue can significantly reformat the character of the reactivity produced in the gas phase prior to that reactivity reaching the underlying tissue. To examine these fluences, the fluxes of selected species incident onto the underlying tissue were integrated over the discharge three pulses and the 1 s treatment time of the simulation. We represented the tissue as a lossy dielectric with which all aqueous radicals had unity reaction probability. We did not include reaction products back into the liquid. The fluences of selected charged and neutral species incident onto the surface for the base case, without photolysis, without dissolved O_{2aq} and when having 30 ppm of RH_{aq} are shown in Fig. 4.10. The majority of RNS incident onto the tissue are in the form of negative ions, dominantly $ONOO^-_{aq}$ and $NO_3^-{}_{aq}$, whose fluences exceed 10^{11} cm^{-2}. There are 10^{15} sites/cm^{-2} on, for example, a lipid layer that might cover a cell. So nearly every site on the cell would receive an RNS negative ion after a few thousand pulses. The treatment of such surfaces is therefore likely not flux limited but is rather reaction rate limited. The RNS species are not extremely sensitive to the presence of RH_{aq}. Since aqueous RNS result from diffusion of gas phase RNS into the liquid and RNS is not particularly reactive with RH_{aq}, once hydrolyzed the RNS simply diffuses through the water layer. Although HO_{2aq} can react with RH_{aq}, the reaction is very slow. HO_{2aq} is already reacted with NO_{aq} to RNS before RH_{aq} takes action. The RNS is sensitive to lack of UV/VUV photons and the presence of O_{2aq}. Since HO_{2aq} is a precursor to $HOONO_{aq}$ which then quickly hydrolyzes, the fluences of RNS negative ions are reduced in the absence of UV/VUV photons or O_{2aq}. $H_3O^+_{aq}$ is similarly insensitive to these variations since its production is supported by the

hydrolysis of $HNO_{xaq,}$.

With the exception of O_{3aq}, the fluences of ROS are sensitive to all variables. The fluences of ROS after 3 discharge pulses and 1 s afterglow are generally 10^{10}-10^{11} cm^{-2}, similar to RNS. Photolysis, which produces OH_{aq}, is an initiator of reactions which result in H_2O_{2aq} and HO_{2aq}, and so the absence of photolysis decreases the fluences of these species by more than a factor of 10. The absence of O_{2aq} most directly affects the fluences of HO_{2aq}, reducing its fluence by a factor of 200. The fluence of H_{aq} has the opposite trend, increasing in the absence of O_{2aq} due to lack of the reaction that produces HO_{2aq}. H_{aq} further recombines with H_2O_{2aq} and reduces H_2O_{2aq} fluences. Meanwhile, the fluence of OH_{aq} is compensated since the recombination produces OH_{aq}. But the sum of the fluence OH_{aq} and H_2O_{2aq} is reduced. The fluence of O_{3aq}, 10^{13} cm^{-2}, is the largest of any ROS or RNS by a factor of nearly 100 and is nearly insensitive to the absence of photolysis or O_{2aq}, since O_{3aq} originates from the diffusion of O_3 into the liquid. So even if the reactivity of O_{3aq} with the underlying tissue is a small fraction that of other ROS or RNS, its large fluence may enable significant influence.

The largest uncertainty in this analysis is the influence of RH_{aq}. When including 30 ppm of $RH_{aq,}$ essentially all ROS reactivity is converted to $R\bullet_{aq}$, whose fluence to the tissue exceeds 10^{13} cm^{-2}. Biological fluids have orders of magnitude more organic material in the liquid than used in this analysis. The reaction sequences with RH_{aq} forming $R\bullet_{aq}$ initiated by solvated ROS are likely as important as the form of the ROS that is incidence onto the liquid from the gas phase. In our previous discussion, we predict that a 5 min plasma treatment is necessary for ROS to *burn through* the RH_{aq}. Here we assume that in the reaction with ROS only one H atom is abstracted from RH_{aq}, but actually RH_{aq} could have multiple H atoms abstracted, resulting in more consumption of ROS. In this scenario, it would be difficult for the plasma produced ROS to reach the underlying tissue. Again, it would be $R\bullet_{aq}$ that reaches the underlying tissue in the interim.

Fluences to the underlying tissue are shown in Fig. 4.11 for thicknesses of the liquid layer of 50 μm to 400 μm but otherwise the base case conditions. The post-discharge integration times were chosen to be sufficiently long that the majority of radicals reached the underlying tissue regardless of thickness. In DBDs, the liquid layer serves as a dielectric which is in series with the applicator dielectric. From 50 μm to 400 μm, the capacitance of the water layer decreases, but overall the change in radical production is not large. The changes in fluence to the

tissue are dominantly attributed to reactions in the liquid layer.

The fluence of OH_{aq} decreases from 2.7×10^{9} cm^{-2} for the 50 μm layer to 1×10^{8} cm^{-2} for the 400 μm layer. OH_{aq} is produced mainly at the top surface of the liquid layer and quickly converts to H_2O_{2aq}. For the 50 μm liquid layer, a significant amount of OH_{aq} can reach the underlying tissue before the conversion to H_2O_{2aq}, while OH_{aq} is nearly completely converted for the thicker 400 μm layer. In the thicker layer, OH_{aq} is also more likely to be consumed by NO_{aq}. The fluence of H_2O_{2aq} decrease slightly from 2.8×10^{11} cm^{-2} in 200 μm liquid layer to 2.6×10^{11} cm^{-2} in 50 μm liquid layer due to the loss of OH_{aq}. The fluence of H_2O_{2aq} in 400 μm layer, 2.5×10^{11} cm^{-2}, is also slightly smaller than the 200 μm layer due to H_2O_{2aq} reacting with H_{aq}. However, these differences are small. The reaction of H_{aq} and H_2O_{2aq} produces OH_{aq}, which compensates for other OH_{aq} losses. The fluences of HO_{2aq} decrease from 9.2×10^{9} cm^{-2} to 2.2×10^{9} cm^{-2} with an increase of layer thickness. HO_{2aq} tends to slowly hydrolyze and react with NO_{aq} so a thicker water layer provides more opportunity for HO_{2aq} to react through these channels before reaching the tissue. The fluence of H_{aq} decreases from 2.2×10^{9} cm^{-2} to 4×10^{7} cm^{-2} with increasing layer thickness due to its conversion to H_{2aq} and reaction with H_2O_{2aq}. Since O_{3aq} is only produced through solvation and, in the absence of RH_{aq}, has few reactions in the water, its fluence is basically the same for all thicknesses, 6.7×10^{12} cm^{-2}. The small differences are attributed to differences in O_3 production in the gas phase.

The fluences of $H_3O^{+}_{aq}$, $O_3^{-}{}_{aq}$ and $ONOO^{-}_{aq}$ are nearly the same for different thicknesses of the water layer, about 3×10^{11} cm^{-2}, 1.5×10^{10} cm^{-2}, 8×10^{10} cm^{-2}, respectively. In the absence of RH_{aq}, these ions are quite stable in the liquid. The small differences in $ONOO^{-}_{aq}$, decreasing with decreasing thickness, are attributed to OH_{aq}, which is a precursor producing $ONOO^{-}_{aq}$. In the thinner liquid layer, OH_{aq} is consumed by the underlying tissue so the fluences of $ONOO^{-}_{aq}$ decrease. $O_3^{-}{}_{aq}$ is produced by reaction of O_{2aq} and O^{-}_{aq}, in which O^{-}_{aq} traces its origin to OH_{aq}. So the small differences in $O_3^{-}{}_{aq}$ are also attributed to the consumption of OH_{aq}. An increase in the thickness of the water layer extends the residence time of radicals before reaching the underlying tissue. The fluence of $O_2^{-}{}_{aq}$ decreases and the fluence of $NO_3^{-}{}_{aq}$ increases with increasing thickness. During the longer residence time, NO_{aq} is continually refreshed by solvation from the gas phase while $O_2^{-}{}_{aq}$ reacts with NO_{aq} to produce $NO_3^{-}{}_{aq}$. With thin liquid layers, the majority of $O_2^{-}{}_{aq}$ reaches the tissue before sufficient NO_{aq} is solvated to

react with it.

4.4 Concluding Remarks

DBDs in contact with water and radical production mechanisms in the adjacent water layers overlying tissue were discussed using results from a computational investigation. The discharges were operated at -18 kV with 3 pulses followed by a 1-20 s afterglows. Water evaporation from the liquid layer was taken into account and significantly enhances the OH and H_2O_2 production in the gas phase. Plasma produced species, especially neutral ROS and RNS, diffuse onto the water surface and are quickly solvated as determined by Henry's law constants. In some cases, solvated species are determined dominantly by gas phase processes. For example, O_3 is dominantly produced in gas phase and diffuses into the liquid to become aqueous ozone. Through either charge exchange or attachment processes, charged species, including electrons, eventually become $O_2^-{}_{aq}$, $NO_3^-{}_{aq}$ and $H_3O^+{}_{aq}$, which are terminal species and dominate the aqueous ions in the water. UV/VUV radiation from the DBD filaments produces photoionization and photodissociation of water at the liquid surface, and plays a significant role in producing OH radicals and hydrogen atoms, which are responsible for initiating many reactions in the water. Species such as H_2O_{2aq} and HO_{2aq}, which trace their origin to OH_{aq} and H_{aq}, are strongly affected by photolysis. By blocking UV /VUV photons, the densities of these species are reduced by more than 50%. These observations are consistent with measurements by Tresp and Reuter who have shown that VUV illumination of buffered solution during plasma jet exposure can produce significant quantities of OH and O_2^- through photolysis, and in some cases dominate production.[51] Dissolved O_{2aq} aids in the production of ROS as well as $NO_3^-{}_{aq}$ and $ONOO^-{}_{aq}$. Formation of HO_{2aq} relies on O_{2aq} combining with H_{aq}. $O_2^-{}_{aq}$, formed by attachment by O_{2aq} from solvated electrons, is a precursor to $NO_3^-{}_{aq}$ and $ONOO^-{}_{aq}$.

In the absence of dissolved hydrocarbons, the dominant ROS species reaching the underlying tissue after a few seconds are H_2O_{2aq} and O_{3aq}. RNS fluences are dominated by $NO_3^-{}_{aq}$ and $ONOO^-{}_{aq}$. The ROS fluences are sensitive to dissolved hydrocarbons. A significant RH_{aq} density will consume most ROS, converting their reactivity to a fluence of $R\bullet_{aq}$ (alkyl radical) to the underlying tissue. RNS are less affected by RH_{aq}. These fluences are also affected by the thickness of the liquid layer, which determines the residence time of radicals in the liquid. For

thinner liquid layers, having shorter residence times, a significant fluence of OH_{aq} and HO_{2aq}, for example, are able to reach the underlying tissue. These species would otherwise be consumed in formation of H_2O_{2aq} and RNS ions.

In summary, this chapter focuses on understanding of interactions of DBDs with thin liquid layer. The interactions include electrical response of the liquid layer and underlying tissue, solvation of incident species, aqueous reactions during the discharge and in the afterglow. The liquid layer blocks all the kinetic energies carried by incident species from reaching the underlying tissue, where only chemical reactivity is able to reach. The short-lived reactive species, like OH_{aq}, are processed by the liquid layer to long-lived reactive species, like H_2O_{2aq}, which eventually reach the tissue. The reactivity is generally reduced but the interaction duration is increased. The importance of the liquid layer is well demonstrated by the simulation.

4.5 Tables

Table 4.1 Dimensionless Henry's Law Constants for Various Species at 300 K and 1 atm.[15,16]

Species	Henry's Law Constant
OH	6.92×10^{2}
H_2O_2	1.92×10^{6}
O_3	3×10^{-1}
NO	4.4×10^{-2}
NO_2	2.8×10^{-1}
NO_3	4.15×10^{1}
N_2O_3	6×10^{2}
N_2O_4	3.69×10^{1}
N_2O_5	4.85×10^{1}
HNO_2	1.15×10^{3}
HNO_3	4.8×10^{6}
HOONO	4.8×10^{6}[a]

[a] Approximated by analogy to HNO_3.

Table 4.2 Water Reaction Mechanism.

Reaction[a]	Rate Coefficient[a]	Ref.
Solvation Reactions		
$e + H_2O_{aq} \rightarrow e_{aq} + H_2O_{aq}$	2×10^9	[22]b
$N_2^+ + H_2O_{aq} \rightarrow N_2^+{}_{aq} + H_2O_{aq}$	3×10^6	b
$N_4^+ + H_2O_{aq} \rightarrow N_4^+{}_{aq} + H_2O_{aq}$	3×10^6	b
$O_2^+ + H_2O_{aq} \rightarrow O_2^+{}_{aq} + H_2O_{aq}$	3×10^6	b
$NO^+ + H_2O_{aq} \rightarrow NO^+{}_{aq} + H_2O_{aq}$	3×10^6	b
$O^- + H_2O_{aq} \rightarrow O^-{}_{aq} + H_2O_{aq}$	3×10^6	b
$O_2^- + H_2O_{aq} \rightarrow O_2^-{}_{aq} + H_2O_{aq}$	3×10^6	b
$H^+ + H_2O_{aq} \rightarrow H_3O^+{}_{aq}$	3×10^6	b
$H_3O^+ + H_2O_{aq} \rightarrow H_3O^+{}_{aq} + H_2O_{aq}$	3×10^6	b
$H_5O_2^+ + H_2O_{aq} \rightarrow H_3O^+{}_{aq} + H_2O_{aq} + H_2O_{aq}$	3×10^6	b
$O + H_2O_{aq} \rightarrow O_{aq} + H_2O_{aq}$	3×10^6	b
$O_3 + H_2O_{aq} \rightarrow O_{3aq} + H_2O_{aq}$	3×10^6	b
$H + H_2O_{aq} \rightarrow H_{aq} + H_2O_{aq}$	3×10^6	b
$H_2 + H_2O_{aq} \rightarrow H_{2aq} + H_2O_{aq}$	3×10^6	b
$HO_2 + H_2O_{aq} \rightarrow HO_{2aq} + H_2O_{aq}$	3×10^6	b
$OH + H_2O_{aq} \rightarrow OH_{aq} + H_2O_{aq}$	3×10^6	b
$H_2O_2 + H_2O_{aq} \rightarrow H_2O_{2aq} + H_2O_{aq}$	3×10^6	b
$NO + H_2O_{aq} \rightarrow NO_{aq} + H_2O_{aq}$	3×10^6	b
$N_xO_y + H_2O_{aq} \rightarrow N_xO_{y\,aq} + H_2O_{aq}$	3×10^6	b
N_xO_y = NO_2, NO_3, N_2O_3, N_2O_4 and N_2O_5		
$HNO_x + H_2O_{aq} \rightarrow HNO_{xaq} + H_2O_{aq}$	3×10^6	b
HNO_x = HNO_2 and HNO_3		
$HOONO + H_2O_{aq} \rightarrow HOONO_{aq} + H_2O_{aq}$	3×10^6	b
In Water Reactions		
$e_{aq} + H_2O_{aq} \rightarrow H\bullet_{aq} + OH^-{}_{aq}$	1.9×10^1	[21]
$e_{aq} + H_2O^+{}_{aq} \rightarrow H\bullet_{aq} + OH_{aq}$	6×10^{11}	[21]
$e_{aq} + e^-{}_{aq} + H_2O_{aq} + H_2O_{aq} \rightarrow H_{2aq} + OH^-{}_{aq} + OH^-{}_{aq}$	1.0×10^8 $M^{-3}s^{-1}$	[21]

$e_{aq} + H\bullet_{aq} + H_2O_{aq} \rightarrow H_{2aq} + OH^-_{aq}$	2.5×10^{10} $M^{-2}s^{-1}$	[21]
$e_{aq} + \bullet OH_{aq} \rightarrow OH^-_{aq}$	3.0×10^{10}	[21]
$e_{aq} + \bullet O^-_{aq} + H_2O_{aq} \rightarrow OH^-_{aq} + OH^-_{aq}$	2.2×10^{10} $M^{-2}s^{-1}$	[21]
$e_{aq} + H_3O^+_{aq} \rightarrow H\bullet_{aq} + H_2O_{aq}$	2.3×10^{10}	[21]
$e_{aq} + H_2O_{2aq} \rightarrow \bullet OH_{aq} + OH^-_{aq}$	1.1×10^{10}	[21]
$e_{aq} + HO_2^-{}_{aq} + H_2O_{aq} \rightarrow \bullet OH_{aq} + OH^-_{aq} + OH^-_{aq}$	3.5×10^{9} $M^{-2}s^{-1}$	[21]
$e_{aq} + O_{2aq} \rightarrow O_2^-{}_{aq}$	1.9×10^{10}	[21]
$e_{aq} + O_{aq} \rightarrow O^-_{aq}$	1.9×10^{10}	[21],c
$H\bullet_{aq} + H_2O_{aq} \rightarrow H_{2aq} + \bullet OH_{aq}$	1×10^{1}	[21]
$H\bullet_{aq} + H\bullet_{aq} \rightarrow H_{2aq}$	7.5×10^{9}	[21]
$H\bullet_{aq} + \bullet OH_{aq} \rightarrow H_2O_{aq}$	7×10^{9}	[21]
$H\bullet_{aq} + OH^-_{aq} \rightarrow e_{aq} + H_2O_{aq}$	2.2×10^{7}	[21]
$H\bullet_{aq} + H_2O_{2aq} \rightarrow \bullet OH_{aq} + H_2O_{aq}$	9×10^{7}	[21]
$H_{2aq} + H_2O_{2aq} \rightarrow H\bullet_{aq} + \bullet OH_{aq} + H_2O_{aq}$	6×10^{6}	[21]c
$H\bullet_{aq} + O_{2aq} \rightarrow HO_2\bullet_{aq}$	2.1×10^{10}	[21]
$H\bullet_{aq} + HO_2\bullet_{aq} \rightarrow H_2O_{2aq}$	1×10^{10}	[21]
$O\bullet_{aq} + H_2O_{aq} \rightarrow \bullet OH_{aq} + \bullet OH_{aq}$	1.3×10^{4}	[21]c
$O\bullet_{aq} + O_{2aq} \rightarrow O_{3aq}$	3×10^{9}	[21]c
$\bullet OH_{aq} + \bullet OH_{aq} \rightarrow H_2O_{2aq}$	5.5×10^{9}	[21]
$\bullet OH_{aq} + \bullet O^-_{aq} \rightarrow HO_2^-{}_{aq}$	2×10^{10}	[21]
$\bullet OH_{aq} + H_{2aq} \rightarrow H\bullet_{aq} + H_2O_{aq}$	4.2×10^{7}	[21]
$\bullet OH_{aq} + OH^-_{aq} \rightarrow \bullet O^-_{aq} + H_2O_{aq}$	1.3×10^{10}	[21]
$\bullet OH_{aq} + HO_2\bullet_{aq} \rightarrow H_2O_{aq} + O_{2aq}$	6×10^{9}	[21]
$\bullet OH_{aq} + O_2^-{}_{aq} \rightarrow OH^-_{aq} + O_{2aq}$	8×10^{9}	[21]
$\bullet O^-_{aq} + H_2O_{aq} \rightarrow OH^-_{aq} + \bullet OH_{aq}$	1.8×10^{6}	[21]
$\bullet O^-_{aq} + H_{2aq} \rightarrow OH^-_{aq} + H\bullet_{aq}$	8.0×10^{7}	[21]
$\bullet O^-_{aq} + H_2O_{2aq} \rightarrow O_2^-{}_{aq} + H_2O_{aq}$	5×10^{8}	[21]
$\bullet O^-_{aq} + HO_2^-{}_{aq} \rightarrow O_2^-{}_{aq} + OH^-_{aq}$	4×10^{8}	[21]
$\bullet O^-_{aq} + O_{2aq} \rightarrow O_3^-{}_{aq}$	3.6×10^{9}	[21]
$\bullet O^-_{aq} + O_2^-{}_{aq} + H_2O_{aq} \rightarrow OH^-_{aq} + OH^-_{aq} + O_{2aq}$	6×10^{8} $M^{-2}s^{-1}$	[21]
$\bullet OH_{aq} + H_2O_{2aq} \rightarrow H_2O_{aq} + HO_2\bullet_{aq}$	2.7×10^{7}	[21]

$\bullet OH_{aq} + HO_2^-{}_{aq} \rightarrow OH^-_{aq} + HO_2\bullet_{aq}$	7.5×10^9	[21]
$H_2O^+_{aq} + H_2O_{aq} \rightarrow H_3O^+_{aq} + \bullet OH_{aq}$	6×10^3	[21]
$\bullet OH_{aq} + NO_2^-{}_{aq} \rightarrow OH^-_{aq} + NO_{2aq}$	1×10^{10}	[23]
$H_2O_{2aq} + NO_2^-{}_{aq} \rightarrow OONO^-_{aq} + H_2O_{aq}$	4.5×10^8	[23]
$H\bullet_{aq} + NO_2^-{}_{aq} \rightarrow OH^-_{aq} + NO_{aq}$	1.2×10^9	[23]
$\bullet O^-_{aq} + NO_2^-{}_{aq} + H_2O_{aq} \rightarrow OH^-_{aq} + OH^-_{aq} + NO_{2aq}$	3.6×10^8 $M^{-2}s^{-1}$	[23]
$NO_{aq} + NO_{aq} + O_{2aq} \rightarrow NO_{2aq} + NO_{2aq}$	2.3×10^6 $M^{-2}s^{-1}$	[23]
$NO_{aq} + NO_{2aq} + H_2O_{aq} \rightarrow HNO_{2aq} + HNO_{2aq}$	2×10^8 $M^{-2}s^{-1}$	[23]
$H\bullet_{aq} + HNO_{2aq} \rightarrow NO_{aq} + H_2O_{aq}$	4.5×10^8	[23]
$NO_{aq} + \bullet OH_{aq} \rightarrow HNO_{2aq}$	2×10^{10}	[23]
$NO_{2aq} + H\bullet_{aq} \rightarrow HNO_{2aq}$	1×10^{10}	[23]
$HNO_{3aq} + \bullet OH_{aq} \rightarrow NO_{3aq} + H_2O_{aq}$	1.2×10^8	[23]
$NO_{aq} + HO_2\bullet_{aq} \rightarrow HNO_{3aq}$	8×10^9	[23]
$NO_{2aq} + \bullet OH_{aq} \rightarrow HNO_{3aq}$	3×10^{10}	[23]
$O_2^-{}_{aq} + NO_{aq} \rightarrow NO_3^-{}_{aq}$	1.6×10^{10}	[23]
$NO_{aq} + HO_2\bullet_{aq} \rightarrow HOONO_{aq}$	3.2×10^9	[23]
$NO_{2aq} + \bullet OH_{aq} \rightarrow HOONO_{aq}$	1.2×10^{10}	[23]
$O_2^-{}_{aq} + NO_{aq} \rightarrow OONO^-_{aq}$	6.6×10^9	[23]
$H_3O^+_{aq} + OH^-_{aq} \rightarrow \bullet H_{aq} + \bullet OH_{aq} + H_2O_{aq}$	6×10^{10}	[23]
$HO_2\bullet_{aq} + H_2O_{aq} \rightarrow H_3O^+_{aq} + O_2^-{}_{aq}$	2×10^3	D
$H_3O^+_{aq} + O_2^-{}_{aq} \rightarrow HO_2\bullet_{aq} + H_2O_{aq}$	6×10^1	[24],d
$HNO_{2aq} + H_2O_{aq} \rightarrow H_3O^+_{aq} + NO_2^-{}_{aq}$	1.8×10^1	[24],d
$H_3O^+_{aq} + NO_2^-{}_{aq} \rightarrow HNO_{2aq} + H_2O_{aq}$	1.8	[24],d
$HNO_{3aq} + H_2O_{aq} \rightarrow H_3O^+_{aq} + NO_3^-{}_{aq}$	2×10^3	[24],d
$H_3O^+_{aq} + NO_3^-{}_{aq} \rightarrow HNO_{3aq} + H_2O_{aq}$	2×10^2	[24],d
$N_2O_{3aq} + H_2O_{aq} \rightarrow HNO_{2aq} + HNO_{2aq}$	1.1×10^4 $M^{-2}s^{-1}$	[23]
$N_2O_{4aq} + H_2O_{aq} \rightarrow HNO_{2aq} + HNO_{3aq}$	8×10^2 $M^{-2}s^{-1}$	[23]
$N_2O_{5aq} + H_2O_{aq} \rightarrow HNO_{3aq} + HNO_{3aq}$	1.2 $M^{-2}s^{-1}$	[23]
$NO_{2aq} + NO_{2aq} + H_2O_{aq} \rightarrow HNO_{2aq} + H_3O^+_{aq} + NO_3^-{}_{aq}$	1.5×10^8 $M^{-2}s^{-1}$	[24]
$NO_{2aq} + NO_{2aq} + H_2O_{aq} \rightarrow H_3O^+_{aq} + NO_2^-{}_{aq} + H_3O^+_{aq} + NO_3^-{}_{aq}$	5×10^7 $M^{-2}s^{-1}$	[24]

Photon Reactions

$h\nu + H_2O_{aq} \rightarrow H_3O^+_{aq} + OH^-_{aq}$	1×10^{-20} cm^2	[25],c
$h\nu + H_2O_{aq} \rightarrow H\bullet_{aq} + \bullet OH_{aq}$	1×10^{-20} cm^2	[25],c

Reactions with hydrocarbon

$\bullet OH_{aq} + RH_{aq} \rightarrow R\bullet_{aq} + H_2O_{aq}$	2.6×10^8	[26],c
$H_2O_{2aq} + RH_{aq} \rightarrow R\bullet_{aq} + \bullet OH_{aq} + H_2O_{aq}$	3×10^7	[26],c
$HO_{2aq} + RH_{aq} \rightarrow R\bullet_{aq} + H_2O_{2aq}$	3×10^4	[26],c
$O\bullet_{aq} + RH_{aq} \rightarrow R\bullet_{aq} + \bullet OH_{aq}$	6×10^6	[27],c
$O_{3aq} + RH_{aq} \rightarrow R\bullet_{aq} + \bullet OH_{aq} + O_{2aq}$	5×10^5	[27],c
$H\bullet_{aq} + RH_{aq} \rightarrow R\bullet_{aq} + H_{2aq}$	5×10^5	[26],c

a) Aqueous species have an "aq" subscript. Rate coefficients have unit of $M^{-1}s^{-1}$ ($l\bullet mole^{-1}s^{-1}$) unless noted otherwise. "•" represents a free radical.

b) The solvation rate coefficient was estimated to be faster than other liquid reactions in order to not be rate limiting.

c) Approximated by analogy.

d) The rate coefficient is estimated according to the thermodynamic hydrolysis in liquid water.

Table 4.3 Contributions of Reactions to Aqueous Radical Production

Species	Reactions	Contribution
OH_{aq}	$h\nu + H_2O_{aq} \rightarrow H\bullet_{aq} + \bullet OH_{aq}$	39%
	$H_2O^+_{aq} + H_2O_{aq} \rightarrow H_3O^+_{aq} + \bullet OH_{aq}$	28%
	$H_3O^+_{aq} + OH^-_{aq} \rightarrow \bullet H_{aq} + \bullet OH_{aq} + H_2O_{aq}$	25%
	$e_{aq} + H_2O^+_{aq} \rightarrow H\bullet_{aq} + OH_{aq}$	4%
	$OH + H_2O_{aq} \rightarrow OH_{aq} + H_2O_{aq}$	3%
	$H_{2aq} + H_2O_{2aq} \rightarrow H\bullet_{aq} + \bullet OH_{aq} + H_2O_{aq}$	1%
H_2O_{2aq}	$\bullet OH_{aq} + \bullet OH_{aq} \rightarrow H_2O_{2aq}$	88%
	$H + HO_{2aq} \rightarrow H_2O_{2aq}$	8%
	$H_2O_2 + H_2O_{aq} \rightarrow H_2O_{2aq} + H_2O_{aq}$	4%
HO_{2aq}	$H\bullet_{aq} + O_{2aq} \rightarrow HO_2\bullet_{aq}$	100%
O_{3aq}	$O_3 + H_2O_{aq} \rightarrow O_{3aq} + H_2O_{aq}$	100%
HNO_{2aq}	$HNO_2 + H_2O_{aq} \rightarrow HNO_{2aq} + H_2O_{aq}$	40%
	$NO_{aq} + \bullet OH_{aq} \rightarrow HNO_{2aq}$	27%
	$N_2O_{3aq} + H_2O_{aq} \rightarrow HNO_{2aq} + HNO_{2aq}$	26%
	$NO_{aq} + NO_{2aq} + H_2O_{aq} \rightarrow HNO_{2aq} + HNO_{2aq}$	7%
HNO_{3aq}	$NO_{aq} + HO_2\bullet_{aq} \rightarrow HNO_{3aq}$	89%
	$HNO_3 + H_2O_{aq} \rightarrow HNO_{3aq} + H_2O_{aq}$	11%
$HOONO_{aq}$	$NO_{aq} + HO_2\bullet_{aq} \rightarrow HOONO_{aq}$	89%
	$HOONO + H_2O_{aq} \rightarrow HOONO_{aq} + H_2O_{aq}$	11%

4.6 Figures

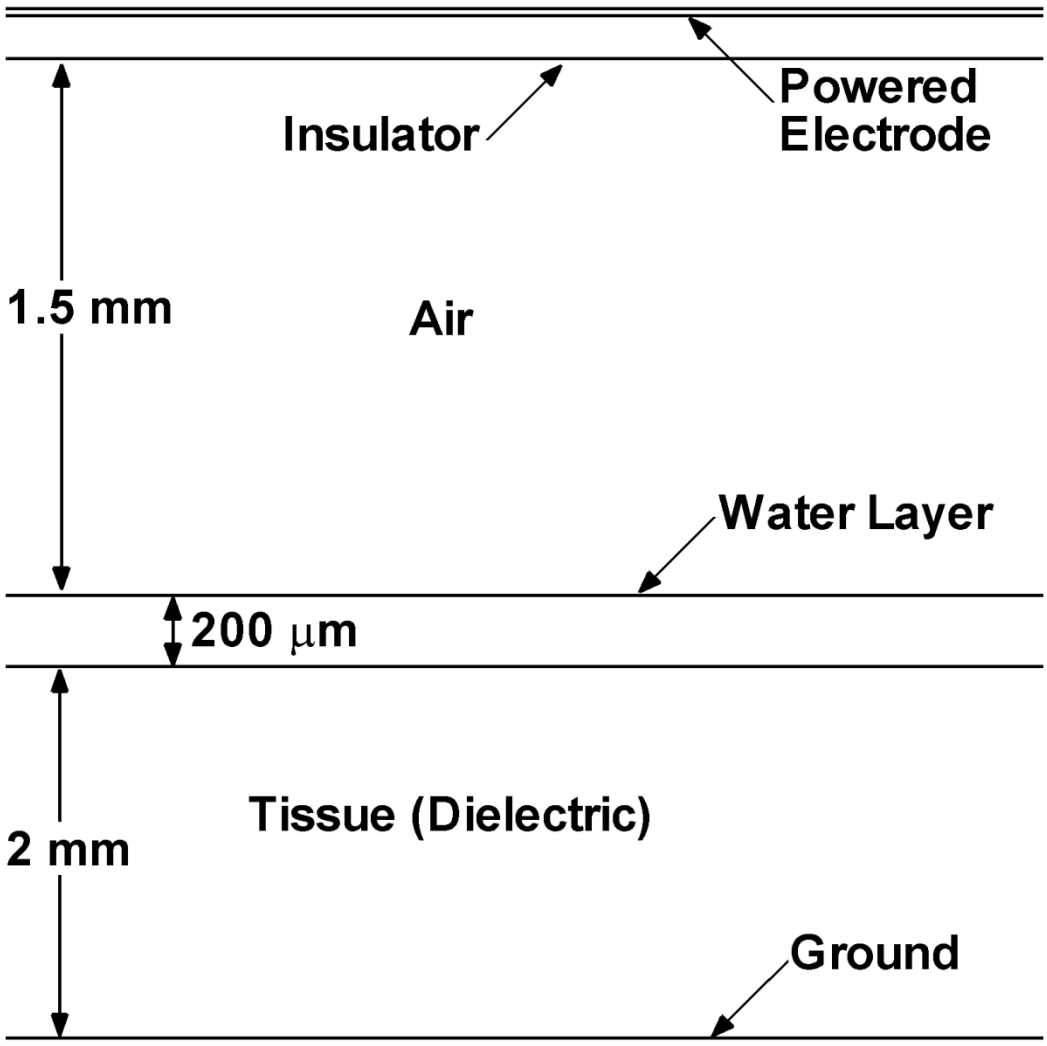

Figure 4.1 Schematic of the geometry where the plasma filament propagates. The total computational domain is 4 mm × 4 mm.

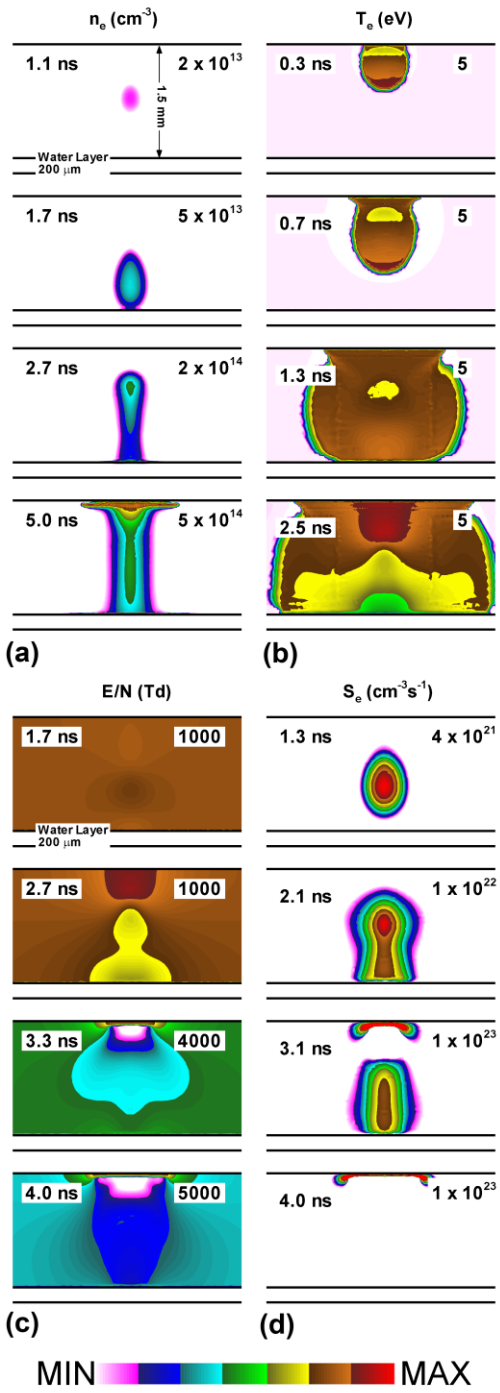

Figure 4.2 Time evolution of (a) electron density, n_e,, (b) electron temperature, T_e, (c) *E/N* (electric field/gas number density) and (d) electron impaction ionization source, S_e, for a negative discharge operated at -18kV for 5 ns over a 200 μm water layer. The gas gap and water layer are shown. The initial gas is 1 atm, $N_2/O_2/H_2O$ = 79.9/20/0.1, and water evaporates from the surface. The contours for n_e and S_e are plotted on a log scale over three decades, and for E/N over 2 decades. Maximum values shown in each frame.

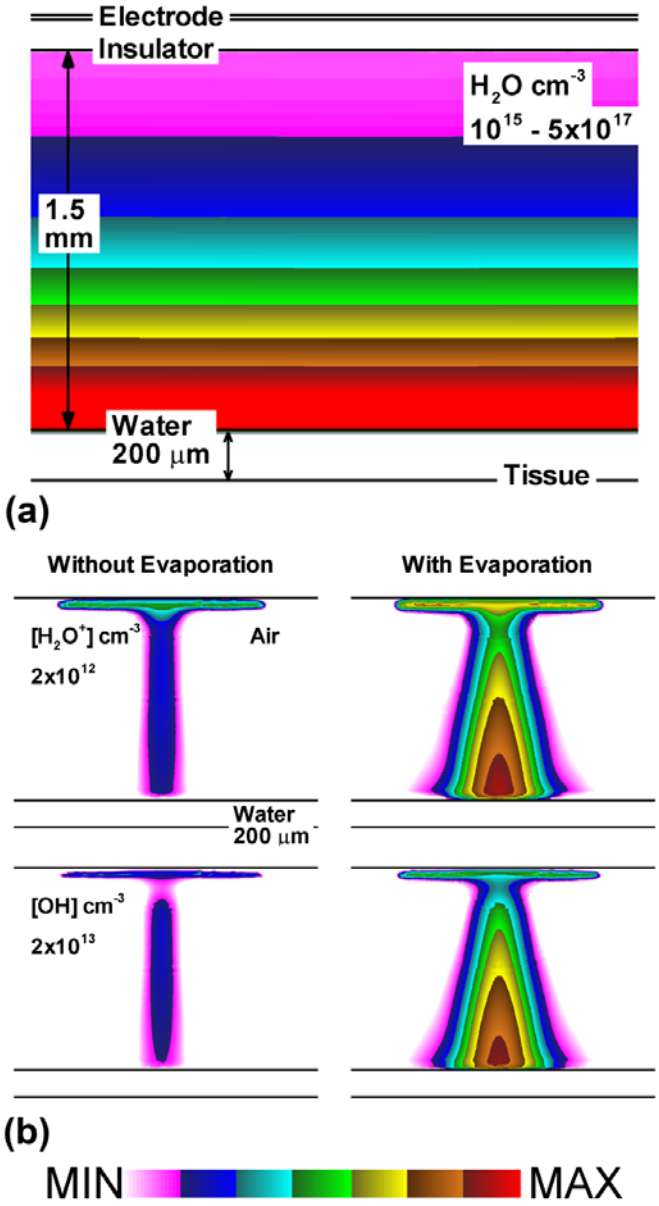

Figure 4.3 Properties due to water evaporation. (a) Density of water vapor in the gap for 10 ms evaporation. The density of the saturated water vapor at the water surface is about 3% of the ambient gases at 300 K. (b) Densities of H_2O^+ and OH in the discharge with and without evaporation. The initial gas mixture is 1 atm, $N_2/O_2/H_2O$ = 79.9/20/0.1. Contours for H_2O^+ and OH are plotted on a log scale over three decades with the maximum density shown in each frame.

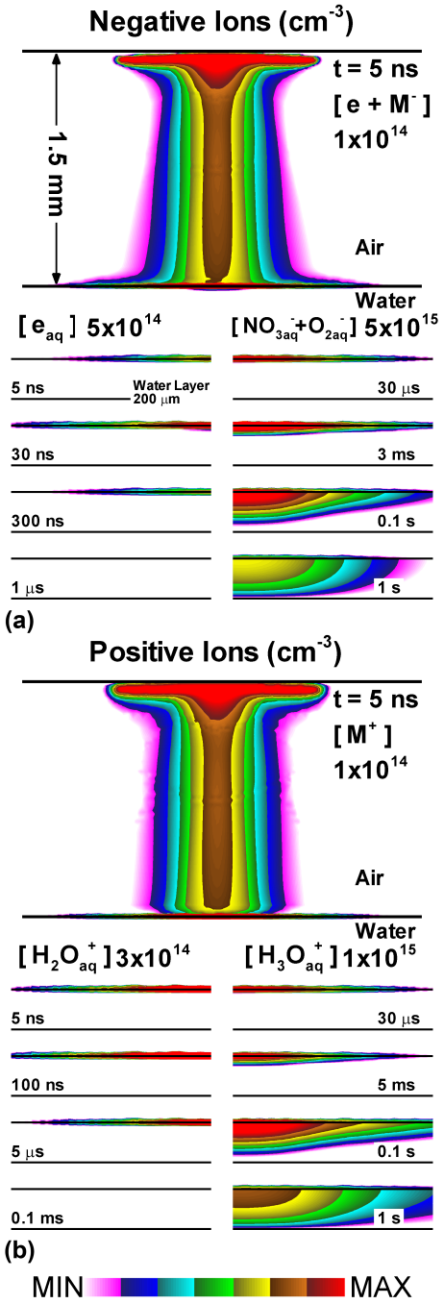

Figure 4.4 In the top of each frame is the density in the gas phase at the end of the first discharge pulse. In the bottom of each frame are time histories of ions in the 200 μm water layer a times during the three discharge pulses, interpulse afterglow and terminal afterglow. (a) Electrons and negative ions in the gas gap, and solvated $O_2^-{}_{aq}$ and $NO_3^-{}_{aq}$ in the liquid. Electrons dominate the negatively charged species in gas gap. (b) Positive ions in gas gap, and $H_2O^+{}_{aq}$ and $H_3O^+{}_{aq}$ in liquid. The contours are plotted on a 3-decade log-scale with the maximum values noted in each frame.

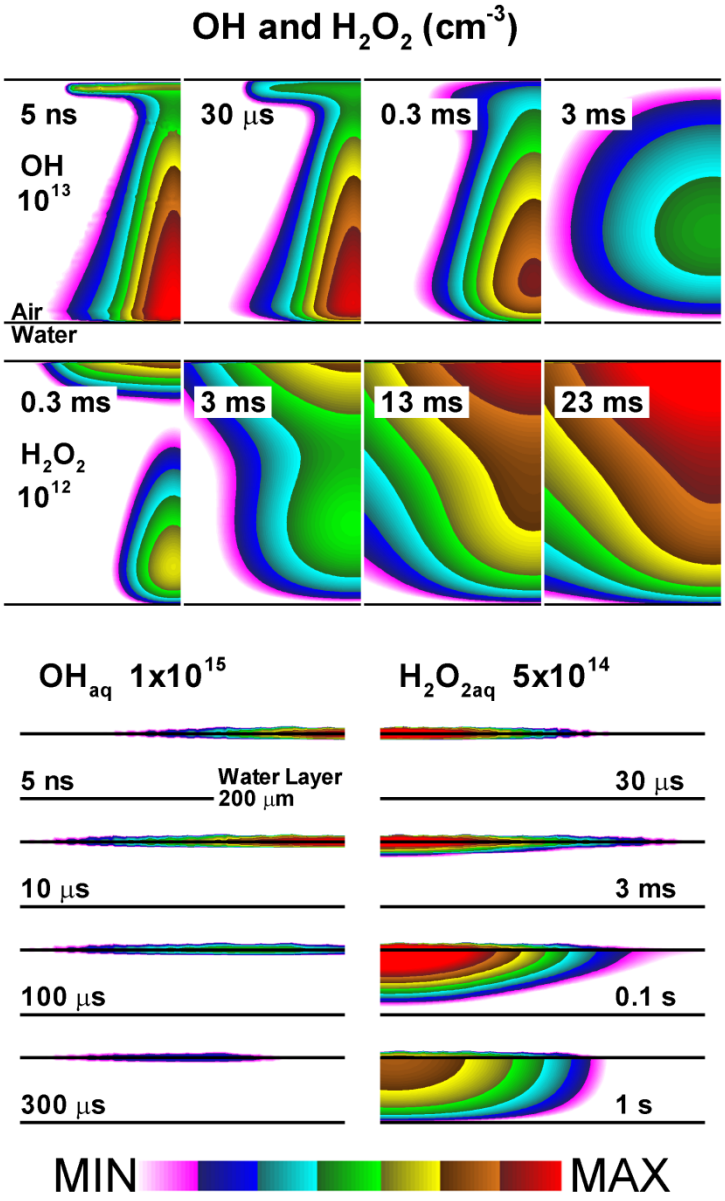

Figure 4.5 The time evolution of OH and H_2O_2 densities in the (top) gas gap and (bottom) 200 μm water layer. Densities of OH and OH_{aq} are shown during the first pulse and interpulse afterglow. H_2O_2 and H_2O_{2aq} densities are shown accumulating after each pulse (0, 100 ms, 200 ms) and during the terminal afterglow. The contours are plotted on a 3-decade log-scale with the maximum values noted in each frame.

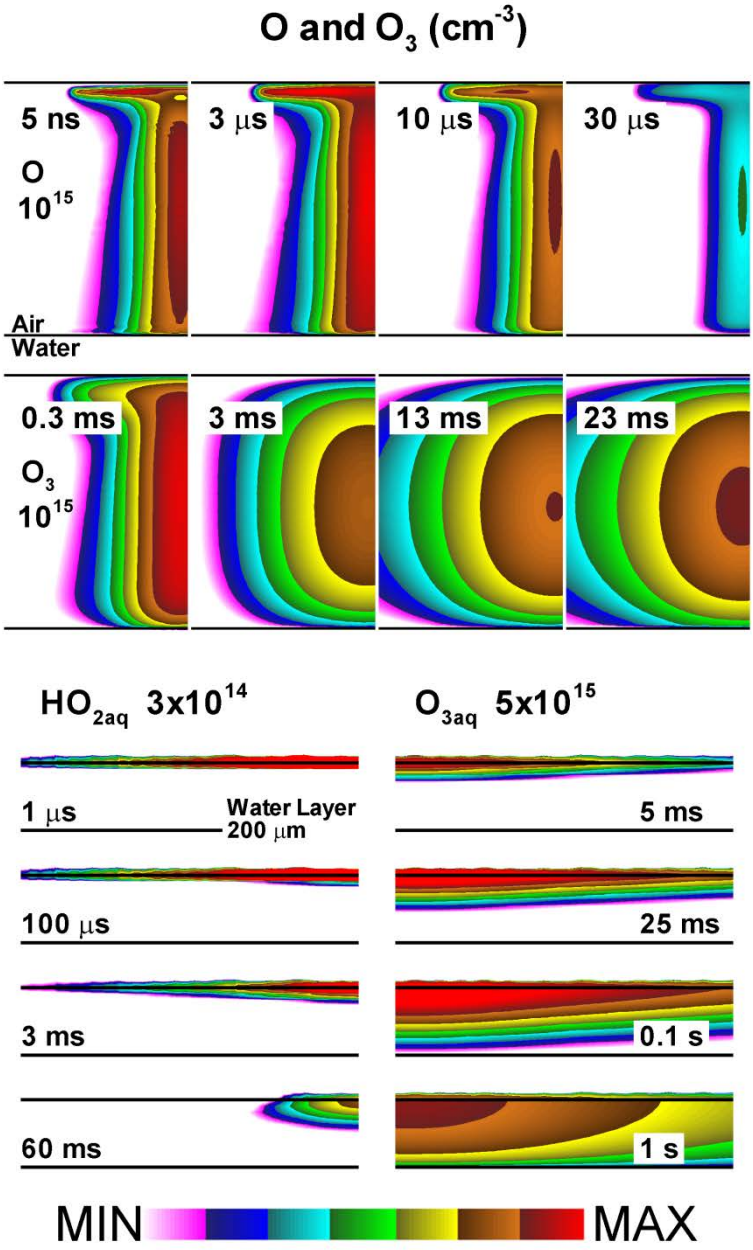

Figure 4.6 The evolution of ROS densities in the (top) gas gap and (bottom) 200 μm water layer. The O density is shown during the first pulse and interpulse afterglow. The O_3 density is shown accumulating after each pulse (0, 100 ms, 200 ms) and during the terminal afterglow.. O_{3aq} and HO_{2aq} are shown in the liquid during the discharge pulses and through the terminal afterglow. The contours are plotted on a 3-decade log-scale with the maximum values noted in each frame.

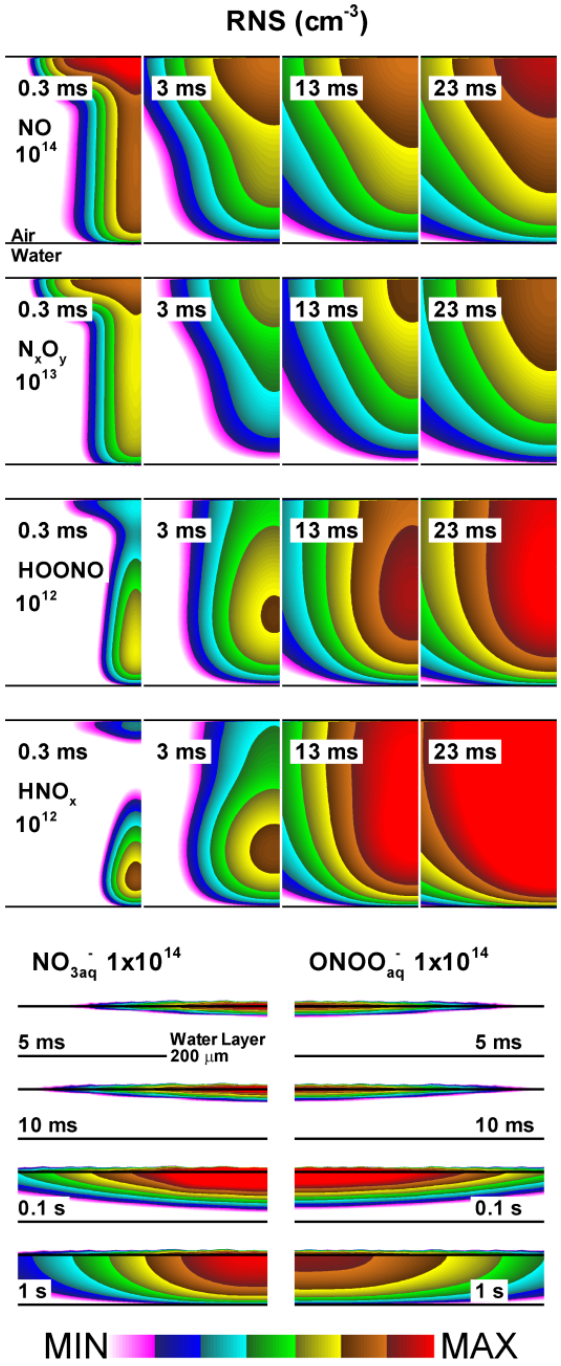

Figure 4.7 The evolution of RNS densities in the (top) gas gap and (bottom) 200 μm water layer. The densities of NO, N_xO_y, HOONO, HNO_x are shown accumulating following each of the three discharge pulses and into the terminal afterglow. In the gas phase, N_xO_y , except NO, consists of NO_2, NO_3, N_2O_3, N_2O_4 and N_2O_5; and HNO_x consists of HNO_2 and HNO_3. The contours are plotted on a 3-decade log-scale with the maximum values noted in each frame.

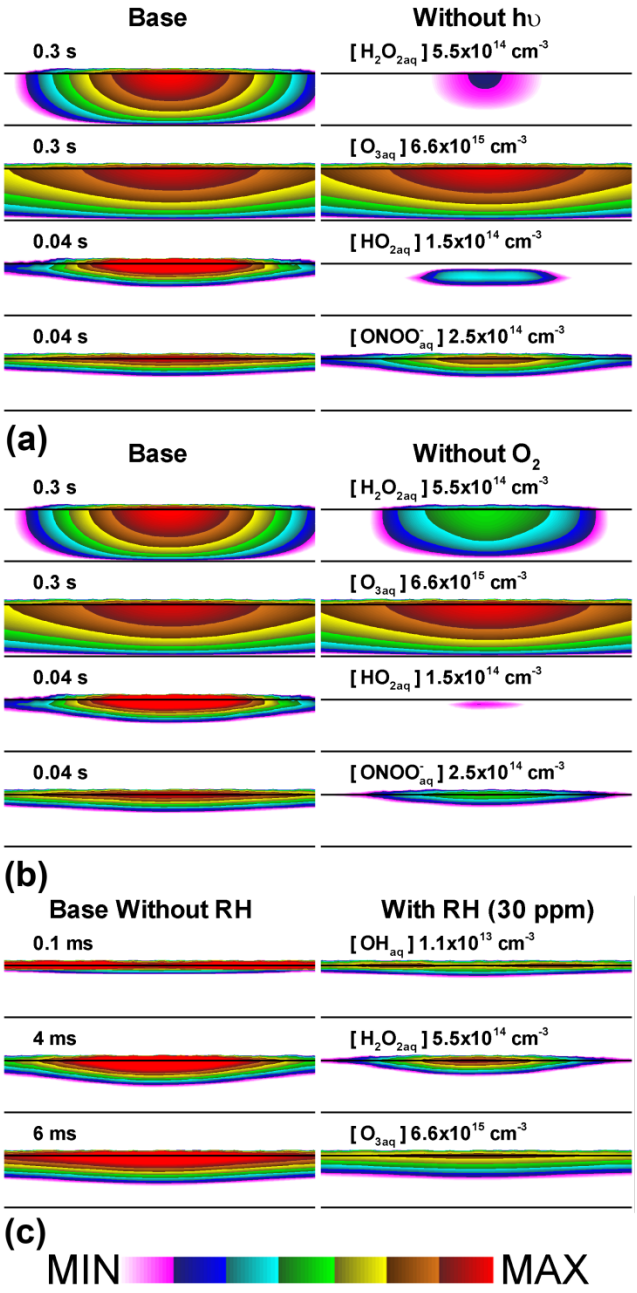

Figure 4.8 Comparison of radical densities in the 200 μm water layer under different conditions. The base case is for 3 discharge pulses at 100 Hz over water with 8 ppm O_{2aq} and with UV/VUV illumination. Densities of H_2O_{2aq}, O_{3aq}, HO_{2aq} and $ONOO^-_{aq}$ for (a) base case compared to without photon reactions in the water, and (b) Base case compared to degassed water without dissolved O_{2aq}. (c) Densities of H_2O_{2aq}, O_{3aq} and OH_{aq} for the base case without dissolved hydrocarbon RH compared to a water layer with RH of 30 ppm. The contours are plotted on a 3-decade log-scale with the maximum values noted in each frame.

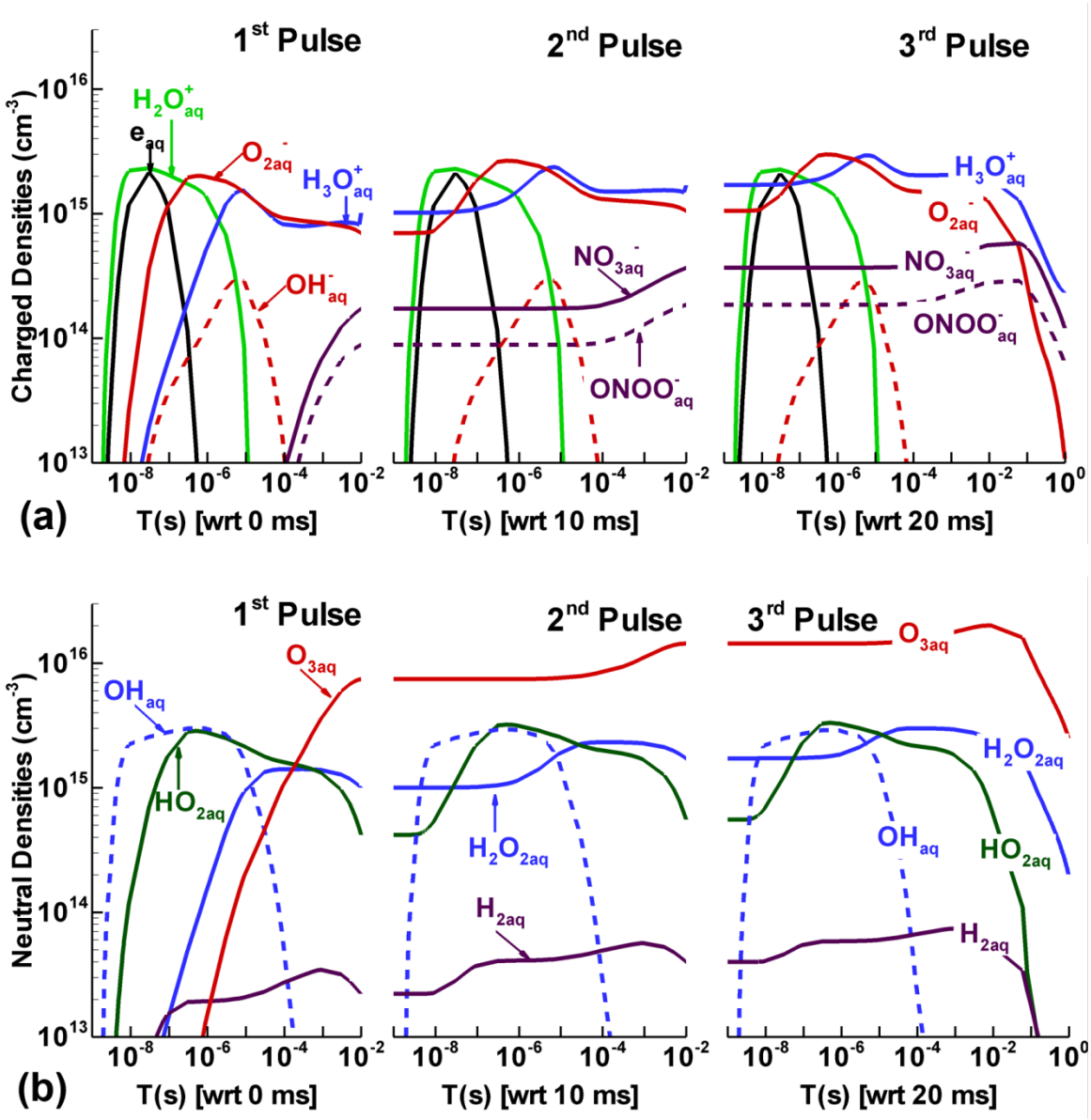

Figure 4.9 The time evolution of (a) charged and (b) neutrals densities at the top surface of the 200 μm water layer over three discharge pulses. The time axis in each plot is relative to the start of the first, second and third discharge pulse.

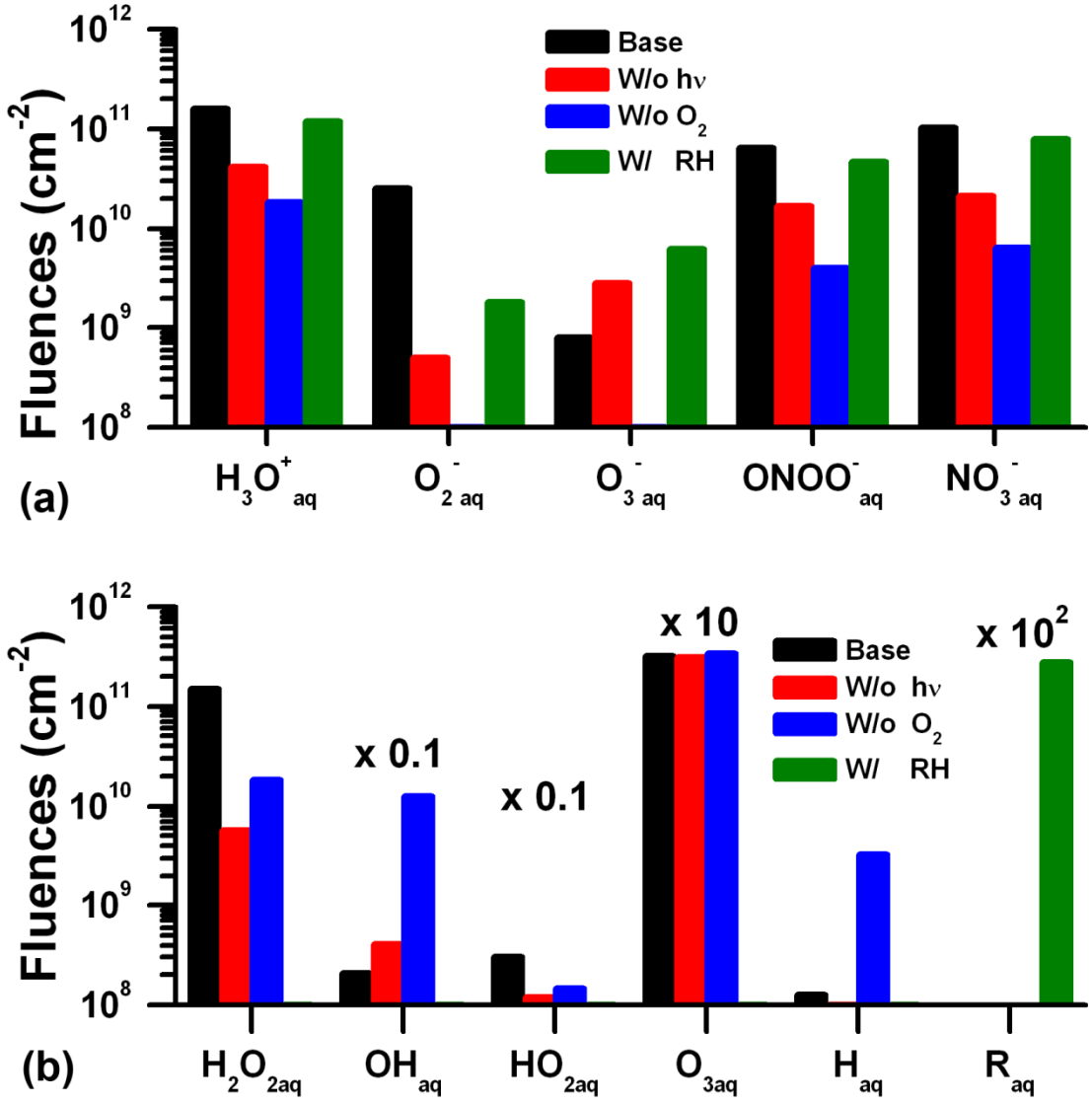

Figure 4.10 Integrated fluences of (a) charged and (b) neutral species over 1 s onto the tissue underlying the 200 μm water layer. Results are shown for the base case, without UV/VUV fluxes, without dissolved O_{2aq} and with 30 ppm RH. The ROS fluences are very sensitive to the presence of organic matter in the water.

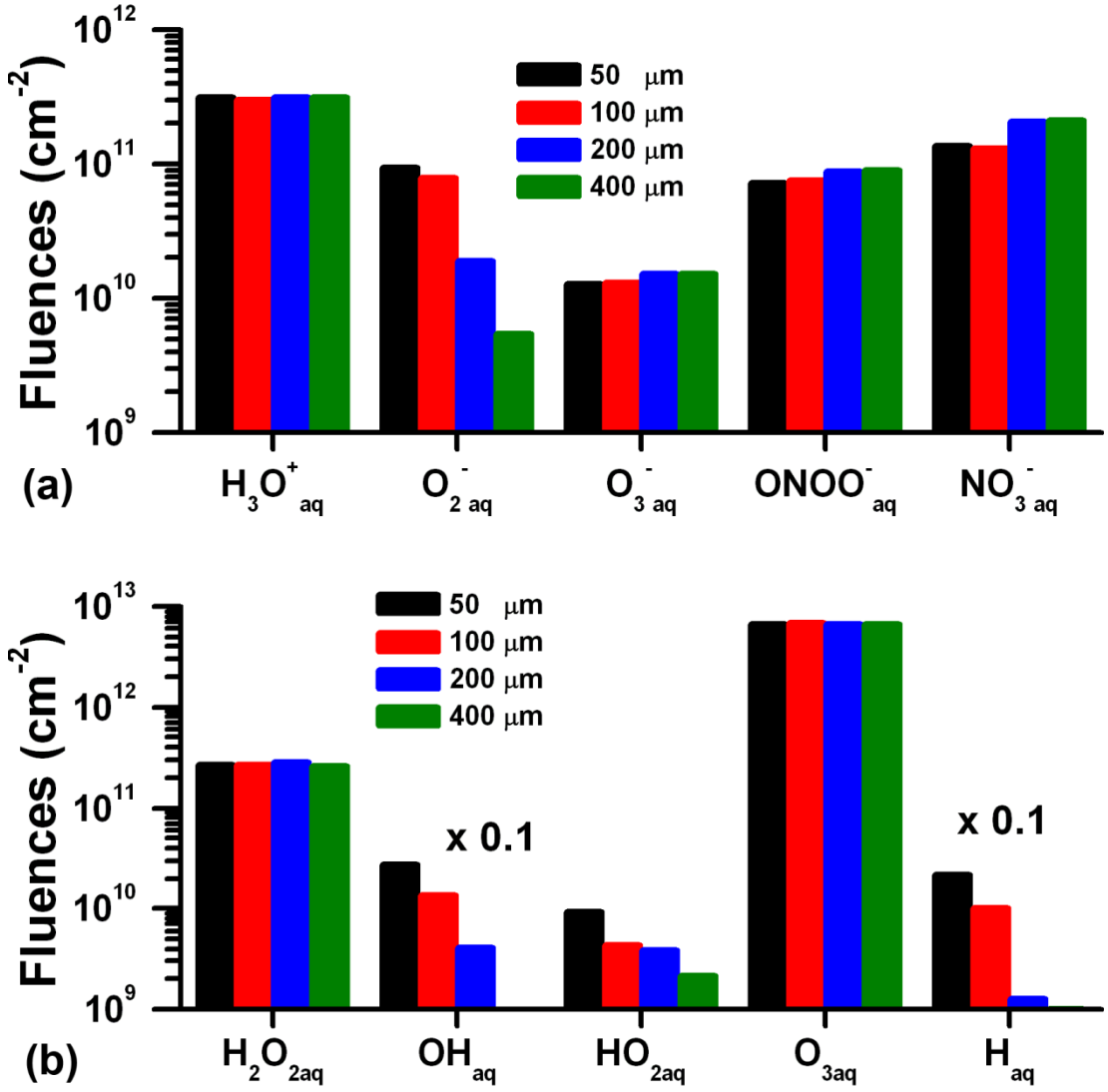

Figure 4.11 Integrated fluences of (a) charged and (b) neutral species over times up to 20 s onto the tissue underlying the water layers from 50 μm to 400 μm thick. In each case, the three discharge pulses produce nearly the same gas phase fluxes onto the top of the water layer. Species that slowly react (such as $O_2^-{}_{aq}$) are consumed in the thicker layer and so their fluences decrease with increasing thickness. Rapidly reacting species, such as OH_{aq}, reach the tissue for thin layers but not for thick layers.

4.7 References

[1] M. G. Kong, G. Kroesen, G. Morfill, T. Nosenko, T. Shimizu, J. van Dijk and J. L. Zimmermann, N. J. Phys. **11**, 115012 (2009).

[2] K.-D. Weltmann, E. Kindel, T. von Woedtke, Ma. Hähnel, M. Stieber, and R. Brandenburg, Pure Appl. Chem. **82,** 1123 (2010).

[3] G. Lloyd, G. Friedman, S. Jafri, G. Schultz, A. Fridman and K. Harding, Plasma Process. Polym. **7**, 194 (2010).

[4] G. Fridman, M. Peddinghaus, H. Ayan, A. Fridman, M. Balasubramanian, A. Gutsol, A. Brooks and G. Friedman, Plasma Chem. Plasma Process. **26**, 425 (2006).

[5] A. V. Nastuta, I. Topala, C. Grigoras, V. Pohoata and Gheorghe Popa, J. Phys. D: Appl. Phys. **44**, 105204 (2011).

[6] T. C. Montie, K. Kelly-Wintenberg and J. R. Roth, IEEE Trans. Plasma Sci. **28**, 41 (2000).

[7] M. Laroussi and T. Akan, Plasma Process. Polym. **4**, 777 (2007).

[8] S. Emmert, F. Brehmer, H. Hänßle, A. Helmke, N. Mertens, R. Ahmed, D. Simon, D. Wandke, W. Maus-Friedrichs, G. Däschlein, M. P. Schön, and W. Viöl, Clinical Plasma Medicine, **1**, (1) 24-29 (2013)

[9] G. Isbary, W. Stolz, T. Shimizu, R. Monetti, W. Bunk, H.-U. Schmidt, G. E. Morfill, T. G. Klämpfl, B. Steffes, H. M. Thomas, J. Heinlin, S. Karrer, M. Landthaler, and J. L. Zimmermann, Clinical Plasma Medicine **1** (2) 25 (2013).

[10] R. A. Rhoades and D. R. Bell, , "Medical Physiology: Principles for Clinical Medicine", (Lippincott Williams & Wilkins, Baltimore, 4th Edition, 2012), page 167-177

[11] M. J. Traylor, M. J. Pavlovich, S. Karim, P. Hait, Y. Sakiyama, D. S. Clark and D. B. Graves, J. Phys. D: Appl. Phys. **44**, 472001 (2011).

[12] Y. Sakiyama, D. B. Graves, H. Chang, T. Shimizu and G. E. Morfill, J. Phys. D: Appl. Phys. **45**, 425201 (2012).

[13] S. Ikawa, K. Kitano, S. Hamaguchi, Plasma Process. Polym. **7**, 33 (2010).

[14] G. Fridman, A. D. Brooks, M. Balasubramanian, A. Fridman, A. Gutsol, V. N. Vasilets, H. Ayan and G. Friedman, Plasma Process. Polym. **4**, 370 (2007).

[15] R. Sander, "Compilation of Henry's Law Constants for Inorganic and Organic Species of Potential Importance in Environmental Chemistry", available at "www.henrys-law.org/henry.pdf" (1999).

[16] D. Mackay and W. Y. Shiu, J. Phys. Chem. Ref. Data **10**, 1175 (1981).

[17] R. E. Skyner, J. L. McDonagh, C. R. Groom, T. van Mourik and J. B. O. Mitchell, Phys. Chem. Chem. Phys. **17**, 6174 (2015).

[18] A. Dokoumetzidis and P. Macheras, Inter. J. Pharmaceutics **321**, 1(2006)

[19] R. Parsons, Chem. Rev. **90**, 813 (1990).

[20] *NIST Thermophysical Properties of Fluid Systems*, [Online]. Available: http://webbook.nist.gov/chemistry/fluid/

[21] K. P. Maddena and S. P. Mezyka, J. Phys. Chem. Ref. Data **40**, 023103 (2011).

[22] W. J. Chase and J. W. Hunt, J. Phys. Chem. **79**, 2835 (1975).

[23] *NDRL/NIST Solution Kinetics Database*, [Online]. Available: http://kinetics.nist.gov/solution/

[24] S. N. Pandis and J. H. Seinfeld, J. Geophys. Res. **94**, 1105 (1989).

[25] R. D. Hudson, Rev. Geophys. Space Phys. **9**, 305 (1971).

[26] R. A. Cox and J. A. Cole, Combustion and flame **60**, 109 (1985).

[27] J. Hotgne and H. Bader, Water Res. **17**, 173 (1983).

[28] J. L.. Fry, S. A. Nizkorodov, M. Okumura, C. M. Roehl, J. S. Francisco and P. O. Wennberg, J. Chem. Phys. **121**, 1432 (2004).

[29] C. A. J. van Gils, S. Hofmann, B. K. H. L. Boekema, R. Brandenburg and P. J. Bruggeman, J. Phys. D: Appl. Phys. **46**, 175203 (2013).

[30] S. Hamaguchi, : AIP Conference Proceedings 1545, 214 (2013).

[31] Z. Machala, B. Tarabova, K. Hensel, E. Spetlikova, L. Sikurova and P. Lukes, Plasma Process. Polym. **10**, 649 (2013).

[32] J.L. Francea, M.D. Kinga, and J. Lee-Taylorb, Atmos. Environ. **41**, 5502 (2007).

[33] E. Neyens and J. Baeyens, J. Hazard. Mater. **98**, 33 (2003).

[34] M. J Pavlovich, H.-W. Chang, Y. Sakiyama, D. S. Clark and D. B. Graves, J. Phys. D: Appl. Phys. **46**, 145202 (2013).

[35] B. Ruscic, A. F. Wagner, L. B. Harding, R. L. Asher, D. Feller, D. A. Dixon, K. A. Peterson, Y. Song, X. Qian, C.-Y. Ng, J. Liu, W. Chen and D. W. Schwenke, J. Phys. Chem. A **106**, 2727 (2002).

[36] C. Szabó, Harry Ischiropoulos and Rafael Radi, Nat. Rev. Drug Discovery **6**, 662 (2007).

[37] P. Pacher, J. S. Beckman, and L. Liaudet, Physiol Rev **87**, 315 (2007).

[38] M. Reist, K.-A. Marshall, P. Jenner and B. Halliwell, J. Neurochem. **71**, 2431 (1998).

[39] J. D. Laskin and D. L. Laskin, “Cellular and Molecular Biology of Nitric Oxide”, CRC Press (1999).

[40] R. Atkinson, D. L. Baulch, R. A. Cox, J. N. Crowley, R. F. Hampson, R. G. Hynes, M. E. Jenkin, M. J. Rossi and J. Troe, Atmos. Chem. Phys. **4**, 1461 (2004).

[41] S. A. Nizkorodov and P. O. Wennberg, J. Phys. Chem. 106, 855 (2002).

[42] H. Hippler, S. Nasterlack and F. Striebel, Phys. Chem. Chem. Phys. **4**, 2959 (2002).

[43] D. M. Golden, J. R. Barker and L. L. Lohr, J. Phys. Chem. A **107**, 11057 (2003).

[44] R. S. Zhu and M. C. Lin, J. Chem. Phys. **119**, 10667 (2003).

[45] K. Oehmigen, M. Ha¨hnel, R. Brandenburg, Ch. Wilke, K.-D. Weltmann and Th. von Woedtke, Plasma Process. Polym. **7**, 250 (2010).

[46] N. Velpula, S. Ugrappa and S. Kodangal, Int. J. Basic Clin. Pharmacol. **2**, 677 (2013).

[47] E. Denisov, C. Chatgilialoglu, A. Shestakov and T. Denisova, Int. J. Chem. Kinet. **41**, 284 (2009).

[48] A. Fridman and G. Friedman, “Plasma Medicine” (Wiley, Oxford, 2013), page 115 – 120.

[49] H. Tresp, M. U. Hammer, J. Winter, K.-D. Weltmann and S. Reuter, J. Phys. D **46**, 435401 (2013).

[50] N. Yu. Babaeva and M. J. Kushner, J. Phys. D: Appl. Phys. **46**, 025401 (2013).

[51] H. Tresp and S. Reuter, private communication, 2013.

CHAPTER 5 LONG-TERM EFFECTS OF MULTIPLY PULSED DIELECTRIC BARRIER DISCHARGES IN AIR ON THIN WATER LAYERS OVER TISSUE: STATIONARY AND RANDOM STREAMERS

5.1 Introduction

As described in the previous chapter, dielectric barrier discharges (DBDs) in contact with wet tissue were investigated based on computation using three pulses. This approach sufficed for investigation of production mechanisms of reactive species and transport of aqueous species through the liquid layer. However, in experiments or clinical treatment, DBDs are often run for seconds to minutes consisting of 100's to 10,000's pulses or cycles.[1-3] Therefore, the biomedical outcomes depend in a large part on long-term effects such as a change of liquid characteristics[4-7], uniformity of fluences onto underlying tissue[8-12] and dose uptake by cells.[13-20]

The characteristics of the liquid layer, such as electrical conductivity and pH value are altered by long term treatment by DBDs. For example, the conductivity of distilled water was increased by 100 μS/cm after 60 minutes of discharge treatment and the discharge characteristics were found to be sensitive to changes in the conductivity of the solution.[4] Double layers can occur at the surface of conductive liquids. This affects the electric field at the surface and influences the transport of charged species into the liquid. DBD treatment usually results in a reduction of pH value in the liquid layer [5,6], although some studies [7] have reported an increase in pH value. The chemical reactivity of radicals in liquids is sensitive to these changes in pH.

Given the different potential outcomes on cells resulting from fluxes of different reactive oxygen and nitrogen species (RONS), there is a need to control the uniformity and

reproducibility of the reactive fluxes to ensure consistent treatment. A measure of reproducibility is the dose of plasma treatment, which typically refers to the time integrated fluxes of radicals, ions, photons, and electric fields that are incident onto the liquid or tissue surface.[8] To first order, the dose should scale with the total energy deposition, J/cm^2, delivered to the surface. That energy deposition is a function of the power deposition (W/cm^2), pulse power waveform (pulse length), and pulse repetition frequency (PRF). However, there are strong second order effects, such as thickness of the liquid layer and time between pulses that influence the identity of the RONS incident onto the tissue. This implies that half the energy per pulse at twice the PRF does not necessarily deliver the same fluence (time integrated fluxes) of RONS as double the energy at half the PRF. In any event, dose increases with treatment time and it is typical that few seconds to a few minutes are necessary to achieve significant bacterial sterilization.[9,10] Bruggeman and co-workers [11] measured deactivation of *P. aeruginosa* in 100 µl of saline solution as a function of treatment time. Deactivation was not observed until after 20s of treatment, with longer treatment producing a rapid increase in the rate of deactivation. Although there is selectivity between normal cells and cancer cells or bacteria in their response to RONS, exposure to a high dose of plasma can also cause normal cell death.[12]

In addition to treatment time, the dose can also spatially vary in DBDs. The DBDs are often filamentary, which in turn produce spatially non-uniform reactive species. Typical DBDs have filaments that are hundreds of microns in diameter, although DBDs excited by short voltage pulses may appear to be uniform.[13-15] The typical DBDs used in plasma treatment, using microsecond pulses or AC sine-wave voltage, are filamentary.[16-18] In conventional DBDs, self-organization of filaments can produce nearly stationary patterns of plasma filaments with lateral spacing larger than the gap size.[19,20] The spacing can be much larger than the diameter of an individual streamer. This self-organization can result in the same plasma filament striking the same location on the surface for an extended period of time. In other cases, the filaments may strike randomly, or movement of the applicator averages self-organized patterns over the surface. When treating liquid covered tissues, particularly when the thickness of the liquid is small, the spatial distribution of the filaments at the surface may have a significant effect on the spatial distribution of reactive fluences onto the underlying tissue.

In this chapter, we report on the results from a 2-dimensional computational investigation

of multiply pulsed DBDs in contact with liquid covered tissue comprised of water with dissolved O_2. A 100-pulse, 100 Hz negative discharge in humid air, and its afterglow are investigated for the plasma produced reactivity in both the gas and liquid phase. The tissue underlying the liquid is modeled as a dielectric material with no conductivity. The liquid layer is computationally treated identically to gas as a partially ionized substance, but with a higher density and a specified permittivity. The same equations (e.g., continuity, energy, radiation transport, Poisson's equation) are solved in the gas phase and the liquid phase, albeit with different species and reaction mechanisms. To investigate the variability that may occur in DBD treatment of tissue, we modelled two extreme schemes – filaments that are stationary for 100 pulses and filaments that strike random locations on the liquid surface on each pulse.

We found that different solvation rates of gas phase species result in different spatial distributions of species entering the liquid. Gas phase species formed during the discharge pulse having large Henry's law constants for solvation enter the liquid near where the filament strikes. Gas phase species requiring many reactions and having a small Henry's law constant enter the liquid in a more spatially averaged manner. The spatial overlap between these two classes of species entering the liquid then differs between fixed and random streamers. For example, NO_{aq} is produced by solvation of NO from the gas phase. NO is formed by multiple reactions and has a low Henry's law constant, and so NO_{aq} is produced fairly uniformly over the surface of the liquid. OH in the gas phase is formed by a single reaction and has a large Henry's law constant. OH_{aq} is therefore produced in close vicinity of the streamer. When both NO_{aq} and OH_{aq} enter the liquid in the same location, NO_{aq} is rapidly depleted by reactions with OH_{aq}. With randomly striking streamers, little NO_{aq} survives to reach the tissue. For stationary streamers, NO_{aq} can reach the tissue a few streamer diameters away from where the streamer strikes.

We will briefly discuss the modelling platform used in this investigation in section Sec. 4.2. In Sec. 4.3, we will discuss production of radicals and charged species in multiple pulsed DBDs, with a comparison of stationary and randomly striking streamers. Concluding remarks are presented in Sec. 4.4.

5.2 Description of the Model

In this chapter, we use the computer model, *nonPDPSIM* to investigate a DBD sustained in humid air interacting with a thin liquid layer covering an underlying tissue. The model has been described in detail in Chapter 2. The base case for the simulation addresses 100 pulses followed by 10 seconds of afterglow. In the model, the DBD dynamics of the first pulse is fully solved for 10 ns by a time integration of the continuity equations for gas phase and liquid phase species, while considering transport of these species between phases and radiation transport. For a given timestep, Poisson's equation and continuity equations are first simultaneously integrated for electric potential; and for densities of electrons and ions including surface charges. The time steps for the plasma module, including solution of the electron energy equation and photon-transport are 0.1-5 ps. Computing the electric discharge properties, while solving Poisson's equation and charged particle dynamics, is computationally intensive. A direct computation of Poisson's equation and charged particle dynamics for hundreds of pulses would be computationally prohibitive.

At the end of the first pulse, the source terms, such as the production terms for species and radiation transport, are recorded. In the interpulse period, Poisson's equation is not solved and we assume quasi-neutral conditions. For successive pulses, these source terms are introduced into the gas gap and liquid to represent the production of species by the next discharge pulse. Since the interpulse period is 10 ms (or longer) and the discharge pulse is 10 ns, these sources appear to be instantaneous on the time scale of the interpulse period even during the first fully resolved pulse. Therefore, the level of approximation by having source terms appear instantaneously in pulses after the first is not severe.

Since the same source terms are used to represent successive pulses, from a plasma dynamics perspective, the 100 discharge pulses are identical and do not reflect changes in the composition of the gas. With successive pulses, long-lived species such as O_3 and NO accumulate in the gas gap, mixing with the air. In the liquid layer, ions such as $H_3O^+_{aq}$ and $NO_3^-_{aq}$ accumulate and the liquid becomes conductive. These long-term effects could influence later discharge pulses. However, the described level of approximation is required in order to simulate the hundreds of pulses needed to achieve quasi-steady state values of species in the liquid.

The rates of solvation of plasma produced species are estimated by considering Henry's law. The estimation in detail has been already discussed in Chapter 4 and only selected species are listed in Table 5.1. The rates of solvation of gaseous species have a significant influence on the fluences onto the tissue through liquid layers. For example, the solvation rate of OH is much larger than that of NO by a factor of about 10^3. Under the stationary scheme, OH concentrates where the plasma streamer strikes, while NO spreads over the liquid surface. NO_{aq} at the center is nearly completely consumed by OH_{aq} but accumulates and reaches the underlying tissue at more distant locations. OH_{aq} is limited to the radius of the plasma streamer due to this reaction with NO_{aq}.

The complete liquid reaction mechanism was discussed in Chapter 4. A subset of the reactions is shown in Table 5.2 and is discussed here. The majority of O_{3aq} results from solvation of O_3 from the gas phase. In the liquid phase, O_{3aq} can be produced through O_{aq} reacting with dissolved O_{2aq}. However, since the flux of O atoms entering the liquid is small, little O_{aq} is produced through this channel. O_{3aq}, with an oxidation potential of 2.07 eV, eventually dominates the ROS in liquid layer after many pulses. In the gas phase, •OH is dominantly produced by electron impact dissociation of H_2O. The •OH then either solvates in the water or forms H_2O_2 through mutual reactions. In the liquid phase, $•OH_{aq}$ is also produced in significant amounts through photolysis of H_2O. As in the gas phase, H_2O_{2aq} is created through mutual reactions of $•OH_{aq}$ and is relatively stable compared to $•OH_{aq}$ in the absence of organics. H_2O_{2aq} with an oxidation potential of 1.77 eV, compared to 2.85 eV for $•OH_{aq}$, is able to survive long enough to transport through the liquid. NO is the initiating species for the formation of nitrogen oxides, N_xO_y (NO, NO_2, N_2O_3, N_2O_4 and N_2O_5), and acids, HNO_x (HNO_2 and HNO_3). Since many gas phase reactions are required to form the higher N_xO_y and HNO_x, these species solvate into the liquid during the afterglow after discharge pulses. Once in the liquid, N_xO_{yaq} either quickly reacts with OH_{aq} to form HNO_{xaq} or slowly reacts with H_2O_{aq} to form HNO_{xaq}. Nitrogen acids, HNO_{2aq} and HNO_{3aq}, will hydrolyze in the liquid and produce hydronium, $H_3O^+_{aq}$, and their conjugate ions, $NO_2^-_{aq}$ and $NO_3^-_{aq}$. Nitrous acid, HNO_{2aq}, is a weak acid and only a few percent hydrolyzes, while HNO_{3aq} is a strong acid and nearly completely hydrolyzes. With O_{3aq} in the liquid, $NO_2^-_{aq}$is slowly oxidized to $NO_3^-_{aq}$ by reactions with O_{3aq} which assists the hydrolysis of nitrous acid.

5.3 Multipulse DBDs Treatment of Wet Tissue

The Cartesian geometry used in this study is shown in Fig. 5.1, and represents a DBD sustained in humid air over liquid covered tissue. The computational domain is 6 mm × 4 mm. The powered electrode is at the top and covered by an insulator 0.12 mm thick with a dielectric constant of $\varepsilon/\varepsilon_0 = 3$. Under the insulator is a 1.5 mm gas gap filled with humid air ($N_2/O_2/H_2O$ = 79.0/20.9/0.1) at 1 atmospheric pressure. The tissue beneath the gap is treated as a lossy dielectric with dielectric constant of $\varepsilon/\varepsilon_0 = 6$ and the bottom of the tissue is in contact with a grounded metal plate. A 200 um thick liquid layer covers the tissue and is in contact with the gas. The layer consists of liquid water with a density of 3.32×10^{22} cm^{-3} and 8 ppm of pre-dissolved O_{2aq}, which is in equilibrium with the O_2 in the gas phase. The liquid is initially not conductive. However, its conductivity naturally increases during treatment as the discharges produce ions in the liquid. Reactive species reaching the underlying tissue through the liquid are uniformly consumed. An unstructured mesh is used with refinement regions along the insulator and in the liquid layer. The mesh size varies from 20 μm along the insulator and liquid surface to 50 μm in the remote gas gap. The spacing of the mesh in the liquid layer is not able to resolve double layer structures.

5.3.1 DBD Dynamics

The evolution of a DBD discharge during the first pulse is shown in Fig. 5.2, where the electron density, n_e, and electron impact ionization source, S_e, are shown. A -18 kV pulse with rise time of 0.1 ns and duration of 10 ns was applied to the powered electrode at the top of the domain. A neutral plasma (electrons and N_2^+) with a density of 10^8 cm^{-3} and diameter of 100 μm was placed adjacent to the middle of the insulator to initiate the plasma, after which the plasma self sustains by gas phase and secondary processes on the surface. The magnitude of the seed electrons does not affect the properties of the plasma streamer with a factor of 10 larger or smaller density. After applying the pulse, the negative avalanche begins from the seed electron cloud and propagates downward. At 2.5 ns, the plasma streamer with an electron density of 2×10^{13} cm^{-3} strikes the liquid layer and a restrike avalanche proceeds backwards to the upper insulator. S_e reaches 9×10^{22} $cm^{-3}s^{-1}$ at the head of the backward streamer. After 5 ns, the top

insulator is nearly full charged and a conductive channel forms across the gap. Plasma then begins to spread over the surface of the insulator. The electron density is maximum at 2×10^{14} cm^{-3} and S_e is 2×10^{23} $cm^{-3}s^{-1}$ adjacent to the insulator. The electron density at the surface of the liquid reaches 10^{14} cm^{-3}. These electrons quickly solvate into the liquid.

5.3.2 Stationary Scheme vs. Random Scheme

In pulses following the first, the source terms obtained from the fully resolved first discharge pulse are placed in the gap. As mentioned above, two extremes are discussed in this work, illustrated in Fig. 5.3, which shows the electron density in a subset of the computational domain. In the stationary scheme, the plasma streamer strikes at the same location on the surface of the liquid for all pulses. In the second scheme, the streamer randomly strikes the liquid on a pulse-to-pulse basis. The 1^{st}, 54^{th} and 88^{th} pulses shown in Fig. 3(b), are intended to show that the locations at which the streamers randomly strike can be separated by many streamer diameters.

The resulting spatial distributions in the gas phase of quickly formed and solvating species (e.g., OH and H_2O_2), and slowly formed and solvating species (e.g., N_xO_y) significantly differ. For example, the sum of the densities of OH and H_2O_2, N_xO_y and O_3 are shown in Fig. 5.4 after the 1^{st}, 54^{th} and 88^{th} pulses for stationary and random streamers. The OH is formed by direct electron impact dissociation of H_2O vapor and H_2O_2 is formed with one reaction between OH radicals. Their densities are maximum, $\approx 10^{13}$ cm^{-3}, adjacent to the water where the saturated water vapor has its highest densities. Both these species quickly solvate into the liquid. OH, in particular, is also reactive with gas phase species (such as NO_2 in the formation of HNO_3) with nearly gas kinetic rate coefficients. As a result, OH and H_2O_2 do not significantly accumulate in the gas phase. The solvation of these species into the liquid basically occurs at the location where the streamer strikes the surface.

The nitrogen oxides (N_xO_y) do not quickly solvate in the liquid due to their small Henry's law constants. Many reactions are required to form the higher N_xO_y in the gas phase, which requires additional residence time in the gas phase. The end result is that N_xO_y accumulates and diffuses in the gas phase, before solvating and retains little memory of where the plasma

streamers hit. This accumulation is shown in Fig. 5.4, where the average gas phase density of N_xO_y after 100 pulses exceeds 10^{13} cm^{-3}. Even for the stationary streamer, there is a broad distribution of N_xO_y due to its diffusion during the interpulse periods. The composition of N_xO_y is about 90% NO.

The evolution over successive pulses of gaseous ozone (O_3) is shown in Fig. 5.4(c). Similar to the nitrogen oxides, O_3 accumulates in the gas phase. O_3 is primarily produced by O reacting with O_2. With a Henry's law constant of 0.011 mol/L-atm, O_3 solvates into the liquid faster than nitrogen oxides. However, its rate of solvation is still much lower than OH and H_2O_2. Therefore, the accumulation of O_3 is not severely affected by the locations where the plasma streamer strikes the liquid surface. The peak density of O_3 reaches as high as 10^{15} cm^{-3} and average density exceeds 10^{14} cm^{-3} after 100 pulses. In our mechanism about 10% of O_3 reacts with the upper dielectric and so the density of O_3 decreases near the wall. In the gas phase, there is no significant depletion of O_3 except for solvating into the liquid layer. As a result, virtually all O_3 will eventually be solvated into the liquid form O_{3aq}.

The evolution of H_2O_{2aq} and NO_{aq} over 100 pulses (5^{th}, 10^{th}, 50^{th} and 100^{th} pulses) is shown in Fig. 5.5(a) for stationary streamers and in Fig. 5.5(b) for randomly striking streamers. OH_{aq} is largely formed where the streamer strikes the liquid through photolysis of water by UV/VUV photons or solvation of gaseous OH, both of which reflect the diameter of the streamer. The source of OH_{aq} being local to the streamer is exacerbated by charge exchange reactions of gas phase ions with H_2O_{aq}. The gas phase ions do not diffuse far from the streamer before entering the liquid. The charge exchange reactions with liquid H_2O_{aq} produce $H_2O^+_{aq}$, which then charge exchanges with H_2O_{aq} to form $H_3O^+_{aq}$ and OH_{aq}. Photoionization reactions which produce $H_2O^+_{aq}$ also occur only in the direct vicinity of the streamer. OH_{aq}, whose density at the surface of the liquid has a maximum density of 9.5×10^{14} cm^{-3}, reacts with a sub-millisecond lifetime. In pure water, OH_{aq} is dominantly depleted by formation of H_2O_{2aq} through mutual reaction, and whose density accumulates to 10^{16} cm^{-3} at the surface of the liquid. The density of OH_{aq} is depleted so rapidly that its density is not easily shown in Fig. 5.5. The trace of where OH_{aq} was formed is the resulting density of H_2O_{2aq}.

As NO_{aq} and N_xO_{yaq} are formed at the surface of the liquid, reactions with the surface resident OH_{aq} quickly occur. As N_xO_y only slowly solvates into the liquid, the initial distribution

of N_xO_{yaq} is fairly uniform reaching densities of 5×10^{15} cm^{-3} at the surface. The reactivity of H_2O_{2aq} with N_xO_{yaq} is much lower than for OH_{aq}, and so H_2O_{2aq} can accumulate and transport through the liquid to reach the underlying tissue. There is a wider distribution of H_2O_{2aq} (5^{th} pulse) before a significant amount of NO_{aq} is solvated. After 10 pulses, when NO_{aq} begins to appear in the liquid, the distribution of H_2O_{2aq} is narrowed. This narrowing results from the consumption of OH_{aq} by reactions with N_xO_{yaq} and NO_{aq} in particular. Since H_2O_{2aq} only slowly reacts with NO_{aq}, H_2O_{2aq} begins to laterally expand by free diffusion after 80 pulses. For thin water layers, this lateral diffusion is not great, and so the flux of H_2O_{2aq} to the underlying tissue is localized under the streamer

Since the rate of solvation of NO is much lower than for OH, and NO spreads in the gas gap prior to solvation, NO_{aq} solvation occurs along the entire surface even for a stationary streamer. Since the source of NO_{aq} is only from NO solvation as it cannot be initially produced locally in the liquid, the initial distribution of NO_{aq} mirrors that of NO in the gas phase. However, directly under the streamer where OH_{aq} is produced, NO_{aq} is nearly completely consumed by its conversion to nitrous and nitric acids by reaction of OH_{aq}. At locations a few streamer radii distant from where the streamer strikes, the density of OH_{aq} is sufficiently small that NO_{aq} can diffuse away from the surface without reacting with OH_{aq}. This NO_{aq} eventually reaches the underlying tissue by the 50^{th} pulse (0.5 s). This disparity in the disposition of NO_{aq} and H_2O_{2aq}, could for example, produce an over-dose of H_2O_{2aq} and an under-dose of NO_{aq} at the location where the streamer strikes. Elsewhere the situation would be reversed.

The evolution of H_2O_{2aq} and NO_{aq} over 100 pulses with randomly striking streamers is shown in Fig. 5.5(b). With randomly striking streamers, both OH_{aq} and NO_{aq} are initially formed across the entire surface of the liquid. The resulting density of H_2O_{2aq} at the surface, $\approx 10^{15}$ cm^{-3}, is about an order of magnitude smaller than under the stationary streamer as its formation is now averaged over the entire surface instead of being concentrated in a single location. The initially uniform distribution of NO_{aq} solvating into the liquid results from its low reactivity in the gas phase and low rates of solvation into the liquid. The initial distribution of OH_{aq} at the surface of the liquid is produced from an accumulated average of the randomly striking streamers which results in solvation of OH_{aq} or formation of OH_{aq} in the water under the streamer. These impulsive sources of OH_{aq} occur randomly, but discretely, across the surface of the liquid. It is

for this reason that the distribution of H_2O_{2aq} is not perfectly smooth – it reflects the discrete injections of OH_{aq} with each randomly placed pulse. The now fairly uniform distribution of OH_{aq} consumes NO_{aq} in about 0.3 ms, before NO_{aq} can diffuse away from the surface. Since the OH_{aq} is now fairly uniformly formed at the surface and NO_{aq} uniformly enters the liquid, little NO_{aq} survives reactions with OH_{aq} to reach the tissue below. NO_{aq} can only be seen in significant amounts at the surface of the liquid with a density of 10^{14} cm^{-3}, a factor of nearly 50 times smaller than that in the case of the stationary streamer (See Fig. 5.5(b)). After 5 pulses, the density of H_2O_{2aq} is 10^{15} cm^{-3} and concentrated at the liquid surface before diffusion distributes the density. After 10 pulses, diffusion of H_2O_{2aq} begins to homogenize its density. After 100 pulses, there is little NO_{aq} in the bulk liquid whereas H_2O_{2aq} eventually reaches the tissue across the entire surface. NO solvation is slow but continues on a pulse-to-pulse basis and so NO_{aq} continues to be produced. This steady production of NO_{aq} consumes OH_{aq}, which is also now uniformly distributed. This consumption of OH_{aq} then decreases the formation of H_2O_{2aq}.

The evolution of O_{3aq} and $NO_2^-{}_{aq}$ is quite similar to that of H_2O_{2aq} and NO_{aq}, and is shown in Fig. 5.6(b). With stationary streamers, the density of O_{3aq} peaks at the center where the source of O_3 and O produced in the streamer is maximum. Recall that the rate of solvation O_3 is slow compared to $OH_{aq,}$ but rapid when compared to NO. So the center peak of gas phase O_3 reflects diffusion away from the centered streamer where O quickly reacts with O_2. O_{3aq} is dominantly produced through solvation of O_3, with less than 2% of its production in the liquid layer being due to reactions of O_{aq} with O_{2aq}. After 100 pulses, the peak density of O_{3aq} is as high as 5×10^{17} cm^{-3} at the middle of the liquid.

The spatial distribution of $NO_2^-{}_{aq}$, having a maximum density of 10^{14} cm^{-3}, mirrors that of NO_{aq}. Similar to NO_{aq}, $NO_2^-{}_{aq}$ reacts with OH_{aq} to make $NO_3^-{}_{aq}$, and so its density is depleted in the center where OH_{aq} is produced – its density accumulates elsewhere. $NO_2^-{}_{aq}$, is also oxidized by O_{3aq} with a lower rate coefficient, which contributes to its depletion near the center where O_{3aq} is higher. OH_{aq} is depleted approaching the underlying tissue and so it is not important to the consumption of $NO_2^-{}_{aq}$ away from the surface. However, $NO_2^-{}_{aq}$ is consumed by reactions with O_{3aq} through the entire depth of the liquid, which results in a wider region of depletion of $NO_2^-{}_{aq}$. At the side of the domain many streamer radii away from the center, the density of O_{3aq} decreases to below 10^{16} cm^{-3} and $NO_2^-{}_{aq}$ is able to transport through the liquid layer after 0.5 s.

However, $NO_2^-{}_{aq}$ is still depleted at a finite rate by reaction with O_{3aq}. At 1.0 s the density of $NO_2^-{}_{aq}$ near the tissue is smaller than that at 0.5 s since by this time O_{3aq} has also reached the underlying tissue. The density of O_{3aq} is much higher than that of $NO_2^-{}_{aq}$, and so its density is not significantly affected by these reactions.

The evolution of O_{3aq} and $NO_2^-{}_{aq}$ for randomly striking streamers is shown in Fig. 6(b). O_{3aq} now has fairly uniform distributions in the liquid. For similar reasons as for OH_{aq} and H_2O_{2aq}, these uniform profiles result from the cumulative average of the discretely local contributions of individual streamers. The liquid layer becomes O_{3aq} rich after 100 pulses with a density of 10^{17} cm^{-3} at the top surface. Since $NO_2^-{}_{aq}$ is consumed by OH_{aq} and O_{3aq}, $NO_2^-{}_{aq}$ only appears at the liquid surface with a density of 10^{14} cm^{-3} and does not diffuse deeper into the liquid. Much like NO_{aq}, the $NO_2^-{}_{aq}$ is blocked from reaching the tissue by the now uniform distribution of its oxidizing agents.

The aqueous RNS reactivity represented by the solvation of N_xO_y, which is 90% NO, does not disappear with the reaction with OH_{aq} – it is converted into a different species. For example, the terminal species, $NO_3^-{}_{aq}$ and $ONOO^-{}_{aq}$, produced by OH_{aq} reacting with nitrogen oxides (N_xO_{yaq}) are shown in Fig. 7(a) for the stationary striking streamer. Before 10 pulses, the density of $NO_3^-{}_{aq}$ peaks at the center at 3×10^{14} cm^{-3}. After 50 pulses, three regions with concentrations of 10^{15} cm^{-3} appear. The center region of high concentration forms due to reaction of the centrally produced OH_{aq} with NO_{aq}. This reaction generates $HNO_{2aq,}$ which hydrolyzes to form its conjugate ion, $NO_2^-{}_{aq}$. HNO_{2aq} is a weak acid and only 1-3% of HNO_{2aq} will hydrolyze to $NO_2^-{}_{aq}$.[26] Usually, $NO_2^-{}_{aq}$ is fairly stable in water. However, in the presence of O_{3aq}, $NO_2^-{}_{aq}$ is oxidized to $NO_3^-{}_{aq}$. This process also ends in the conversion of HNO_{2aq} to $NO_3^-{}_{aq}$, since hydrolysis of HNO_{2aq} cannot be in equilibrium due to the loss of $NO_2^-{}_{aq}$. HNO_{3aq} and its conjugate ion, $NO_3^-{}_{aq}$, are the dominant acid and negative ion in liquid. HNO_{3aq} is a strong acid and almost completely hydrolyses. The peaks of $NO_3^-{}_{aq}$, appearing off center result from the solvation and diffusion of NO_{aq} outside where the streamer strikes. NO_{aq} then slowly produces HNO_{3aq} and $NO_3^-{}_{aq}$ by reaction with water.

Different from $NO_3^-{}_{aq}$, the distribution of $ONOO^-{}_{aq}$ is peaked at the center where OH_{aq} is formed by the stationary streamer. Since $ONOOH_{aq}$ and its conjugate ion, $ONOO^-{}_{aq}$, are dominantly produced through OH_{aq} related reactions, the source of $ONOO^-{}_{aq}$ reflects the location

where OH_{aq} is formed and quickly depleted. The peak density of $ONOO^-_{aq}$ grows from 10^{14} cm^{-3} after the 5th pulse to 1.2×10^{15} cm^{-3} after the 100th pulse. $ONOOH_{aq}$ and its conjugate ion, $ONOO^-_{aq}$, are reactive species which are believed to play an important role in plasma treatment of biological tissues since they have high oxidizing power.[28] These species have been experimentally detected in plasma treated water.[29] In our model, the density of $ONOO^-_{aq}$ may be over-estimated. A large density of OH_{aq} and NO_{2aq} make it possible to produce significant amounts of $ONOOH_{aq}$, which soon hydrolyses to $ONOO^-_{aq}$. Although $ONOOH_{aq}$ is not as strong an acid as HNO_{3aq}, it still rapidly hydrolyzes and in our model $ONOOH_{aq}$ nearly completely hydrolyzes. In deionized water, $ONOO^-_{aq}$ will eventually naturally convert to $NO_3^-_{aq}$. The characteristic time for conversation is believed to be as short as a few seconds.[30] In our model, the conversion time is about 10 seconds. If the shorter conversion time is the actual case, we may over-estimate the production and transport of $ONOO^-_{aq}$, and underestimate that for $NO_3^-_{aq}$.

Superoxide anion, $O_2^-_{aq}$, is also an important oxidant, which can induce oxidative stress in cells. It is experimentally observed in plasma activated water and growth media.[27] In our reaction mechanism, $O_2^-_{aq}$ can be formed by reaction of dissolved O_2 with solvated electrons, and for that reason $O_2^-_{aq}$ should have a reasonably large density. However, in DBD discharges in air which produce significant amount of NO_{aq}, $O_2^-_{aq}$ is depleted by reactions with NO_{aq} to form peroxynitrite, $ONOO^-_{aq}$. In the absence of NO_{aq}, as occurring under the stationary streamer, $O_2^-_{aq}$ charge exchanges to OH^-_{aq} by reacting with residual OH_{aq}. Even though OH_{aq} quickly reacts, its depleted density of 5×10^{11} cm^{-3} is still large compared to $O_2^-_{aq}$ having a density of 10^{11} cm^{-3}.

The density of hydronium, $H_3O^+_{aq}$, which dominates the positive ions in the liquid, is shown in Fig. 5.7(a) for stationary striking streamers. The spatial distribution of $H_3O^+_{aq}$, follows the profiles of the major negative ions $NO_3^-_{aq}$ and $ONOO^-_{aq}$ since charge neutrality is maintained in the liquid layer. The density of $H_3O^+_{aq}$ is up to 2×10^{15} cm^{-3} at the center of the layer. Charge exchange by incident positive gas phase ions with water molecules during the discharge pulse (followed by charged exchange of $H_2O^+_{aq}$) dominantly occurs under the streamer and accounts for about 11% of $H_3O^+_{aq}$ production. The remaining 89% occurs through hydrolysis of HNO_{2aq}, $HNO_{3aq,}$ and $HOONO_{aq}$ during the interpulse period over a wider area. The production of HNO_{2aq}, $HNO_{3aq,}$ and $HOONO_{aq}$ trace their origins to plasma produced N_xO_y, which slowly

solvates during the interpulse period. $H_3O^+_{aq}$ acidifies the liquid and increases its conductivity, which will be discussed later.

The evolution of the densities of $NO_3^-_{aq}$, $ONOO^-_{aq}$, and $H_3O^+_{aq}$ with randomly striking streamers is shown in Fig. 5.7(b). The production channels of these species are the same as discussed for the stationary streamer. As a result of uniformly mixing OH_{aq} and NO_{aq} by the randomly striking streamers, the densities of $NO_3^-_{aq}$ and $ONOO^-_{aq}$ are quite uniform compared to the stationary scheme. Since OH_{aq} reacts with nitrogen oxides, $ONOO^-_{aq}$ has a higher density, 10^{15} cm^{-3} across the entire surface after 100 pulses compared to the stationary streamer. $NO_3^-_{aq}$ also has a uniform profile with a density of 9×10^{14} cm^{-3}, which is slightly lower than $ONOO^-_{aq}$. The distribution of $H_3O^+_{aq}$ is fairly uniform as well, following the profile of $NO_3^-_{aq}$ and $ONOO^-_{aq}$.

The volume average densities of solvated species are shown in Fig. 5.8, for stationary and randomly striking streamers. Since the DBD is operated in air, significant amounts of O_3 are produced in the gas phase which then solvate into the liquid layer. The average density of O_{3aq} increases with the number of pulses and is nearly independent of the pulse scheme, stationary or random. At the end of 100 pulses, the average density of O_{3aq} reaches 10^{17} cm^{-3}. HNO_{2aq} and its conjugate ion, $NO_2^-_{aq}$, are slowly converted in ozone-rich liquid to HNO_{3aq} and its conjugate ion, $NO_3^-_{aq}$. Otherwise, a significant density of HNO_{2aq} and $NO_2^-_{aq}$ would be formed. For example, in He or Ar discharges in contact with water, O_3 production is much reduced and HNO_{2aq} and $NO_2^-_{aq}$ are found to be terminal species.[26,27] H_{aq} and H_{2aq} are also oxidized by O_{3aq} in the liquid to produce OH_{aq} and then H_2O_{2aq}. The density of H_2O_{2aq} is therefore increased in ozone-reach environments. With a stationary streamer, the densities of H_2O_{2aq} and NO_{aq} monotonically increase, resulting from the separation in space of OH_{aq} and NO_{aq}, as shown in Fig. 5. After 100 pulses, the average densities of H_2O_{2aq} and NO_{aq} reach 5×10^{14} cm^{-3} and 4×10^{14} cm^{-3}. H_2O_{2aq} is a terminal species with its only major loss being to the underlying tissue. NO_{aq} slowly reacts with water and can last for 10 seconds. With pulses occurring at 100 Hz, the production of H_2O_{2aq} is greater than its rate of diffusion loss to the underlying tissue. As a result, the density of H_2O_{2aq} increases with the number of pulses. At lower frequencies with a longer interpulse period, the loss of H_2O_{2aq} to the underlying tissue between pulses would produce lower average densities.

With randomly striking streamers, OH_{aq} and NO_{aq} are well mixed and react throughout the liquid. NO_{aq} therefore does not accumulate and reaches a density of only 10^{12} cm^{-3} after 100 pulses. H_2O_{2aq} rises to 2×10^{14} cm^{-3} after about 13 pulses and then decreases. The peak is due to the slowly solvating NO from the gas phase. Prior to NO solvating into the liquid, H_2O_{2aq} accumulates by self-reactions of OH_{aq}. After NO begins to solvate into the liquid, OH_{aq} is consumed by reaction with NO_{aq}, which then reduces the production of H_2O_{2aq}. This is a significant difference compared to the stationary streamer in which H_2O_{2aq} is formed under the streamer where NO_{aq} is depleted. The density of H_2O_{2aq} decreases below 1.6×10^{14} cm^{-3} after 100 pulses since consumption OH_{aq} by NO_{aq} surpasses its loss in the formation of H_2O_{2aq}. For these conditions, the density of H_2O_{2aq} will not increase by increasing the number of pulses. In order to produce more H_2O_{2aq} in liquid, a cross flow (>270 sccm for a 100 Hz DBD) through the gas gap might be necessary to blow away NO before it solvates. OH_{aq} would then be less consumed by reactions with NO_{aq}, resulting in more production of H_2O_{2a}.

The average densities of the ions $H_3O^+_{aq}$, $NO_3^-{}_{aq}$, and $ONOO^-_{aq}$ are shown in Fig. 5.8(c). These densities monotonically increase with both stationary and randomly striking streamers. $H_3O^+_{aq}$ reaches a density of 9×10^{14} cm^{-3} after 100 pulses in the random scheme. Although charge exchange of $H_2O^+_{aq}$ with water molecules produces $H_3O^+_{aq}$, the hydrolysis of acids, such as HNO_{3aq} and $HOONO_{aq}$, dominates the production of $H_3O^+_{aq}$ in the long term. Therefore, the density of $H_3O^+_{aq}$ nearly equates to about the sum of $NO_3^-{}_{aq}$ and $ONOO^-_{aq}$. With randomly striking streamers, OH_{aq} and N_xO_{yaq} are well mixed, more $HOONO_{aq}$ is produced than HNO_{3aq}, which then results in larger densities of $ONOO^-_{aq}$ compared to $NO_3^-{}_{aq}$. In the stationary scheme, the production channels for ions are similar. However, since OH_{aq} is spatially separated from N_xO_{yaq}, the production of the precursors to hydrolysis are significantly reduced, which then reduces the production of $H_3O^+_{aq}$, $NO_3^-{}_{aq}$ and $ONOO^-_{aq}$. In general, the average densities of ions are lower with stationary streamers by a factor of ≈2.

What ultimately matters to the treatment of the tissue are the fluences of reactive species to its surface. These fluences are shown in Fig. 5.9. There is significant spatial variation in the fluences for the discharges that have stationary streamers and significant differences in which species reach the tissue between the stationary and random schemes. With stationary streamers, the tissue can receive a significant fluence of NO_{aq}, while the tissue receives virtually no NO_{aq}

with randomly striking streamers. In the stationary scheme, the fluence of NO_{aq} to the tissue is a minimum under the streamer and maximum many radii away due to the diffusion of NO_{aq} around the location that the streamer strikes the liquid. In contrast, the fluence of H_2O_{2aq} is maximum under the streamer, decreasing from 10^{15} cm^{-2} at the center to $<10^{12}$ cm^{-2} less than 1 mm away. These trends could result in an over-dose of H_2O_{2aq} under the streamer and under-dose elsewhere. In the random striking scheme, the fluence of H_2O_{2aq} is uniform, but with a lower value of 2×10^{12} cm^{-2} due to the uniform consumption of its precursor OH_{aq}. The fluence of O_{3aq} also has a peak value, 2×10^{15} cm^{-2}, at the center and decreases to 2×10^{14} cm^{-2} to the edge in the stationary scheme. In the random scheme, the fluence of O_{3aq} is quite uniform with a value around 10^{15} cm^{-2}.

The trends for the fluences of neutral species are reflected in the fluences of charged species. With stationary streamers, the fluence of $ONOO^-_{aq}$ basically follows that of H_2O_{2aq}, since $ONOO^-_{aq}$ is produced in large part from reactions related to OH_{aq}. At the center, the fluence of $ONOO^-_{aq}$ is 3×10^{13} cm^{-2} and decreases to $<10^{12}$ cm^{-2} a mm away. The fluence of $NO_3^-{}_{aq}$ is fairly uniform since it is produced through N_xO_{yaq} reacting with water. The local maxima in the fluence of $NO_3^-{}_{aq}$ reflect the interaction of OH_{aq} and NO_{aq} at the interface where the density of OH_{aq} is large in the center and the density of NO_{aq} is large in the periphery. $H_3O^+_{aq}$ is basically given by the sum of negative ions, dominated by $NO_3^-{}_{aq}$ and $ONOO^-_{aq}$, and so the fluence of $H_3O^+_{aq}$ also reflects the peak of $ONOO^-_{aq}$ and the broader distribution of $NO_3^-{}_{aq}$.

With randomly striking streamers, the fluences of ions become more uniform. The fluence of $ONOO^-_{aq}$ is higher than in the stationary scheme since nitrogen oxides and OH_{aq} are well mixed. As expected, the fluences of reactive species are more uniform with randomly striking streamers which could result in higher quality treatment in plasma medicine applications. However, for example, if NO_{aq} is a desired agent for treatment, only the stationary scheme can produce significant fluences of NO_{aq} to the tissue.

One of the consequences of long-term DBD treatment is altering the characteristics of the liquid layer. As discussed above, after 100 pulses the liquid becomes O_{3aq} rich, decreasing the ability to produce large densities of HNO_{2aq} and $NO_2^-{}_{aq}$. Another effect is that the liquid layer becomes acidified and conductive, as shown in Fig. 5.10. After 100 pulses, the pH decreases to 6 for stationary streamers and 5.8 for randomly striking streamers. The pH value calculated in

our model is determined by the density of hydronium, $H_3O^+_{aq}$, in which we assumed all hydronium ions to be reactive. These pH values can be considered an upper limit as the consumption of species by the tissue reduces the densities of $H_3O^+_{aq}$ and results in a higher pH value than might otherwise be produced.

In experiments by Hamaguchi *et al*[31], pH values of a plasma jet treated aqueous solution were evaluated from hydronium concentrations, which were assumed to be equal to that of the measured $NO_x^-{}_{aq}$ (x = 2, 3) ions. The estimated pH values from the $NO_x^-{}_{aq}$ concentration were in good agreement with those directly measured by a pH meter. The pH decreased to 4.5 after 3 minutes of plasma treatment from an initial value of 5.7. In another indirect surface DBD treatment [32], the pH decreased from 7 to less than 4 in non-buffered physiological saline within the first 5 minutes of plasma treatment, followed by a slower decrease to between 2 and 3 in 30 minutes. Reduction of pH value or acidification of liquid is known to affect the viability of bacteria through either directly interacting or assisting other reactive species. Our predicted values of pH extrapolate to 4.8 after 100 s plasma treatment with 10,000 pulses. Considering that only a single streamer is modelled in this computational investigation, the acidification is already significant.

The predicted conductivity of the liquid after 100 pulses, also shown in Fig. 5.10, increases to 2.8 μS/cm for stationary streamers and 3.5 μS/cm for randomly striking streamers. (The conductivity in our model is determined by the total ion density in the liquid with collision cross sections approximated by Lenard-Jones potentials.) This value is likely a lower limit due to the consumption of ions on the tissue. Extrapolating these results to 5 minutes of treatment and 30,000 pulses, the predicted conductivity is 1 mS/cm. For comparison, in a DC discharge with deionized liquid as cathode [1], the liquid conductivity was observed to increase to 30 μS/cm after a 10-minute treatment and by 150 μS/cm after a 1-hour treatment. High quality deionized water has a conductivity of about 0.1 μS/cm and the conductivity of typical tap water is in the range of 100-1000 μS/cm. Therefore, the conductivity of deionized water is altered within seconds of treatment, whereas significant treatment (many minutes or more) is required to affect the conductivity of tap water.

The effects of the conductivity of the liquid on discharge properties can be complex. One such effect results from the reduced voltage drop in the liquid due to its higher conductivity.

This in turn increases the voltage drop in the gas above the liquid. For example, an otherwise identical discharge was modeled with pre-dissolved NaCl in the liquid giving a conductivity of 1 mS/cm. The electric field in the gas gap was enhanced by the reduced voltage drop in the liquid and the accumulation of surface charges from polarization of the conductive liquid. The electron density in the plasma streamer increased by a factor of 2 compared to a streamer over an initially non-conducting liquid. The plasma streamer spread over a wider area and so delivered plasma produced species (e.g., ions, rapidly solvating neutrals, photons) over this broader area. For conditions where the conductivity of the liquid approaches 1 mS/cm, our assumption that each discharge pulse is identical is no longer valid.

5.3.3 Lower Frequency of Multipulse DBD

We discussed that NO_{aq} and $NO_2^-{}_{aq}$ are consumed by reactions with OH_{aq} and O_{3aq}, and so conditions for which there is an abundance of OH_{aq} and O_{3aq} in spatial coincidence with NO_{aq} and $NO_2^-{}_{aq}$ will reduce their densities. Considering the possible biomedical effects produced by NO_{aq} and $NO_2^-{}_{aq}$, it may be desirable to control the densities and fluences of these species to the tissue by controlling the coincidence of NO_{aq} and $NO_2^-{}_{aq}$ with OH_{aq} and O_{3aq}. One such method is to change the repetition rate of the discharge. The densities of H_2O_{2aq}, NO_{aq} and $NO_2^-{}_{aq}$ produced by a 10 Hz DBD with a stationary streamer are shown in Fig. 5.11 at 1 μs after discharge pulses. In a 10 Hz DBD, the interpulse period is 0.1 s, which is long enough for transport of aqueous species significantly through the liquid layer. So at 10 Hz, species produced on a prior pulse are able to diffuse away from the surface before species produced by the next pulse solvate into the liquid. For example, due to the longer interpulse period, H_2O_{2aq} diffuses to a wider distribution having a lower density compared to the 100 Hz case where H_2O_{2aq} accumulates on a pulse-to-pulse basis.

The density of NO_{aq} demonstrates these repetition rate dependent dynamics. NO uniformly solvates into the liquid throughout the interpulse period. OH_{aq}, is produced under the streamer coincident with each discharge pulse. This surface resident OH_{aq} depletes NO_{aq} at the center of the liquid layer. Due to the reactivity of OH_{aq}, it does not penetrate far beyond the surface and does not survive for longer than 0.6 ms. At 10 Hz, the interpulse period is long

enough so that NO_{aq} is able to diffuse into the center of the liquid layer where OH_{aq} is depleted. At the higher 100 Hz repetition rate, NO_{aq} is consumed by the replenished OH_{aq} produced by the next pulse before NO_{aq} can reach the center of the layer. The separation of NO_{aq} and OH_{aq} both in space and time due to the longer interpulse period results in a significant amount of NO_{aq} reaching the tissue at the center of the layer.

The coincidence (or lack thereof) of species afforded by the 10 Hz PRF also affects the density of $NO_2^-{}_{aq}$. With the longer interpulse period, $NO_2^-{}_{aq}$ can diffuse deeper into the liquid layer and almost reach the underlying tissue. The density of $NO_2^-{}_{aq}$ increases to 10^{14} cm^{-3} within 10 pulses before decreasing to 10^{13} cm^{-3} after the following 90 pulses. During the initial pulses, $NO_2^-{}_{aq}$ is produced in a nearly pristine water layer and with the longer interpulse period reaches the tissue. However, after tens of pulses, the increasing density of O_{3aq} consumes $NO_2^-{}_{aq}$, thereby decreasing its flux to the tissue.

The densities of H_2O_{2aq}, NO_{aq}, and $NO_2^-{}_{aq}$ produced by 10 Hz DBDs with randomly striking streamers are shown in Fig. 5.12. The density of H_2O_{2aq} is lower by a factor of 2 than that produced in 100 Hz DBDs due to the loss of H_2O_{2aq} to the underlying tissue during the interpulse period. The profile of H_2O_{2aq} always has a peak where the previous plasma streamer strikes due to the impulsive production of H_2O_{2aq} by the rapid (but isolated in time) injection of OH_{aq}. The interpulse period is long enough at 10 Hz that NO_{aq} is able to diffuse away from the surface before the next pulse produces the surface resident OH_{aq}. Since the discharge pulses randomly strike the surface of the liquid, the NO_{aq} may have many interpulse periods to diffuse away from the surface before another streamer strikes close enough to produce additional OH_{aq} that would reduce the density NO_{aq}. In the 100 Hz discharge, the NO_{aq} is not able to diffuse away from the surface before another discharge produces OH_{aq} that consumes it. For example, NO_{aq} appears at two locations in the bulk liquid layer after 5 pulses. These are regions where, statistically, NO_{aq} was able to diffuse away from the surface prior to a subsequent discharge pulse producing OH_{aq} at the surface. After 10 pulses, this statistical *escape* of NO_{aq} from the surface results in its accumulation of NO_{aq} in the bulk liquid to a density of 10^{14} cm^{-3}. After 50 and 100 pulses, NO_{aq} accumulates uniformly to 5×10^{14} cm^{-3}, while its distribution shows isolated regions near the surface where a recent streamer striking the liquid produced OH_{aq} that locally consumed NO_{aq}. Compared to 100 Hz PRFs, the longer interpulse period in 10 Hz DBDs

enables NO_{aq} to survive diffusing through the liquid layer and reaching the underlying tissue.

Similar to NO_{aq}, in the 10 Hz DBD with the longer interpulse period, $NO_2^-{}_{aq}$ is able to diffuse into bulk liquid layer instead of being consumed by OH_{aq} at the liquid surface. However, $NO_2^-{}_{aq}$ is still not able to diffuse entirely through the liquid layer due to its consumption by O_{3aq}. Although not shown here, due to its lower reactivity in the liquid O_{3aq} still fills the liquid layer at the lower PRF with densities as high as 5×10^{16} cm^{-3}. In the ozone-rich liquid layer, $NO_2^-{}_{aq}$ is slowly converted to $NO_3^-{}_{aq}$. The interpulse period of 0.1 s is just long enough for this slow process resulting in $NO_2^-{}_{aq}$ being converted to $NO_3^-{}_{aq}$ by O_{3aq} just before it reaches the underlying tissue. To be clear, a small amount of $NO_2^-{}_{aq}$ does reach the underlying tissue since the conversion process is not complete.

5.3.4 Fluences of Multipulse DBD Under Various Conditions

Reducing the pulse frequency from 100 Hz to 10 Hz results in NO_{aq} being able to diffuse through the liquid to reach the underlying tissue. This suggests that the fluences of some species to the underlying tissue can be controlled by varying the PRF. Fluences of reactants to the tissue are shown in Fig. 5.13(a) for PRFs of 10 Hz to 10 kHz with randomly striking streamers. In each case, 100 pulses are computed followed by 10 - 60 s of afterglow. The fluence of NO_{aq} to the tissue is negligible for 10 kHz and 1 kHz as the production of OH_{aq} at the surface is frequent enough to prevent the *escape* of NO_{aq} into the bulk liquid. The fluence of NO_{aq} increases to 1.5×10^{10} cm^{-2} for 100 Hz and sharply increases to 1.9×10^{12} cm^{-2} for 10 Hz. Similarly, the fluence of $NO_2^-{}_{aq}$ increases from 1.8×10^{10} cm^{-2} for 10 kHz to 4.5×10^{11} cm^{-2} for 10 Hz. The fluence of H_2O_{2aq} also increases by a factor of 3 from higher frequency to lower frequency. This increase in H_2O_{2aq} results from less NO_{aq} reacting with OH_{aq}, which is the source of H_2O_{2aq}. For the same reason the fluence of $ONOO^-{}_{aq}$ decreases with lower frequency since $ONOO^-{}_{aq}$ is produced by reaction between NO_{aq} and OH_{aq}. The fluence of $H_3O^+{}_{aq}$ has a small decrease at low frequency following the decrease in $ONOO^-{}_{aq}$. The fluences of $NO_3^-{}_{aq}$ and O_{3aq} are not particularly sensitive PRF since their fluences are determined by the rate of solvation of gas phase species averaged over pulses.

The sensitivity of fluences to PRF results from an accumulation effect, diffusion

processes and reactions between long-lived and short-lived species. Accumulation of long-lived species, like O_{3aq}, is able to alter the characteristics of the liquid layer. Diffusion away from the surface reduces the coincidence of reactants, as is the case for NO_{aq} being consumed by OH_{aq} at the liquid surface. However, lack of coincidence between NO_{aq} and OH_{aq} may reduce production $HOONO_{aq}$, which is an important oxidizing agent in medical treatment. Lower frequencies and longer interpulse periods reduce the interactions between pulses of short lived species whereas interactions with longer lived species such as O_{3aq} is less sensitive to PRF. The interactions between pulses also occur in the gas phase. Higher PRFs results in accumulation of reactants that favor formation of species requiring many reactions, such as N_xO_y.[19]

In addition to frequency, the thickness of the liquid layer also affects the fluences of species. For example, for the randomly striking streamers, NO_{aq} has a significant density only at the liquid surface, as shown in Fig. 5.5(b). This implies that the underlying tissue can still receive a large fluence of NO_{aq} if the liquid layer is thin enough. Fluences of reactive species onto the underlying tissue with randomly striking streamers are shown in Fig. 5.13(b). The fluence of NO_{aq} increases from 10^{10} cm^{-2} with a 1 mm liquid layer to 10^{11} cm^{-2} with 50 μm liquid layer. The fluence of $NO_2^-{}_{aq}$ increases from 10^{10} cm^{-2} with 1 mm liquid layer to 10^{13} cm^{-2} with 50 μm. The thin liquid layer enables more $NO_2^-{}_{aq}$ to reach the tissue before being consumed by O_{3aq}. OH_{aq} is also able to reach the tissue for thin liquid layer of 50 μm with a influence of 2×10^{11} cm^{-2}. For a thick liquid layer of 1 mm the fluence of OH_{aq} is reduced to 10^{10} cm^{-2}. The corresponding fluence of H_2O_{2aq} increases a small amount with the thickness of the liquid layer since more OH_{aq} converts to H_2O_{2aq} instead of being lost to the tissue. The fluences of $H_3O^+{}_{aq}$, $NO_3^-{}_{aq}$, $ONOO^-{}_{aq}$ and O_{3aq} are not sensitive to the thickness of the liquid layer. The characteristic time for species to diffuse through the liquid layer increases proportionally with the square of the thickness of the liquid layer. From 50 μm to 1 mm, the characteristic time for diffusion through the liquid increases by a factor of 400. This difference in diffusion time enables short-lived species like OH_{aq}, $NO_{aq,}$ and $NO_2^-{}_{aq}$ to reach the surface. Thinner liquid layers tend to increase the fluences of short-lived species, while thicker liquid layers tend to remove short-lived species. Long-lived species are generally not affected by the thickness for the range we investigated.

The spatial distribution of fluences of species with stationary pulses is more sensitive to the thickness of the liquid compared to the randomly striking streamers. In both schemes, the

magnitudes of the fluences are sensitive to the transient time, which then discriminate between short- and long-lives species. For example, the fluences of species to the tissue for stationary streamers for a 2 mm thick liquid layer, 100 pulses at 100 Hz, and a 2 min afterglow are shown in Fig. 14. In general, the fluences in Fig. 5.14 are more uniform compared to those for a 200 μm layer as shown in Fig. 9. The longer transit time required for a 2 mm layer enables the majority of the reaction chemistry to proceed converting most reactivity to terminal species. This leaves diffusion to be the dominant process determining the spatial distribution of fluences, a process that tends to make the fluences more uniform. The end result is that some control over both composition and uniformity can be achieved by combinations of repetition rate and thickness of the water layer. For example, for more uniform and larger fluences of NO_{aq}, one should operate at lower PRF and thicker layers. As the layer becomes thicker, the importance of fluid dynamics within the layer increases.[33,34] In this model, we consider only diffusion within the liquid layers, a simplification enabled by the layers being thin. However, as the layer thickens, convection becomes more important, either natural or forced. With sufficient convection, the *well-stirred* approximation is approached. For example, a *well-stirred*, but still thin water layer would result in mixing OH_{aq} with NO_{aq}. This mixing would result in the uniform consumption of NO_{aq}, and uniform production of nitric acid, and peroxynitrous acid. However, in the case of plasma treating wound in a clinical or surgical setting, the liquid is usually thin and adheres strongly to the tissue. Significant fluid dynamics within the layer are likely not important. In these cases, the distinctions between stationary and randomly striking streamers, low PRF and high PRF, and thickness are likely still important.

5.4 Concluding Remarks

The influence of streamer placement, repetition rate, and liquid thickness on the fluences of reactive species through think liquid layers was discussed using results from a computational investigation of DBDs in contact with water overlying tissue. The DBDs were simulated for 100 stationary or randomly striking streamers at different repetition rates in contact with liquid layers of various thicknesses followed by 10 seconds to 2 minutes of afterglow. With stationary plasma streamers striking the same location, different rates of solvation of gaseous species produce spatial separation of aqueous species in the liquid. For example, OH with a higher rate of

solvation concentrates in both the gas and liquid phase where the plasma streamer strikes. NO with a much lower rate of solvation spreads over the liquid surface. NO_{aq} at the center is nearly completely consumed by $OH_{aq,}$ while NO_{aq} accumulates and reaches the underlying tissue at more distant locations. OH_{aq} is partly constrained to the radius of plasma streamer due to this reaction with NO_{aq}. With streamers randomly striking the liquid surface, nearly all solvating species are mixed at the surface of the liquid. For example, NO_{aq} is consumed by OH_{aq} over the entire liquid surface and does not reach the underlying tissue for moderate repetition rates. OH_{aq} becomes fairly uniform in liquid.

Even for exposures of only a few seconds the characteristics of the liquid layer can be altered by plasma treatment. The liquid becomes acidic, conductive, and ozone-rich after even 100 pulses. An acidic environment enhances the reactivity of species such as peroxynitrite. Nitrous acid and nitrite ions are converted to nitric acid and nitrates ion, respectively, in ozone-rich liquids. The plasma dynamics can also be affected by the conductivity of the liquid layer due to charge separation at the surface and voltage division.

In addition to the spatial locations of the streamers, frequency combined with thickness of the liquid layer is also a method of controlling the plasma produced aqueous species reaching the underlying tissue. Reducing the pulse frequency produces a higher density of short-lived species, such as NO_{aq}, in the liquid. For example, with a 10 Hz DBDs, NO_{aq} is able to diffuse from the liquid surface where OH_{aq} is produced during the 0.1 s interpulse and avoids being consumed by the OH_{aq} generated by the next pulse. The NO_{aq} can then reach the underlying tissue. With higher frequencies, the consumption of NO_{aq} by OH_{aq} at the liquid surface is increased.

The transit time for species to the underlying tissue is determined by the thickness of the liquid layer in our model as diffusion in the liquid is the only transport mechanism. Hence, the fluences of short-lived species are sensitive to the thickness of the liquid layer. Short-lived species are able to reach the underlying tissue through a thin liquid layer through which the transit time is short. However, the transit time through a thick liquid layer may be longer than the lifetime of short-lived species, which are eventually depleted before reaching the tissue. As a result, DBDs at lower frequency with a thin liquid layer will result in higher fluences of short-lived species. The thickness of the liquid layer also affects the spatial distribution of fluences to

the tissue resulting from stationary pulses. With a 200 μm thick liquid layer, the reactant fluences are non-uniform. For example, the fluence of H_2O_{2aq} peaks at the center where the fluence of NO_{aq} is a minimum. With a 2 mm thick liquid layer, the fluences of H_2O_{2aq} and NO_{aq} become fairly uniform.

Many of these trends strictly apply to thin liquid layers where convection is not important. As the convective component of transport increases and the well-stirred reactor approximation is approached, some of these trends will no longer apply. For example, in the well-stirred limit, NO_{aq} will not have an opportunity to *escape* from the surface where OH_{aq} is formed or to avoid regions of high OH_{aq} afforded by stationary streams. NO_{aq} would then likely be more consumed by OH_{aq}. For the same reasons, more mixing of O_{3aq} with $NO_2^-{}_{aq}$ would produce larger densities of $NO_3^-{}_{aq}$. The well stirred limit would likely enable more uniform reactions between OH_{aq} and NO_{xaq}, which ultimately will produce a more acidic solution.

5.5 Tables

Table 5.1 Solubilities at 300 K and 1 atm.[21,22]

Species	Henry's Law Constant (mol/L-atm)
OH	2.5×10
H_2O_2	1.0×10^{5}
NO	1.9×10^{-3}
O_3	1.1×10^{-2}

Table 5.2 Selected Aqueous Reactions

Reaction[a]	Rate Coefficient[a]	Ref.
$O\bullet_{aq} + O_{2aq} \rightarrow O_{3aq}$	3×10^{9}	[24][b]
$\bullet OH_{aq} + \bullet OH_{aq} \rightarrow H_2O_{2aq}$	5.5×10^{9}	[24]
$NO_{aq} + NO_{aq} + O_{2aq} \rightarrow NO_{2aq} + NO_{2aq}$	2.3×10^{6} $M^{-2}s^{-1}$	[25]
$NO_{aq} + NO_{2aq} + H_2O_{aq} \rightarrow HNO_{2aq} + HNO_{2aq}$	2×10^{8} $M^{-2}s^{-1}$	[25]
$NO_{aq} + \bullet OH_{aq} \rightarrow HNO_{2aq}$	2×10^{10}	[25]
$NO_{aq} + HO_2\bullet_{aq} \rightarrow HNO_{3aq}$	8×10^{9}	[25]
$NO_{2aq} + \bullet OH_{aq} \rightarrow HNO_{3aq}$	3×10^{10}	[25]
$NO_{aq} + HO_2\bullet_{aq} \rightarrow HOONO_{aq}$	3.2×10^{9}	[25]
$NO_{2aq} + \bullet OH_{aq} \rightarrow HOONO_{aq}$	1.2×10^{10}	[25]
$NO_2^-{}_{aq} + O_{3aq} \rightarrow NO_3^-{}_{aq} + O_{2aq}$	5.0×10^{5}	[25]
$HNO_{2aq} + H_2O_{aq} \rightarrow H_3O^+{}_{aq} + NO_2^-{}_{aq}$	1.8×10^{1}	[26][c]
$H_3O^+{}_{aq} + NO_2^-{}_{aq} \rightarrow HNO_{2aq} + H_2O_{aq}$	1.8	[26][c]
$HNO_{3aq} + H_2O_{aq} \rightarrow H_3O^+{}_{aq} + NO_3^-{}_{aq}$	2×10^{3}	[26][c]
$H_3O^+{}_{aq} + NO_3^-{}_{aq} \rightarrow HNO_{3aq} + H_2O_{aq}$	2×10^{2}	[26][c]
$N_2O_{3aq} + H_2O_{aq} \rightarrow HNO_{2aq} + HNO_{2aq}$	1.1×10^{4}	[25]
$N_2O_{4aq} + H_2O_{aq} \rightarrow HNO_{2aq} + HNO_{3aq}$	8×10^{2}	[25]
$N_2O_{5aq} + H_2O_{aq} \rightarrow HNO_{3aq} + HNO_{3aq}$	1.2	[25]
$NO_{2aq} + NO_{2aq} + H_2O_{aq} \rightarrow HNO_{2aq} + H_3O^+{}_{aq} + NO_3^-{}_{aq}$	1.5×10^{8} $M^{-2}s^{-1}$	[26]
$NO_{2aq} + NO_{2aq} + H_2O_{aq} \rightarrow H_3O^+{}_{aq} + NO_2^-{}_{aq} + H_3O^+{}_{aq} + NO_3^-{}_{aq}$	5×10^{7} $M^{-2}s^{-1}$	[26]
Photon Reactions		
$h\nu + H_2O_{aq} \rightarrow H\bullet_{aq} + \bullet OH_{aq}$	1×10^{-20} cm^2	[27][b]

a) Aqueous species have an "aq" subscript. Rate coefficients have unit of $M^{-1}s^{-1}$ ($l \bullet mole^{-1}s^{-1}$) unless noted otherwise. "•" represents a free radical.
b) Approximated by analogy.
c) The rate coefficient is estimated according to thermodynamic hydrolysis in liquid water.

5.6 Figures

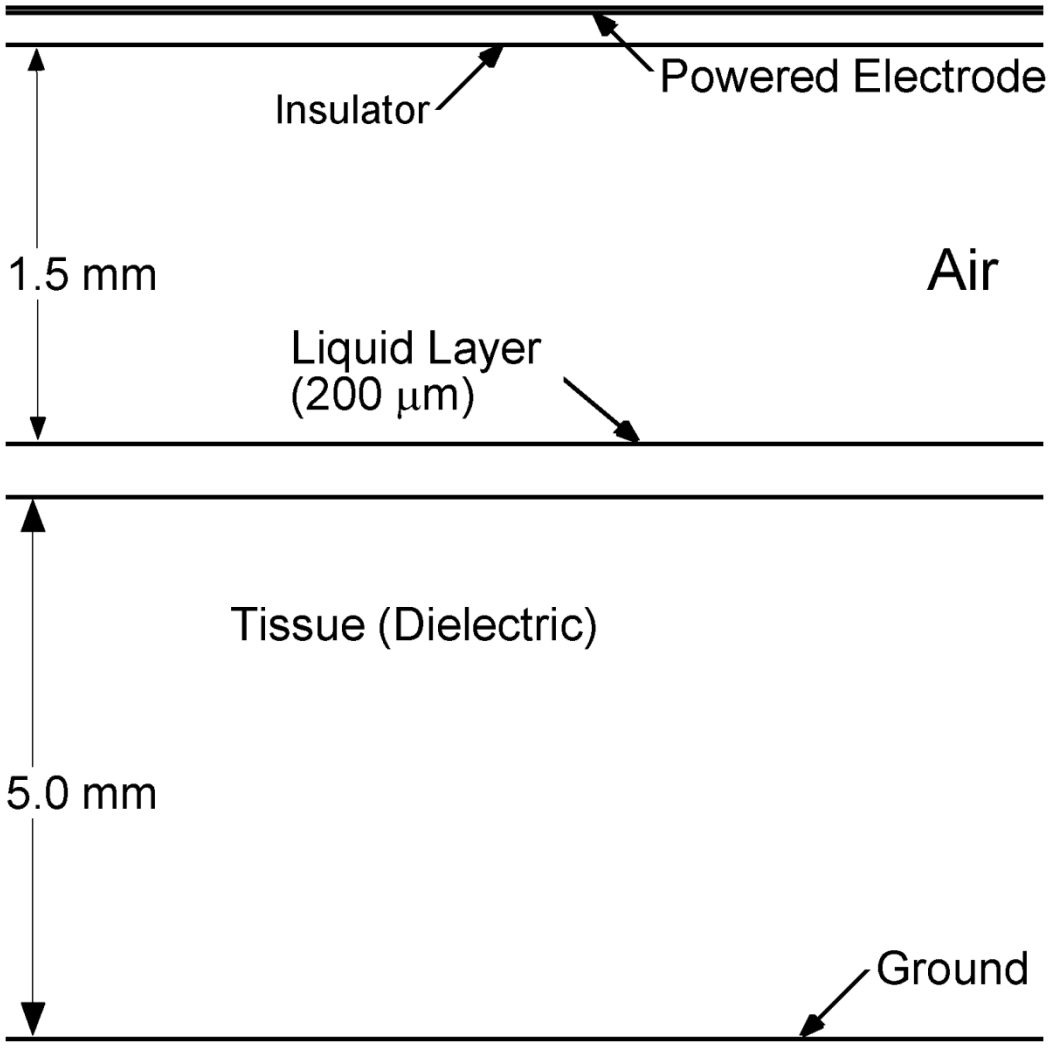

Figure 5.1 Schematic of the geometry where the plasma interacts with liquid layer covering tissue. The total computational domain is 6 mm × 4 mm.

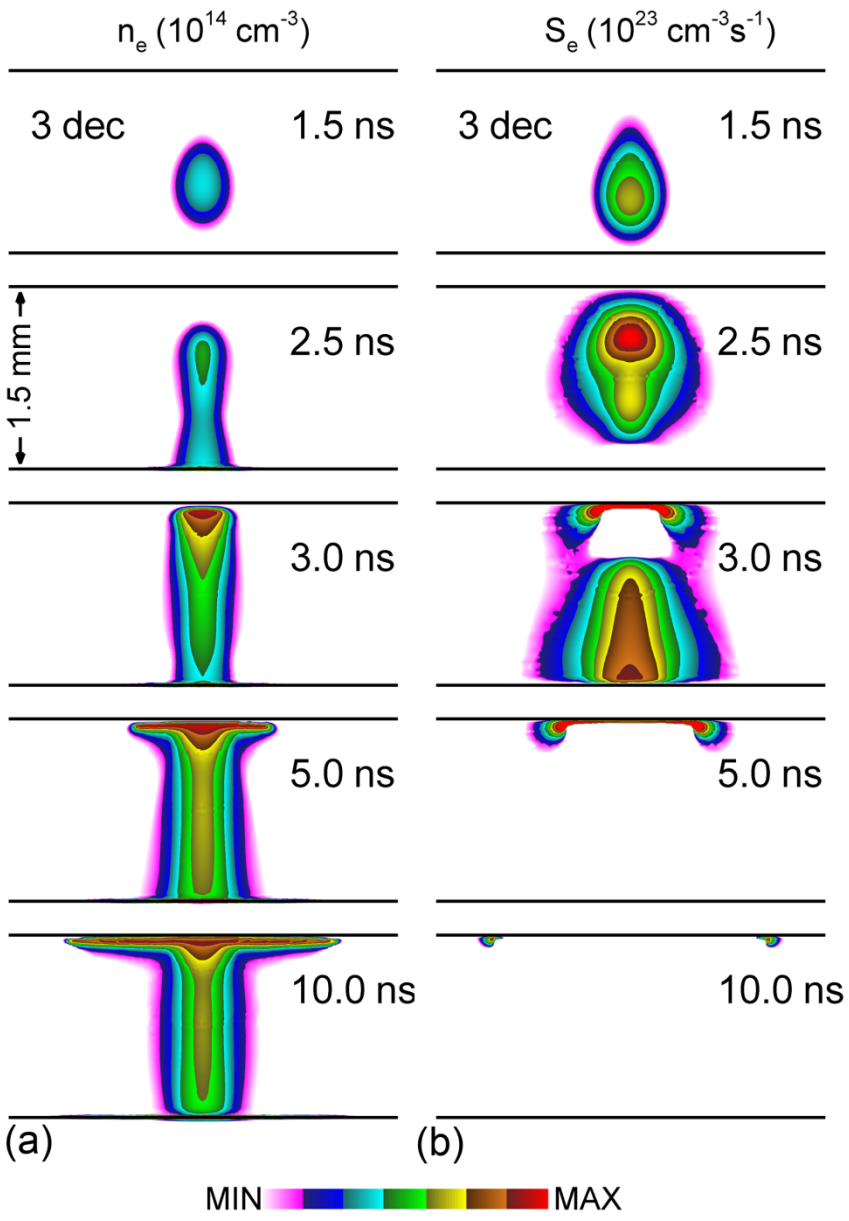

Figure 5.2 Time evolution of (a) electron density, n_e, and (b) electron impaction ionization source, S_e, for a negative discharge operated at -18kV for 10 ns over a 200 μm water layer. Only the gas gap is shown. The initial gas is 1 atm, $N_2/O_2/H_2O$ = 79.9/20/0.1, and water evaporates from the surface. The contours for n_e and S_e are plotted on a log scale over three decades with maximum values shown at the top.

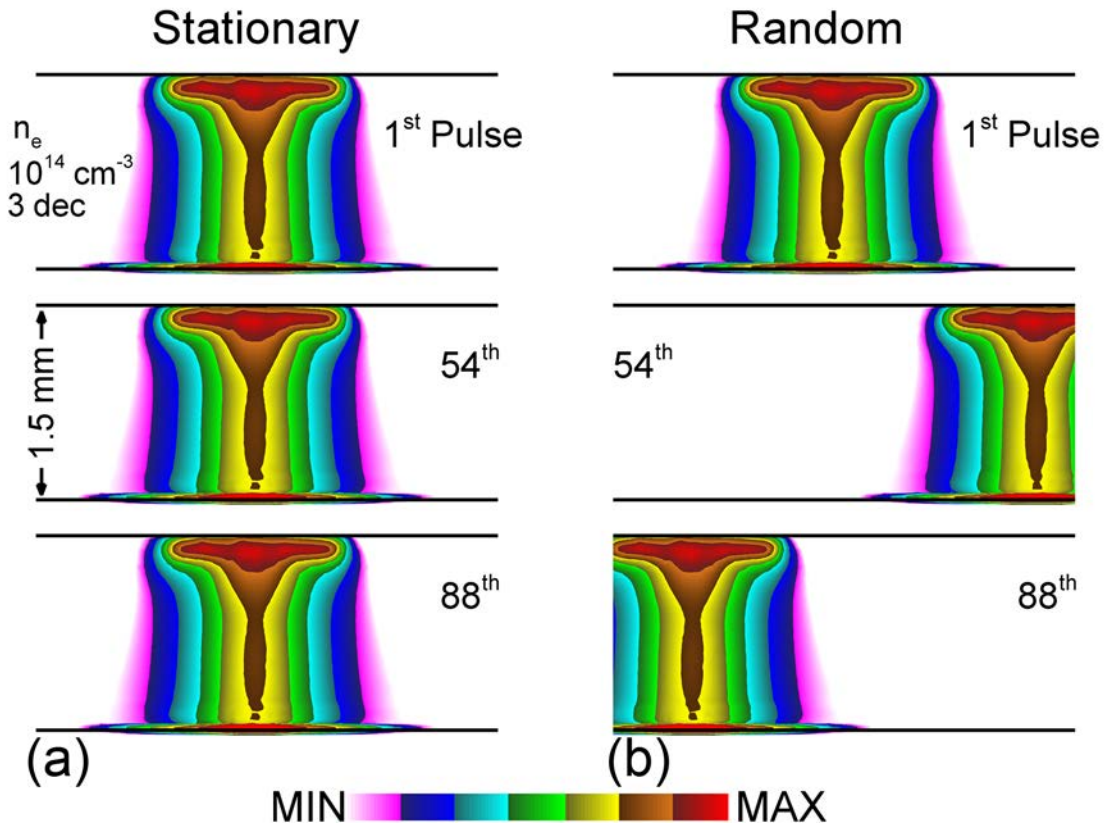

Figure 5.3 Stationary and randomly striking streamers represented by electron density in the gas gap. (a) Stationary scheme in which the plasma streamer continues to strike at the same location of the liquid layer on pulse-to-pulse basis. (b) Randomly striking scheme where the plasma streamer strikes at a different location on the liquid layer on a pulse-to-pulse basis. The contours are plotted on a 3-decade log-scale with the maximum values noted in each frame.

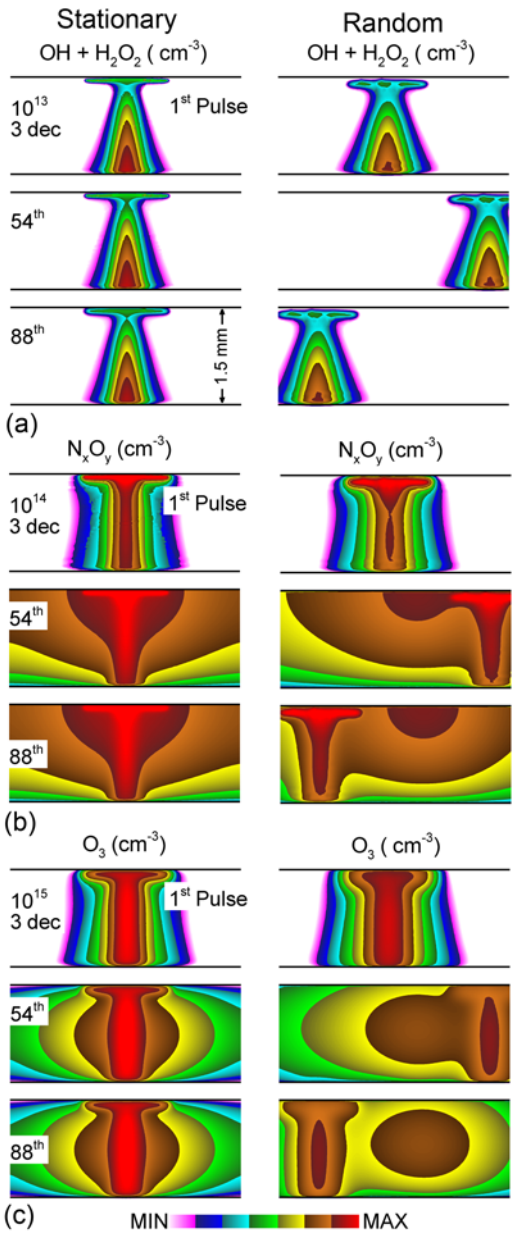

Figure 5.4 Densities of (a)OH, H_2O_2, (b)N_xO_y (sum of NO, NO_2, N_2O_3, N_2O_4 and N_2O_5) and (c)O_3 in the gas gap at the beginning of 1st, 54th and 88th pulse for the stationary and random schemes. The contours are plotted on a 3-decade log-scale with the maximum values noted in each frame.

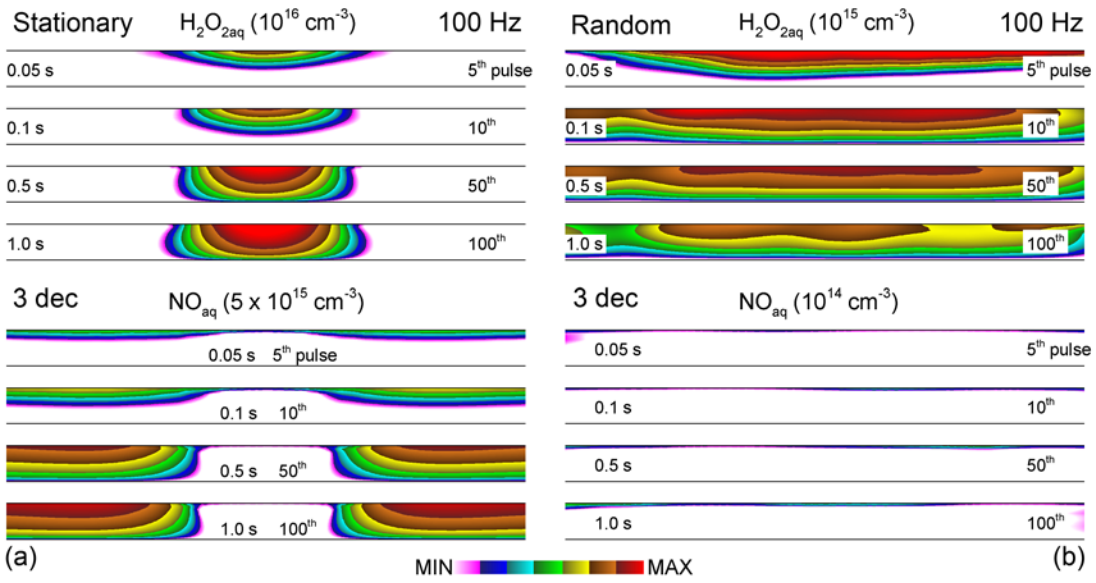

Figure 5.5 The time evolution of H_2O_{2aq} and NO_{aq} densities in the 200 μm water layer ("$_{aq}$" represents an aqueous species) at the end of the 5th, 10th, 50th and 100th pulse for (a) stationary streamers and (b) randomly striking streamers. The time and corresponding pulse number are shown in each frame. The contours are plotted on a 3-decade log-scale with the maximum values at the top.

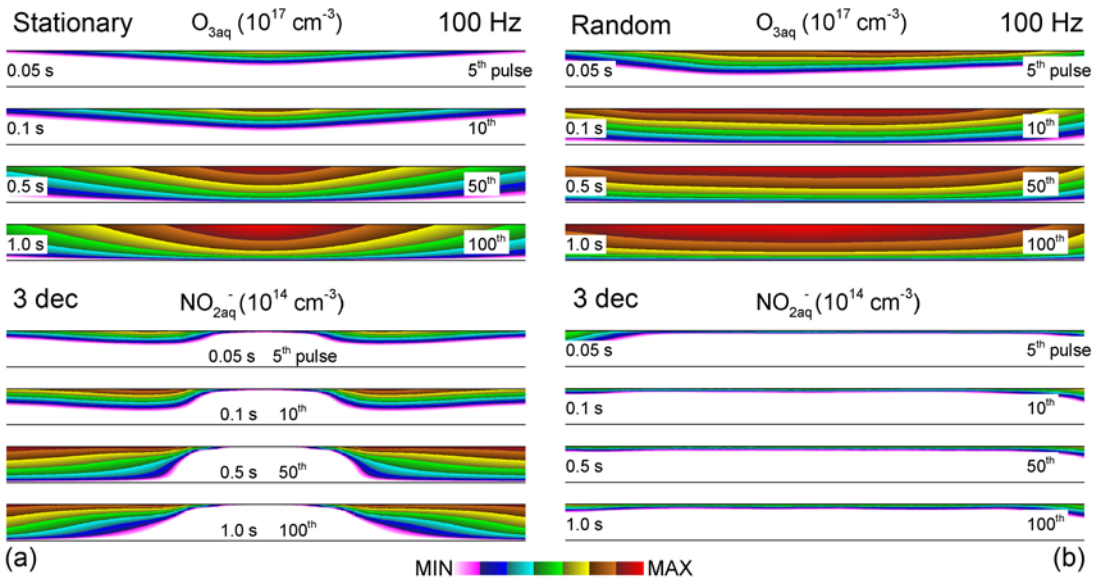

Figure 5.6 The time evolution of O_{3aq} and $NO_2^-{}_{aq}$ densities in the 200 μm water layer at the end of the 5th, 10th, 50th and 100th pulse for (a) stationary streamers and (b) randomly striking streamers. The time and pulse number are shown in each frame. The contours are plotted on a 3-decade log-scale with the maximum values at the top.

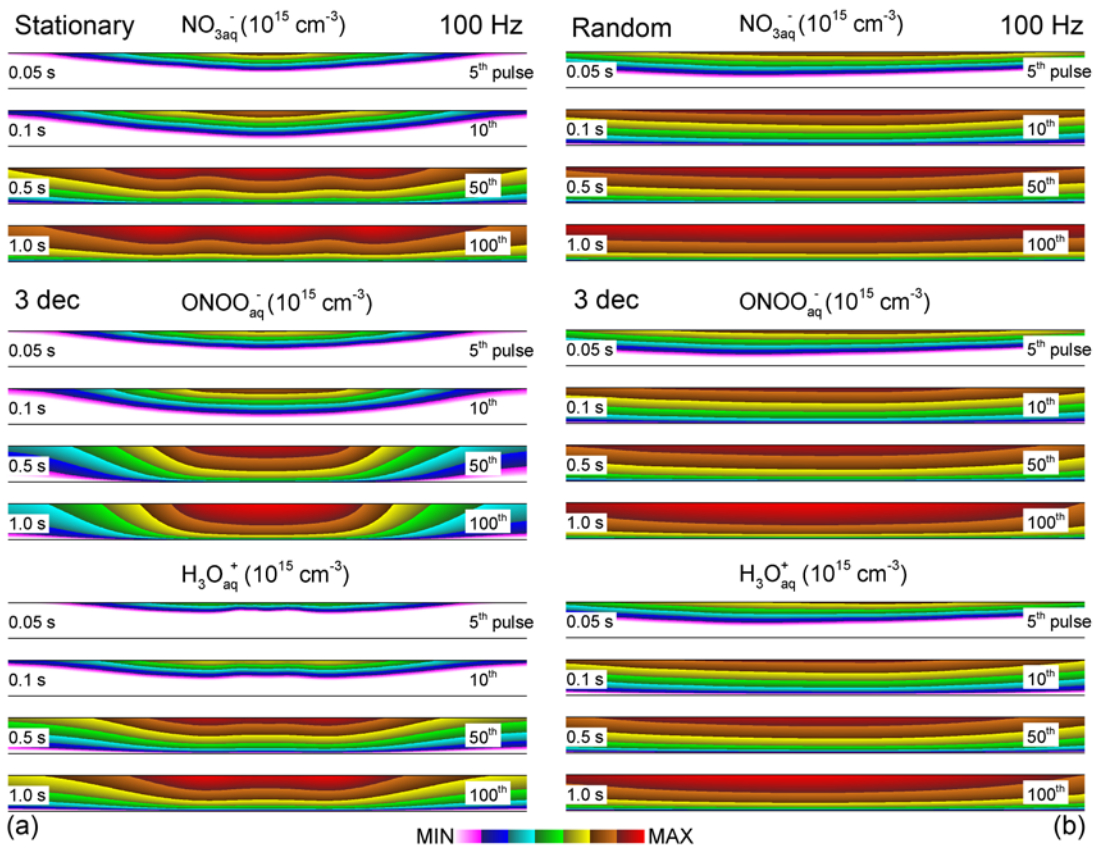

Figure 5.7 The time evolution of (a)$NO_3^-{}_{aq}$, (b)$ONOO^-_{aq}$, and (c)$H_3O^+_{aq}$ densities in the 200 μm water layer at the end of the 5th, 10th, 50th and 100th pulse for the randomly striking streamer. The time and pulse number are shown in each frame. The contours are plotted on a 3-decade log-scale with the maximum values at the top.

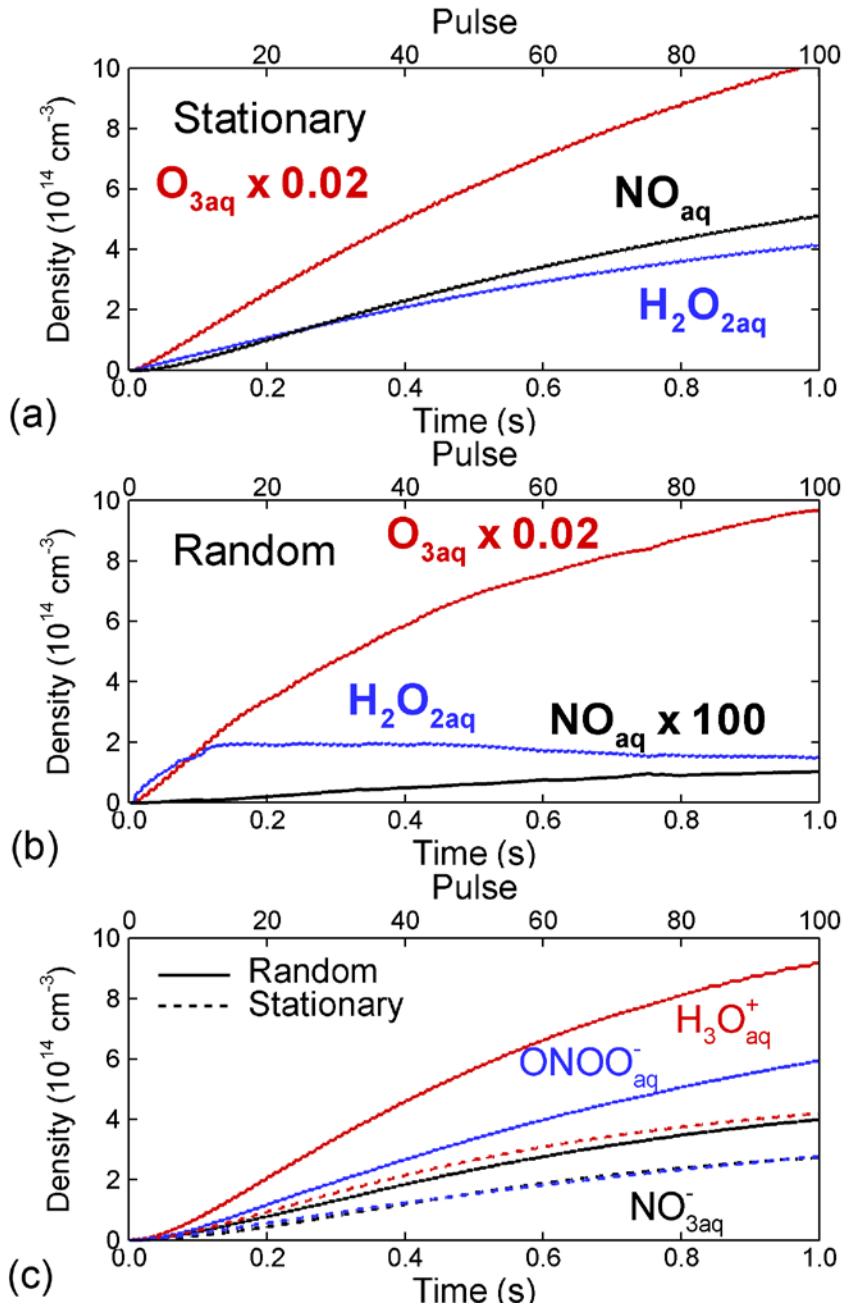

Figure 5.8 The time evolution of densities averaged in the liquid layer over 100 pulses for neutral species with (a) stationary and (b) random streamers, and for (c) charged species for both schemes. The O_{3aq} density is reduced by a factor of 50 and that of NO_{aq} is increased by a factor of 100. The time axis and corresponding pulse number are shown at the bottom and top axes.

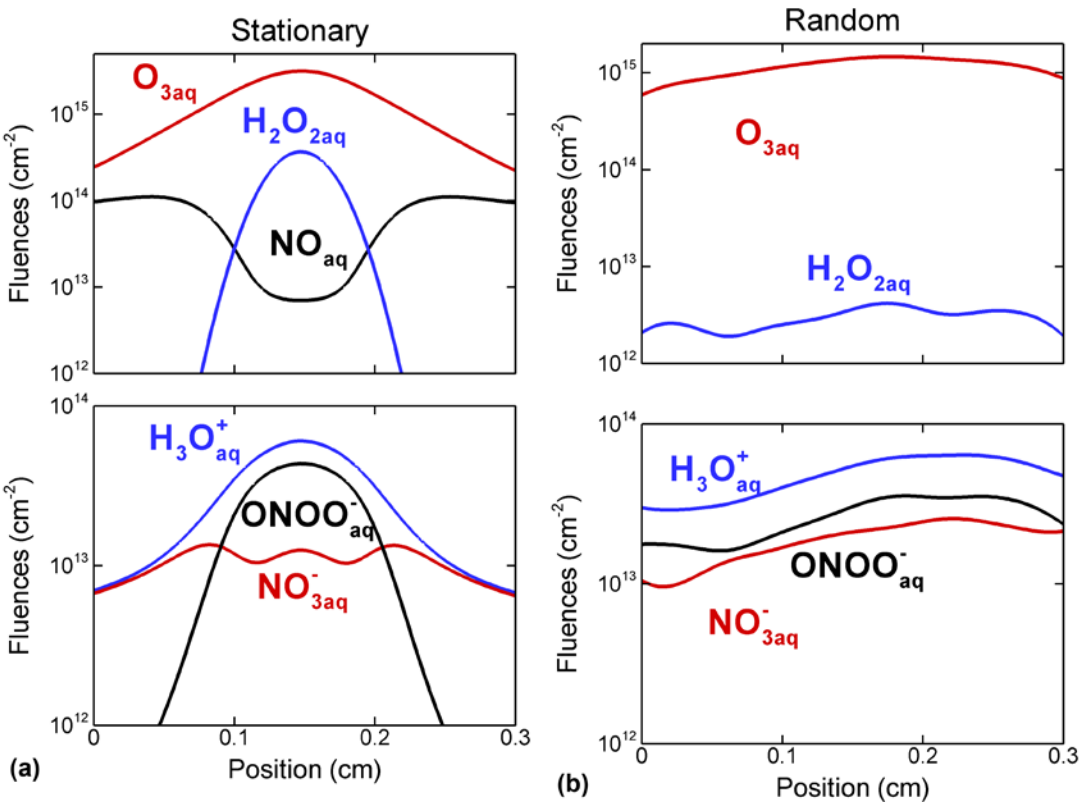

Figure 5.9 Fluences of neutral and charged species integrated over 100 pulses and a 10 s afterglow onto the tissue underlying the 200 μm water layer. Neutral and charged species for (a) stationary pulses and (b) randomly striking pulses.

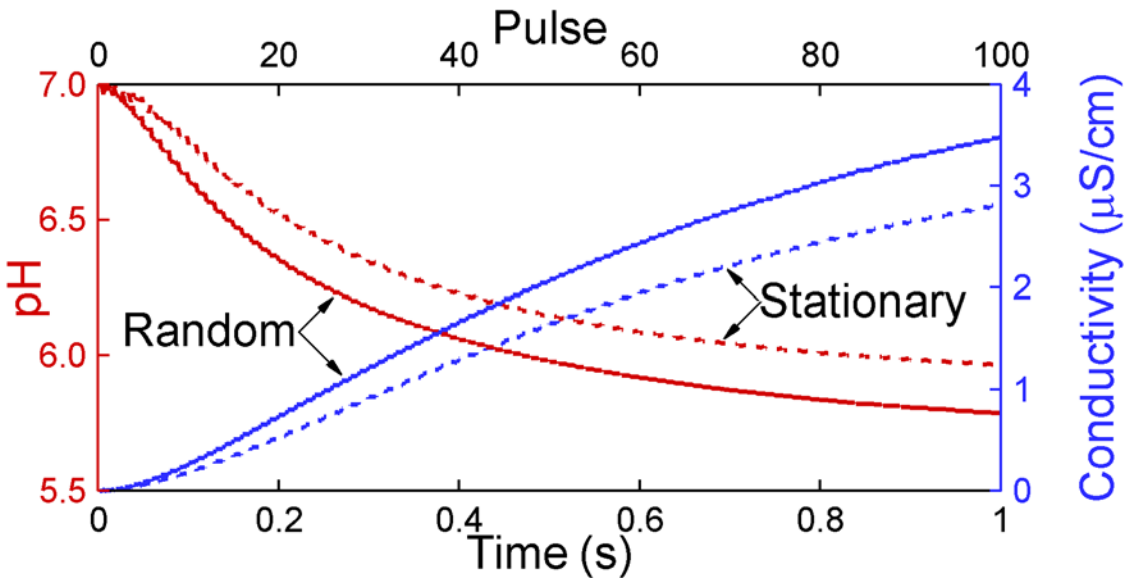

Figure 5.10 The time evolution of average pH and conductivity of the liquid layer over 100 discharge pulses in the stationary and random schemes. The time axis and corresponding pulse number are shown at the bottom and top.

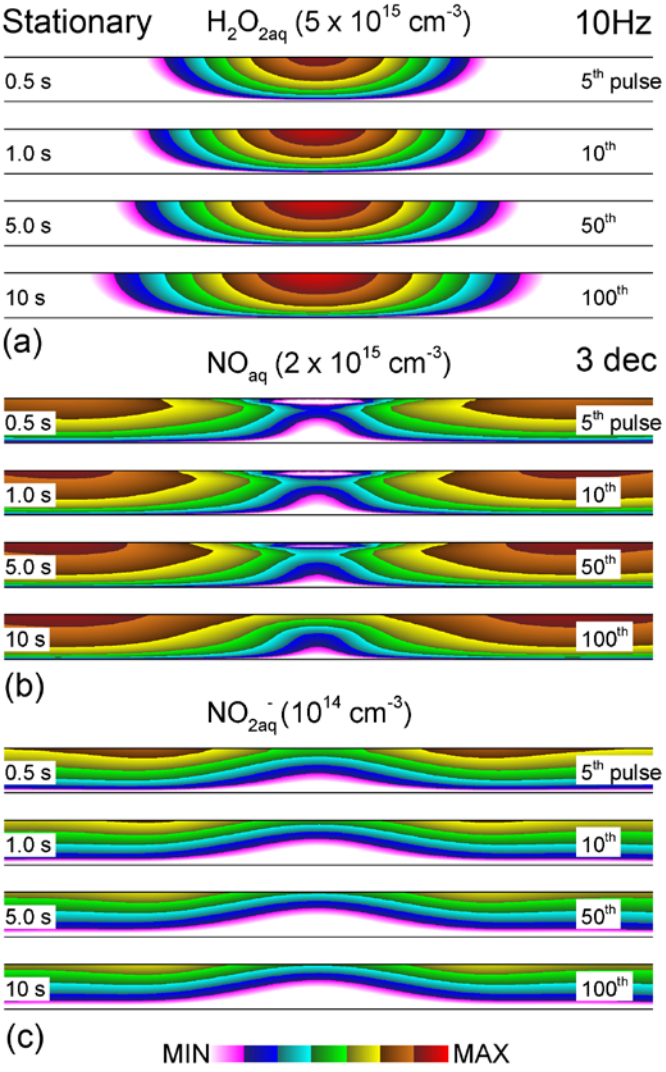

Figure 5.11 The densities of (a) H_2O_{2aq}, (b) NO_{aq} and (c) $NO_2^-{}_{aq}$ in the 200 μm water layer during 10 Hz DBDs treatment for the stationary streamer. The densities are shown accumulating after the 5th, 10th, 50th and 100th pulse. The time and corresponding pulse number are shown in each frame. The contours are plotted on a 3-decade log-scale with the maximum values at the top.

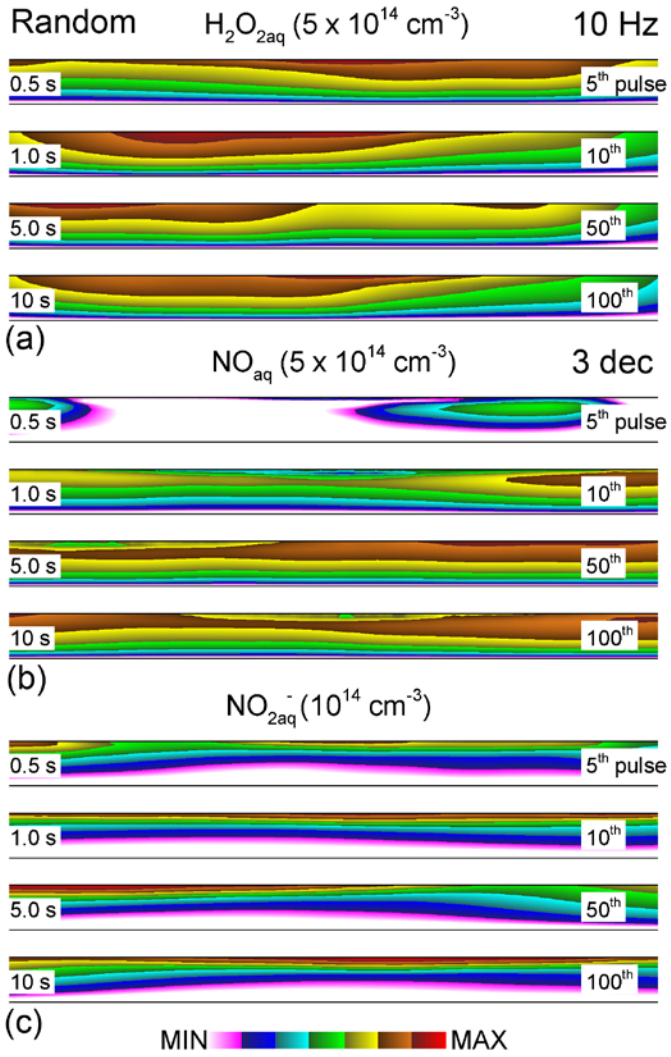

Figure 5.12 The densities of (a) H_2O_{2aq}, (b) NO_{aq} and (c) $NO_2^-{}_{aq}$ in the 200 μm water layer during 10 Hz DBDs treatment for randomly striking streamer. The densities are shown accumulating after the 5th, 10th, 50th and 100th pulse. The time and corresponding pulse number are shown in each frame. The contours are plotted on a 3-decade log-scale with the maximum values at the top.

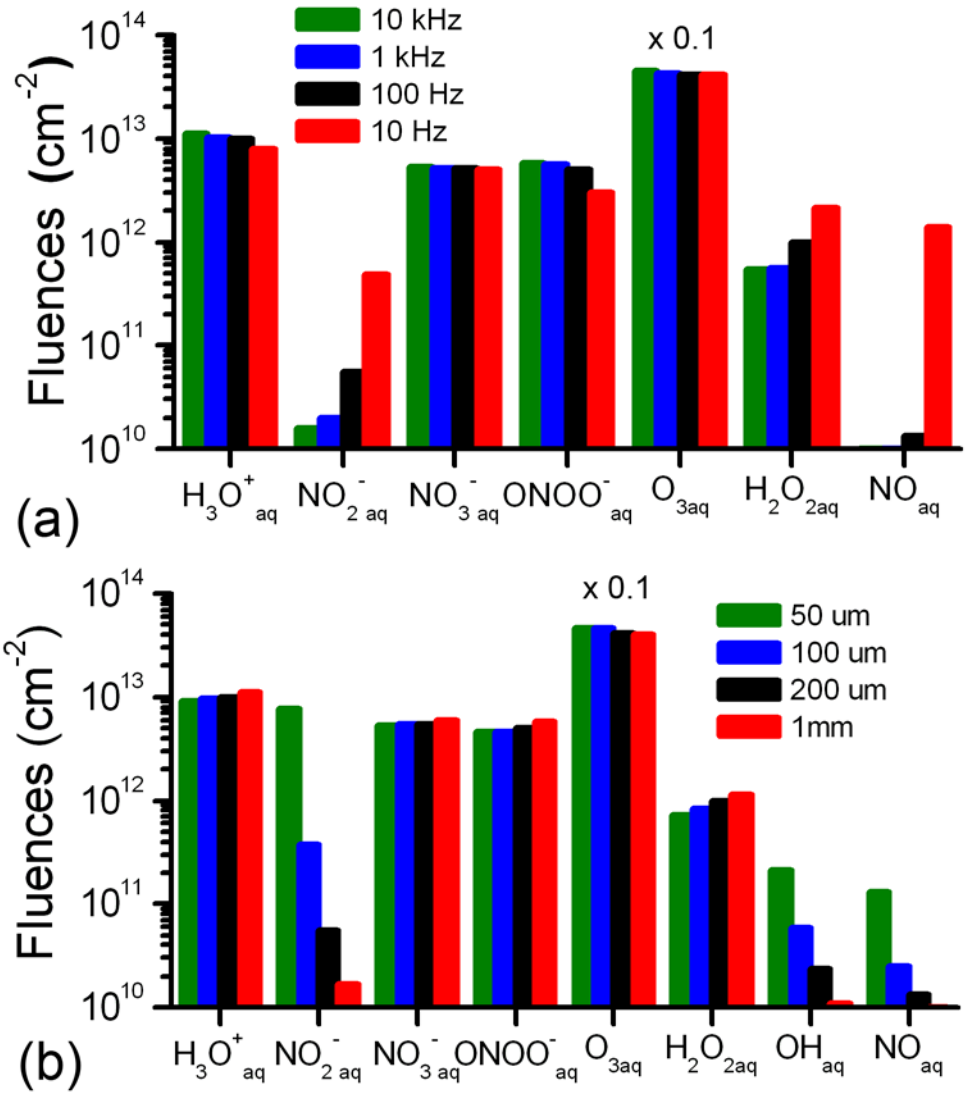

Figure 5.13 Integrated fluences of reactive species over 10 s onto the underlying tissue. (a) Fluences for pulse repetition frequencies of 10 Hz to 10 kHz for a 200 μm liquid layer. (b) Fluences for a 100 Hz DBD with liquid thickness varying from 50 mm to 1 mm. The fluence of O_{3aq} is reduced by a factor of 10.

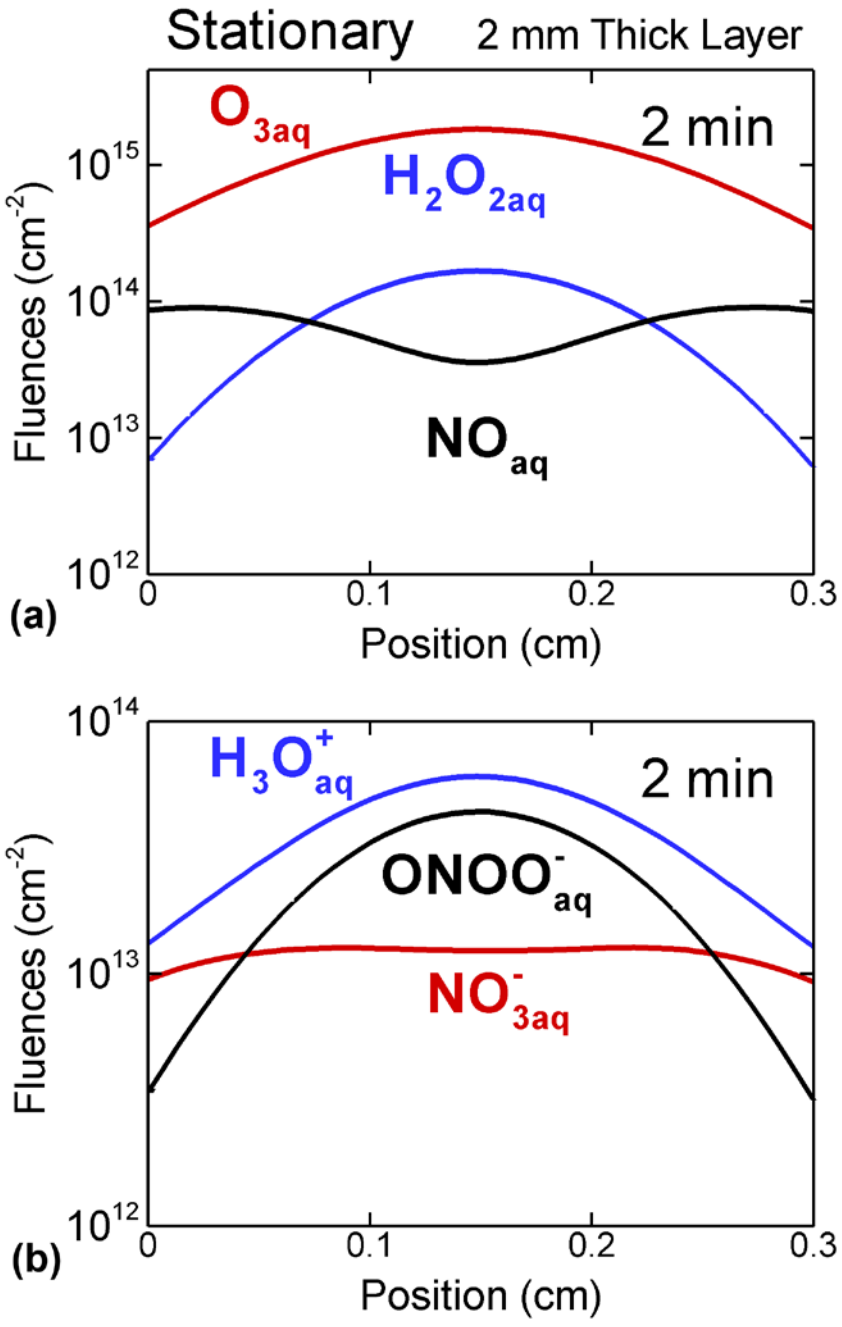

Figure 5.14 Fluences integrated over 100 pulses and a 2 minute afterglow onto the tissue underlying the 2 mm water layer. (a) Neutral and (b) charged species for the stationary streamer.

5.7 References

[1] J. Heinlin, G. Isbary, W. Stolz, G. Morfill, M. Landthaler, T. Shimizu, B. Steffes, T. Nosenko, J. L. Zimmermann and S. Karrer, J. Eur. Acad. Dermatol. Venereol. **25**, 1 (2011)

[2] G. Isbary, T. Shimizu, J. L. Zimmermann, H. M. Thomas, G. Morfil and W. Stolz, New Microbes New Infect. **1**, 41 (2013)

[3] J. Schlegel, J. Koritzer and V. Boxhammer, Clin. Plasma Med. **1**, 2 (2013)

[4] P. Bruggeman, E. Ribezl, A. Maslani, J. Degroote, A. Malesevic, R. Rego, J. Vierendeels and C. Leys, Plasma Sources Sci. Technol. **17**, 025012 (2008).

[5] S. Ikawa, K. Kitano and S. Hamaguchi, Plasma Process. Polym. **7**, 33 (2010).

[6] K. Oehmigen, M. Hahnel, R. Brandenburg, Ch. Wilke, K.-D. Weltmann and T. von Woedtke, Plasma Process. Polym. **7**, 250 (2010).

[7] M. C. Garcia, M. Mora, J. E. Foster, A. Gamero, A. Sola, C. Jiménez-Sanchidrián, F. J. Romero-Salguero, "Generation of Hydrogen Peroxide in Liquid Water Using an Argon Microwave Surface Wave Sustained Discharge", paper WG4-1, COST Action TD1208 "Electrical Discharges with liquids for Future Application", Barcelona, Spain, February, 2015.

[8] M. G. Kong, G. Kroesen, G. Morfill, T. Nosenko, T. Shimizu, J. van Dijk and J. L. Zimmermann, N. J. Phys. **11**, 115012 (2009).

[9] J. Heinlin, G. Isbary, W. Stolz, G. Morfill, M. Landthaler, T. Shimizu, B. Steffes, T. Nosenko, J. L. Zimmermann and S. Karrer, J. Eur. Acad. Dermatol. Venereol. **25**, 1 (2011).

[10] N. Barekzi and M. Laroussi, J. Phys. D: Appl. Phys. **45**, 422002 (2012).

[11] C. A. J. van Gils, S. Hofmann, B. K. H. L. Boekema, R. Brandenburg and P. J. Bruggeman, J. Phys. D: Appl. Phys. **46**, 175203 (2013).

[12] G. Fridman, A. Shereshevsky, M. M. Jost, A. D. Brooks, A. Fridman, A. G. V. Vasilets and G. Friedman, Plasma Chem. Plasma Process **27**, 163 (2007).

[13] Ch. Liu, D. Dobrynin and A. Fridman, J. Phys. D: Appl. Phys. **47**, 252003 (2014).

[14] H. Ayan, G. Fridman, A. F. Gutsol, V. N. Vasilets, A. Fridman and G. Friedman, IEEE Trans. Plasma Sci. **36**, 504 (2008).

[15] P.-C. Jiang, W.-C. Wang, S. Zhang, L. Jia, D.-Z. Yang, K. Tang and Z.-J. Liu,

Spectrochim. Acta A: Mol. Biomol. Spectrosc. **122**, 107 (2014).

[16] A. Belinger, N. Naudé and N. Gherardi, IEEE Trans. Plasma Sci. **42**, 2816 (2014).

[17] J. P. Boeuf, B. Bernecker, Th. Callegari, S. Blanco and R. Fournier, Appl. Phys. Lett. **100**, 244108 (2012).

[18] Y. Yang, Y. I. Cho, G. Friedman, A. Fridman and G. Fridman, IEEE Trans. Plasma Sci. **39**, 2060 (2011).

[19] T. Callegari, B. Bernecker and J. P. Boeuf, Plasma Sources Sci. Technol. **23**, 054003 (2014).

[20] K. Takashima (Udagawa), Y. Zuzeek, W. R. Lempert and I. V. Adamovich, Plasma Sources Sci. Technol. **20**, 055009 (2011).

[21] R. Sander, "Compilation of Henry's Law Constants for Inorganic and Organic Species of Potential Importance in Environmental Chemistry", available at "www.henrys-law.org/henry.pdf" (1999).

[22] D. Mackay and W. Y. Shiu, J. Phys. Chem. Ref. Data **10**, 1175 (1981).

[23] R. E. Skyner, J. L. McDonagh, C. R. Groom, T. van Mourik and J. B. O. Mitchell, Phys. Chem. Chem. Phys. **17**, 6174 (2015).

[24] K. P. Maddena and S. P. Mezyka, J. Phys. Chem. Ref. Data **40**, 023103 (2011).

[25] *NDRL/NIST Solution Kinetics Database*, [Online]. Available: http://kinetics.nist.gov/solution/

[26] S. N. Pandis and J. H. Seinfeld, J. Geophys. Res. **94**, 1105 (1989).

[27] R. D. Hudson, Rev. Geophys. Space Phys. **9**, 305 (1971).

[28] C. Szabó, H. Ischiropoulos and R. Radi, Nat. Rev. Drug Disc. **6**, 662 (2007).

[29] P. Lukes, E. Dolezalova, I. Sisrova and M. Clupek, Plasma Sources Sci. Technol. **23**, 015019 (2014).

[30] R. Atkinson, D. L. Baulch, R. A. Cox, J. N. Crowley, R. F. Hampson, R. G. Hynes, M. E. Jenkin, M. J. Rossi and J. Troe, Atmos. Chem. Phys. **4**, 1461 (2004).

[31] S. Ikawa, K. Kitano and S. Hamaguchi, Plasma Process. Polym. **7**, 33 (2010).

[32] K. Oehmigen, M. Hahnel, R. Brandenburg, Ch. Wilke, K.-D. Weltmann and T. von Woedtke, Plasma Process. Polym. **7**, 250 (2010).

[33] A. Lindsay, C. Anderson, E. Slikboer, S. Shannon and D. B. Graves, "Momentum, heat and neutral mass transport in convective atmospheric pressure plasma-liquid systems and

implications for aqueous targets", to be published in J. Phys. D.

[34] J. F. M. van Rens, J. T. Schoof, F. C. Ummelen, D. C. van Vugt, P. J. Bruggeman, and E. M. van Veldhuizen, Trans. Plasma Sci. 42, 2622 (2014).

CHAPTER 6 SUMMARY AND FUTURE WORK

Atmospheric DBDs have been widely used for environmental and biomedical applications. This thesis focused on the plasma dynamics, plasma-liquid interaction and aqueous reactions in applications of interest such as discharges in bubbles in water and discharges over the liquid covering tissue. By using a 2-D multi-fluid simulation platform, *nonPDPSIM*, this work contributes to improving the fundamental understanding of interactions of plasma with liquids and aqueous chemistry and ways to control outcomes in the applications of interest. Summaries and future works of each chapter are discussed in Sec. 6.1. This is followed by the list of resulting publications in Sec. 6.2.

6.1 Summary

Chapter 3 discussed the investigation of discharges in He, Ar and N_2 bubbles of 2 mm in water and the computational results were compared to experiments. The discharges in bubbles in water act as surface discharges along the gas-liquid interface, which in return influences the discharges. The water vapor evaporated from the liquid surface makes the injected gas humid and affects the chemical reactions in the discharges. H_α and OH(A-X) emissions are generally confined to the surface where both the H_2O vapor density and electron temperature are largest. The excitation channels are analyzed. It was found that the formation of OH(A) is dominated by dissociative excitation transfer to H_2O from excited states of He, Ar and N_2. The formation of H(n=3) is dominated by electron impact excitation of ground state H in Ar an N_2 discharges, and dissociative excitation transfer to H_2O in He discharges. These results suggest that some degree of optimization or customization of radical production is possible by choice of the gas forming the bubble. This work follows a very good practice comparing computational results to experimental measurements. The computational model and chemical reaction mechanisms are validat-

ed and can be used further to investigate the scenarios which cannot be easily experimentally diagnosed. In order to provide more designing rules for applications, future works and recommendations are listed as follows:

a. In real applications, the size of bubbles is as large as 1 cm in diameter. The size of bubble could affect the discharges and then the radical production. Investigations in scaling with bubble size are needed.
b. Air discharges in bubbles in water may be very interesting due to its low cost. Although N_2 discharges can be seen as a good precursor of air discharges, the addition of O_2 may influence significantly the plasma produced reactive oxygen species. Investigations of plasmas in air bubbles in water, especially the role of O_2, are needed.
c. In order to compare our model to experimental results quantitatively, a 3-dimensional model needs to be developed. With 3-dimensional model, the filamentary discharges could be better resolved.

Chapter 4 discussed the investigation of the interaction of DBDs with liquid covering tissue and the ways to control the biomedical outcomes. This is one of the first works on modeling the direct interaction of plasmas with liquids. The breakdown and development of the discharge act like traditional DBDs with liquid layer as dielectric barriers. The DBDs are affected by the liquid layer through water evaporation. The addition of H_2O in air significantly increases the production of reactive species such as HO_2 and OH. The influence of the DBDs on liquid layer is mainly through solvation. When the plasma reaches the liquid, the plasma produced species get solvated and aqueous reactions start. The rates of solvation are determined by Henry's law equilibrium. UV/VUV photons also reach the liquid resulting in ionization and dissociation of water molecules. Both short-lived radicals, like hydroxyl and superoxide, and long-lived reactive species, like hydrogen peroxide and ozone, are observed and their production pathways are discussed. The fluences of reactive species to the underlying tissue are recorded and found to be sensitive to dissolved oxygen, alkane-like hydrocarbons, UV/VUV photons and the thickness of liquid layer. Due to the high density of liquids compared to gases, plasmas are generally not sustained in liquids. Certain photons and electric fields are able to penetrate into bulk liquids. However, they are beyond the discussions of the current model. The interactions of plasmas with liquids are constrained at the liquid surface, probably within nanometers. Therefore, the

surface properties of liquids play a dominant role in the gas-liquid interactions. Investigation on such interactions requires not only sufficient knowledge of liquid surface but also a powerful model with the capability of covering timescales from nanoseconds to minutes and spatial scales from nanometers to centimeters. Our current model is able to address these timescales very well. But to address the spatial scale, a sub-model focusing on molecular level may be needed. In order to suggest more means to control the outcomes, future works and recommendations are listed as follows:

a. DBDs consist of positive and negative streamers. With AC pulses in experiments, positive and negative streamers are generated in an alternate manner to prevent charging the liquid. In this work, only negative streamers were discussed. Positive streamers should also be included.
b. In the model, incident electrons and ions lose their kinetic energies simultaneously when they reach the liquid layer. Their kinetic energies should be addressed since they could significantly increase the yield of aqueous radicals, like OH_{aq}.
c. The liquid layer can be much more complex than water containing dissolved oxygen and hydrocarbon. Carbon dioxide is another species often seen dissolved in liquid water. Blood serum contains ferric and ferrous ions which can dissociate hydrogen peroxide to produce hydroxyl, which is more destructive to bacteria.
d. The sensitivity of the model with the aqueous reaction mechanism should be addressed.

Chapter 5 discussed the investigation of multipulse DBDs interacting with liquid covering tissue and effects of their discharge schemes on the biomedical outcomes. This work tends to address the long-term effects of multiple pulses as well as means to control the outcomes. The multipulse DBDs are operated with two schemes: a stationary scheme where the plasma streamer strikes at the same location of the liquid layer and a random scheme where the plasma streamer randomly strikes at the liquid layer. The two schemes result in different fluences into the underlying tissue in term of uniformity. The alternation of characteristics of the liquid layer is observed after multipulses. The liquid layer is acidified and becomes conductive after plasma treatment. The liquid layer becomes ozone-rich and nitrous acid will be slowly converted to nitric acid by ozone. The frequency of multipulse DBDs is found to influence the interaction between pulses. Although not fully investigated in this work, the influence of liquid layer on plas-

mas expands its scopes beyond water evaporation. The increase of aqueous conductivity in the liquid layer is one long-term effect which is believed to directly affect the discharges. Usually, a conductive liquid layer will enhance the discharges in the gap. Acidification and becoming ozone-rich in the liquid layer alters the plasma produced reactivity. This change can beneficial or harmful depending on the desired outcomes. This work steps forward to make it possible to compare the computational results to experiments. In order to suggest more means to control the outcomes, future works and recommendations are listed as follows:

a. In real applications, multipulse DBDs operate with positive and negative pulses in turn and accumulation of surface charging is prevented. In this work, only negative streamer ere used for multipulses. The positive streamer should also be included.
b. An increase in gas temperature is reported after long-term DBDs treatment in experiments. The rise of gas temperature could result in reduction of background gas density and enhancement of water evaporation. In the current model, the gas temperature is not calculated. This can be done in the future work.
c. An air flow across the discharge gap may influence the residual time of plasma produced species. For example, with a flow rate of 500 sccm, only species with large rates of solvation can solvate in liquids, while species with small rates of solvation are blown out of the domain. Therefore, the solvation processes are controlled by the air flow and so are aqueous species.

6.2 Publications

Research presented in this thesis has resulted in the following peer-reviewed journal articles, conference proceedings, and presentations.

Referred Journal Articles:

[1] Wei Tian and Mark J. Kushner, “Long-term effect of wet tissue treated by multipulse dielectric barrier discharges in air”, submitted to J. Phys. D: Appl. Phys.

[2] Seth A. Norberg, Wei Tian, Eric Johnsen and Mark J. Kushner, “Atmospheric pressure plasma jets interacting with liquid covered tissue: touching and not-touching the liquid”, J. Phys. D: Appl. Phys. 47 475203 (2014)

[3] Wei Tian and Mark J. Kushner, “Atmospheric pressure dielectric barrier discharges interacting with liquid covered tissue”, J. Phys. D: Appl. Phys. 47 165201 (2014).

[4] Natalia Yu Babaeva, Wei Tian and Mark J. Kushner, “The interaction between plasma filaments in dielectric barrier discharges and liquid covered wounds: electric fields delivered to model platelets and cells”, J. Phys. D: Appl. Phys. 47 235201 (2014).

[5] Wei Tian, Kunhide Tachibana and Mark J. Kushner, "Plasmas Sustained in Bubbles in Water: Optical Emission and Excitation Mechanisms", J. Phys. D: Appl. Phys. 47, 055202 (2014).

Conference Proceedings and Presentations:

[1] W. Tian and M. J. Kushner, “The long-term effects of random DBDs treatment of tissues”, 2nd COST Meeting, Barcelona, Spain, February 2015.

[2] W. Tian and M. J. Kushner, “The long term effects of dielectric barrier discharges treatment of tissues”, 67th Gaseous Electronics Conference (GEC), Raleigh, North Carolina, USA, November 2014.

[3] W. Tian and M. J. Kushner, “Atmospheric plasma treatment of wet tissues”, 3rd Young Professionals Workshop on Plasma Medicine, Mecklenburg-Western Pomerania, Germany, September 2014.

[4] W. Tian and M. J. Kushner, “Long term exposure of atmospheric dielectric barrier discharges onto wet tissue”, 41st IEEE International Conference on Plasma Science (ICOPS), Washington DC, USA, May 2014.

[5] W. Tian and M. J. Kushner, “Atmospheric pressure dielectric barrier discharge interaction with wet tissue – modeling long(er) term exposure”, The 1st International Workshop on Plasma for Cancer Treatment (IWPCT), Washington DC, USA, March 2014.

[6] W. Tian and M. J. Kushner, “Atmospheric pressure dielectric barrier discharges interacting with liquid covered tissue”, 66th Gaseous Electronics Conference (GEC), Princeton, New Jersey, USA, October 2013.

[7] W. Tian and M. J. Kushner, “The interaction of atmospheric pressure plasmas with liquid covered tissues”, 40th IEEE International Conference on Plasma Science (ICOPS), San Francisco, California, USA, June 2013.

[8] W. Tian, S. Norburg, N. Babaeva and M. J. Kushner, “The interaction of atmospheric pressure dbds with liquid covered tissues”, Department of Energy (DOE), Baltimore, Maryland, June 2013

[9] W. Tian, K. Tachibana and M. J. Kushner, “Simulations of plasma dynamics of electrical discharges sustained in bubbles in water”, 7th International Workshop on Mciroplasmas (IWM), Beijing, China, May 2013.

[10] W. Tian and M. J. Kushner, “Simulations of images and optical spectra of plasmas sustained in bubbles in water”, 65th Gaseous Electronics Conference (GEC), Austin, Texas, USA, October 2012.

[11] W. Tian and M. J. Kushner, “Simulations of plasma dynamics of electrical discharges sustained in bubbles in water: images and optical spectra”, Gordon Research Conference on Plasma Processing Science (GRC), Smithfield, Rhode Island, August 2012.

[12] W. Tian and M. J. Kushner, “Steamer initiation and propagation in water with the assistance of bubbles and electric field initiated rarefaction”, 64th Gaseous Electronics Conference (GEC), Slat Lake City, Utah, USA, October 2011.

APPENDIX I LIST OF REACTIONS

Reaction	Rate Coefficient[a]	Ref.
He Reactions		
$e + He \rightarrow He + e$	b	[1]
$e + He \leftrightarrow He^{*} + e$	b,c	[2]
$e + He \leftrightarrow He^{**} + e$	b,c	[2]
$e + He \leftrightarrow He^{***} + e$	b,c	[2]
$e + He^{*} \leftrightarrow He^{**} + e$	b,c	[2]
$e + He^{*} \leftrightarrow He^{***} + e$	b,c	[2]
$e + He^{**} \leftrightarrow He^{***} + e$	b,c	[2]
$e + He \rightarrow He^{+} + e + e$	b	[3]
$e + He^{*} \rightarrow He^{+} + e + e$	b	[4]
$e + He^{**} \rightarrow He^{+} + e + e$	b	[4]
$e + He^{***} \rightarrow He^{+} + e + e$	b	[4]
$e + He^{+} \rightarrow He^{*}$	$6.76 \times 10^{-13}\ T_e^{-0.5}$	[5]
$e + e + He^{+} \rightarrow He^{*} + e$	$6.2 \times 10^{-27}\ T_e^{-4.4}\ cm^6s^{-1}$	[5]
$e + He + He^{+} \rightarrow He^{*} + He$	$6.6 \times 10^{-30}\ T_e^{-2}\ cm^6s^{-1}$	[6]
$e + He_2^{+} \rightarrow He^{*} + He$	$7.12 \times 10^{-15}\ (T_e/T_g)^{-1.5}$	[1]
$e + He + He_2^{+} \rightarrow He_2^{*} + He$	$1.5 \times 10^{-27}\ cm^6s^{-1}$	[1]
$e + He + He_2^{+} \rightarrow He^{*} + He + He$	$3.5 \times 10^{-27}\ cm^6s^{-1}$	[1]
$e + e + He_2^{+} \rightarrow He_2^{*} + e$	$1.2 \times 10^{-21}\ cm^6s^{-1}$	[1]
$e + e + He_2^{+} \rightarrow He^{*} + He + e$	$2.8 \times 10^{-20}\ cm^6s^{-1}$	[1]
$e + He_2^{*} \rightarrow He + He + e$	3.8×10^{-9}	[1]
$(He^{*}, He^{**}, He^{***}) + (He^{*}, He^{**}, He^{***}) \rightarrow He + He^{+} + e$	$5 \times 10^{-10}\ T_n^{0.5}$	[1],e

$He^+ + He \rightarrow He + He^+$	$6 \times 10^{-10}\ T_n^{0.5}$	[7]
$He^+ + He + He \rightarrow He + He_2^+$	$1.41 \times 10^{-31}\ T_n^{-0.5}\ cm^6s^{-1}$	[8]
$(He^*, He^{**}, He^{***}) + He + He \rightarrow He + He_2^*$	$1.6 \times 10^{-32}\ cm^6s^{-1}$	[1],e
Ar Reactions		
$e + Ar \rightarrow Ar + e$	b	[9]
$e + Ar \leftrightarrow Ar^* + e$	b,c	[9]
$e + Ar \leftrightarrow Ar^{**} + e$	b,c	[9]
$e + Ar \leftrightarrow Ar^{***} + e$	b,c	[9]
$e + Ar^* \leftrightarrow Ar^{**} + e$	b,c	[9]
$e + Ar^* \leftrightarrow Ar^{***} + e$	b,c	[10]
$e + Ar^{**} \leftrightarrow Ar^{***} + e$	b,c	[10]
$e + Ar \rightarrow Ar^+ + e + e$	b	[3]
$e + Ar^* \rightarrow Ar^+ + e + e$	b	[11]
$e + Ar^{**} \rightarrow Ar^+ + e + e$	b	[11]
$e + Ar^{***} \rightarrow Ar^+ + e + e$	b	[4]
$e + Ar^+ \rightarrow Ar^{***}$	$4 \times 10^{-13}\ T_e^{-0.5}$	[12]
$e + e + Ar^+ \rightarrow Ar^{***} + e$	$5 \times 10^{-27}\ T_e^{-4.5}\ cm^6s^{-1}$	[12]
$e + Ar_2^* \rightarrow Ar_2^+ + e + e$	$9 \times 10^{-8}\ T_e^{0.7}$	[13]
$e + Ar_2^* \rightarrow Ar + Ar + e$	1×10^{-7}	[13]
$e + Ar_2^+ \rightarrow Ar^{***} + Ar$	$5.38 \times 10^{-8}\ T_e^{-0.66}$	[13]
$(Ar^*, Ar^{**}, Ar^{***}) + (Ar^*, Ar^{**}, Ar^{***}) \rightarrow Ar + Ar^+ + e$	$5 \times 10^{-10}\ T_n^{0.5}$	[13],e
$Ar^+ + Ar \rightarrow Ar + Ar^+$	$5.66 \times 10^{-10}\ T_n^{0.5}$	[7]
$Ar^+ + Ar + Ar \rightarrow Ar + Ar_2^+$	$1.41 \times 10^{-31}\ T_n^{-0.5}\ cm^6s^{-1}$	[13]
$(Ar^*, Ar^{**}, Ar^{***}) + Ar + Ar \rightarrow Ar + Ar_2^*$	$1.14 \times 10^{-32}\ cm^6s^{-1}$	[13],e
N_2 Reactions		
$e + N_2 \rightarrow N_2 + e$	b	[14]
$e + N_2 \leftrightarrow N_2^* + e$	b,c	[14]
$e + N_2 \leftrightarrow N_2^{**} + e$	b,c	[14]
$e + N_2 \leftrightarrow N_2^{***} + e$	b,c	[14]
$e + N_2^* \leftrightarrow N_2^{**} + e$	b,c	[14]

$e + N_2^* \leftrightarrow N_2^{***} + e$	b,c	[14]
$e + N_2^{**} \leftrightarrow N_2^{***} + e$	b,c	[14]
$e + N_2 \rightarrow N_2^+ + e + e$	b	[14]
$e + N_2^* \rightarrow N_2^+ + e + e$	b	[14]
$e + N_2^{**} \rightarrow N_2^+ + e + e$	b	[14]
$e + N_2^{***} \rightarrow N_2^+ + e + e$	b	[15]
$e + N_2 \rightarrow N + N + e$	b	[14]
$e + N_2 \leftrightarrow N_2(v) + e$	b,c	[14]
$e + N_2(v) \rightarrow N_2(v) + e$	b	[14]
$e + N_2(v) \leftrightarrow N_2^* + e$	b,c	[14]
$e + N_2(v) \rightarrow N_2^+ + e + e$	b	[14]
$e + N \rightarrow N + e$	b	[16]
$e + N \leftrightarrow N^* + e$	b,c	[17]
$e + N \rightarrow N^+ + e + e$	b	[18]
$e + N^* \rightarrow N^+ + e + e$	b	[17]
$e + N_2^+ \rightarrow N^* + N$	$2 \times 10^{-7}\ T_e^{-0.5}$	[19]
$e + N_4^+ \rightarrow N_2 + N_2$	$2 \times 10^{-7}\ T_e^{-0.5}$	[19],d
$N^* + N_2 \rightarrow N + N_2$	2.4×10^{-14}	[20]
$N_2^* + N_2 \rightarrow N_2 + N_2$	1×10^{-11}	[21]
$N_2^{**} + N_2 \rightarrow N_2 + N_2$	1×10^{-11}	[21],d
$N_2^{**} + N_2 \rightarrow N_2^{***} + N_2$	1×10^{-11}	[21],d
$N_2^{***} + N_2 \rightarrow N_2^* + N_2$	1×10^{-11}	[21],d
$N_2^* + N_2^* \rightarrow N_2 + N_2^{**}$	1×10^{-10}	[22]
$N_2(v) + N_2 \rightarrow N_2 + N_2$	1×10^{-11}	[21],d
$N_2(v) + N \rightarrow N_2 + N$	1×10^{-11}	[21],d
$N_2^{***} + N_2^* \rightarrow N_4^+ + e$	5×10^{-11}	[23]
$N_2^{***} + N_2^{**} \rightarrow N_4^+ + e$	5×10^{-11}	[23],d
$N_2^{***} + N_2^{***} \rightarrow N_4^+ + e$	2×10^{-10}	[23]
$N^+ + N \rightarrow N + N^+$	5×10^{-12}	[24],d
$N_2^+ + N \rightarrow N_2 + N^+$	5×10^{-12}	[24]
$N_2^+ + N^* \rightarrow N_2 + N^+$	1×10^{-10}	[24]

$N_2^+ + N_2 + N_2 \rightarrow N_2 + N_4^+$	$6.8 \times 10^{-29}\ T_n^{-1.64}$	[24]
$N_4^+ + N_2 \rightarrow N_2 + N_2 + N_2^+$	$9.35 \times 10^{-13}\ T_n^{1.5}$	[24]
<u>H_2O, OH, H Reactions</u>		
$e + H_2O \rightarrow H_2O + e$	b	[25]
$e + H_2O \rightarrow H_2O(v1,2; v3,4) + e$	b	[25],g
$e + H_2O \rightarrow H_2O^+ + e + e$	b	[25]
$e + H_2O \rightarrow O^- + H_2$	b	[25]
$e + H_2O \rightarrow OH^- + H$	b	[25]
$e + H_2O \rightarrow OH + H + e$	b	[25]
$e + H_2O \rightarrow OH + H^* + e$	b	[25]
$e + H_2O \rightarrow OH + H^{**} + e$	b	[25]
$e + H_2O \rightarrow OH + H^{***} + e$	b	[25]
$e + H_2O \rightarrow OH^* + H + e$	b	[25]
$e + H_2O^+ \rightarrow OH + H$	$5.1 \times 10^{-8}\ T_e^{-0.5}$	[26]
$e + H \rightarrow H + e$	b	[27]
$e + H \leftrightarrow H^* + e$	b,c	[28]
$e + H \leftrightarrow H^{**} + e$	b,c	[28]
$e + H \leftrightarrow H^{***} + e$	b,c	[28]
$e + H^* \leftrightarrow H^{**} + e$	b,c	[28]
$e + H^* \leftrightarrow H^{***} + e$	b,c	[28]
$e + H^{**} \leftrightarrow H^{***} + e$	b,c	[28]
$e + OH \rightarrow OH^* + e$	$2.7 \times 10^{-10}\ T_e^{0.5}$	[29]
$e + OH^* \rightarrow O + H + e$	$1.5 \times 10^{-7}\ T_e^{-0.75} \exp(-3.9/T_e)$	[30]
$H_2O^+ + H_2O \rightarrow H_2O + H_2O^+$	5.1×10^{-11}	[24],d
$(H^*, H^{**}, H^{***}) + H_2O \rightarrow H + H_2O$	9.1×10^{-9}	[31],d,e
$(H^{**}, H^{***}) + H_2O \rightarrow H^* + H_2O$	9.1×10^{-9}	[31],e
$H^{***} + H_2O \rightarrow H^{**} + H_2O$	9.1×10^{-9}	[31],d
$OH^* + H_2O \rightarrow OH + H_2O$	9.1×10^{-9}	[31],d
$OH^- + H \rightarrow H_2O + e$	1.8×10^{-9}	[32],d
$(OH, OH^*) + H \rightarrow H_2O$	$6.87 \times 10^{-31} T_n^{-2}$	[33],d,e
$(OH, OH^*) + (OH, OH^*) + M \rightarrow H_2O_2 + M$	$6.9 \times 10^{-31} T_n^{-0.8}\ cm^6 s^{-1}$	[33],e,j

$H_2 + HO_2 \rightarrow H_2O_2 + H$	$5 \times 10^{-11}\exp(-T_g/11310)$	[33]
$HO_2 + HO_2 \rightarrow H_2O_2 + O_2$	$8.05 \times 10^{-11} T_n^{-1}$	[33]
$HO_2 + HO_2 + M \rightarrow H_2O_2 + O_2 + M$	$1.9 \times 10^{-33}\exp(980/T_g)$ cm^6s^{-1}	[33],d,j
$HO_2 + H_2O \rightarrow H_2O_2 + OH$	$4.65 \times 10^{-11}\exp(-11647/T_g)$	[33]
$H + H_2O_2 \rightarrow HO_2 + H_2$	$8 \times 10^{-11}\exp(-4000/T_g)$	[33]
$H + H_2O_2 \rightarrow OH + H_2O$	$4 \times 10^{-11}\exp(-2000/T_g)$	[33]
$O_2 + H_2O_2 \rightarrow HO_2 + HO_2$	$9 \times 10^{-11}\exp(-19965/T_g)$	[33]
$O + H_2O_2 \rightarrow HO_2 + OH$	$1.4 \times 10^{-12}\exp(-2000/T_g)$	[33]
$O^* + H_2O_2 \rightarrow O_2 + H_2O$	5.2×10^{-10}	[33]
$OH + H_2O_2 \rightarrow HO_2 + H_2O$	$2.9 \times 10^{-12}\exp(-160/T_g)$	[33]
$H_2O_2 \rightarrow OH + OH$	$1.96 \times 10^{-09} T_n^{-4.86}\exp(-26800/T_g)$ s^{-1}	[33]
$(H, H^*, H^{**}, H^{***}) + H_2O_2 \rightarrow OH + H_2O$	$4 \times 10^{-11}\exp(-2000/T_g)$	[34],e
$OH^- + OH^+ + M \rightarrow H_2O_2 + M$	$2 \times 10^{-25} T_n^{-2.5}$ cm^6s^{-1}	h,j
$OH^- + H^+ + M \rightarrow H_2O + M$	$2 \times 10^{-25} T_n^{-2.5}$ cm^6s^{-1}	h,j
$OH^- + H_2O^+ + M \rightarrow OH + H_2O + M$	$2 \times 10^{-25} T_n^{-2.5}$ cm^6s^{-1}	h,j
$O^- + OH^+ + M \rightarrow HO_2 + M$	$2 \times 10^{-25} T_n^{-2.5}$ cm^6s^{-1}	h,j
$O^- + H^+ + M \rightarrow OH + M$	$2 \times 10^{-25} T_n^{-2.5}$ cm^6s^{-1}	h,j
$O^- + H_2O^+ + M \rightarrow O + H_2O + M$	$2 \times 10^{-25} T_n^{-2.5}$ cm^6s^{-1}	h,j
$O^- + O \rightarrow O_2 + e$	5×10^{-10}	[23]
<u>Excitation and Charge Transfer</u>		
$He^+ + H_2O \rightarrow He + H_2O^+$	6.05×10^{-11}	[35]
$He^+ + H_2O \rightarrow He + H + OH^+$	2.86×10^{-10}	[35]
$He_2^+ + H_2O \rightarrow He + He + H_2O^+$	6.05×10^{-11}	[35],d
$He_2^+ + H_2O \rightarrow He + He + H + OH^+$	2.86×10^{-10}	[35],d
$(He^*, He^{**}, He^{***}) + H_2O \rightarrow He + H_2O^+ + e$	6.6×10^{-10}	[35],d,e
$(He^*, He^{**}, He^{***}) + H_2O \rightarrow He + OH + H^+ + e$	2.6×10^{-11}	[35],e
$(He^*, He^{**}, He^{***}) + H_2O \rightarrow He + OH^* + H^+ + e$	2.6×10^{-11}	[35],e
$(He^*, He^{**}, He^{***}) + H_2O \rightarrow He + H + OH^+$	1.5×10^{-10}	[35],d,e

+ e		
(He*, He**, He***) + H_2O → He + OH + H	1.5×10^{-10}	[36],e
(He*, He**, He***) + H_2O → He + OH^* + H	1.5×10^{-10}	[36],d,e
(He*, He**, He***) + H_2O → He + OH + H^*	1.5×10^{-10}	[36],d,e
(He*, He**, He***) + H_2O → He + OH + H^{**}	1.5×10^{-10}	[36],d,e
(He*, He**, He***) + H_2O → He + OH + H^{***}	1.5×10^{-10}	[36],d,e
He_2^* + H_2O → He + He + H_2O^+ + e	6.6×10^{-10}	[35]
He_2^* + H_2O → He + He + (OH, OH^*) + H^+ + e	2.6×10^{-11}	[35],e
He_2^* + H_2O → He + He + H + OH^+ + e	1.5×10^{-10}	[35]
He_2^* + H_2O → He + He + H_2O^+ + e	6.6×10^{-10}	[36]
He_2^* + H_2O → He + He + OH + (H, H*, H**, H***)	1.5×10^{-10}	[36],e
He_2^* + H_2O → He + He + OH^* + H	1.5×10^{-10}	[36],d
He^+ + O^- + M → He + O + M	$2 \times 10^{-25} T_n^{-2.5}$ $cm^6 s^{-1}$	h,j
He_2^+ + O^- + M → He + He + O + M	$2 \times 10^{-25} T_n^{-2.5}$ $cm^6 s^{-1}$	h,j
He^+ + OH^- + M → He + OH + M	$2 \times 10^{-25} T_n^{-2.5}$ $cm^6 s^{-1}$	h,j
He_2^+ + OH^- + M → He + He + OH + M	$2 \times 10^{-25} T_n^{-2.5}$ $cm^6 s^{-1}$	h,j
Ar^+ + H_2O → Ar + H_2O^+	1.5×10^{-10}	[24]
Ar_2^+ + H_2O → Ar + Ar + H_2O^+	1.5×10^{-10}	[24],d
(Ar^*, Ar**, Ar***) + H_2O → Ar + OH + H	4.8×10^{-10}	[37],d,e
(Ar^*, Ar**, Ar***) + H_2O → Ar + OH* + H	4.8×10^{-10}	[37],d,e
Ar_2^* + H_2O → Ar + Ar + (OH, OH^*) + H	4.8×10^{-10}	[37],d,e
Ar^+ + O^- + (Ar, H_2O) → Ar + (Ar, H_2O) + O	$2 \times 10^{-25} T_n^{-2.5}$ $cm^6 s^{-1}$	h,e
Ar_2^+ + O^- + (Ar, H_2O) → Ar + Ar + (Ar ,H_2O) + O	$2 \times 10^{-25} T_n^{-2.5}$ $cm^6 s^{-1}$	h,e
Ar^+ + OH^- + (Ar, H_2O) → Ar + (Ar, H_2O) + OH	$2 \times 10^{-25} T_n^{-2.5}$ $cm^6 s^{-1}$	h,e
Ar_2^+ + OH^- + (Ar, H_2O) → Ar + Ar + (Ar, H_2O) + OH	$2 \times 10^{-25} T_n^{-2.5}$ $cm^6 s^{-1}$	h,e
N_2^+ + H_2O → N_2 + H_2O^+	2.4×10^{-9}	[24]
N^+ + H_2O → N + H_2O^+	2.4×10^{-9}	[24],d

$N_4^+ + H_2O \rightarrow N_2 + N_2 + H_2O^+$	2×10^{-10}	[24]
$N_2^+ + O^- + M \rightarrow N_2 + O + M$	$2 \times 10^{-25} T_n^{-2.5}$ $cm^6 s^{-1}$	h,j
$N_4^+ + O^- + M \rightarrow N_2 + N_2 + O + M$	$2 \times 10^{-25} T_n^{-2.5}$ $cm^6 s^{-1}$	h,j
$N_2^+ + OH^- + M \rightarrow N_2 + OH + M$	$2 \times 10^{-25} T_n^{-2.5}$ $cm^6 s^{-1}$	h,j
$N_4^+ + OH^- + M \rightarrow N_2 + N_2 + OH + M$	$2 \times 10^{-25} T_n^{-2.5}$ $cm^6 s^{-1}$	h,j
$(N_2^{**}, N_2^{***}) + H_2O \rightarrow N_2 + OH + H$	4.5×10^{-10}	[38],d,e
$N_2^{**} + H_2O \rightarrow N_2 + OH^* + H$	4.5×10^{-10}	[38],d
<u>Air Reactions</u>		
$e + N_2 \rightarrow N_2 + e$	b	[14]
$e + N_2 \leftrightarrow N_2^* + e$	b,c	[14]
$e + N_2 \leftrightarrow N_2^{**} + e$	b,c	[14]
$e + N_2^* \leftrightarrow N_2^{**} + e$	b,c	[14]
$e + (N_2, N_2^*, N_2^{**}) \rightarrow N_2^+ + e + e$	b	[14],e
$e + (N_2, N_2^*, N_2^{**}) \rightarrow N + N + e$	b	[14],e
$e + N_2^+ \rightarrow N + N$	$2 \times 10^{-7}\ T_e^{-0.5}$	[19]
$e + O_2 \rightarrow O_2 + e$	b	[39]
$e + O_2 \leftrightarrow O_2^* + e$	b,c	[39],d,e
$e + (O_2, O_2^*) \rightarrow O_2^+ + e + e$	b	[39],e
$e + (O_2, O_2^*) \rightarrow O + O + e$	b	[39],e
$e + (O_2, O_2^*) \rightarrow O^- + O$	b	[39],e
$e + O_2^+ \rightarrow O + O$	$1.2 \times 10^{-8}\ T_e^{-0.7}$	[40,41]
$e + H_2O \rightarrow H_2O + e$	b	[25]
$e + H_2O \rightarrow H_2O^+ + e + e$	b	[25]
$e + H_2O \rightarrow H + OH + e$	b	[25]
$e + H_2O \rightarrow H_2 + O^-$	b	[25]
$e + H_2O^+ \rightarrow H + OH$	$1.2 \times 10^{-8}\ T_e^{-0.7}$	[26,42]
$N_2^+ + N_2 + (N_2, O_2, H_2O) \rightarrow N_4^+ + (N_2, O_2, H_2O)$	$6.8 \times 10^{-29}\ T_n^{-1.64}$	[24],d,e
$N_4^+ + (N_2, O_2, H_2O) \rightarrow N_2^+ + N_2 + (N_2, O_2, H_2O)$	$9.35 \times 10^{-13}\ T_n^{1.5}$	[24],d,e
$O_2^- + N_4^+ \rightarrow O_2 + N_2 + N_2$	2×10^{-6}	[20,43],d

$O_2^- + N_2^+ \rightarrow O_2 + N_2$	2×10^{-6}	[20,43]
$O_2^- + O_2^+ \rightarrow O_2 + O_2$	2×10^{-6}	[44,45]
$O_2^- + H_2O^+ \rightarrow O_2 + H_2O$	2×10^{-6}	[44]
$O^- + N_4^+ \rightarrow O + N_2 + N_2$	3×10^{-6}	[43,44],d
$O^- + N_2^+ \rightarrow O + N_2$	3×10^{-6}	[43,44]
$O^- + O_2^+ \rightarrow O + O_2$	3×10^{-6}	[44]
$O^- + H_2O^+ \rightarrow O + H_2O$	3×10^{-6}	[44]
$O^- + O_2^+ + (N_2 , O_2, H_2O) \rightarrow O + O_2 + (N_2 , O_2, H_2O)$	$2.0 \times 10^{-25}\ T_n^{-2.5}$	[46]
$O^- + O_2 \rightarrow O_2^- + O$	1.5×10^{-20}	[43,44]
$O^- + O \rightarrow O_2 + e$	1.9×10^{-10}	[24,40]
$O^- + O_3 \rightarrow O_2 + O_2 + e$	3.1×10^{-10}	[24,40]
$O^- + O_3 \rightarrow O_2 + O_2^-$	1×10^{-11}	[24,40]
$O_2^- + O \rightarrow O_3 + e$	1.5×10^{-10}	[43,44]
$O_2^- + O \rightarrow O^- + O_2$	1.5×10^{-10}	[43,44]
$O_2^- + O_2^* \rightarrow O_2 + O_2 + e$	2×10^{-10}	[43,44]
$N_2^+ + O_2 \rightarrow O_2^+ + N_2$	5.1×10^{-11}	[24,40]
$O_2^+ + O_2 \rightarrow O_2 + O_2^+$	1×10^{-9}	[24,40]
$H_2O^+ + H_2O \rightarrow H_2O + H_2O^+$	5.1×10^{-11}	[24,40]
$O_2^* + (N_2 , O_2, H_2O) \rightarrow O_2 + (N_2 , O_2, H_2O)$	2.2×10^{-18}	[40,47]
$O_2^* + O_2 \rightarrow O + O_3$	2.9×10^{-21}	[40,47]
$O_2^* + O_3 \rightarrow O_2 + O_2 + O$	9.9×10^{-11}	[40,47]
$(N_2^* , N_2^{**}) + N_2 \rightarrow N_2 + N_2$	1.9×10^{-13}	[21,40]
$(N_2^* , N_2^{**}) + O_2 \rightarrow N_2 + O_2$	2.8×10^{-11}	[21,40]
$(N_2^* , N_2^{**}) + O_2 \rightarrow N_2 + O + O$	1.5×10^{-12}	[21,40]
$O + O_2 + (N_2 , O_2, H_2O) \rightarrow O_3 + (N_2 , O_2, H_2O)$	$6.9 \times 10^{-34}\ T_n^{-1.2}$	[33]
$O + O + (N_2 , O_2, H_2O) \rightarrow O_2 + (N_2 , O_2, H_2O)$	5.2×10^{-35}	[33]
$N + N + (N_2 , O_2, H_2O) \rightarrow N_2 + (N_2 , O_2, H_2O)$	3.9×10^{-33}	[33]
$OH + OH + (N_2 , O_2, H_2O) \rightarrow H_2O_2 + (N_2 , O_2, H_2O)$	$6.9 \times 10^{-35}\ T_e^{-0.8}$	[33]

$HO_2 + HO_2 \rightarrow H_2O_2 + O_2$	$8 \times 10^{-11}\ T_e^{-1.0}$	[33]
$HO_2 + HO_2 + (N_2 , O_2, H_2O) \rightarrow H_2O_2 + O_2 + (N_2 , O_2, H_2O)$	1.9×10^{-33}	[33]
$N + O + (N_2 , O_2, H_2O) \rightarrow NO + (N_2 , O_2, H_2O)$	5.5×10^{-33}	[33]
$N + O_2 \rightarrow NO + O$	8.5×10^{-17}	[33]
$N + O_3 \rightarrow NO + O_2$	5×10^{-16}	[33]
$N + NO_2 \rightarrow N_2O + O$	1.2×10^{-11}	[33]
$NO + O_2^* \rightarrow NO + O_2$	3.5×10^{-17}	[33],d
$NO + O_2^* \rightarrow NO_2 + O$	4.9×10^{-18}	[33],d
$NO + O_3 \rightarrow NO_2 + O_2$	1.8×10^{-14}	[33]
$NO_2 + O_3 \rightarrow NO_3 + O_2$	3.2×10^{-17}	[33]
$NO + NO_2 \rightarrow N_2O_3$	7.9×10^{-12}	[33]
$NO_2 + NO_2 \rightarrow N_2O_4$	1×10^{-12}	[33]
$NO_2 + NO_3 \rightarrow N_2O_5$	1.9×10^{-12}	[33]
$NO + NO + O_2 \rightarrow NO_2 + NO_2$	2×10^{-38}	[33]
$NO + O + (N_2 , O_2, H_2O) \rightarrow NO_2 + (N_2 , O_2, H_2O)$	1×10^{-31}	[33]
$NO + NO_2 + (N_2 , O_2, H_2O) \rightarrow N_2O_3 + (N_2 , O_2, H_2O)$	3.1×10^{-34}	[33]
$NO_2 + NO_2 + (N_2 , O_2, H_2O) \rightarrow N_2O_4 + (N_2 , O_2, H_2O)$	1.4×10^{-33}	[33]
$NO_2 + NO_3 + (N_2 , O_2, H_2O) \rightarrow N_2O_5 + (N_2 , O_2, H_2O)$	3.6×10^{-30}	[33]
<u>Solvation</u>		
$e + H_2O_{aq} \rightarrow e_{aq} + H_2O_{aq}$	2×10^9	[37],k
$N_2^+ + H_2O_{aq} \rightarrow N_2^+{}_{aq} + H_2O_{aq}$	$10^7 - 10^5$	k
$N_4^+ + H_2O_{aq} \rightarrow N_4^+{}_{aq} + H_2O_{aq}$	$10^7 - 10^5$	k
$O_2^+ + H_2O_{aq} \rightarrow O_2^+{}_{aq} + H_2O_{aq}$	$10^7 - 10^5$	k
$NO^+ + H_2O_{aq} \rightarrow NO^+{}_{aq} + H_2O_{aq}$	$10^7 - 10^5$	k

$O^- + H_2O_{aq} \rightarrow O^-_{aq} + H_2O_{aq}$	$10^7 - 10^5$	k
$O_2^- + H_2O_{aq} \rightarrow O_2^-{}_{aq} + H_2O_{aq}$	$10^7 - 10^5$	k
$H^+ + H_2O_{aq} \rightarrow H_3O^+_{aq}$	$10^7 - 10^5$	k
$H_3O^+ + H_2O_{aq} \rightarrow H_3O^+_{aq} + H_2O_{aq}$	$10^7 - 10^5$	k
$H_5O_2^+ + H_2O_{aq} \rightarrow H_3O^+_{aq} + H_2O_{aq} + H_2O_{aq}$	$10^7 - 10^5$	k
$O + H_2O_{aq} \rightarrow O_{aq} + H_2O_{aq}$	$10^7 - 10^5$	k
$O_3 + H_2O_{aq} \rightarrow O_{3aq} + H_2O_{aq}$	$10^7 - 10^5$	k
$H + H_2O_{aq} \rightarrow H_{aq} + H_2O_{aq}$	$10^7 - 10^5$	k
$H_2 + H_2O_{aq} \rightarrow H_{2aq} + H_2O_{aq}$	$10^7 - 10^5$	k
$HO_2 + H_2O_{aq} \rightarrow HO_{2aq} + H_2O_{aq}$	$10^7 - 10^5$	k
$OH + H_2O_{aq} \rightarrow OH_{aq} + H_2O_{aq}$	$10^7 - 10^5$	k
$H_2O_2 + H_2O_{aq} \rightarrow H_2O_{2aq} + H_2O_{aq}$	$10^7 - 10^5$	k
$NO + H_2O_{aq} \rightarrow NO_{aq} + H_2O_{aq}$	$10^7 - 10^5$	k
$N_xO_y + H_2O_{aq} \rightarrow N_xO_{y\,aq} + H_2O_{aq}$	$10^7 - 10^5$	k
N_xO_y = NO_2, NO_3, N_2O_3, N_2O_4 and N_2O_5		
$HNO_x + H_2O_{aq} \rightarrow HNO_{xaq} + H_2O_{aq}$	$10^7 - 10^5$	k
HNO_x = HNO_2 and HNO_3		
$HOONO + H_2O_{aq} \rightarrow HOONO_{aq} + H_2O_{aq}$	$10^7 - 10^5$	k
In Water Reactions		
$e_{aq} + H_2O_{aq} \rightarrow H\bullet_{aq} + OH^-_{aq}$	1.9×10^1	[48]
$e_{aq} + H_2O^+_{aq} \rightarrow H\bullet_{aq} + OH_{aq}$	6×10^{11}	[48]
$e_{aq} + e^-_{aq} + H_2O_{aq} + H_2O_{aq} \rightarrow H_{2aq} + OH^-_{aq} + OH^-_{aq}$	1.0×10^8 $M^{-3}s^{-1}$	[48]
$e_{aq} + H\bullet_{aq} + H_2O_{aq} \rightarrow H_{2aq} + OH^-_{aq}$	2.5×10^{10} $M^{-2}s^{-1}$	[48]
$e_{aq} + \bullet OH_{aq} \rightarrow OH^-_{aq}$	3.0×10^{10}	[48]

$e_{aq} + \bullet O^-_{aq} + H_2O_{aq} \rightarrow OH^-_{aq} + OH^-_{aq}$	2.2×10^{10} $M^{-2}s^{-1}$	[48]
$e_{aq} + H_3O^+_{aq} \rightarrow H\bullet_{aq} + H_2O_{aq}$	2.3×10^{10}	[48]
$e_{aq} + H_2O_{2aq} \rightarrow \bullet OH_{aq} + OH^-_{aq}$	1.1×10^{10}	[48]
$e_{aq} + HO_2^-{}_{aq} + H_2O_{aq} \rightarrow \bullet OH_{aq} + OH^-_{aq} + OH^-_{aq}$	3.5×10^{9} $M^{-2}s^{-1}$	[48]
$e_{aq} + O_{2aq} \rightarrow O_2^-{}_{aq}$	1.9×10^{10}	[48]
$e_{aq} + O_{aq} \rightarrow O^-_{aq}$	1.9×10^{10}	[48],d
$H\bullet_{aq} + H_2O_{aq} \rightarrow H_{2aq} + \bullet OH_{aq}$	1×10^{1}	[48]
$H\bullet_{aq} + H\bullet_{aq} \rightarrow H_{2aq}$	7.5×10^{9}	[48]
$H\bullet_{aq} + \bullet OH_{aq} \rightarrow H_2O_{aq}$	7×10^{9}	[48]
$H\bullet_{aq} + OH^-_{aq} \rightarrow e_{aq} + H_2O_{aq}$	2.2×10^{7}	[48]
$H\bullet_{aq} + H_2O_{2aq} \rightarrow \bullet OH_{aq} + H_2O_{aq}$	9×10^{7}	[48]
$H_{2aq} + H_2O_{2aq} \rightarrow H\bullet_{aq} + \bullet OH_{aq} + H_2O_{aq}$	6×10^{6}	[48]
$H\bullet_{aq} + O_{2aq} \rightarrow HO_2\bullet_{aq}$	2.1×10^{10}	[48]
$H\bullet_{aq} + HO_2\bullet_{aq} \rightarrow H_2O_{2aq}$	1×10^{10}	[48]
$O\bullet_{aq} + H_2O_{aq} \rightarrow \bullet OH_{aq} + \bullet OH_{aq}$	1.3×10^{4}	[48],d
$O\bullet_{aq} + O_{2aq} \rightarrow O_{3aq}$	3×10^{9}	[48],d
$\bullet OH_{aq} + \bullet OH_{aq} \rightarrow H_2O_{2aq}$	5.5×10^{9}	[48]
$\bullet OH_{aq} + \bullet O^-_{aq} \rightarrow HO_2^-{}_{aq}$	2×10^{10}	[48]
$\bullet OH_{aq} + H_{2aq} \rightarrow H\bullet_{aq} + H_2O_{aq}$	4.2×10^{7}	[48]
$\bullet OH_{aq} + OH^-_{aq} \rightarrow \bullet O^-_{aq} + H_2O_{aq}$	1.3×10^{10}	[48]
$\bullet OH_{aq} + HO_2\bullet_{aq} \rightarrow H_2O_{aq} + O_{2aq}$	6×10^{9}	[48]
$\bullet OH_{aq} + O_2^-{}_{aq} \rightarrow OH^-_{aq} + O_{2aq}$	8×10^{9}	[48]
$\bullet O^-_{aq} + H_2O_{aq} \rightarrow OH^-_{aq} + \bullet OH_{aq}$	1.8×10^{6}	[48]
$\bullet O^-_{aq} + H_{2aq} \rightarrow OH^-_{aq} + H\bullet_{aq}$	8.0×10^{7}	[48]
$\bullet O^-_{aq} + H_2O_{2aq} \rightarrow O_2^-{}_{aq} + H_2O_{aq}$	5×10^{8}	[48]

$\bullet O^-_{aq} + HO_2^-{}_{aq} \rightarrow O_2^-{}_{aq} + OH^-_{aq}$	4×10^8	[48]
$\bullet O^-_{aq} + O_{2aq} \rightarrow O_3^-{}_{aq}$	3.6×10^9	[48]
$\bullet O^-_{aq} + O_2^-{}_{aq} + H_2O_{aq} \rightarrow OH^-_{aq} + OH^-_{aq} + O_{2aq}$	6×10^8 $M^{-2}s^{-1}$	[48]
$\bullet OH_{aq} + H_2O_{2aq} \rightarrow H_2O_{aq} + HO_2\bullet_{aq}$	2.7×10^7	[48]
$\bullet OH_{aq} + HO_2^-{}_{aq} \rightarrow OH^-_{aq} + HO_2\bullet_{aq}$	7.5×10^9	[48]
$H_2O^+_{aq} + H_2O_{aq} \rightarrow H_3O^+_{aq} + \bullet OH_{aq}$	6×10^3	[48]
$\bullet OH_{aq} + NO_2^-{}_{aq} \rightarrow OH^-_{aq} + NO_{2aq}$	1×10^{10}	[49]
$H_2O_{2aq} + NO_2^-{}_{aq} \rightarrow OONO^-_{aq} + H_2O_{aq}$	4.5×10^8	[49]
$H\bullet_{aq} + NO_2^-{}_{aq} \rightarrow OH^-_{aq} + NO_{aq}$	1.2×10^9	[49]
$\bullet O^-_{aq} + NO_2^-{}_{aq} + H_2O_{aq} \rightarrow OH^-_{aq} + OH^-_{aq} + NO_{2aq}$	3.6×10^8 $M^{-2}s^{-1}$	[49]
$NO_{aq} + NO_{aq} + O_{2aq} \rightarrow NO_{2aq} + NO_{2aq}$	2.3×10^6 $M^{-2}s^{-1}$	[49]
$NO_{aq} + NO_{2aq} + H_2O_{aq} \rightarrow HNO_{2aq} + HNO_{2aq}$	2×10^8 $M^{-2}s^{-1}$	[49]
$H\bullet_{aq} + HNO_{2aq} \rightarrow NO_{aq} + H_2O_{aq}$	4.5×10^8	[49]
$NO_{aq} + \bullet OH_{aq} \rightarrow HNO_{2aq}$	2×10^{10}	[49]
$NO_{2aq} + H\bullet_{aq} \rightarrow HNO_{2aq}$	1×10^{10}	[49]
$HNO_{3aq} + \bullet OH_{aq} \rightarrow NO_{3aq} + H_2O_{aq}$	1.2×10^8	[49]
$NO_{aq} + HO_2\bullet_{aq} \rightarrow HNO_{3aq}$	8×10^9	[49]
$NO_{2aq} + \bullet OH_{aq} \rightarrow HNO_{3aq}$	3×10^{10}	[49]
$O_2^-{}_{aq} + NO_{aq} \rightarrow NO_3^-{}_{aq}$	1.6×10^{10}	[49]
$NO_{aq} + HO_2\bullet_{aq} \rightarrow HOONO_{aq}$	3.2×10^9	[49]
$NO_{2aq} + \bullet OH_{aq} \rightarrow HOONO_{aq}$	1.2×10^{10}	[49]
$O_2^-{}_{aq} + NO_{aq} \rightarrow OONO^-_{aq}$	6.6×10^9	[49]
$H_3O^+_{aq} + OH^-_{aq} \rightarrow \bullet H_{aq} + \bullet OH_{aq} + H_2O_{aq}$	6×10^{10}	[49]
$HO_2\bullet_{aq} + H_2O_{aq} \rightarrow H_3O^+_{aq} + O_2^-{}_{aq}$	2×10^3	l
$H_3O^+_{aq} + O_2^-{}_{aq} \rightarrow HO_2\bullet_{aq} + H_2O_{aq}$	6×10^1	[50],l

$HNO_{2aq} + H_2O_{aq} \rightarrow H_3O^+_{aq} + NO_2^-{}_{aq}$	1.8×10^1	[50],l
$H_3O^+_{aq} + NO_2^-{}_{aq} \rightarrow HNO_{2aq} + H_2O_{aq}$	1.8	[50],l
$HNO_{3aq} + H_2O_{aq} \rightarrow H_3O^+_{aq} + NO_3^-{}_{aq}$	2×10^3	[50],l
$H_3O^+_{aq} + NO_3^-{}_{aq} \rightarrow HNO_{3aq} + H_2O_{aq}$	2×10^2	[50],l
$N_2O_{3aq} + H_2O_{aq} \rightarrow HNO_{2aq} + HNO_{2aq}$	1.1×10^4 $M^{-2}s^{-1}$	[49]
$N_2O_{4aq} + H_2O_{aq} \rightarrow HNO_{2aq} + HNO_{3aq}$	8×10^2 $M^{-2}s^{-1}$	[49]
$N_2O_{5aq} + H_2O_{aq} \rightarrow HNO_{3aq} + HNO_{3aq}$	1.2 $M^{-2}s^{-1}$	[49]
$NO_{2aq} + NO_{2aq} + H_2O_{aq} \rightarrow HNO_{2aq} + H_3O^+_{aq} + NO_3^-{}_{aq}$	1.5×10^8 $M^{-2}s^{-1}$	[49]
$NO_{2aq} + NO_{2aq} + H_2O_{aq} \rightarrow H_3O^+_{aq} + NO_2^-{}_{aq} + H_3O^+_{aq} + NO_3^-{}_{aq}$	5×10^7 $M^{-2}s^{-1}$	[51]
Radiative Transitions		
$He^{**} \rightarrow He$	5.7×10^4 s^{-1}	[33],d
$He^{***} \rightarrow He^*$	9.5×10^6 s^{-1}	[33]
$He^{**} \rightarrow He^*$	1.0×10^7 s^{-1}	[33]
$He_2^* \rightarrow He + He$	1×10^7 s^{-1}	[33]
$Ar^{***} \rightarrow Ar^*$	3.3×10^7 s^{-1}	[33]
$Ar^{***} \rightarrow Ar$	3.1×10^5 s^{-1}	[33],d
$Ar^{**} \rightarrow Ar$	5.3×10^5 s^{-1}	[33],d
$Ar_2^* \rightarrow Ar + Ar$	6×10^7 s^{-1}	[13]
$N_2^{***} \rightarrow N_2$	2×10^5 s^{-1}	[33],d
$N_2^{**} \rightarrow N_2^*$	3×10^7 s^{-1}	[24],d
$N_2^{***} \rightarrow N_2^*$	2×10^6 s^{-1}	[33],d
$N^* \rightarrow N$	6×10^7 s^{-1}	[33]
$H^* \rightarrow H$	4.7×10^8 s^{-1}	[33]
$H^{**} \rightarrow H$	5.6×10^7 s^{-1}	[33]
$H^{**} \rightarrow H^*$	4.4×10^7 s^{-1}	[33]

$H^{***} \rightarrow H^{*}$	8.4×10^{6} s^{-1}	[33]
$OH^{*} \rightarrow OH$	1.3×10^{6} s^{-1}	[52]
Photon Reactions		
$h\nu + H_2O_{aq} \rightarrow H_3O^{+}_{aq} + OH^{-}_{aq}$	1×10^{-20} cm^2	[53],l
$h\nu + H_2O_{aq} \rightarrow H\bullet_{aq} + \bullet OH_{aq}$	1×10^{-20} cm^2	[53],l
$h\nu + H_2O \rightarrow H_2O^{+} + e$	1×10^{-17} cm^2	[53],d

a) Rate coefficients have unit of cm^3s^{-1} unless noted otherwise. Electron temperature T_e is in eV. Gas temperature T_g is in K. T_n is the normalized gas temperature, (T_g/300)
b) Rate coefficient was obtained by solving Boltzmann's equation for the electron energy distribution. Cross sections for the process are from the indicated reference.
c) Cross section and rate coefficient obtained by detailed balance.
d) Approximated by analogy.
e) Reactants and products in parenthesis denote the same rate coefficient was used for all species.
f) Electron impact excitation into vibrational states 1-8 was lumped into a single vibrational state $N_2(v)$.
g) Electron energy loss in exciting H_2O to vibrational states was included in calculation of the electron energy distribution, however $H_2O(v)$ was not explicitly followed as an excited state in the model.
h) Charge neutralization reactions. Rate coefficients are estimated by the recombination reactions in the afterglow.
i) The radiation trapping factor is estimated to be 10^3 to 10^4 for UV and VUV emission.
j) M = He, Ar, N_2, H_2O
k) The solvation rate coefficient was estimated to be faster than other liquid reactions in order to not be rate limiting.
l) The rate coefficient is estimated according to the thermodynamic hydrolysis in liquid water.

[1] R. Deloche, P. Monchicourt, M. Cheret and F. Lambert, Phys. Rev. A 13, 1140 (1976).

[2] L. L. Alves, G. Gousset and C. M. Ferreira, J. Phys. D 25, 1713 (1992).

[3] D. Rapp and P. Englander-Golden, J. Chem. Phys. 43, 1464 (1965).

[4] L. Vriens, Phys. Lett. 8, 260 (1964).
[5] G. Bekefi, Radiation Processes in Plasmas, New York: Wiley, 1966.
[6] F. Emmert, H. H. Angermann, R. Dux and H. Langhoff, J. Phys. D 21, 667 (1988).
[7] H. W. Ellis, R. Y. Pai and E. W. McDaniel, At. Data Nucl. Data Tables 17, 177 (1976).
[8] Q. Wang, D. J. Economou and V. M. Donnelly, J. Appl. Phys. 100, 023301 (2006).
[9] K. Tachibana, Phys. Rev. A 34, 1007 (1986).
[10] I. P. Zapesochyni and L. L. Shimon, Opt. Spectrosc. 11, 155 (1966).
[11] R. H. McFarland and J. D. Kinney, Phys. Rev. A 137, 1058 (1965).
[12] M. A. Biondi in Principles of Laser Plasmas, G. Bekefi, ed. (New York: Wiley, 1976).
[13] F. Kannari, A. Suda, M. Obara and T. Fujioka, IEEE J. Quant. Electron. 19, 1587 (1983).
[14] Y. Itikawa, M. Hayashi, A. Ichimura, K. Onda, K. Sakimoto, K. Takayanagi, M. Nakamura, H. Nishimura and T. Takayanagi, J. Phys. Chem. Ref. Data 15, 985 (1986).
[15] A. V. Phelps and L. C. Pitchford, Phys. Rev. 31, 2932 (1985).
[16] S. Geltman, Quant J. Spectrosc. Radiat. Transfer 13, 601 (1973).
[17] R. Henry, P. G. Burke and A.-L. Sinfailam, Phys. Rev. 178, 218 (1969).
[18] A. Smith, Phys. Rev. 127, 1647 (1962).
[19] J. Mitchell, Physical Reports 186, 215 (1990).
[20] J. C. Person and D. O. Ham, Radiat. Phys. Chem. 31, 1 (1988).
[21] L. G. Piper, J. Chem. Phys. 87, 1625 (1987).
[22] L. G. Piper, J. Chem. Phys. 88, 231 (1988).
[23] A. Kossyi, A. Y. Kostinsky, A. A. Matveyev and V. P. Si, Plasma Sources Sci. Technol. 1, 207 (1992).
[24] Y. Ikezoe, S. Matsuoka, M. Takebe and A. Viggiano, Gas Phase Ion-Molecule Reaction Rate Constants Through 1986,, Ion Reaction Research Group of the Mass Spectroscopy Society of Japan, Tokyo, 1987.
[25] Y. Itikawa and N. Mason, J. Phys. Chem. Ref. Data 34, 1 (2005).
[26] B. R. Rowe, F. Vallee, J. L. Queffelec, J. C. Gomet and M. Morlais, J. Chem. Phys. 88, 845 (1988).
[27] P. Banks, Planet. Space Sci. 14, 1085 (1966).
[28] R. K. Janev, W. D. Langer, D. J. Evans and D. E. Post, Elementary Processes in Hydrogen and Helium Containing Plasmas, Berlin: Springer, 1987.

[29] K. N. Joshipuru, M. Vinodkumar and U. M. Patel, J. Phys. B:At. Mol. Opt. Phys. 34, 509 (2001).

[30] R. Riahi, P. Teulet, Z. B. Lakhdar and A. Gleizes, Eur. Phys. J. D 40, 223 (2006).

[31] T. I. Quickenden, S. M. Trotman, J. A. Irvin and D. F. Sangster, Chem. Phys. 71, 497 (1979).

[32] K. P. Madden and S. P. Mezyk, J. Phys. Chem. Ref. Data 40, 023103(2011).

[33] "NIST Chemical Kinetics Database.," [Online]. Available: http://kinetics.nist.gov/kinetics/index.jsp.

[34] F. J. Gordillo-Vazquez, J. Phys. D: Appl. Phys. 41, 234016 (2008).

[35] T. J. Miller, P. Farquhar and K. Willacy, Astron. Astrophys. Suppl. Ser. 121, 139 (1997).

[36] R. A. Sanders and E. E. Muschlitz, Int. J. Mass Spectrosc. Ion Phys. 23, 99 (1977).

[37] H. D. Jong, Chem. Phys. Lett. 25, 129 (1974).

[38] S. V. Pancheshnyi, S. M. Starikovskaia and A. Y. Starikovskii, Chem. Phys. 262, 349 (2000).

[39] A. V. Phelps, “Tabulations of Collision Cross Sections and Calculated Transport and Reaction Coefficients for Electron Collisions with O2”, JILA Information Center Report No. 28, 1985.

[40] D.S. Stafford and M.J. Kushner, J. Appl. Phys. 96, 2451 (2004).

[41] B. F. Gordiets, C. M. Ferreira, V. L. Guerra, J. Loureiro, J. Nahorny, D. Pagnon, M. Touzeau, and M. Vialle, IEEE Trans. Plasma Sci. 23, 750 (1995).

[42] A. W. Johnson and J. B. Gerardo, PRA 5, 1410 (1972).

[43] R. Dorai, PhD Thesis Department of Chemical Engineering, University of Illinois at Urbana-Champaign (2002).

[44] Y. Sakiyama, D.B. Graves, H-W. Chang, T. Shimizu, and G. Morfill, J. Phys. D: Appl. Phys. 45, 425201 (2012).

[45] M. Capitell, C.M. Ferreira, B.F. Gordiets, and A. Osipov, Plasma Kinetics in Atmospheric Gases, Springer, Berlin, 2000.

[46] R. E. Olson, J. R. Peterson, and J. Moseley, J. Chem. Phys. 53, 3391 (1970).

[47] K. Niemi, J. Waskoenig, N. Sadeghi, T. Gans, and D. O’Connell, Plasma Sources Sci. Technol. 20, 055005 (2011).

[48] K. P. Maddena and S. P. Mezyka, J. Phys. Chem. Ref. Data 40, 023103 (2011).

[49] NDRL/NIST Solution Kinetics Database, [Online]. Available: http://kinetics.nist.gov/solution/

[50] S. N. Pandis and J. H. Seinfeld, J. Geophys. Res. 94, 1105 (1989).

[51] M. Reist, K.-A. Marshall, P. Jenner and B. Halliwell, J. Neurochem. 71, 2431 (1998).

[52] W. R. Binns and J. L. Ahl, J. Chem. Phys. 68, 538 (1978).

[53] R. D. Hudson, Rev. Geophys. Space Phys. 9, 305 (1971).